



भारत सरकार
Government of India



BARC NEWSLETTER

FOUNDER'S DAY SPECIAL ISSUE

OCTOBER 2016





सत्यमेव जयते

भारत सरकार
Government of India

BARC NEWSLETTER

FOUNDER'S DAY SPECIAL ISSUE

OCTOBER 2016



भाभा परमाणु अनुसंधान केंद्र
Bhabha Atomic Research Centre

Editorial Committee

Chairman

Dr. G.K. Dey
Materials Group

Editor

Dr. G. Ravi Kumar
SIRD

Members

Dr. G. Rami Reddy, RSD
Dr. A.K. Tyagi, Chemistry Divn.
Dr. S. Kannan, FCD
Dr. C.P. Kaushik, WMD
Dr. S. Mukhopadhyay,
Seismology Divn.
Dr. S.M. Yusuf, SSPD
Dr. B.K. Sapra, RP&AD
Dr. J.B. Singh, MMD
Dr. S.K. Sandur, RB&HSD
Dr. R. Mittal, SSPD
Dr. Smt. S. Mukhopadhyay, ChED

From the Editor's Desk...

The Founder's day Special issue of the BARC Newsletter published on the eve of Founder's day celebration, carries award winning works of our Scientists and Engineers. Articles by the 2014 DAE awardees are being published in this issue.

This year a total of twenty five papers are being published in this issue. The CD contains articles from the recipients of the following awards:

1. Homi Bhabha Science & Technology Award
2. Scientific & Technical Excellence Award
3. Young Applied Scientist/Technologist Award
4. Young Scientist Award
5. Young Engineer Award
6. INSA Young Scientist Award.

Individual papers can be accessed from the Contents as well as from the Author Index by clicking on the hyperlinks.



Dr. G. Ravi Kumar

On behalf of the Editorial Committee

CONTENTS

DAE AWARDS 2014

DAE Homi Bhabha Science & Technology Award [2014]

- 1 Development of New Formulations for Mitigation of Radiation Injury and Improving the Outcome of Radiotherapy** **1**
Santosh Kumar Sandur
Radiation Biology & Health Sciences Division
- 2 Targeting G-quadruplex Structures with Extrinsic Probes: Prospect of Selective and Efficient G-quadruplex Inducers in Therapeutics** **6**
A. C. Bhasikuttan
Radiation & Photochemistry Division
- 3 Design and Development of Magnetic Lenses for Proton Accelerators** **10**
Vikas Teotia, Elina Mishra, Prashant Kumar and Sanjay Malhotra*
Accelerator Control Division
- 4 Setting up of In-situ X ray Absorption Spectroscopy measurement facility at Indus-2 SRS & Indigenous development of thin film multilayer neutron supermirrors** **18**
D.Bhattacharyya*, C.Nayak, A. Biswas, S.N. Jha and N.K. Sahoo
Atomic & Molecular Physics Division
- 5 Design of AHWR with Passive Systems: Challenges and Accomplishments** **24**
A.K. Nayak*, Mukesh Kumar, D.K. Chandraker and P.P. Kulkarni
Reactor Engineering Division

* Recipient of the award

DAE Scientific & Technical Excellence Award [2014]

- 6 Prediction of Materials for Hydrogen Storage: Quantum Chemical Methods and Materials Modeling are Indispensable Tools** 35
K.R.S. Chandrakumar
Theoretical Chemistry Section, Chemistry Group
- 7 Mechanical Design and Development of DC, RF Accelerator and ECR Ion Source Programme of APPD, BARC** 42
S.R. Ghodke*, Rajesh Barnwal, Mahendra Kumar, Susanta Nayak, D. Bhattacharjee, J. Mondal, A.S. Dhavle, Vijay Sharma, Shiv Chandan, Nishant Choudwary, R.I. Bakhatsing V. T. Nimje, K.P. Dixit, S. Acharya and P. Roychowdhury
Electron Beam Centre, Accelerator & Pulse Power Division
- 8 Improvements to Gang Type Spent Fuel Chopper at TRP, Tarapur** 51
Abhishant*, A.K. Jha, K. Agarwal
NRPSD, NRB, Mumbai
- 9 Augmentation of Blood Transfusion Services through Blood Component Therapy** 56
Susan Cherian
Medical Division
- 10 Suspendable Servo Manipulator for Hot Cell Application** 61
B. Sony*, P.V. Sarngadharan*, K. Jayarajan, and D.N. Badodkar
Division of Remote Handling & Robotics
- 11 Design and Development of Radiation Detectors for Nuclear Reactors** 65
Mary Alex
Electronics Division
- 12 Development of Technologically Important/Special Glasses and Glass-Ceramics for Various Strategic Applications** 71
Madhumita Goswami
Glass & Advanced Materials Division

* Recipient of the award

- | | |
|--|-------------------|
| <p>13 Experimental and Analytical Study for Safety of Nuclear Research Reactors Samiran Sengupta*, Aniruddha Ghosh and S. Mammen Research Reactor Design & Projects Division C. Sengupta Research Reactor Maintenance Division S. Bhattacharya Reactor Group</p> | <p>77</p> |
| <p>14 Theory of electronic structure and optical properties of graphene nanoribbons Kondayya Gundra Theoretical Physics Section Multidisciplinary Research Group</p> | <p>83</p> |
| <p>DAE Young Applied Scientist / Technologist Award [2014]</p> | |
| <p>15 Growth of Single Crystal Scintillators and Development of Nuclear Radiation Detectors Mohit Tyagi Technical Physics Division</p> | <p>89</p> |
| <p>16 Recovery of Uranium from Tummalapalle Leach Solution Using Novel Precipitating Method Sujoy Biswas Uranium Extraction Division</p> | <p>93</p> |
| <p>17 Design of a Permanent Magnet Based Focusing Lens for a Miniature Klystron Kumud Singh*, Janvin Itteera and Sanjay Malhotra Applied Physics Division</p> | <p>98</p> |
| <p>18 Augmented Reality Assisted Telerobotics System for Autonomous Pick and Place Operations Pritam Prakash Shete*, Abhishek Jaju, Prabir Pal and Surojit Kumar Bose Computer Division</p> | <p>102</p> |
| <p>19 An Insight in to the Effect of Ternary Alloying on Hydrogen Isotope Storage Properties of ZrCo Based Alloys Ram Avtar Jat Product Development Division</p> | <p>106</p> |

* Recipient of the award

DAE Young Scientist Award [2014]

- 20 Development of Novel Radionuclide Generators for Use in Nuclear Medicine** 110
Rubel Chakravarty
Isotope Production and Applications Division
- 21 Speciation and Binding of Uranyl Ion in Different Environments** 116
Mahesh Sundararajan
Radiation Biology & Health Sciences Division
- 22 Computational Modeling of Novel Materials for Hydrogen Energy Related Applications** 119
K. Srinivasu
Theoretical Chemistry Section, Chemistry Group

DAE Young Engineer Award [2014]

- 23 Design and Development of Precision Scientific Instruments and Parallel Manipulators** 124
Ramnik Singh*, S.P. Srivastava, V.K. Mishra, P.I. Hadagali and K.N. Karn
Centre for Design and Manufacture
Mala N.Rao and Saibal Basu
Solid State Physics Division
- 24 Design and Development of High Power Ultra Wideband Systems** 127
Sandeep Kumar Singh*, S. Mitra, Senthil K., Ranjeet Kumar, Archana Sharma, K.C. Mittal and R.K. Rajawat
Accelerator and Pulse Power Division

INSA Award

- 25 Reaction Dynamics Around Coulomb Barrier with Weakly Bound Nuclei** 133
Vivek Vijay Parkar
Nuclear Physics Division
- Author Index** 138

* Recipient of the award

Development of new formulations for mitigation of radiation injury and improving the outcome of radiotherapy

Santosh Kumar Sandur

Radiation Biology & Health Sciences Division

Dr. Santosh Kumar Sandur is the recipient of the DAE Homi Bhabha Science and Technology Award for the year 2014

Abstract

We have used phytochemicals, semisynthetic and synthetic molecules and rational drug design approach for prevention and treatment of radiation induced toxicity which will be useful for improving the outcome of radiotherapy and also for creating national stockpile for management of radiation emergencies in India. These novel formulations were tested in *in vitro* systems and their efficacy was established in preclinical animal models. The key research findings on discovery of radio-protective drugs have been transferred to private pharmaceutical company for translation to clinic. These formulations have also been studied for their safety, pharmacokinetics, detailed mechanism of action and intended route of administration. Here we present the progress on development of these new drugs and formulations and their possible health benefits to humans.

Introduction

Almost every second cancer patient receives radiotherapy in the form of external beam or internal irradiation given as brachytherapy. Despite technical improvements that allow precise deposition of dose in the tumor while progressively reducing any unwanted dose to surrounding normal tissues, many patients still suffer from side effects of normal tissue damage after radiotherapy¹. Acute and long term toxicities associated with radiotherapy of head & neck cancers are skin, mucosal damage and severe mucositis whereas thoracic irradiation for cancers of lung, esophagus and breast results in pneumonitis and fibrosis². There is also risk of unplanned exposures in case of nuclear emergencies or dirty bomb which emphasize the need for developing novel agents that can protect against unwanted side effects of IR. An ideal radioprotector must be non-toxic and should protect normal cells against the harmful effects of radiation without relinquishing the detrimental effects of IR on cancer cells. Several studies have been performed with objective to develop new and effective radiation countermeasures to reduce, prevent or lower the risk of normal tissue toxicity. Several drug targets such as free radicals, pro-survival transcription factors NF-kappaB and Nrf-2, cytokinereceptors, toll-like receptors, and radical scavengers are being explored³.

In house research efforts:

Our research efforts are focussed on development of novel therapeutics for prevention, mitigation and treatment of radiation induced toxicity towards normal tissues and also for improving the outcome of radiotherapy. In order to develop appropriate radio-modifiers and radioprotectors, we have screened a large number of phytochemicals, synthetic compounds, semisynthetic molecules, formulations, proteins and also used *in silico* docking approach for rational drug design. Majority of these compounds showed either anti-oxidant or pro-oxidant action in cell free and cellular systems. The screening of these molecules during past 15 years has helped us in identification of candidate molecules for development of radio-modifier drugs. Two most important formulations developed in our lab are named as BARC Radio-modifier (BRM) and BARC Radioprotector (BRP).

BARC Radio-modifier (BRM):

BRM is a formulation based on a semisynthetic water soluble derivative of green plant pigment chlorophyll. We for the first time demonstrated the direct antioxidant activity of chlorophyllin (BRM) in terms of scavenging of different types of reactive oxygen species (ROS) using electron spin resonance (ESR) spectroscopy. It was able

to scavenge the stable 1,1-diphenyl-2-picrylhydrazyl (DPPH) radicals as well as prevented the formation of 5,5-dimethyl-1-pyrroline-N-oxide adduct with hydroxyl radicals (DMPO-OH adduct) generated by γ -radiation in a dose-dependent manner. It also inhibited $^1\text{O}_2$ -dependent formation of the 2,2,6,6-tetramethyl-piperidine oxide (TEMPO) radical during photosensitization of methylene blue and hydrogen peroxide induced oxidation of phenol red⁴. BRM was also shown to act as an antioxidant and thereby prevent radiation-induced damage to biomolecules like DNA in cell free systems. Based on these cell free system findings, BRM was tested for its anti-oxidant activity in cells and animals. We found that BRM entered lymphocytes and scavenged radiation derived free radicals in a dose dependent manner in vitro as well as in the mice⁵. It also prevented radiation induced apoptosis in the sensitive tissues including lymphocytes. It showed multiple health benefits in experimental animals including augmentation of innate as well as adaptive immune responses via upregulation of anti-apoptotic genes⁶. It significantly protected mice against radiation induced toxicity, morbidity and mortality. In order to improve the radioprotective efficacy of BRM, we have tested several dose regimens and tried a variety of routes of administration in combination with other agents. It was found that a formulation containing BRM dose equivalent to human dose of 15 to 45 mg / kg body weight offered significant protection against whole body irradiation induced mortality in mice (Fig. 1). At these doses, it increased the abundance of hematopoietic stem cells and enhanced the production of granulocytes in the bone marrow. The hematopoietic stem and progenitor cells (HSPCs) are the progenitor cells for all blood cells. The proliferation and differentiation of HSPCs give rise

to the entire hematopoietic system. HSPCs are believed to be capable of self-renewal, expanding their own population of stem cells and being pluripotent are capable of differentiating into any cell in the hematopoietic system. From this rare cell population, the entire mature hematopoietic system, comprising lymphocytes (B and T cells of the immune system) and myeloid cells (erythrocytes, megakaryocytes, granulocytes and macrophages) are formed.

BRM also increased serum levels of granulocyte colony stimulation factor (G-CSF) concurrent with higher frequency of neutrophils in peripheral blood⁷. Neutrophils are the first line of defense in the immune system and they protect the body against most of the infections. Ionizing radiation induced depletion of neutrophils increases the susceptibility to infections. The depletion of hematopoietic stem cells following exposure to radiation suppresses hematopoiesis resulting in long term immune suppression. Percent granulocytes are a biological marker for efficacy of BRM as a radioprotector in vivo. The increase in granulocytes in response to BRM treatment and increased abundance of hematopoietic stem cells would boost the immune system and thus improve the survival following exposure to ionizing radiation. We indeed found that BRM significantly protected mice against whole body irradiation induced mortality. The safety and toxicity profile of BRM was evaluated in detail and it was found that an acute dose of 5000mg / kg body weight was well tolerated in rodents. Further, it did not induce any toxicity in mice when a repeated daily dose of 1000mg / kg body weight was administered for 28 consecutive days.

Our recent studies revealed that BRM significantly prevented radiation induced toxicity in the lungs, bone marrow and gastro-intestinal tract. However, BRM did not offer protection to lymphoma cells, lung cancer cells or breast cancer cells against radiation. On the contrary, it increased the radiosensitivity of these cancer cells by inducing mitotic catastrophe and delaying DNA repair (Fig. 2). BRM also sensitized the human breast cancer cells to ionizing radiation in vivo (Fig. 3A and B).

Based on these findings in the pre-clinical settings, it is proposed that BRM would find application as an adjuvant during cancer radiotherapy. A USA patent application entitled 'A method of adjuvant treatment with chlorophyllin containing therapeutic preparation including for radioprotection of normal tissues during radiation therapy and kit therefor' has been filed.

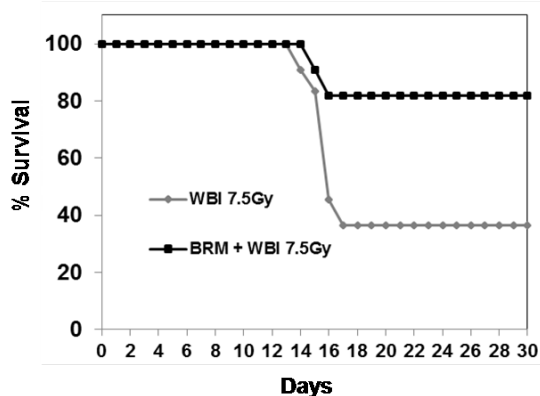


Fig. 1: Radioprotective efficacy of BRM against mortality in mice exposed to 7.5 Gy dose of whole body irradiation.

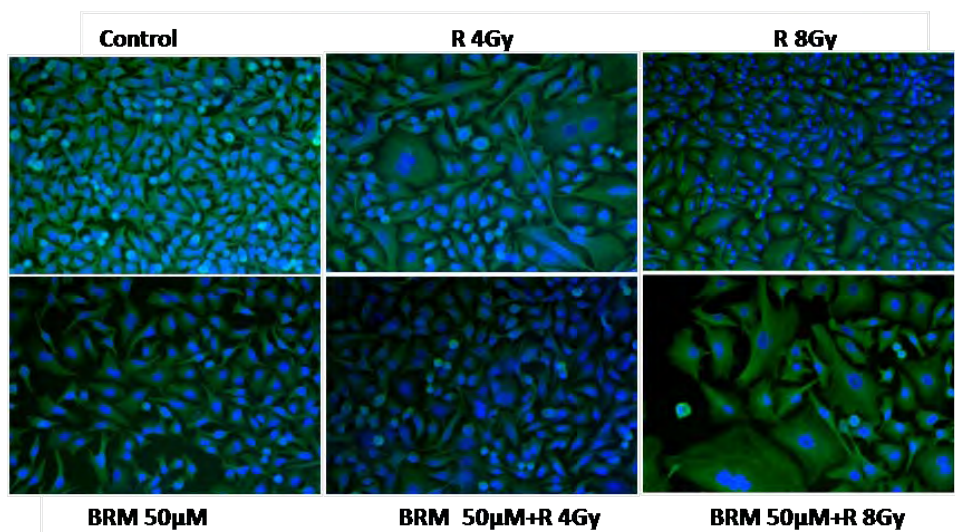


Fig. 2: Microscopic images of Hoechst stained nuclei of MCF7 human breast cancer cells 48 h after exposure to 4 Gy or 8 Gy dose of radiation in presence or absence of BRM.

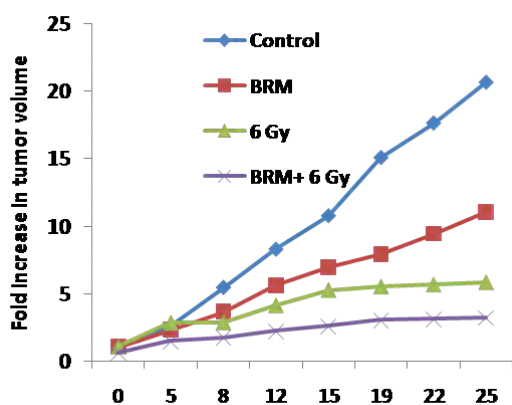


Fig. 3:(A) Photographs of human breast cancer derived tumors isolated from SCID mice after treatment with BRM, radiation (6 Gy) or BRM+ radiation (6Gy) as compared to control. (B) Growth kinetics of human breast cancer derived tumors in SCID mice on different days after treatment with BRM, radiation (6 Gy) or BRM+ radiation (6Gy) as compared to control.

In order to translate these findings to clinic, the technology for development of tablets and oral admissible formulations, it has been incubated with M/S Innovative Drug Research Solutions, Bangalore. The BRM tablets may be administered alone or in combination with pharmaceutically acceptable carriers, vehicles or diluents, in either single or multiple doses. Thus, for purposes of oral administration, tablets containing various excipients have been prepared (Fig. 4). The composition suitable for oral administration will provide immediate, delayed, extended or controlled release of BRM. BRM exhibited dissolution profile such that almost 80% of the active pharmaceutical ingredient is released in less than 25 minutes.



Fig. 4: Photograph of one batch of tablets of BRM manufactured by M/S IDRS Pvt Ltd Bangalore, India.

These formulations will be useful for prevention and treatment of radiation induced toxicity in people exposed to radiation under planned exposure settings. It can also be useful for increasing the radiosensitivity of

breast cancer stem cells and lung cancers. Another novel therapeutic use of BRM based formulations will be for increasing hematopoietic recovery in lymphopenic patients.

BARC Radioprotector (BRP):

The lectin-based formulation developed in our laboratory will be useful for mitigation of radiation induced toxicity in people who may accidentally receive whole body or partial body radiation exposure at high (supra lethal) doses of ionizing radiation. We found that a single intravenous injection of lectin to mice offered protection against 10-12 Gy of γ -radiation-induced mortality and male sterility and also abrogated 12 Gy induced decrease in testosterone levels in the serum of male mice (Fig. 5A & B).



**Pups born to Normal father
+ Normal Mother**



**Pups born to BRP + WBI 10 Gy treated father
+ Normal Mother**

Fig. 5: Photographs of pups born after mating of male mice administered with BRP and exposed to 10Gy dose of whole body irradiation with normal female (A) as compared to pups born after mating of normal unirradiated male and female mice (B).

A single intravenous administration of lectin to mice 4h after irradiation (8.5 Gy) offered 80% survival advantage indicating its potential as a therapeutic agent during unplanned radiation exposure scenarios.

We have also discovered the anti-tumor, immune-suppressive and anti-inflammatory molecules from medicinal plants (*Terminalia arjuna*, *Plumbago zeylanica*, *Mirabilis jalapa*, *Sisandrachinensis*, *Curcuma longa* and *Withaniasomnifera*), tea / coffee and synthetic sources and tested them in preclinical experimental models⁸.

Conclusions

Our preclinical studies on BRM and BRP have shown very promising efficacy as radio-modifier and radioprotective agents. Clinical trials in human subjects will be conducted for using these candidates as drugs for improving the outcome of radio therapy / chemotherapy. The initial trials will be carried out in collaboration with a pharmaceutical company, clinical research organization and Tata Memorial Centre, Mumbai.

References:

1. Begg, A. C.; Stewart, F. A.; Vens, C., Strategies to improve radiotherapy with targeted drugs. *Nat Rev Cancer* **2011**, *11* (4), 239-53.
2. Yazbeck, V. Y.; Villaruz, L.; Haley, M.; Socinski, M. A., Management of normal tissue toxicity associated with chemoradiation (primary skin, esophagus, and lung). *Cancer J* **2013**, *19* (3), 231-7.
3. (a) Burdelya, L. G.; Krivokrysenko, V. I.; Tallant, T. C.; Strom, E.; Gleiberman, A. S.; Gupta, D.; Kurnasov, O. V.; Fort, F. L.; Osterman, A. L.; Didonato, J. A.; Feinstein, E.; Gudkov, A. V., An agonist of toll-like receptor 5 has radioprotective activity in mouse and primate models. *Science* **2008**, *320* (5873), 226-30; (b) Kim, S. B.; Pandita, R. K.; Eskiocak, U.; Ly, P.; Kaisani, A.; Kumar, R.; Cornelius, C.; Wright, W. E.; Pandita, T. K.; Shay, J. W., Targeting of Nrf2 induces DNA damage signaling and protects colonic epithelial cells from ionizing radiation. *Proc Natl Acad Sci U S A* **2012**, *109* (43), E2949-55; (c) Johnke, R. M.; Sattler, J. A.; Allison, R. R., Radioprotective agents for radiation therapy: future trends. *Future Oncol* **2014**, *10* (15), 2345-57.
4. Sandur, S. K.; Devasagayam, T. P.; Bhushan, B.; Verma, N. C., Scavenging of reactive oxygen species by chlorophyllin: an ESR study. *Free Radic Res* **2001**, *35* (5), 563-74.
5. Sandur, S. K.; Shankar, B.; Sainis, K. B., Effect of chlorophyllin against oxidative stress in splenic

- lymphocytes in vitro and in vivo. *Biochim Biophys Acta* **2004**,1672 (2), 100-11.
6. Sharma, D.; Sandur, S. K.; Sainis, K. B., Antiapoptotic and immunomodulatory effects of chlorophyllin. *Mol Immunol* **2007**,44 (4), 347-59.
 7. Suryavanshi, S.; Sharma, D.; Checker, R.; Thoh, M.; Gota, V.; Sandur, S. K.; Sainis, K. B., Amelioration of radiation-induced hematopoietic syndrome by an antioxidant chlorophyllin through increased stem cell activity and modulation of hematopoiesis. *Free Radic Biol Med* **2015**,85, 56-70.
 8. (a) Checker, R.; Gambhir, L.; Sharma, D.; Kumar, M.; Sandur, S. K., Plumbagin induces apoptosis in lymphoma cells via oxidative stress mediated glutathionylation and inhibition of mitogen-activated protein kinase phosphatases (MKP1/2). *Cancer Lett* **2015**,357 (1), 265-78;(b) Patwardhan, R. S.; Sharma, D.; Thoh, M.; Checker, R.; Sandur, S. K., Baicalein exhibits anti-inflammatory effects via inhibition of NF- κ B transactivation. *Biochem Pharmacol* **2016**,108, 75-89;(c) Patwardhan, R. S.; Checker, R.; Sharma, D.; Kohli, V.; Priyadarsini, K. I.; Sandur, S. K., Dimethoxycurcumin, a metabolically stable analogue of curcumin, exhibits anti-inflammatory activities in murine and human lymphocytes. *Biochem Pharmacol* **2011**,82 (6), 642-57.

Targeting G-quadruplex Structures with Extrinsic Probes: Prospect of Selective and Efficient G-quadruplex Inducers in Therapeutics

A. C. Bhasikuttan

Radiation & Photochemistry Division

Dr. A.C. Bhasikuttan is the recipient of the DAE Homi Bhabha Science and Technology Award for the year 2014

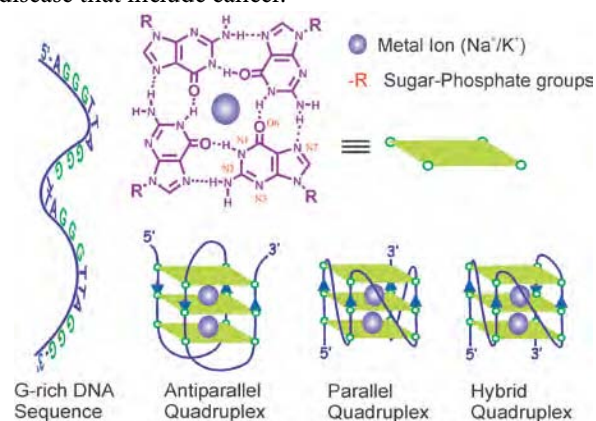
Abstract: The research on the G-quadruplex DNAs has received much attention in recent years and numerous reports appeared probing its detection, structure, stability, reactivity and selectivity, aimed mainly for the chemical intervention of specific biological activity or sensor applications. Our study has demonstrated the use of a fluorogenic dye, Thioflavin T, to stabilize the telomeric DNA strand into a G-quadruplex structure under physiological conditions. We have assessed several other DNA forms and set appropriate conditions to achieve highly selective interaction of the probe with the G-quadruplex structure. In addition, the dye becomes highly fluorescent, more than 2000 times brighter, increasing the sensitivity for the optical detection of the G-quadruplex in the cellular environment against other DNA forms. This work reveals the applicability of Thioflavin T to inhibit telomerase activity and opens up avenues to explore new dyes/drugs based on ThT scaffold, which have the potential to highly specific quadruplex inducing/sensing agents for cancer therapeutics.

Key Words: G-quadruplex, human telomeric DNA, Fluorescence, Thioflavin T.

Introduction

Nucleic acids are capable of forming a wide variety of structures, far indifferent from the Watson-Crick double helix. Among various non-canonical nucleic acid structures, the G-quadruplex motifs have attracted immense research attention as prospective targets for chemical intervention of biological functions. G-quadruplexes (Scheme-1) are formed in guanine rich telomeric and oncogene regions and are implicated in the expression of growth factors. G-quadruplexes are four stranded nucleic acid structures (Scheme-1) formed by stacking of Hoogsteen base paired G-quartets, which are prevalent in G-rich sequences. G-quadruplex structure is considered to be functionally important in the mammalian genome for transcriptional regulation, DNA replication and genome stability and their presence can be explored in assessing cellular functions, or can be utilized for chemical intervention of biological activities. Because of their abundance in functional genomic regions, especially at the end of eukaryotic chromosomes (telomeres), in the promoter regions of important protooncogenes, and in the untranslated regions of mRNAs, they have been recognized as significant drug

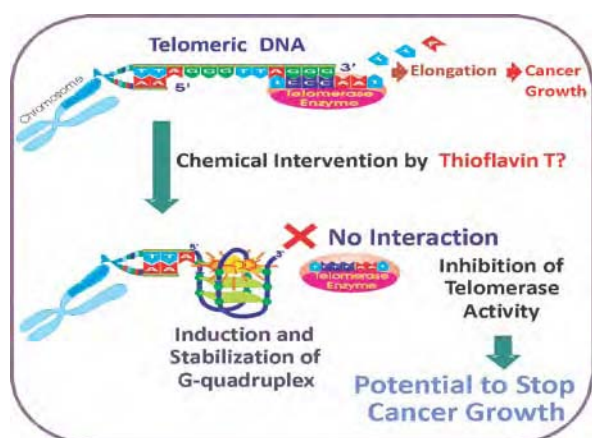
targets to halt the function of telomerase and regulate gene expression. Thus, the functional relevance of G-quadruplexes in human genome is of fundamental importance to life and may well hold the key to new therapeutic approaches in numerous areas of human disease that include cancer.



Scheme 1 Structures of the G-quartet/tetrad and the various common folding topologies found in G-quadruplexes

Even though G-quadruplexes have been extensively studied for more than 20 years, the exact nature of their

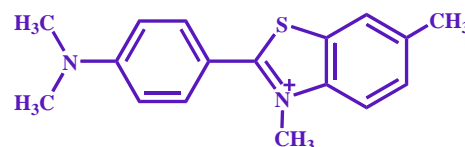
biological significance, apart from the telomerase activity of the single strand telomere overhang, is still poorly understood. The discovery in the mid 1990s that telomeric DNA is maintained in majority of cancer cells by the action of the telomerase enzyme complex, which synthesizes telomeric DNA repeats and maintains the immortalization of cancer cells (Scheme-2). By contrast, in normal somatic cells, telomerase is not significantly expressed and the normal mechanism of DNA replication results in progressive shortening of telomeric DNA and undergoes programmed cell death. This finding developed into the concept of targeting/inhibiting telomerase activity via induction or stabilization of a G-quadruplex as therapeutic strategy for fighting cancer (Scheme-2). This has stimulated intense research in exploring the stabilization of different quadruplex topologies by extrinsic molecular ligands as potential therapeutic agents for anticancer treatment.



Scheme-2: Action of Telomerase enzyme on the Telomeric DNA, causing uncontrolled growth/cancer and the plausible chemical intervention to induce G-quadruplex and stop the action of telomerase enzyme, thus promising to arrest cancer growth.

It has been found that many of the quadruplex binding dyes do equally interact with other DNA forms like the single strand or duplex DNAs, which make them nonspecific. Hence the development of cellular probes for detection of G-quadruplex structures, which can discriminate other DNA/RNA forms in cells, is inherently difficult. Therefore, there is a need to develop quadruplex specific dyes/ligands which can selectively induce and stabilize quadruplex structures and *in-situ* function as selective fluorescent probe for *in vitro* or *in vivo* visualization of key cellular processes. Noncovalent, extrinsic fluorescent probes find extensive usage as local

reporters in many biological applications, especially in various fields of protein/DNA analysis. Here, the specific interaction with the protein/DNA environment may introduce considerable change in the photophysical characteristics of the dye, projecting the details of its local microenvironment.



Thioflavin T (ThT)

Majority of potential G-quadruplex ligands, however, have been developed as telomerase inhibitors by virtue of their ability to stabilize pre-formed G-quadruplex structures in the 3'-telomeric overhang. However, it has been found that many of the quadruplex binding dyes do equally interact with other DNA forms like the single strand or duplex DNAs, which make them nonspecific for quantitative measurements. With this aim, we have investigated the interaction of ThT with human telomeric DNA (22AG: 5' AGGGTTAGGGTTAGGGTTAGGG-3') and compared it with other single stranded (ss-) or double stranded (ds-) DNAs as well as with the calf thymus DNA (ct-DNA).

Gradual titration of the 22AG human telomeric DNA with the ThT solution at specific solution conditions, resulted in significant bathochromic shift in the ThT absorption profile (Fig.1A) with a concomitant enhancement in the fluorescence intensity (I/I_0) to the order of ~1500-fold, as displayed in Fig. 1B. Since the 22AG DNA strand is prone to fold into quadruplex structures in presence of metal ions, it is quite likely that in the presence of ThT and in the absence of any metal ions, the fluorescence enhancement in ThT could originate from its interaction with a quadruplex structure induced by the cationic ThT itself. To explore this, the measurements in presence of K⁺ ions displayed remarkable changes as the titration of pre-folded 22AG quadruplexes (both parallel and antiparallel) with ThT (50 mM KCl, 50 mM Tris, pH 7.2), displayed huge enhancement in the emission intensity to ~2100 fold. In other words, the good agreement among the spectral features of 22AG-ThT system seen both in the presence of K⁺ or in the absence of metal ions, explicitly highlights the role of ThT in inducing quadruplex folding in the

22AG sequence, particularly in the absence of salt. The resulting fluorescence 'light-up' in ThT to ~2100-1700 fold, in the presence and absence of K^+ , respectively, illustrates that ThT acts as an efficient inducer of quadruplex DNA.

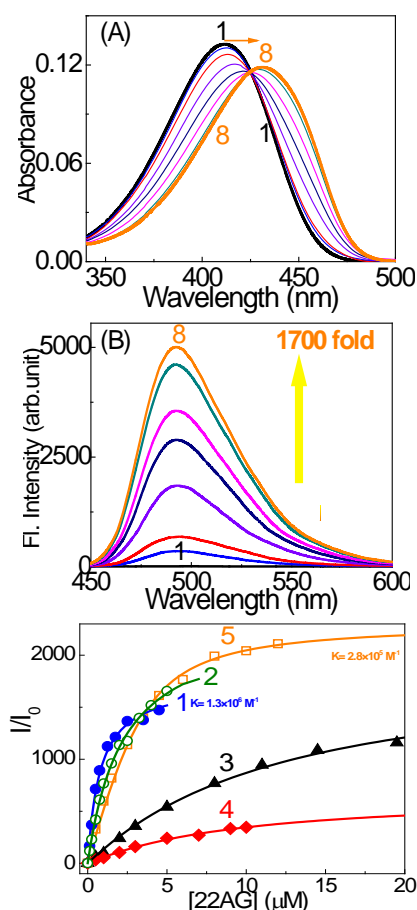


Fig. 1: Absorption (A) and fluorescence (B) spectra of ThT with 22AG DNA at different buffer concentrations. A and B; ThT solution (3.5 μM) containing 5 mM Tris (pH 7.2) with [22AG]/μM: (1) 0, (2) 0.12, (3) 0.25, (4) 0.75, (5) 1.5, (6) 2.5, (7) 4.0, (8) 5.0. λ_{ex} for B is 425 nm (C): Fluorescence intensity enhancement (I/I_0) of ThT (~3 μM) at 490 nm plotted against the 22AG DNA at different solution conditions. (1) Solution containing no buffer and salt; (2) buffered at 5 mM Tris, pH 7.2; (3) 50 mM Tris, pH 7.2; (4) solution containing 50 mM NaCl and 50 mM Tris (pH 7.2); (5) 50 mM KCl and 50 mM Tris (pH 7.2).

Saturation in the emission intensity of ThT observed with very low concentrations of the 22AG DNA at different solution conditions (Fig.1C) suggests strong interaction of ThT with the quadruplex DNA. A 1:1 stoichiometric analysis of this binding curve at 490 nm at different solution conditions provided the binding

constants which varied with the change in the surrounding medium. By circular dichroism (CD) measurements, it has been shown that the 22AG DNA in buffered solution (5-50 mM, Tris, pH 7.2) displayed characteristic CD bands at 265 nm and the 240 nm (Fig.2A,B), which matched well with the standard CD bands reported for parallel quadruplexes. Further, on introducing K^+/Na^+ and ThT, the broad multi shouldered band below 350 nm region, gradually transformed to display a distinct positive band at 295 nm and a trough at 265 nm, a clear signature of change over to the antiparallel topology.

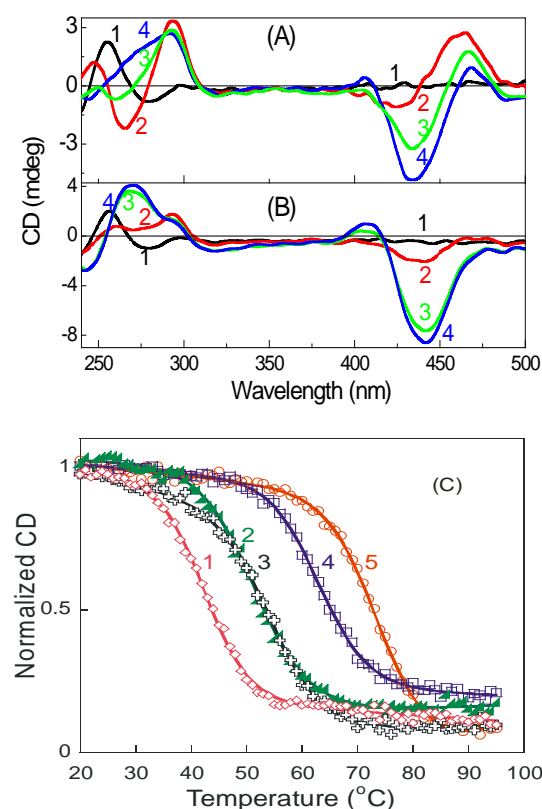


Fig. 2: CD spectra recorded for 22AG DNA (12.5 μM) at different Tris buffer concentrations with ThT. (A) solution buffered with 5 mM Tris (pH 7.2); (B) 50 mM Tris (pH 7.2). ThT: (1) 0 eq; (2) 2eq; (3) 4eq; (4) 8eq. (C) Melting curves for 22AG DNA (12.5 μM) in Tris (50 mM, pH 7.2) in the presence and absence of ThT. (1) 12 eq of ThT; (2) NaCl (50 mM); (3) NaCl (50 mM) with 8 eq of ThT; (4) KCl (50 mM); (5) KCl (50 mM) with 8eq of ThT. Melting of antiparallel quadruplex and parallel quadruplex were monitored at 295 nm and 265 nm respectively.

The extent of quadruplex stabilization in presence of salt and/or ThT was assessed from their melting temperature (T_m) evaluated from the CD thermal denaturation profiles presented in Fig.2C. In the unbuffered 22AG solution containing ThT, the quadruplex melting curve

monitored at 295 nm (antiparallel folding) provided a T_m \sim 55°C, whereas, the parallel quadruplex formed in buffered solution of 22AG and ThT was found to be much less stable, as the T_m monitored at 265 nm (parallel folding) decreased to 42.6 \pm 0.2°C (Fig.2C).

On the other hand, the antiparallel 22AG quadruplex predominant in presence of Na⁺ provided the T_m as 51.6 \pm 0.1°C, which improved only marginally to 55.0 \pm 0.3°C (ΔT_m \sim 3.4°C) on introducing ThT dye. In presence of K⁺ ions, the melting curve for the 22AG at 295 nm provided the T_m as 63.3 \pm 0.2°C, which further increased to 74 \pm 1°C (ΔT_m = 11°C) in presence of ThT, registering significant improvement in the quadruplex stability imparted by the ThT. The melting temperature and hence the stability of the 22AG quadruplexes in presence of ThT/buffer/salt/ conditions are seen in good agreement with the structural transformations and the corresponding spectral features observed from the absorption, fluorescence and the CD measurements. The finding that even in the absence of salt and buffer, the ThT induced antiparallel 22AG quadruplex DNA exhibited better stability and emission enhancement (T_m \sim 55°C, I/I_0 \sim 1500 fold) is prominent, as it allows to explore the quadruplex dynamics in salt-free conditions too, at par with that possible in presence of K⁺ (T_m \sim 74°C, >2000 fold).

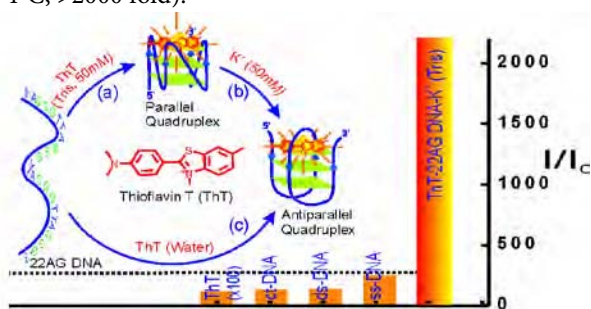


Fig. 3: Emission intensity enhancement (I/I_0) of ThT with various DNAs. Inset: Schematic representation of the topological transformation in the 22AG human telomeric DNA to parallel and antiparallel quadruplex by Thioflavin T (ThT) in the presence of Tris (pH 7.2)/K⁺.

To recognize the selectivity of ThT towards the quadruplex DNA, similar experiments have been carried out with DNAs of nonspecific sequences, as single strands (ss-) and duplex (ds-) DNAs (Fig.3). In both the cases, the fluorescence enhancements were found to be only in the range of 180-220 fold. Particularly, the double stranded calf thymus DNA (ct-DNA) too afforded emission enhancement in ThT \sim 250 fold, which further

decreased in presence of salt. Clearly, the striking dominance of emission enhancement in the 22AG DNA in the absence or presence of salt (especially K⁺) vs other DNA strands, unambiguously establishes the highly selective fluorescence *light-up* of ThT on the quadruplex DNA.

In summary, in this study, we demonstrated the function of a water soluble fluorogenic dye, Thioflavin T (ThT), in a dual role of exclusively inducing quadruplex folding in the 22AG human telomeric DNA and for sensing the same by its remarkable fluorescence *light-up* having emission enhancement \sim 2100 fold in the visible region. This work opens up avenues to explore new dyes based on ThT scaffold, which have the potential to emerge as highly specific quadruplex inducing agent for diagnostic, therapeutic and cation sensing applications. We are optimistic to take up these results to the visualization of G-quadruplex formation in the human transcriptome, and corroborate the selectivity and application of stabilizing ligands that target G-quadruplexes within a cellular context, a positive note on the prospect of intervention in biological processes as an anticancer strategy.

Acknowledgements

I acknowledge the contributions of all my collaborators and co-authors of our published works. I also thank the colleagues in RPCD and CG, BARC for their constant encouragement and support.

References

1. J. Mohanty, N. Barooah, V. Dhamodharan, S. Harikrishna, P. I. Pradeepkumar, A. C. Bhasikuttan, *J. Am. Chem. Soc.* **2013**, *135*, 367-376.
2. A.C. Bhasikuttan, J. Mohanty *Chem. Commun.*, **2015**, *51*, 7581-7597.
3. V. Dhamodharan, S. Harikrishna, A. C. Bhasikuttan, P. I. Pradeepkumar, *ACS. Chem. Biol.*, **2015**, *10*, 821-833.
4. A. C. Bhasikuttan, J. Mohanty, H. Pal. *Angew. Chem. Int. Ed.*, **2007**, *46*, 9305-9307.
5. S. Dutta Choudhury, J. Mohanty, H. Pal, A. C. Bhasikuttan, *J. Chem. Sci.*, **2014**, *126*, 911-917.
6. G. Biffi, D. Tannahill, J. McCafferty, S. Balasubramanian, *Nature Chem.*, **2013**, *5*, 182-186.
7. G. Biffi, M. Di Antonio, D. Tannahill, S. Balasubramanian, *Nature Chem.*, **2013**, *6*, 75-80.

Design and Development of Magnetic lenses for Proton Accelerators

Vikas Teotia, Elina Mishra, Prashant Kumar and Sanjay Malhotra
Electromagnetic Applications Section, Accelerator Control Division

Dr. Sanjay Malhotra is the recipient of the DAE Homi Bhabha Science and Technology Award for the year 2014

Abstract

High Energy Proton beams have application in scientific, industrial and Medical fields. High energy proton accelerators mainly consist of an ion source and array of RF accelerating cavities and focusing magnets. Low energy section of accelerator deploys solenoid magnets as they focus the beam simultaneously in both axes, although they are less efficient than quadrupole focusing magnets. The paper discusses design of Electromagnetic Quadrupole for transverse focusing in 200 MeV sections of a High Energy Proton Accelerator and magnetic measurements carried out on Permanent Magnet Quadrupoles for DTL of LEHIPA (Low Energy High Intensity Proton Accelerator). Optimisation techniques to achieve magnetic field uniformity better than 1000 ppm in Good field region is described. Detailed studies carried out on the influence of Magneto motive forces on figure of merit of the magnet, in terms of uniformity and magnetic field gradient is described. Field uniformity, linearity and higher order modes achieved in the design are elaborated. Based on this design, fabrications of the magnets were taken up. Paper also discusses measurement results of Permanent Magnets based quadrupole focusing lenses developed for LEHIPA project of BARC.

Keywords: Accelerators, proton, PMQ, EMQ, Good Field Region, HEPA, emittance

Introduction

Charged particle beams in accelerators tend to defocus due to Columbic repulsions and transverse kicks attributable to fringe E-fields in the cavity, the strength of which depend on the synchronous phase and Electromagnetic design of RF accelerating cavities [1, 5]. The transverse blow-up of beam increases the cross section of the beam which degrades the spatial current density which is undesirable. Electromagnetic forces are required to annul this transverse defocusing. Among the available options of using Electric field or magnetic field for charged particle focusing, magnetic fields are preferred since generation of an equivalent B-field is convenient than generation of equivalent E-field [2]. However, at low particle energy, E-fields are preferred as magnetic Lorentz forces are low owing to low particle velocity. For high energy beams, B-field focusing is natural choice for transverse focusing. Magnetic Quadrupole are used for focusing of charged particle beams. Depending on design, these quadrupoles could be permanent magnet based [3, 4] or electromagnet based (Warm (iron dominated) or Superconducting (coil design)). The latter choice provides the advantage of ease

in tuning while former is more efficient in terms of power consumption during operations [5]. Magnetic field strength of quadrupole magnet is given in terms of integrated magnetic field gradient denoted as *integral G.dl*. The required integral G.dl depends on beam emittance at entry of the magnetic lens; magnetic quadrupoles are therefore operated normally from 50% to 100% of their rated strength. Electromagnetic Quadrupole becomes the obvious choice for such applications. This paper describes design and analysis of an EMQ for 200 MeV section of a proton accelerator, in detail and also describes the results of magnetic measurements on Permanent Magnet Quadrupoles for LEHIPA. Since quadrupoles provides alternate gradient focusing [5], the focusing and de-focusing quadrupoles are always used in pairs, aptly named as “doublet assembly”.

System specifications

Layout

The high energy section of proton accelerator consists of an array of accelerating cavities and focusing elements. Depending on the particle β , the accelerating cavities

could be normal conducting DTL, half wave resonators, Spoke resonators or elliptical cavities. At 200 MeV elliptical cavities are more efficient than other families of resonators. HEPA (High Energy Proton Accelerator) has

three five-cell elliptical cavities followed by a doublet assembly. The RF cavities and focussing magnet arrangement is periodic, number of which depends on desired output energy.

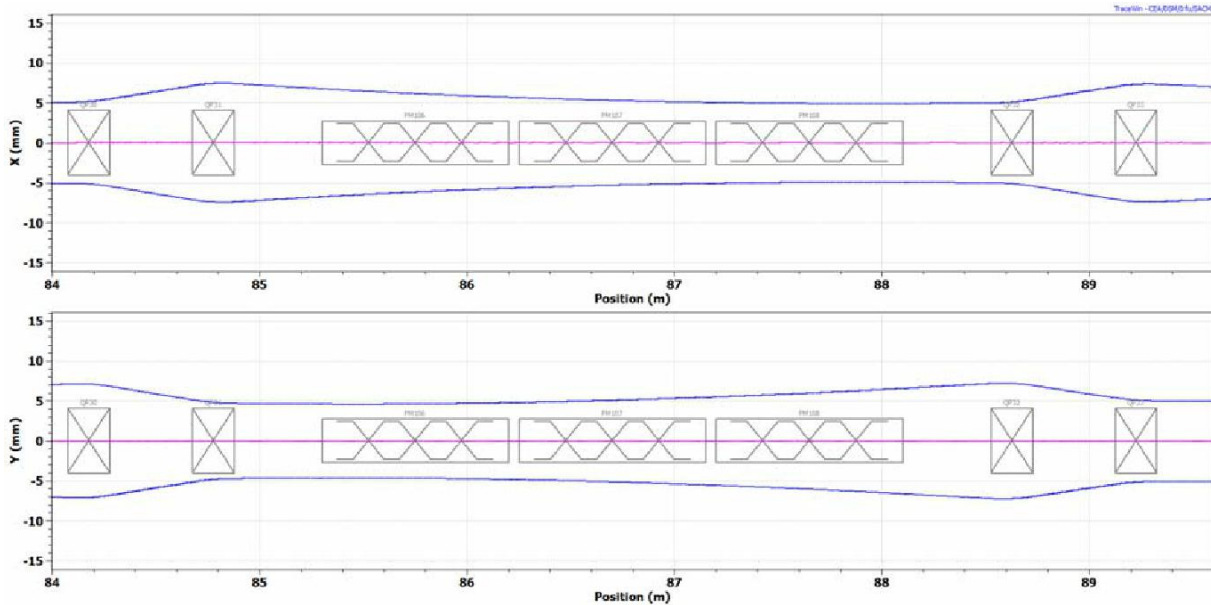


Fig. 1: Beam envelope in one section of the HEPA with doublet assembly and RF cavities

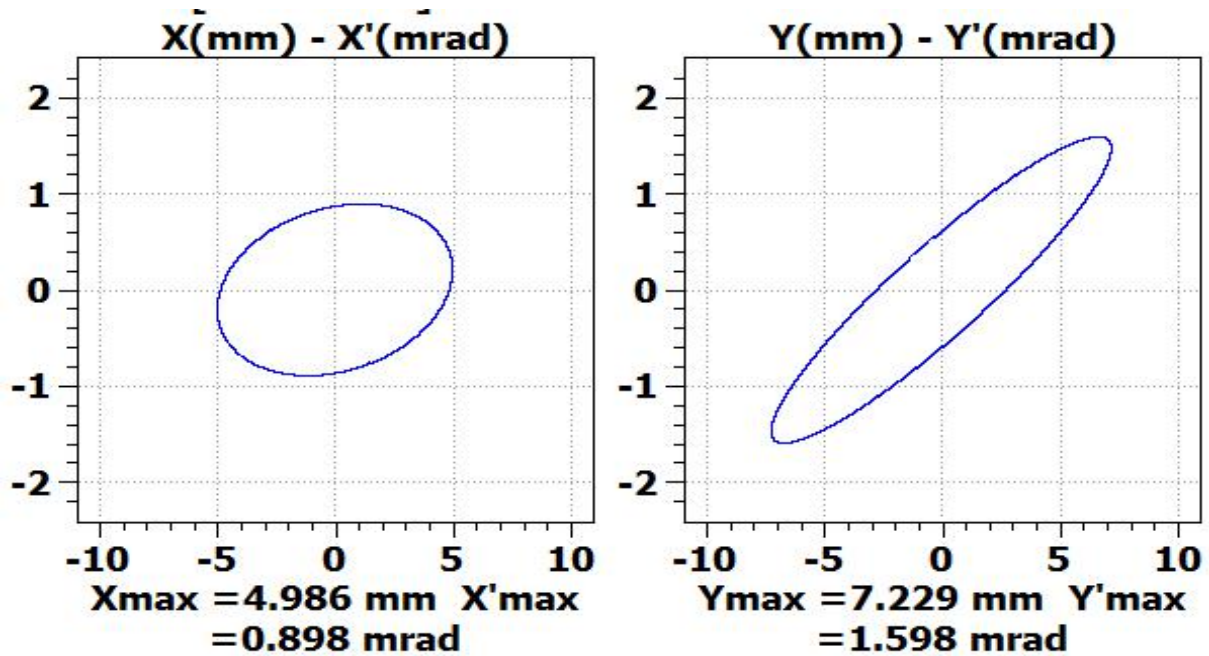


Fig. 2(a): Phase space of beam at entry of Quadrupole Doublet magnet assembly

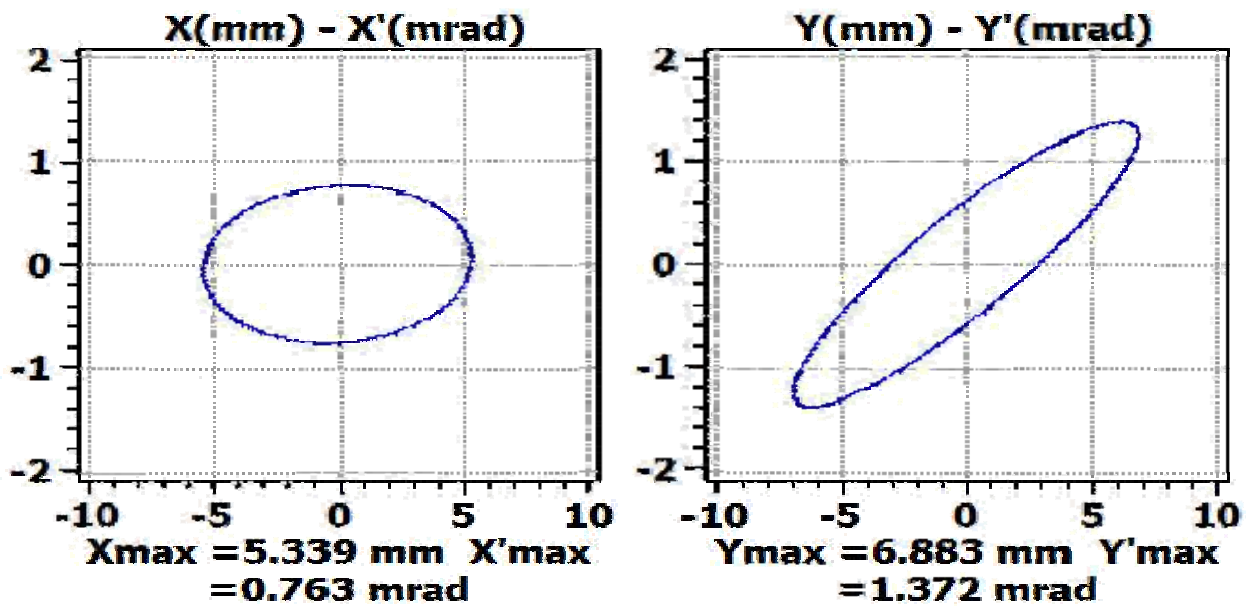


Fig 2(b): Phase space of beam at exit of Quadrupole Doublet magnet assembly

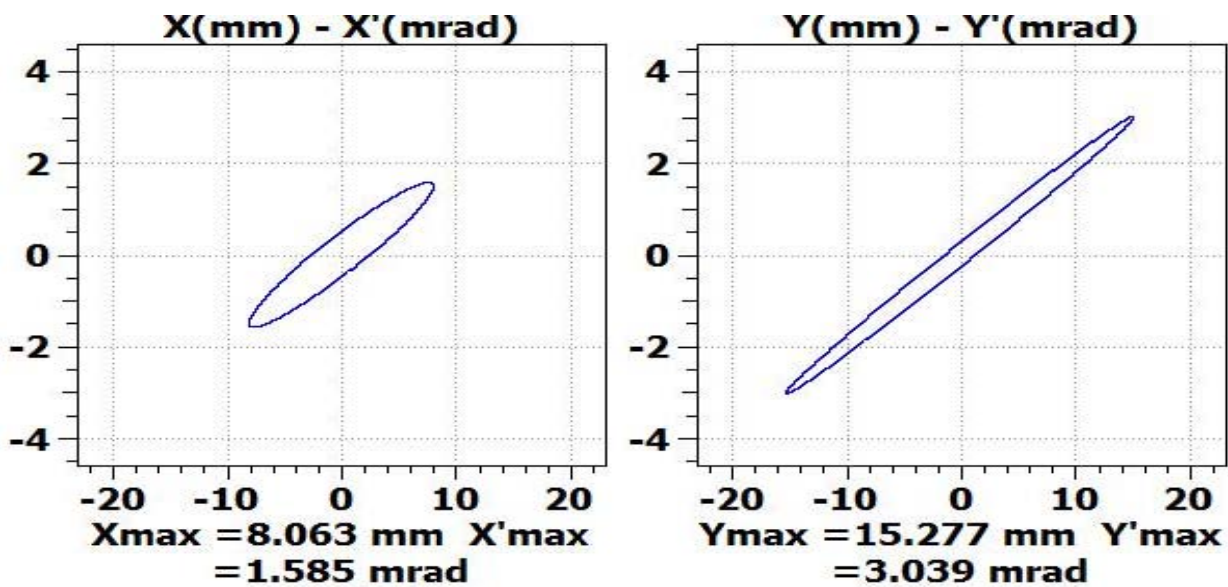


Fig 2(c): Phase space in absence of Quadrupole doublet assembly

Fig. 2. Phase space of beam at entry (a) at exit (b) of the doublet magnet assembly. The bottom figure (c) shows phase space in absence of the quadrupole doublet

Specifications

The beam envelope along one of the sections of the HEPA is shown in figure 1. The input and output phase space of the beam is shown in figure 2. Figure 2(a) and Figure 2(b) shows how quadrupole magnets limit the beam emittance and when quadrupoles are off the beam emittance blow ups as shown Figure 2(c). The integral G.dl in good field region of 24 mm (diameter) with uniformity better than 1000 ppm is a critical requirement. The required value of Integral G.dl is 3 Tesla. The sum of higher order multipoles normalized to

fundamental quadrupole component is required to be less than 0.1 %.

Design and Analysis

The magnetic design of EMQ meeting above specifications is carried out using TOSCA/OPERA-3D from Vector Fields [6]. A perfect Quadrupole have hyperbolic pole, however due to engineering constraints, a perfect hyperbola is truncated which results in systematic multipoles which are odd multiples of quadrupole ($n=2$). The errors in mechanical fabrication results in non-systematic multipoles which are even

multipoles of the quadrupole [7]. The hyperbola pole shape is modified to a customized pole shape which gives high integral magnetic field uniformity. The design consists of optimization of the magnetic pole contour to achieve the required uniformity and minimal higher order multipoles. Second order splines are used for

magnetic pole design and the coordinates of the constituent points are optimized for high integral G.dl uniformity. The magnetic field distribution in the yoke is shown in figure 3. The primary figure of merit of the EMQ is strength, uniformity and linearity of integral G.dl and also the higher order multipoles in the GFR.

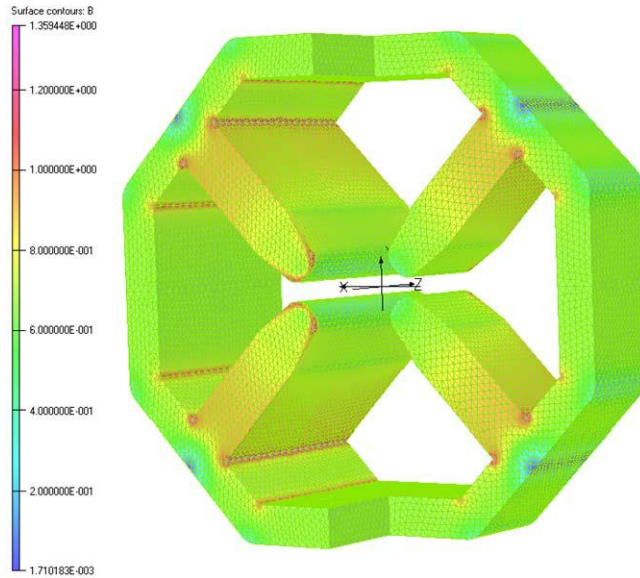


Fig. 3: 3-D model of the magnet with magnetic field profile in the yoke

Integral Magnetic field gradient

The strength of integral G.dl determines the focal length of the Electromagnetic Quadrupole (EMQ) and thereby the phase space of the beam along the axis. Ideally the integral G.dl shall remain constant in the entire good field region. Non-uniform integral G.dl cause beam aberrations. This quantity is therefore studied as function

of radial and azimuthal axis to determine the points of maxima and minima for evaluation of uniformity in the designed EMQ. Figure-4 shows the variation of integral G.dl as function of azimuthal axis at rated current. The linearity of integral G.dl along the radius is shown in figure 5.

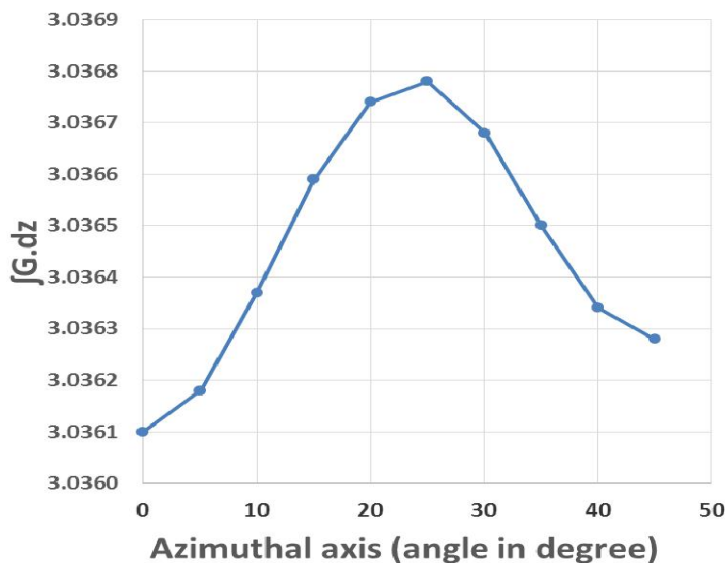


Fig. 4: Integral G.dl as function of azimuthal axis for radius of 12 mm

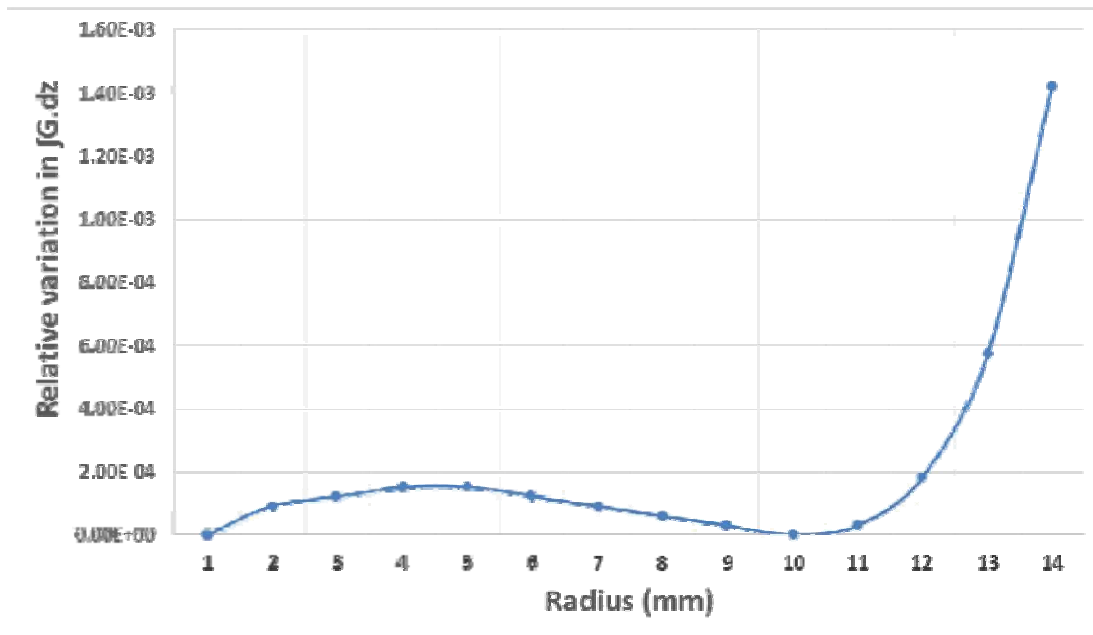


Fig. 5: Linearity of magnetic field gradient as function of radius

The uniformity in integral G.dl remains within specified value for the range of operations which is normally 50% to 100%. The magnetic analysis was conducted for

different values of input magneto motive force (MMF) and is shown graphically in figure 6.

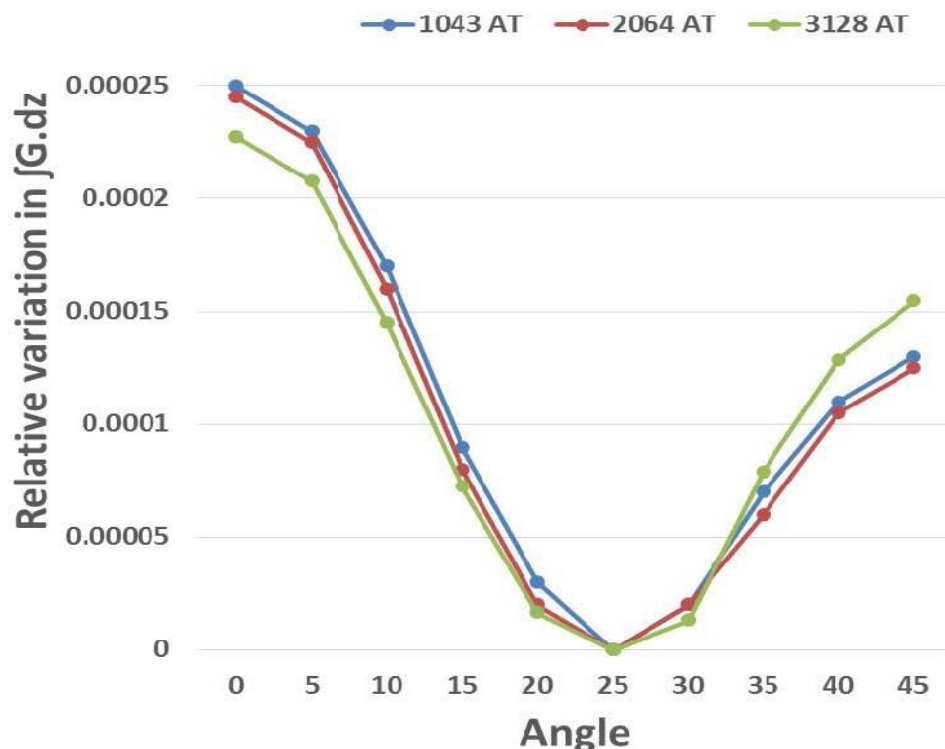


Fig. 6: Relative variation in integral G.dl as function of azimuthal axis for different MMF

Good field region

The uniformity of integral G.dl is inverse function of radius in the beam aperture. At low radius, uniformity is high. The required Good field region is decided on basis

of the beam size and uniformity affects the output beam emittance. The uniformity of integral G.dl as function of radius is shown in figure 7.

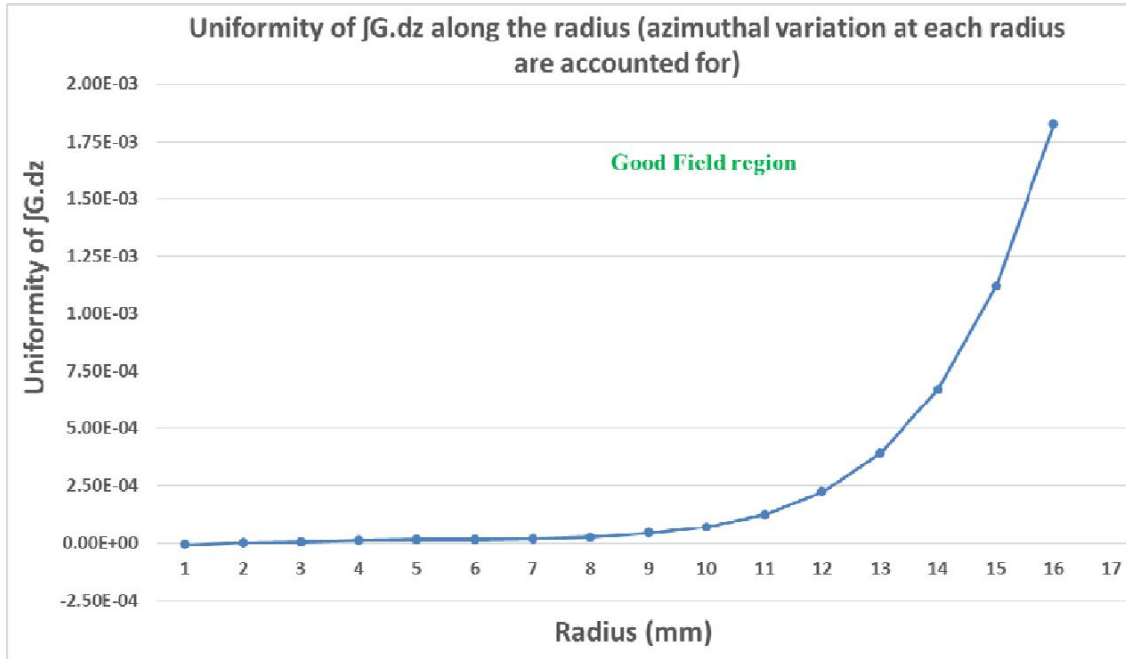


Fig. 7: Uniformity in integral G.dl as function of radius

Higher order multipoles

The sum of amplitudes of the higher order multipoles (from n=3 to n=8) shall be less than 0.1% of the

quadrupole components (n=2). Figure-8 gives spectrum of multipoles in the designed EMQ. The achieved sum of HoMs normalized to quadrupole component is 3.8e-4.

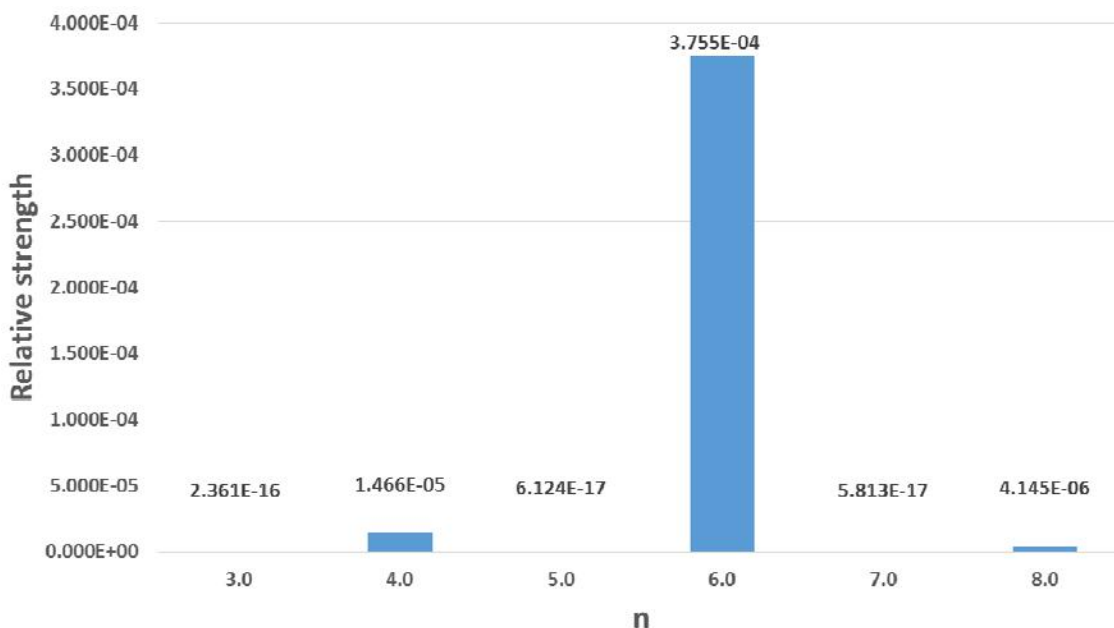


Fig. 8: Spectrum of HoMs

Permanent Magnet Quadrupoles

Drift Tube Linac of LEHIPA consists of array of Drift Tubes (DTs) the dimensions and pitch of which are governed by energy of beam. These DTs fulfils the Physics and functional requirements. DTs consist of Permanent Magnet Quadrupoles (PMQ) which provides transverse focusing to the beam. They are OFE copper made hermetically sealed cavities which are subject to large surface heat generation due to high frequency H-field. This heat is removed by water channels cut through these DTs. The CFD design of DTs ensures less

than 80um dimension changes and hot spot temperature not exceeding 50° C.

The magnetic design of PMQ ensured large good field region with uniformity of JG.dl to be better than 1%. The optimized magnetic pole shape design ensured high linearity and high uniformity in the GFR. The magnetic design has ensured long term stability of magnetic parameters in the PMQ. Figure 9 shows developed Drift Tube and its technical specifications. Figure 10 shows the set-ups used for carrying out the measurements.



Fig 9: Snap shot of developed Drift Tube with embedded PMQ

| | |
|--------------------------|---------------------------------------|
| ▪ Magnets | :Sm ₂ Co ₁₇ |
| ▪ JG.dl | :2.05 Tesla |
| ▪ Uniformity of G.dl | :± 0.5% |
| ▪ Linearity of Gradient | :Better than 1% |
| ▪ Tunability | :-10%, +2% |
| ▪ HoMs relative strength | :<0.5% |
| ▪ Maximum length | :80mm |
| ▪ Maximum diameter | :110mm |
| ▪ Hydrostatic | :6 Kg/cm ² |
| ▪ DM water flow rate | :10 LPM |
| ▪ Stem alignment | :<0.05 ° |
| ▪ Maximum Temp | :50° C |
| ▪ Pole material | :Low C steel |
| ▪ Material of Drift Tube | :OFE Copper |
| ▪ Vacuum level | :1e-8 Tor |
| ▪ Welding | :Laser |
| ▪ Qualification | :Welding,Hydro geometric, Magnetic |



Fig 10(a): PMQs being measured on Hall Probe Magnetometer at BARC



Fig 10(b): PMQs being measured at Harmonic Coil Magnetometer at RRCAT (Measurements & Photo courtesy : AMTD, RRCAT)

The measurements of PMQs were carried out using Hall probe magnetometer and Harmonic Coil Magnetometer. The longitudinal magnetic field profile and Harmonics spectrum of magnetic field in the aperture are shown in

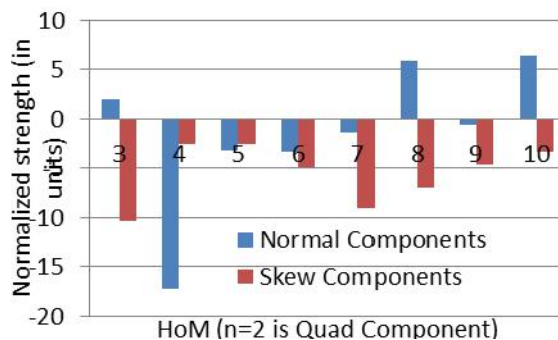


Fig 11 (a) Measured Spectrum of higher order multipoles used for uniformity measurements

Conclusions

The complete cycle of Accelerator magnet design, development and qualifications is established and implemented. Analytical models and Design codes have been validated on number of developed magnets. Stage is reached when series production can be taken up on basis of design. Local industry in and around Mumbai have catered to all fabrication requirements. In house developed magnetic measurement benches are sufficient to meet the requirements of accelerator magnet qualifications.

References

1. Hanna Samy : RF Linear Accelerators for Medical and Industrial Application, 1st Edition, ISBN-13: 978-1608070909

figure 11. The PMQs were tuned to 2.05 Tesla and uniformity better than 0.5% was obtained in about 20 PMQs measured till date.

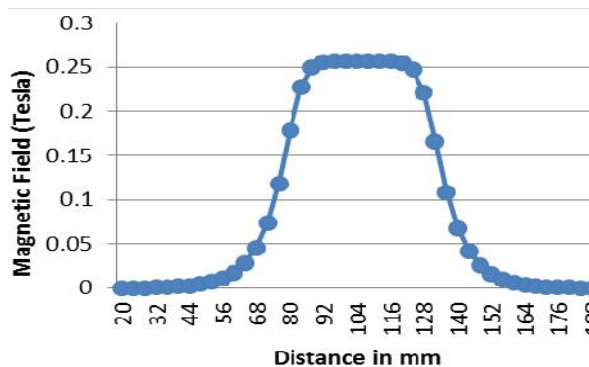


Fig 11(b) Measured longitudinal magnetic field profile

2. Wiedemann Helmut : Particle Accelerator Physics , Third edition, ISBN-13: 978-3540490432
3. Malhotra, Sanjay et al : Electromagnetic design and development of quadrupole focusing lenses for drift tube Linac, Proceedings of International Topical Meeting on Nuclear Re-search Applications and Utilization of Accelerators, AT/P5-18, 4-8 May 2009, Vienna
4. Teotia ,Vikas et al : Focusing Magnets for Drift Tube Linac, Proceedings of Indian particle Accelerator Conference-2011, February 12-15, 2011, New Delhi, India
5. Wangler Thomas P. : RF Linear Accelerators, Second edition, ISBN: 978-3-527-40680-7
6. OPERA-3D (TOSCA), Vector Fields
7. Lee, S.Y. : Accelerator Physics, Second Edition, ISBN-13: 978981256200

Setting up of In-situ X ray Absorption Spectroscopy measurement facility at Indus-2 SRS & Indigenous development of thin film multilayer neutron supermirrors

D.Bhattacharyya, C.Nayak, A. Biswas, S.N. Jha and N.K. Sahoo
Atomic & Molecular Physics Division

Dr. D. Bhattacharyya is the recipient of the DAE Homi Bhabha Science and Technology Award for the year 2014

***In-situ* X-ray Absorption Measurement Facility at Indus-2 SRS**

X-ray absorption spectroscopy (XAS) generally deals with measurement of absorption coefficient as a function of X-ray photon energy around an X-ray absorption edge of an element in a material. X-ray absorption spectrum consists of two parts: (i) The spectrum near the absorption edge (viz., the X-ray near edge structure or the XANES part) gives information about the external perturbations in the valence states to which electrons make transitions from core levels upon absorption of X-ray photon energy and hence can yield information regarding hybridization of orbitals in case of molecule or long range order existing in a crystalline sample apart from the oxidation states of the absorbing atom in the material. (ii) The second part of the spectrum which extends from 50 eV to ~700 eV above the absorption edge is generally called the Extended X-ray absorption fine structure (EXAFS) part which is generally characterized by the presence of fine structure oscillations and can give precise information regarding the short range order and local structure around the particular atomic species in the material. This determination is confined to a distance given by the mean free path of the photoelectron in the condensed matter, which is between 5-7 Å radius from the element. The above characteristic along with the fact that EXAFS is an element specific tool, makes it a powerful structural local probe. With the advent of modern bright Synchrotron radiation sources, XAS has emerged out to be the most powerful local structure determination technique which can be applied to any type of material viz. amorphous, polycrystalline, polymers, surfaces, solutions. Furthermore, XAS does not require any

particular experimental conditions, such as high vacuum and hence samples of various physical forms can be adapted for measurements in the experimental stations [1].

Over the last few years, a comprehensive XAS measurement facility has been developed at INDUS-2 SRS at RRCAT, Indore which consists of two working beamlines viz., Energy Dispersive EXAFS beamline (BL-08) and Energy Scanning EXAFS beamline (BL-09) [2,3]. A large number of users from R&D institutions, universities and industries across the country are using the above facility and more than 85 papers have so far been published in reputed international journals in last 5-6 years where the data measured in the above beamlines have been used. The energy dispersive EXAFS beamline (BL-08) covers the photon energy range of 5-20 keV and in this beamline, the entire EXAFS spectrum of the samples can be recorded in a single shot within a time scale of ~300 msec. Hence this is best suited for studying *in-situ* fast and time-resolved processes. One of the major applications of this beamline is *in-situ* studies on growth of nanoparticles.

Since its invention, nanoparticles find wide varieties of applications in the field of medicine, catalysis, biotechnology, fuel cells, solar cells, sensors and environmental science etc. [4]. This is well established that the properties of these nanoparticles can be tuned over a wide range by controlling their size and shape and this seeks the need to understand the mechanism of nucleation and growth of these nanoparticles. This envisages a new era of "*in-situ*" studies on the growth of nanoparticles. However, the scarcity of suitable fast techniques, which is one of the pre-requisites of *in-situ* studies, that can actually throw some light into the

growth and nucleation process, made these studies unpopular for a long time. UV-Vis spectroscopy is one of the most popular and oldest techniques to study the kinetics of growth. However, this technique is limited to systems which give absorption peak in the UV-Vis wavelength regime. Transmission Electron Microscopy (TEM) is also another popular technique that can be used *in-situ* to study the changes in particle size during nucleation and growth. However, *in-situ* TEM has the limitation that the electron beam can interfere with the reacting species and thus can change the whole redox reaction process to be studied. Also, it is very difficult to be employed *in-situ* in solution phase due to vacuum requirement. Small angle X-ray scattering (SAXS) is an important X-ray based technique which can act as a substitute for TEM measurements revealing the changes in particle size during growth and nucleation. However, all the above techniques mostly yield information on real

time changes in particle sizes only and cannot throw light on the evolution of the reduction process that is mainly responsible for the nucleation and growth of nanoparticles in such systems. Also these techniques cannot find out the coordination of atoms in clusters which are formed in the initial phase of the growth and act as seeds for further growth of the nanoparticles. In this regard XAS has played a crucial role in giving insight into the nucleation and formation process of nanoparticles from a very different aspect as compared to the other popular *in-situ* techniques [5].

An *in-situ* XAS measurement facility has been developed at Indus-2 SRS to study the growth and nucleation of nanoparticles [6]. The experimental facility has been improvised for simultaneous measurement of EXAFS and UV-Vis spectroscopy. Fig. 1(a) shows the schematic diagram of the setup while fig. 1(b) shows the photograph of the same.

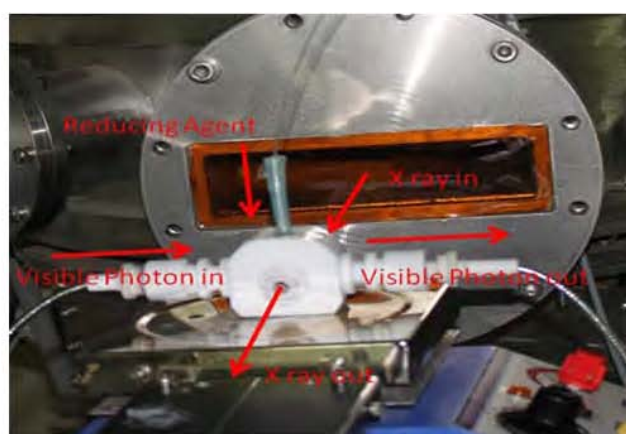
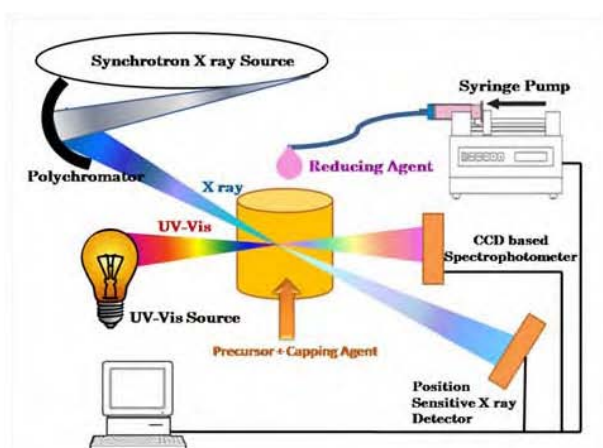


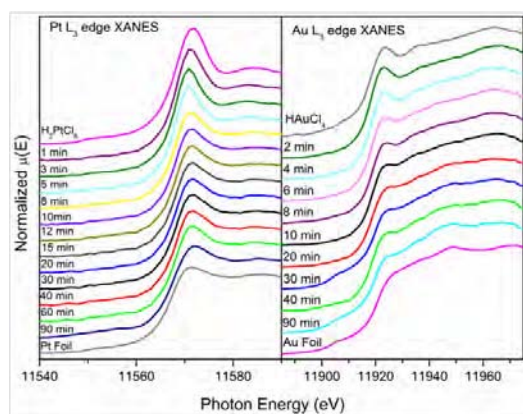
Fig. 1: (a) Schematic diagram and (b) Photograph of the *in-situ* XAS measurement set-up.

In the above set-up, synthesis of nanoparticles is carried out in a specially designed teflon reaction cell having paths for both X-rays and UV-Vis radiation in mutually perpendicular directions. X-ray is transmitted through kapton windows while the optical light is passed using optical fibres which are capped with teflon ferrules and are directly immersed into the solution. The cell has been designed and fabricated in such a way that the optical paths can vary from 5 mm to 20 mm for X-rays and from 2 mm to 20 mm for UV-Vis radiation. The volume of the cell varies according to the adjustment of the kapton windows and optical fibers. The sample mount of the beamline has been modified so that the *in-situ* reaction cell can be placed on a magnetic stirrer-cum-heater for mixing and heating the reaction solution. The precursor is taken in the teflon reaction cell and the reducer is

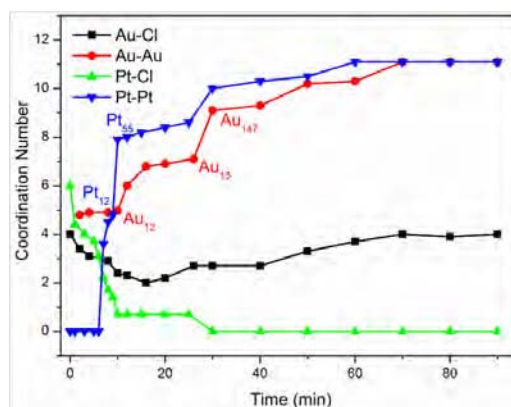
injected into it through teflon tube using a computer-controlled motor-driven syringe pump. Using the above set-up the growth of Au and Pt nanoparticles from their respective chloride precursors using block copolymer based reduce-cum-stabilizer have been studied by simultaneous *in-situ* measurement of XAS and UV-Vis spectroscopy [6]. Figs. 2(a) shows the time-resolved XANES spectra of the precursors showing reduction of Au⁺³ and Pt⁺⁴ ions to metallic states, whereas fig. 2(b) shows the evolution of Au and Pt coordination with time as obtained from time resolved *in-situ* EXAFS spectra.

The growth kinetics of both gold and platinum nanoparticles are found to be almost similar and are found to follow the three stages viz., (i) reduction of metal ions by block copolymer and formation of small

cluster of typical 5 coordinations, (ii) absorption of block copolymer and reduction of metal ions on the surface of the cluster and increase in cluster size and (iii) growth of gold nanoparticles stabilized by block copolymer. It can be observed from fig. 2(b) that the time scale involved in the 2nd and 3rd stages of the nanoparticle formation are similar for both gold and platinum nanoparticles. This may be due to the fact that these stages are mainly governed by the block copolymer which is same in both the cases. However, the 1st stage of nucleation takes place earlier in case of Au than in case of Pt due to the difference in the reduction potential of the respective precursors. The cluster sizes at the various stages of growth of the nanoparticles have been estimated theoretically from the metal-metal coordination numbers obtained from the time-resolved EXAFS spectra shown in fig. 2(b). It has been found that in both the cases, 12-atom clusters are formed which act as seeds for further growth. However, for gold, these 12-atom cluster first grows into the magic number 13-atom cluster and then 147-atom clusters which further grows into gold nanoparticles. For platinum, the 12-atom cluster grows into the magic number 55-atom cluster which further grows into platinum nanoparticles. The first two stages of the growth of Au and Pt nanoparticles as obtained by *in-situ* XAS measurements are also corroborated by simultaneous *in-situ* measurement of UV-Vis spectroscopy.



(a)



(b)

Fig. 2: (a) Time-resolved XANES spectra of the precursors showing reduction of Au³⁺ and Pt⁴⁺ ions to metallic states, (b) Evolution of Au and Pt coordination with time as obtained from time resolved *in-situ* EXAFS spectra.

References:

1. D.C. Konigsberger, R. Prince, X-Ray Absorption: Principles, Applications, Techniques of EXAFS, SEXAFS and XANES (Wiley, New York, 1988).
2. D. Bhattacharyya, A.K. Poswal, S.N. Jha, Sangeeta and S.C. Sabharwal, Nuclear Instruments Method. in Phys. Res., A 609 (2009) 286.
3. S. Basu, C. Nayak, A. K. Yadav, A. Agrawal, A. K. Poswal, D. Bhattacharyya, S. N. Jha, and N. K. Sahoo, J. Phys.: Conf. Ser., 493 (2014) 012032.
4. Gunter Schmid, ed. Nanoparticles: From Theory to Application. 2004, Wiley-VCH, Weinheim.
5. J. Polte, T. T. Ahner, F. Delissen, S. Sokolov, F. Emmerling, A. F. Thünemann and R. Kraehnert, J. Am. Chem. Soc., 132 (2010) 1296.
6. C. Nayak, D. Bhattacharyya, S. N. Jha and N.K. Sahoo, J. Synch. Rad., 23 (2016) 293.

Indigenous development of thin film multilayer neutron supermirrors

Worldwide availability of high flux research reactor boosted the application of neutron as a probe in the research of condensed matter physics. Due to comparable de Broglie wavelength ($\lambda=h/mv$) of neutron with the inter-atomic spacing in many physical systems and comparable energy to many atomic and electronic processes, neutron scattering has become an established technique in material characterisation. Since neutron scattering cross-section of the nucleus of an atom does not depend on its atomic number, neutron can very effectively be used in probing low Z atoms which cannot be probed by X-rays. Also since neutrons are charge-less particles and are not easily absorbed by materials, they can be used in “*in-situ*” experiments where samples are kept inside specialised sample environment equipments, such as furnaces, cryostats or pressure cells. Moreover, magnetic properties of neutron can be used in characterising magnetic structure of materials. Other than scattering, neutrons are excessively used in radiography, tomography and imaging applications also. During all these experiments collimating and focusing of the neutron beam emerging from a reactor source is always a challenging task.

In practice neutrons are generally guided by using total external reflection from a metallic layer (viz., Ni film) at a very narrow grazing angle of incidence. In nature, no material is available which can efficiently reflect neutrons in large wide angle, though artificial periodic and non-periodic thin film multilayer structure can solve this problem to some extent [1]. For a periodic multilayer with uniform bi-layer thickness due to the constructive interference of the neutrons reflected from each interface, a high reflectivity Bragg peak appears at some angular position. Such periodic multilayers with alternate layers of high and low neutron scattering lengths, work as high reflecting neutron mirror and monochromator. In case of non-periodic multilayer where the bilayer thickness varies along the depth, several Bragg peaks due to different portions of the multilayers arise, which subsequently merge and a continuous high reflectivity profile is achieved up to a large value of grazing angle of incidence. Such a structure is known as a supermirror and in case of neutron it is characterised by its ‘*m*-value’ which signifies the ratio of critical angle of the supermirror compared to natural Ni.

Moreover, if these supermirrors are made up with alternate layers of magnetic and non-magnetic elements such as Co/Ti, Fe/Si, FeCoV/Ti etc., so that contrast in neutron scattering lengths increases under the presence of magnetic field then they reflect neutrons of one spin state while neutrons with other spin states are transmitted and in that case these supermirrors are also used as neutron polarizers [2]. These are not only used in polarized neutron reflectivity (PNR) set-ups for measuring magnetization in thin film and multilayer, but also for the separation of nuclear, magnetic and nuclear spin-incoherent scattering on a multi-detector neutron spectrometer and in neutron spin-echo (NSE) spectrometers.

Mezei *et. al.* [3] first proposed the multilayer design structure of neutron supermirrors for increasing the critical angle of total external reflection as well as spin polarization of neutrons. Their design is based on the idea of continuously depth graded multilayer such that successive bilayers vary in thickness. The thickness is chosen by a method analogous to that used in the design of broad band filter for visible optics. However it failed to yield the desired reflectivity. Since then different design structures have been proposed for achieving high reflectivity in the case of high-*m* value supermirrors, among which the most frequently used is the Hayter and Mook model [4].

Electron beam evaporation method was used first time by Mezei [5] for realisation of Fe/Ag neutron supermirror polarizer. However, as have been seen, compared to evaporation method in sputtering techniques, the energy of the adatoms are generally high enough (~10 eV) so that adatoms can re-organise themselves on the surface of the growing films leading to smoother two-dimensional growth. Hence, presently different variants of sputtering technology are generally used to realize these multilayers. Some of the researchers have reported deposition of very large *m*-value supermirrors by Ion Beam Sputtering (IBS) technique [6]. In spite of several advantages of IBS technique like low air pressure plasma, higher stability of process and non-contact of plasma with deposited film, IBS technique is not suitable for large area and high throughput deposition due to the enormous cost involved in procurement of large size ion guns and low

deposition rate of the ion beam sputtering process. DC magnetron sputtering which can yield higher sputtering rate and which has easy scalability and provisions for reactive sputtering in various gaseous ambient is thus a preferred technique for depositing these multilayer neutron supermirrors for actual applications [7,8]. In our laboratory a 9 m long fully computer controlled in-

line dc/rf magnetron sputtering system has been developed recently indigenously where several neutron mirrors consisting of a large number of bilayers and each having 150 mm x 250 mm dimension can be deposited simultaneously. The photograph of the system is shown in fig.3, while the full description of it has been reported elsewhere [9,10].

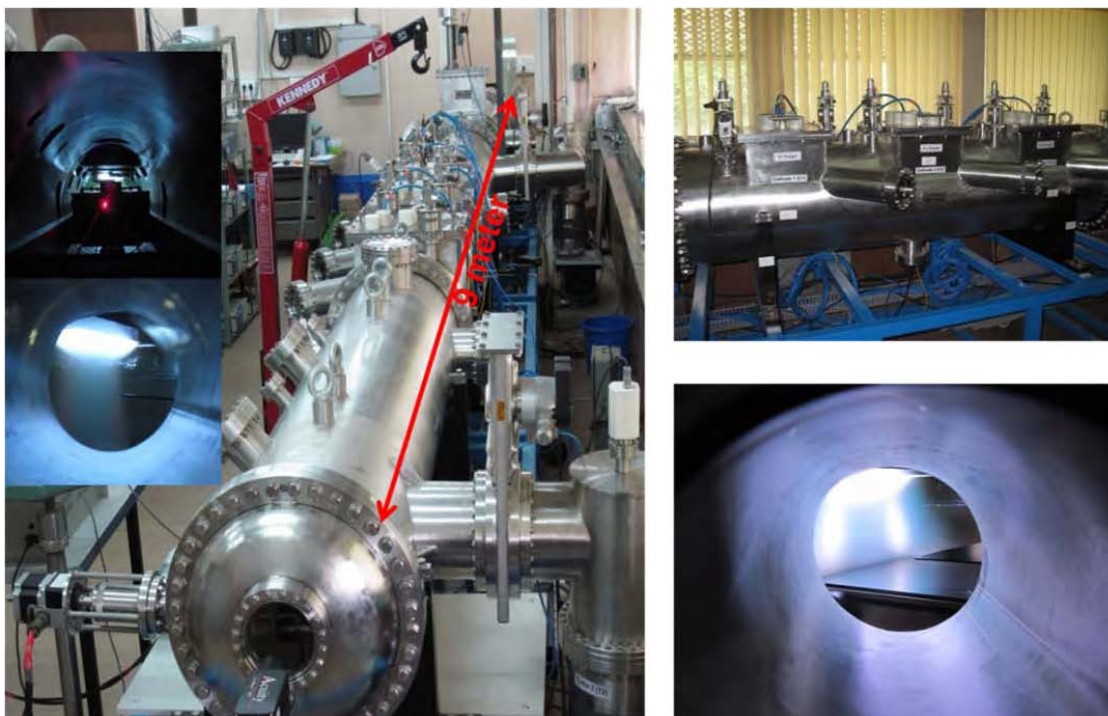


Fig. 3: Photographs of the 9 meter long in-line sputtering system.

Co/Ti neutron supermirror polarizers of $m=2.0$ (100 layers), $m=2.25$ (204 layers) and $m=2.5$ (312 layers) have been developed by using the above system. Prior to the development of the supermirrors, several Co, Ti single layer films and Co/Ti tri-layers have been deposited under various depositions conditions and were characterised by specular and diffused grazing incidence X-ray reflectivity measurements with laboratory X-ray source. Optimum deposition conditions have thereby been achieved to obtain films with very low roughness and sharp interfaces and the supermirrors have been deposited under this optimised deposition condition. Subsequent to the deposition, the supermirror polarizers have been characterized by measuring Polarized Neutron Reflectivity (PNR) with neutron beam of 2.5 Å wavelength at DHRUVA reactor, BARC, Trombay [11]. It has been found that though the spectral characteristics of the $m=2.0$ supermirror polarizer closely matches with the theoretically designed spectra, the PNR spectra of the $m=2.25$ and $m=2.5$ supermirrors contain undesirable

oscillations and the measured reflectivity values of up-spin neutrons are relatively low. On further

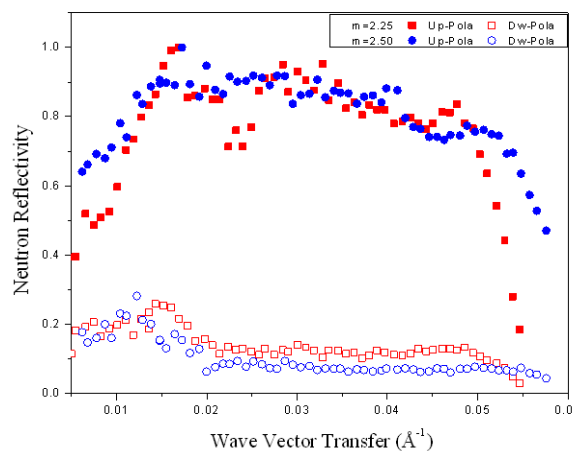


Fig. 4: Polarized neutron reflectivities of $m=2.25$ and $m=2.5$ Co/Ti supermirrors where all Co layers have been deposited under a mixed ambient of argon and air.

investigation, it has been observed that the presence of magnetic roughness or magnetic dead layer at the Co/Ti interface is the reason for such degraded performance of these supermirrors. The above problems have subsequently been rectified by depositing all the Co layers under a mixed ambient of argon and air. In fig. 4, improved neutron reflectivities of $m=2.25$ and 2.5 Co/Ti supermirrors where all Co layers have been deposited under mixed ambient of argon and air are shown. High reflectivity ($\sim 80\%$) up to a reasonably large critical wavevector transfer (q) of $\sim 0.06 \text{ \AA}^{-1}$ have been observed in the above multilayer structures.

The neutron mirror and supermirrors (SM) fabrication facility which has been developed in our laboratory will give a boost to the neutron-based research in the country. The above development has significant commercial implications also since such neutron supermirrors are available from very few commercial sources internationally at a very high cost.

References

1. J. Daillant and A. Gibaud, X-ray and Neutron Reflectivity Principles and Applications, Springer, Berlin Heidelberg, 2009
2. O. Schärpf, AIP Conference Proceedings, 89 (1982) 182.
3. F. Mezei and P.A. Dagleish, Commun. Phys., 2 (1977) 41.
4. J.B. Hayter and H.A. Mook, J. Appl. Cryst., 22 (1989) 35.
5. F. Mezei, Commun. Phys., 1 (1976) 81.
6. D. Yamazaki, R. Maruyama, K. Soyama, H. Takai, M. Nagano and K. Yamamura, Journal of Physics: Conference Series, 251 (2010) 012076.
7. P. Høghøj, I. Anderson, R. Siebrecht, W. Graf and K. Ben-Saidane, Physica B: Condensed Matter, 355 (1999) 267.
8. S. Maidul Haque, A. Biswas, Debarati Bhattacharya, R.B. Tokas, D. Bhattacharyya and N.K. Sahoo, Journal of Applied Physics, 114 (2013) 103508.
9. A. Biswas, R. Sampathkumar, A. Kumar, D. Bhattacharyya, N.K. Sahoo, K.D. Lagoo, R.D. Veerapur, M. Padmanabhan, R.K. Puri, D. Bhattacharya, S. Singh and S. Basu, Rev. Sci. Instrum., 85 (2014) 123103.
10. A. Biswas, S.M. Haque, J. Misal, K.D. Lagoo, R.D. Veerapur, M. Padmanabhan, R.K. Puri, R. Sampathkumar, Ajaykumar, D. Bhattacharya, D. Bhattacharyya and N.K. Sahoo, AIP Conference Proceedings, 1591 (2014) 985.
11. S. Basu and S. Singh, Journal of Neutron Research, 14 (2006) 109.

Design of AHWR with passive systems: Challenges and Accomplishments

A.K. Nayak, Mukesh Kumar, D.K. Chandraker and P.P. Kulkarni
Reactor Engineering Division

**Dr. A.K. Nayak is the recipient of the DAE Homi Bhabha Science and
Technology Award for the year 2014**

Introduction

Ever since the inception of nuclear fission, nuclear energy is considered as one of the vital sources of clean & green energy, which can eliminate or reduce the dependency on the conventional sources of energy. To eliminate the concerns in public against the safety of nuclear power plants, the safety goals for the future nuclear reactors are being enhanced and achieved in a reasonable way. Accordingly a set of objectives, requirements and criteria for the innovative reactors have been formulated in the international project on Innovative Nuclear Reactors and Fuel Cycles (INPRO). The currently operating reactors have extensively used "active engineering safety systems" for reactor control and protection. However, these active safety systems have certain limitations concerning their reliability. In addition, accuracy of factors used in Probabilistic Safety Assessment (PSA) is highly debatable. As a result, there is growing concern about the safety of such plants due to the large uncertainty involved in PSA. In view of this, a desirable goal of an innovative reactor is that its primary defence against any serious accident is achieved through its design features preventing the occurrence of severe accidents without depending either on the operator's action on the active systems.

The future reactor concepts are thus designed on the philosophy of "safety-by-design" for keeping the level of risk to either similar or even lower than other industrial plants. These reactor concepts are much different than the current fleet of reactors. Several inherent safety features are integrated in the design of such reactors to ensure the safety in the event of any kind of accident that may arise due to internal or external initiating events. These safety features are of paramount importance to minimize the necessity of evacuation of public in the

event of any serious accidents, besides preventing the radioactive release to environment.

In this regard, India's innovative reactor 'Advanced Heavy Water Reactor (AHWR)' is a stepping stone for technology demonstration for an inherently safe design so that the reactor can be located close to the population centre apart from producing large scale power from Thorium. This is achieved by incorporating several passive safety systems in reactor design which include core cooling by natural circulation under normal operation, transients and accident scenarios. Additionally, AHWR adopts passive systems for containment cooling following a LOCA. Besides, innovative passive safety systems have been adopted in reactor design for several non-cooling applications such as reactor trip in case of wired shutdown system failure, containment isolation and automatic depressurization in the event of accidents.

Despite the simplicity of design, operation and maintenance offered by passive safety systems; there are many technological challenges associated with them for incorporating in reactors. One of the major issues with passive systems is accurate quantification of their functional behavior and reliability under all operational states. The main difficulties in evaluation of functional behavior and failure of passive systems are due to: a) lack of operational experience of similar plants in past; b) scarcity of adequate test data from integral test facilities or from separate effect tests in order to understand the performance characteristics of these passive systems; c) functional failures of these systems are not well understood; and, d) difficulty in modeling certain physical behavior of these systems.

The AHWR design had several of such challenges for quantification of performance and failure of these passive systems. Since currently used best estimate codes may not be applicable to design of passive systems mainly due to presence of multi-dimensional flow in natural convection; difficulty in modeling the oscillatory flow under boiling conditions due to flashing, geysering, density-waver instability, etc.; flow stratification; condensation in presence of non-condensables; etc.; full scale and many separate effect, test facilities were built to prove the AHWR design with passive safety systems which are essential for regulatory acceptance.

Following sections explain the thermal hydraulic design of AHWR with innovative passive systems and its validation for not only in normal power operation but also during design basis accidents and severe accidents.

Thermal Hydraulic Design and Validation of AHWR

AHWR design targets to produce 920 MW thermal power which is removed by boiling two-phase natural circulation light water coolant from core to turbine. The main design requirement of AHWR is to maintain adequate thermal and stability margins. To establish the design margins under all operational states; several experiments were carried out in separate effect and Integral test Facilities. Models used to quantify the stability and thermal margins were also validated with numerous test data.

Validation of AHWR Stability Characteristics

State-of-art mathematical models were developed for analyzing the stability of AHWR, which adequately modelled the thermo-fluid dynamics of boiling two-phase natural circulation in multiple parallel channels of AHWR and coupled with nuclear fuel dynamics for Pu-Th based fuel using multi-point kinetics and modal kinetics models. For design validation and regulatory clearances, several test facilities were built which include high pressure and temperature boiling natural circulation loops and integral test facilities having geometry and operating conditions one-to-one as that of AHWR. Also, a Parallel Channel Boiling Natural Circulation Loop (PCL) was built wherein the nuclear reactivity feedback of Pu-Th based fuel was simulated by electrical simulation. This is one of the few facilities in the world having reactivity feedback simulation. Figs. 1(a) to (e) show examples of instability mechanism and validity of computational models for instability behaviour of AHWR. The analysis and test data could

substantiate the physics of natural circulation characteristics in AHWR, onset of instability mechanism and strategies to eliminate them during reactor operation. More details of validation can be seen in references [1-3].

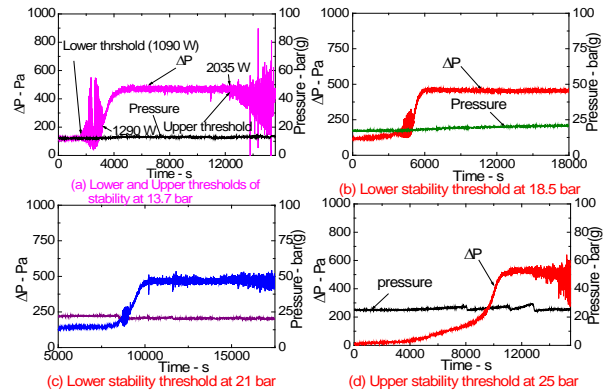


Fig. 1a: Typical Instability Characteristics in Boiling Natural Circulation

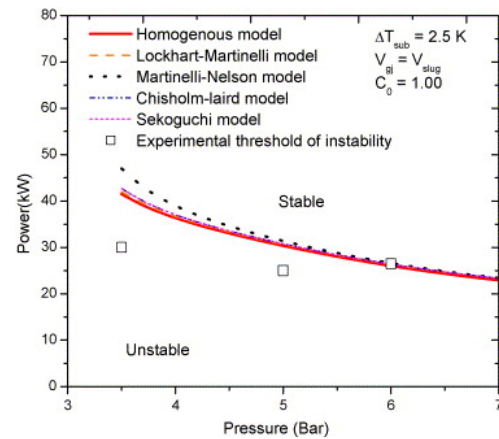


Fig. 1b: Validation of Mathematical Model for Type I instability

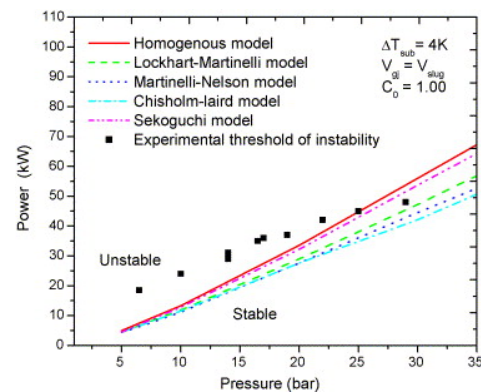


Fig. 1c: Validation of Mathematical Model for Type II instability

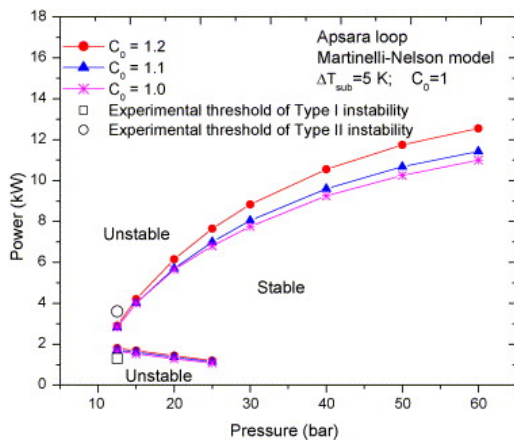


Fig. 1d: Validation of Mathematical Model for both Type I and Type II instability

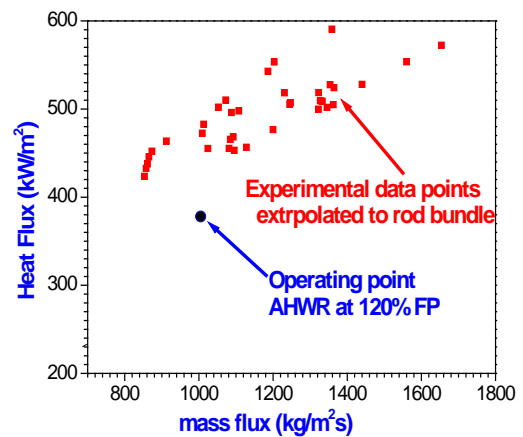


Fig. 2: CHF data and peak heat flux of AHWR showing adequate thermal margin

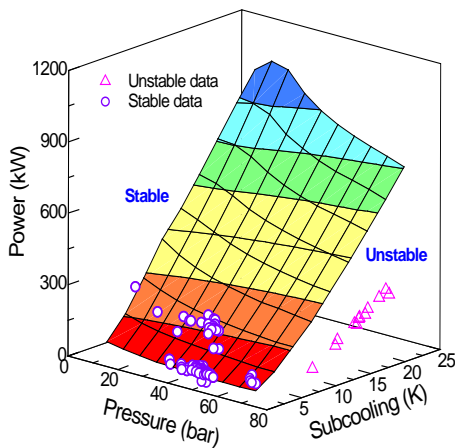


Fig. 1e: Validation of Mathematical Model for instability simulated in Integral Test Loop of AHWR

Fig. 1 (a-e): Validation of mathematical model for instability with experiments

Validation of AHWR Thermal Margin

For determination of thermal margin of AHWR, full scale electrically heated clusters have been developed and installed in AHWR Thermal Hydraulic Test Facility (ATTF) at Tarapur. Prior to bundle experiments, an estimate of AHWR thermal margin has been made by performing experiments in a tubular test section having the same hydraulic diameter and heated length as that of AHWR. The operating conditions of pressure and inlet subcooling had one-to-one correspondence with the operating conditions of the AHWR fuel cluster. The experimental data were extrapolated to AHWR fuel bundle by using bundle correction factor and flux profile. The extrapolated CHF data and AHWR nominal operating point are shown in fig. 2.

The criterion of thermal margin evaluation at 120%FP (as shown in Figure2) comes from the fact that in postulated operational transient involving turbine trip without bypass, the primary system pressure may rise leading to void collapse and increase in reactor power (as AHWR has a negative void coefficient). This is the most limiting transient. Fig. 2 indicates that there is large margin available against CHF under such a transient.

The MCHFR for AHWR fuel bundle has been evaluated by extrapolating the tubular CHF data to AHWR bundle conditions as well as that predicted by using the Janssen-Levy correlation (which is prescribed for BWRs at Tarapur). The MCHFR values thus obtained are shown in Table 1. It is evident from table 1, that AHWR has sufficient margins against CHF.

Table 1: MCHFR for existing core design 920 MWth

| S.No | Method of Estimation | MCHFR (at 20% over power) |
|------|---|------------------------------|
| 1 | Janssen-Levy model (existing design) | 1.62 |
| 2 | Experimental data under AHWR operating conditions | 2.04 |

Establishment of AHWR Operational Domain

The stability characteristics and the thermal margin have been evaluated for AHWR under various operating conditions and an operating domain has been worked out while ensuring sufficient design margins for stability and CHF. The operating line for AHWR is shown in

figure 3 on power-subcooling plane. The unstable domain is also shown in the same map. The thermal margin (MCHFR) corresponding to the operating power at each subcooling is also shown in the same figure. It can be seen that the operating line has sufficient margin both with regard to stability and CHF.

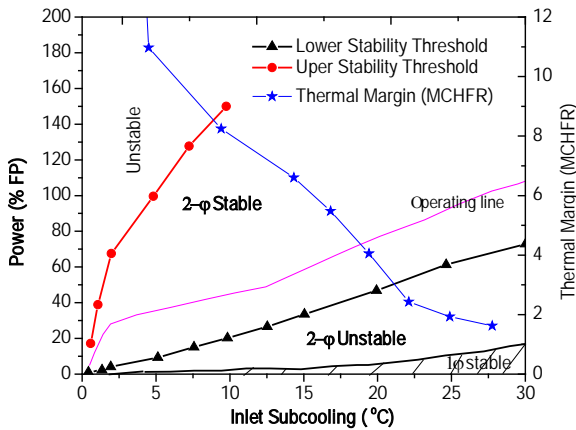


Fig. 3: Thermal and stability margin of AHWR

Quantification of passive systems performance and reliability

To evaluate the reliability of passive systems of AHWR, a methodology known as Assessment of Passive Systems Reliability (APSRA) has been developed in BARC [4]. In the APSRA methodology, the passive system reliability is evaluated from the evaluation of the failure probability of the system to carry out the desired function. For example, in a natural circulation system, the operational mechanism of buoyancy driven natural circulation should never fail as long as there is a heat source and sink with an elevation difference between them. However, even though the mechanism does not fail, it may not be able to drive the required flow rate whenever called in, if there is any fluctuation or deviation in the operating parameters even though the system geometry remains intact. In the case of a motor driven pump, the head vs. flow characteristics are not so much susceptible to a slight change or fluctuation in operating parameter to cause the failure of the system unless there is any mechanical failure of the pump itself. Hence, its performance characteristics are well known and can be simulated accurately while assessing the overall safety of the plant. On the other hand, the characteristics of buoyancy driven natural circulation cannot be accurately predicted under all operational conditions or transients due to the inherent complex phenomena associated with natural convection systems. Since applicability of the best estimate codes to passive systems are neither proven

nor understood enough, hence, APSRA relies more on experimental data for various aspects of natural circulation. APSRA compares the code predictions with the test data to generate the uncertainties on the failure parameter prediction, which is later considered in the code for prediction of failure conditions of the system. In the APSRA approach, the failure surface is generated by considering the deviations of all those critical parameters, which influence the system performance. The causes of deviation of these parameters are found through root diagnosis. It is attributed that the deviation of such physical parameters occurs mainly due to failure of mechanical components, e.g. valves, control systems, etc. The probability of failure of a system is evaluated from the failure probability of these mechanical components through classical PSA treatment.

Figure 4 shows the steps followed in APSRA methodology. Figure 5(a) to (d) show examples of failure surface and failure probability of different passive systems in AHWR, which shows a significantly lower value as compared to pumped circulation systems. More details of reliability of passive systems for AHWR can be seen in references [4-7].

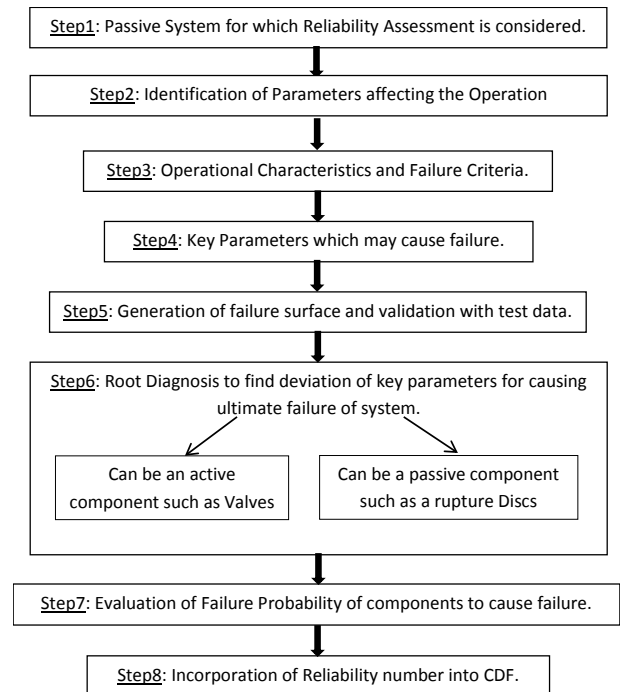


Fig. 4: APSRA methodology

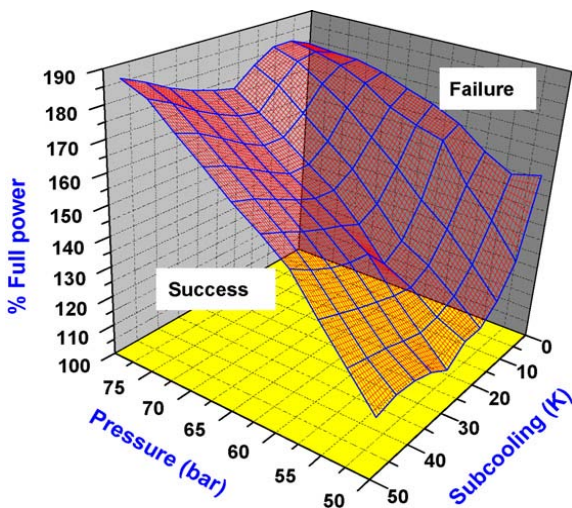


Fig. 5a: Failure Surface for Natural circulation

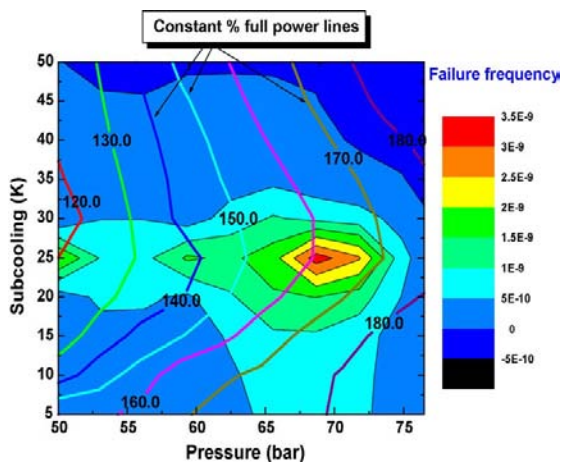


Fig. 5b: Probability of Failure for Natural circulation

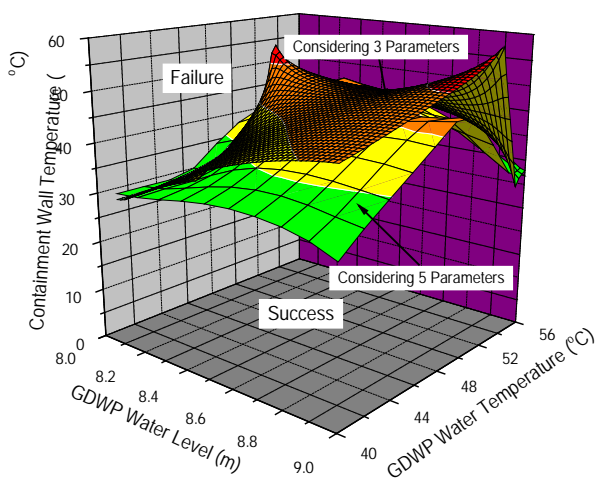


Fig. 5c: Effect of process parameters on Failure Surface for PCCS

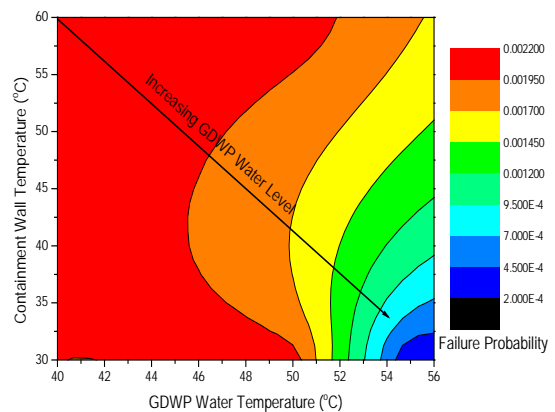


Fig. 5d: Probability of Failure for PCCS

Validation of critical issues for FOAK safety features in AHWR design

Demonstration of adequacy of in-bundle ECC injection in AHWR

In-bundle ECC injection is a unique feature of AHWR. It aims to deliver the emergency coolant directly to the bundle in case of Loss of Coolant Accident (LOCA). ECC water is injected through a perforated central water tube. There are 13 axial locations, each having 8 holes of 1.5 mm diameter. Fig. 6 shows a cross section of the cluster and the location of injection holes. The water ensues as a jet, laterally into the cluster.

The major issue with evaluation of efficacy of in-bundle ECC injection is the scarce availability of data on such an injection scheme. Further, the phenomena which occur due to lateral introduction of the jet into the bundle are distinctly 3-dimensional. This makes usage of widely used 1-D codes like RELAP questionable. Jet impingement leads to formation of droplets of varying sizes and the phenomena are also multi-scale. Such multidimensional, multi-scale phenomena coupled with the complications of simulating boiling heat transfer during rewetting are difficult to simulate even with CFD codes. In view of the above, experimental demonstration of adequacy of in-bundle ECC injection is necessary. Specifically, it is required to demonstrate for AHWR that following a LOCA, ECC water will be able to cool even the outermost ring of pins which are farthest from the injection point.

Experiments have been conducted in a scaled facility to determine, for a particular decay power level, the minimum ECC flow rate required to limit the clad surface temperatures within 500°C. The cross-section of the experimental cluster has been maintained the same

as AHWR. In the experiments, the cluster is first heated to obtain peak clad temperatures of 470-490°C. After this, power is raised to a desired decay power level with injection of emergency coolant at desired flow rate. The experiments were done for a range corresponding to up to 2.6% FP decay power level and 150-290 kg/s ECC flow when scaled to reactor conditions. It was observed in the experiments (Fig. 7) that beyond 1.8%FP, an ECC flow of 240 kg/s is sufficient. At decay power below 1.4%FP 150 kg/s of ECC flow is sufficient. It is seen that in the initial phase of ECC injection, when the decay power levels are high, the available ECC flow rate (computed from RELAP) is 800 kg/s. For longer term ECC injection through GDWP, available ECC flow rate (computed from RELAP) is 160 kg/s. In view of the above, it may be said that the available ECC flow is sufficient to remove the decay heat.

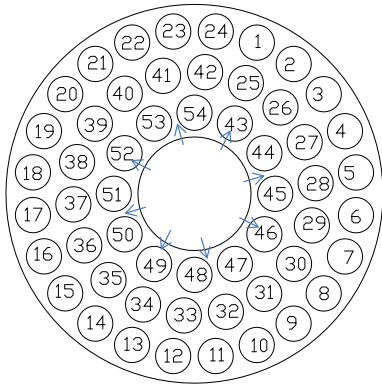


Fig. 6: Cross section of AHWR fuel cluster showing ECC injection locations as arrows

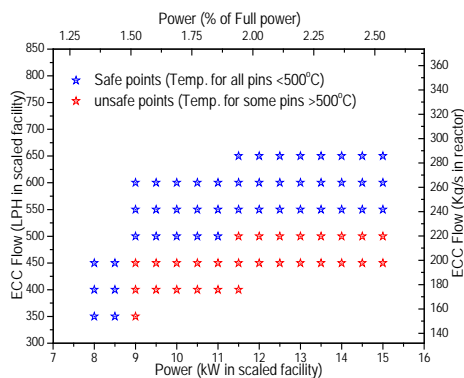


Fig. 7: The limit map showing the conditions for which cooling could and could not be achieved for all the pins

Technology Development for Detection of Stagnation Channel Break and Reactor Trip in AHWR

With pressure tube type design, there is a possibility of occurrence of almost zero coolant flow in the channel under a certain size of small breaks in the inlet feeders.

The situation of very low coolant flow may lead to fuel failure, if reactor is not tripped within a certain time after the break. This is known as stagnation channel break and is a safety concern in AHWR. Due to very small size of the break, the depressurization rate is very small. As a result of which, the conventional reactor trip signals generated based on LOCA, may not be realized. In view of this, AHWR design has a novel safety feature of reactor trip dedicated to stagnation channel break condition. This system functions on detection of breaks (steam leakages) using number of acoustic based sensors housed in V1 volume of the reactor, detection of low flow in the channel using bi-directional venturies and measurement of large void fraction in the tail pipe of each channel (2 out of 3 logic). For design validation with regard to capability of these sensors to detect stagnation channel break and generate reactor trip signal within a short time without causing rise in clad temperature, full scale experiments were performed in the Integral Test Loop.

Experiments were conducted for different sizes of break and operating conditions at which near stagnation conditions was observed in the facility. To detect the steam leak from the break, two acoustics based sensors were installed close to the break setup. Each feeder line was installed with bi-directional venturi to measure the flow in the channel. Our experiments showed that (Figure. 8a to d) upon occurrence of the simulated break in the inlet feeder line, the venturies could generate the feedback signal of low flow in the channel within 2 seconds. The acoustics sensors could detect break and send the feedback signal within 5 seconds. The trip was realized within 7 seconds with both the feedbacks. The pin temperature was found not to rise during this period (Figure-8d) conforming the design safety of the reactor against stagnation channel break.

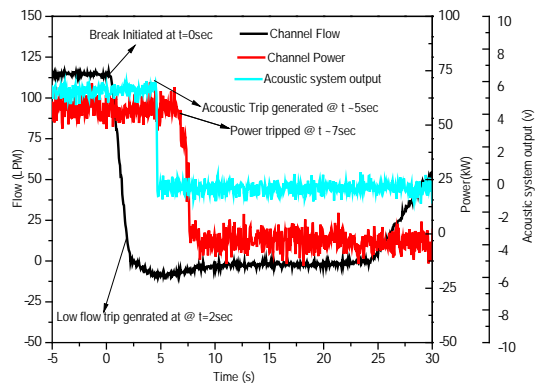


Fig. 8a: Channel Flow and FCS Power @70 bar

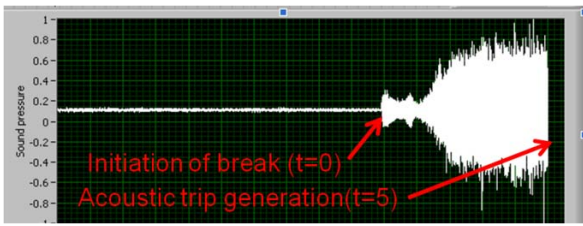


Fig. 8b: Acoustic signature during the test @70 bar

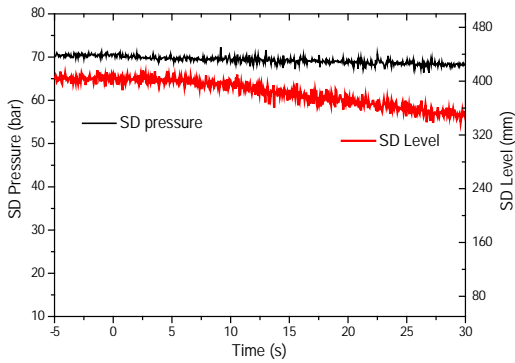


Fig. 8c: Steam Drum Pressure and Level @ 70 bar

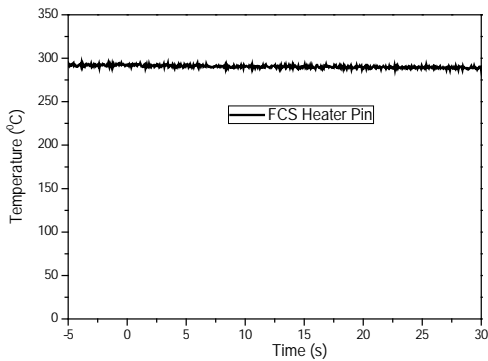


Fig. 8d: Heater Pin Surface Temperature @70 bar

Demonstration of safety under extreme events:

The Fukushima accident was essentially an extreme event caused by strong earthquake and high magnitude Tsunami. In addition, the natural calamity rendered the plant site inaccessible for several days to preclude external intervention to rescue the situation and thus further aggravated the accident. Though SBOs have always been considered in the reactor design and safety philosophy, the Fukushima accident raised a question on the ‘Grace Period’ that the design must consider in view of such a prolonged SBO. It may be noted that the plant withstood a beyond-design basis earthquake without any impact on the structural integrity and the reactor could be safely shutdown, thus demonstrating the reliability of the structural design and shutdown system. In the context of AHWR, though the Indian coasts are not prone to such tsunamis because of geographical factors, and layout provisions ensure the safety of diesel

generator sets; a prolonged SBO was considered to demonstrate the robustness of the in-built design features. Our analysis shows that the reactor design is capable of removing the decay heat for 110 days[8]. The primary side depressurizes to 3 bar within 2 hrs and remained same for rest of the time as seen in Fig.-9a. Clad surface temperature was found to be within safe limits (Fig.-9b). The containment pressure reaches 2.75 bar in 10 days and required venting of the containment after 10 days.

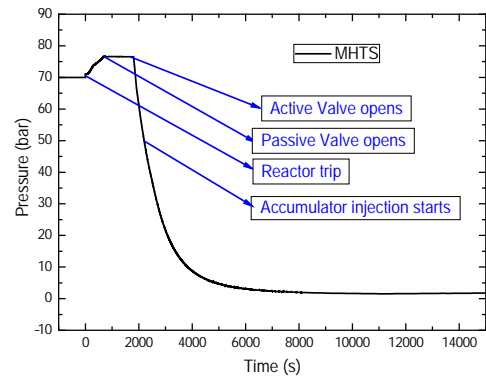


Fig.9a: MHTS Pressure variation during prolonged SBO

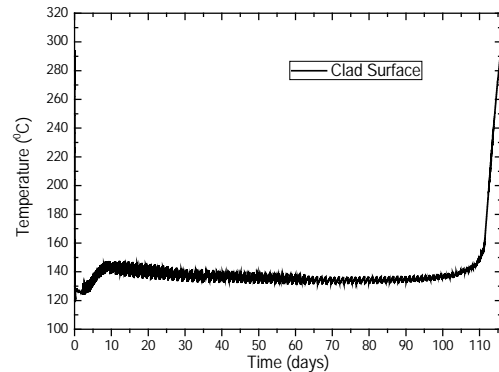


Fig. 9b: Clad Surface Temperature variation during prolonged SBO

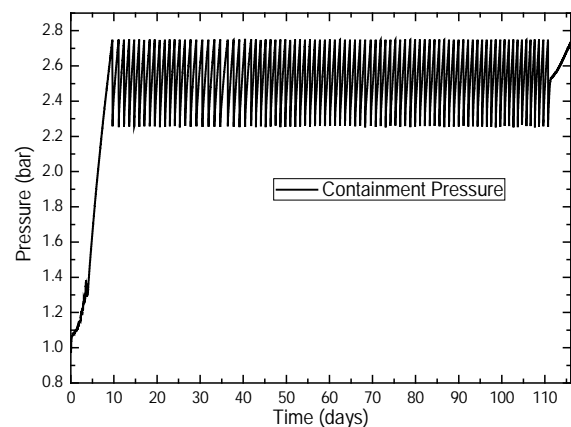


Fig. 9c: Containment Pressure variation during prolonged SBO

Lessons learnt from Fukushima and new passive systems incorporated in AHWR design based on feedback:

It is seen from the analysis that the decay heat can be removed safely for 110 days by Isolation Condensers. However, there arises a need for containment venting after 10 days as the pressure of the containment rises. Besides, the moderator and end-shield coolant temperature start rising as the pump cooling system is not available due to SBO. For addressing these issues, dedicated Passive Moderator (Figure10) [9] and Passive End-shield Cooling system (Figure11) have been introduced in the reactor design as Post Fukushima design modifications. These systems operate passively and transfer the heat to the GDWP by passive means to maintain the safe conditions of moderator and end-shield system. With the introduction of these passive features in the reactor design, the grace period of the reactor for such accident is extended to 7 days.

For venting the containment after 10 days, a Containment Filtered Vent System (CFVS) (Figure12) has been incorporated in the reactor design. CFVS depressurizes the containment and maintains the integrity of the containment. It also retains more than 99% of released radio-nuclides (if any) through a scrubbing system.

In addition, considering the design trend in current and future generation reactors to enhance safety, a dedicated core catcher (Figure13) is also introduced in the reactor design. The core catcher cools and stabilizes the molten core for prolonged period in case of severe accident. Besides, to mitigate the hydrogen issues, several Passive Catalytic Recombiner Device (PCRD) developed in-house are installed in the containment of AHWR to limit the hydrogen concentration inside containment below the flammability limit by controlled combustion of hydrogen using catalysts.

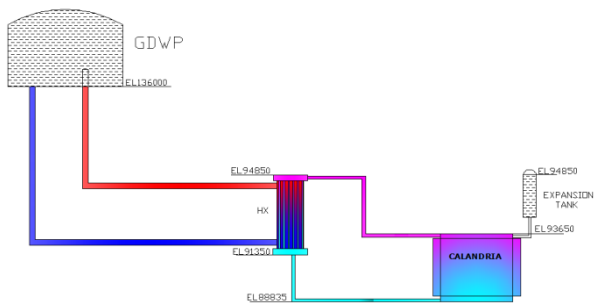


Fig. 10: Schematic of PMCS

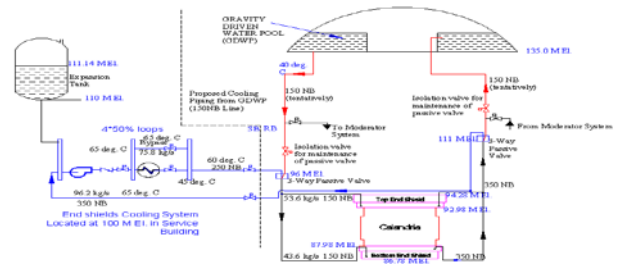


Fig. 11: Schematic of PECS

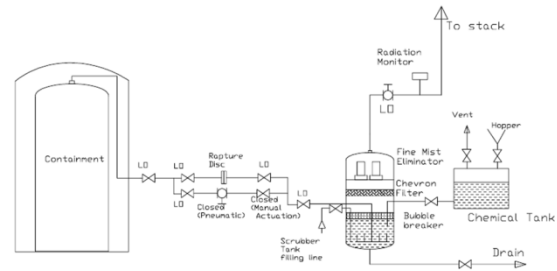


Fig. 12: Schematic of the Filtered Hardened Vent System

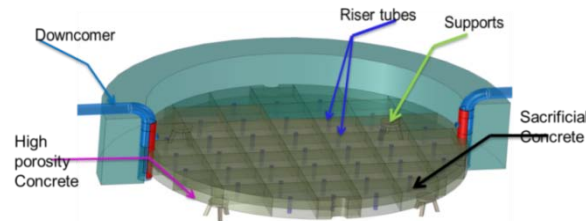


Fig. 13: Structure of the Core Catcher

Experimental demonstration of AHWR safety with new passive systems in place

Experimental Demonstration of AHWR Safety during Prolonged Station Black Out

In order to simulate the Fukushima type scenario in AHWR, an integrated test facility comprising of Passive Moderator Cooling System Test Facility (PMCS), Passive End-shield Cooling System Test Facility (PECS) and GDWP tank with submerged Isolation condensers was built (Fig. 14). Appropriate scaling laws were used for maintaining the geometrical and dynamic similitude in the facilities for accurate simulations of prototypic behavior. Experiment was conducted for 7 days without operator intervention with decay power level in each scaled PMCS and PECS and in simulated IC systems. Fig. 15 shows the temperature variation of the moderator and GDWP water for 7 days. The temperatures at calandria outlet rises to 60°C after 1 day and reaches to 70°C in 7 days. Figure 16 shows the temperature variation in the Passive End-shield Cooling

System Test facility reaching to maximum 65°C in 7 days. The temperature at the outlet of the calandria vessel and end-shield vessel remains well within safe limits of 100°C.

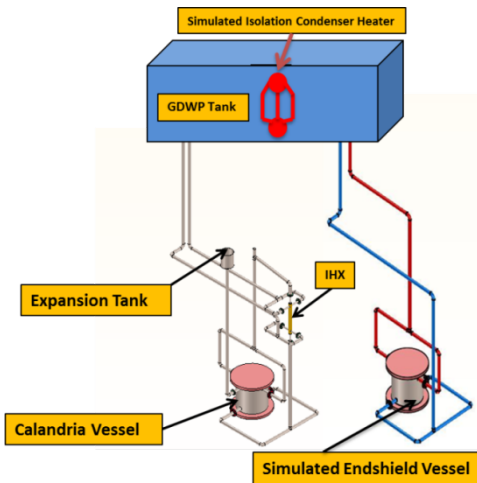


Fig. 14: Schematic of Integral test facility for simulating Fukushima type scenario

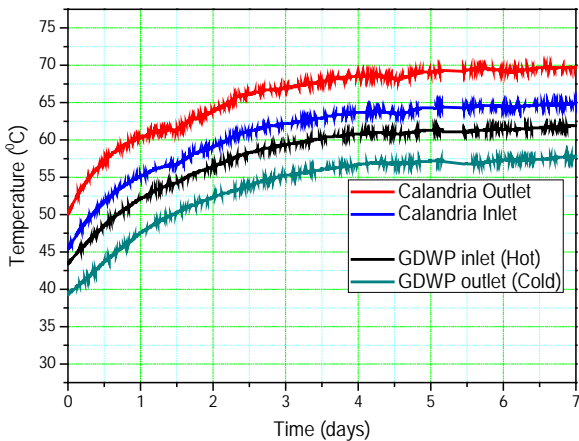


Fig. 15: Fluid Temperature Variation at Calandria inlet/Outlet and GDWP Inlet/Outlet

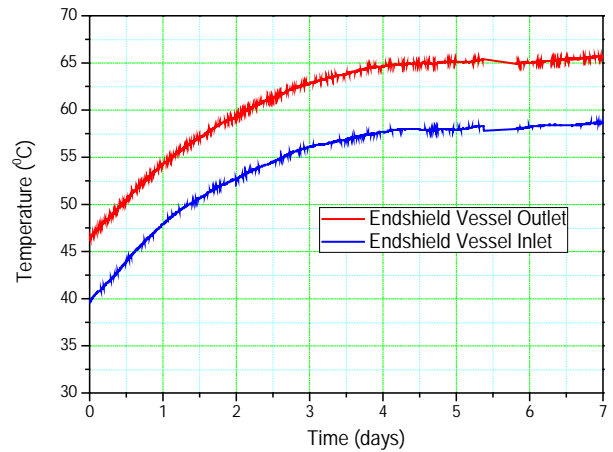


Fig. 16: Fluid Temperature Variation at Endshield vessel inlet and outlet

Experimental demonstration of decay Heat Removal by submerged feeders in AHWR during severe seismic conditions

Following a strong seismic event, cracks may develop in GDWP leading to leak of GDWP tank and causing unavailability of GDWP water for decay heat removal through submerged isolation condensers. In such a scenario, the GDWP water will be relocated in the primary containment and will fill the V2 volume of the primary containment. A new passive system called PAUSE (Passive Union of V1 and V2 Volume) has been incorporated in AHWR design after Fukushima accident that facilitates the flow of water from V2 volume to V1 volume of the primary containment until the water level in both the volumes becomes equal. It is estimated that the level in both the volumes will be around 6.67 meters when all the water of GDWP relocates in the containment. The relocated GDWP water thus submerges the feeders of the reactor after filling into the reactor cavity. There is a regulatory concern with regard to heat removal capability of the submerged feeders because of the relocated heat sink at the bottom as compared to the core. For this, full scale experiments were carried out in the integral test facility simulating the above conditions. Figure 17 shows the schematic of the experimental setup for the feeder submergence experiment. Our experiments demonstrated that the submerged feeders could remove the decay heat for several days without increasing the pin temperature even without the presence of ECCS. The Primary system could get depressurized to almost 10 bar in a period of 24 hrs as seen from Figure 18a. Figure 18b shows the channel flow during the test. An intermittent flow was observed in the loop after 15 hrs at low pressure. The clad surface

temperature was decreasing (Figure18a) during the experiment. This established the robustness of AHWR design against extreme events like that of Fukushima accident.

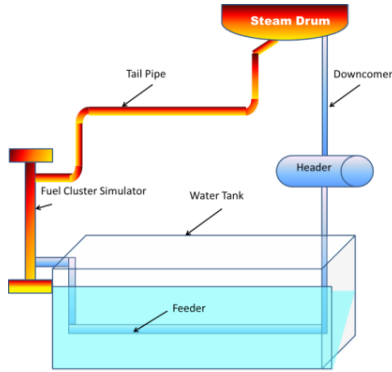


Fig.17: Schematic of setup for Submerged Feeders

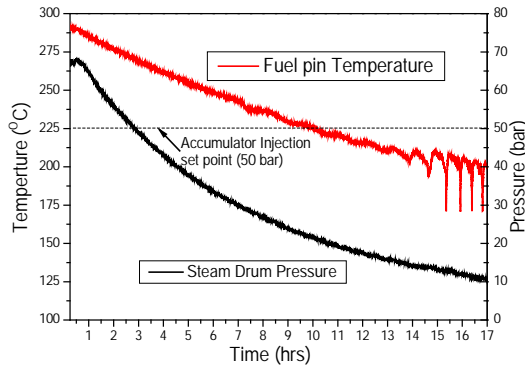


Fig.18a: Fuel Pin Temperature and MHT pressure

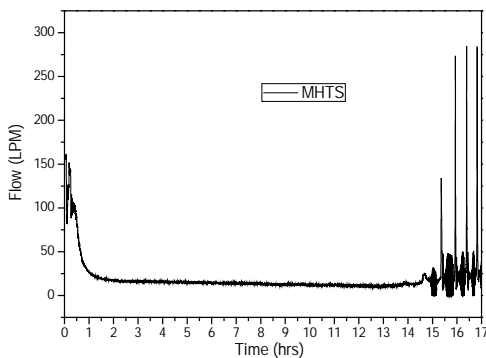


Fig.18b: Channel Flow

Demonstration of safety in prolonged SBO with core melt condition

In case of a core melt down accident, the molten corium is relocated into the core catcher, which interacts with sacrificial material and loses its enthalpy. Subsequently the core catcher is flooded with water from GDWP through nozzles located at bottom of core catcher. Typical cooling curve of corium is shown in Figure 19.

Several tests have been conducted to validate the core catcher design as shown in Figure19 and details can be seen in references [10-13].

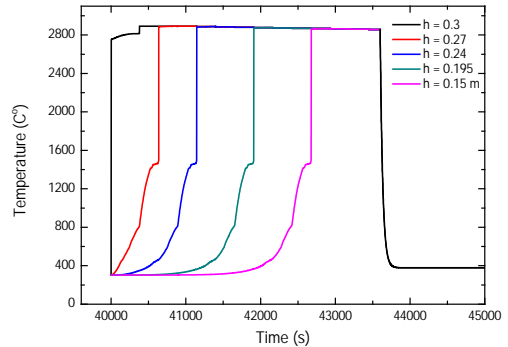


Fig. 19 (a): Cooling of Corium in the core catcher



Fig. 19 (b): Picture of Test Facility



Fig. 19 c: Experimental demonstration of quenching of melt stimulant

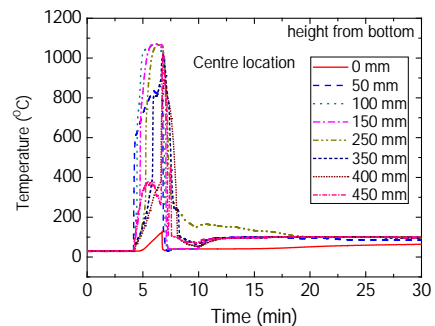


Fig. 19 d: Debris formation during melt eruption in core catcher

Roadmap ahead

Power uprating for AHWR

The experiments at AHWR operating conditions show that large thermal margin exists in AHWR, indicating the possibilities of power uprating of AHWR above existing design of 920 MW by 30%. The design margins be further confirmed in the full scale facility, ATTF.

Th-Pu based fuel properties and material behavior

In AHWR, the fuel composition is substantially different as compared to common LWRs. While, for typical LWRs, the corium typically consists of 76 % UO₂ + 9 % ZrO₂ + 15 % Zr, In AHWR, the fuel composition is (Th:Pu:U233)O₂ : (95.8:2.64:1.56). Since this is a first of a kind fuel, properties of corium, its interaction with sacrificial material and resulting phase equilibria needs to be determined.

References

1. A.K. Nayak, P.K. Vijayan, D. Saha, V. Venkat Raj and M. Aritomi, Analytical study of nuclear-coupled density-wave instability in a natural circulation pressure tube type Boiling Water Reactor”, Nuclear Engineering and Design, vol. 195, 27-44, 2000.
2. A.K. Nayak, P. Dubey, D.N. Chavan and P.K. Vijayan, Study on the Stability Behaviour of Two-phase Natural Circulation Systems Using a Four-equation Drift Flux Model”, Nuclear Engineering and Design Journal, Volume 237, Issue 4, February 2007, Pages 386–39
3. A.K. Nayak, P. K. Vijayan, V. Jain, D. Saha and R.K. Sinha, Study on the flow-pattern-transition instability in a natural circulation heavy water moderated boiling light water cooled reactor”, Nucl. Engg. Design, vol. 225, 159-172, 2003.
4. A.K. Nayak, M.R. Gartia, A. Antony, G. Vinod, R.K. Sinha, Passive system reliability analysis using the APSRA methodology, Nuclear Engineering and Design, 238 (2008), 1430–1440
5. A.K. Nayak, Vikas Jain, M.R. Gartia, Hari Prasad, A. Anthony, S.K. Bhatia, R.K. Sinha, Reliability assessment of passive isolation condenser system of AHWR using APSRA methodology, Reliability Engineering and System Safety, 94(2009), 1064–1075.
6. A.K. Nayak, Vikas Jain, M.R. Gartia, A. Srivastava, Hari Prasad, A. Anthony, A.J. Gaikwad, S. Bhatia, R.K. Sinha, Reliability assessment of passive containment isolation system using APSRA methodology, Annals of Nuclear Energy 35 (2008) 2270–2279.
7. Mukesh Kumar, Aranyak Chakravarty, A.K. Nayak, Hari Prasad, V. Gopika, Reliability assessment of Passive Containment Cooling System of an Advanced Reactor using APSRA methodology; Nuclear Engineering and Design; Volume 278; p. 17-28 (2014).
8. Mukesh Kumar, A. K. Nayak, Vikas Jain, P. K. Vijayan, K.K. Vaze, Managing a prolonged Station Blackout condition in AHWR by passive means”, NUCLEAR ENGINEERING AND TECHNOLOGY, VOL.45 NO.5 OCTOBER 2013. 605-611
9. Mukesh Kumar, Eshita Pal, A. K. Nayak, P. K. Vijayan, “Conceptual design of a passive moderator cooling system for a pressure tube type natural circulation boiling water cooled reactor”, Nuclear Engineering and Design; Volume 291; p. 261-270 (2015).
10. N. Singh, P.P. Kulkarni, A.K. Nayak, Experimental investigation of melt coolability under bottom flooding with and without decay heat simulation”, Nuclear Engineering and Design Journal (2015), Volume 285, Pages 48–57.
11. P.P. Kulkarni, A.K. Nayak, Study on coolability of melt pool with different strategies; Nuclear Engineering and Design; 270 (2014) 379–388.
12. P.P. Kulkarni, A.K. Nayak; A simple model to understand physics of melt coolability under bottom flooding; Nuclear Engineering and Design, 262 (2013) 81– 87.
13. P. P. Kulkarni, A. K. Nayak, Quenching Behaviour of Top Flooded Molten Pool; International Journal of Nuclear Energy Science and Engineering Volume 4 (2014); 20-25.

Prediction of Materials for Hydrogen Storage: Quantum Chemical Methods and Materials Modeling are Indispensable Tools

K. R. S. Chandrakumar

Theoretical Chemistry Section, Chemistry Group

Dr. K.R.S. Chandrakumar is the recipient of the DAE Scientific & Technical Excellence Award for the year 2014

Abstract

The basic understanding of hydrogen molecular interaction with the solid surface is one of the important criteria to design the hydrogen storage materials. Such understanding at the molecular scale can only be achieved by employing appropriate electronic structure methods. Accordingly, the present article reports the theoretical work carried out in our laboratory for designing the hydrogen storage materials. In particular, we demonstrate the theoretical prediction and design of the materials for hydrogen storage using some of the elegant chemical concepts: (a) Ion-Molecule interaction mediated hydrogen adsorption (b) Aromaticity induced hydrogen adsorption (c) Nanoscale curvature induced hydrogen adsorption. The suitability of these complexes for developing fullerene-based hydrogen storage materials is discussed along with the experimental reports.

Introduction

In recent years, it has been unambiguously comprehended that theoretical modeling in many areas of research applied at different scales (matter and time), is being largely practiced and pursued by almost all universities and institutes. The level of confidence that has been accomplished from the accurate predictions and explanations of numerous phenomena by various levels of *ab initio* and phenomenological theories, have transformed the mindset of research groups to the extent that these theoretical tools have now become an indispensable tool like any other sophisticated instruments in a laboratory. Many of the proposed models as well as theoretical methods have together made a profound impact on our understanding of the natural observations at the microscopic and macroscopic levels in an elegant way. These theoretical methods are simply the mathematical methods or models which basically emerge from the fundamental basic laws of science to unravel several phenomena and understand the nature of systems ranging from atomistic scales to mesoscale materials.

Although the successes of theories and associated models are very well known in the literature, the successful predictions heavily rely on the type of systems which are under scrutiny.¹ For example, the role of theoretical models is inevitable for optimizing the structural design, automotive applications, optimizing several parameters for a specific function, at the mesoscale level, etc. However, applicability of the theoretical models for understanding the physical and chemical systems at the atomistic level significantly depends to a large extent on the nature of the quantum mechanical properties of the particles involved in the system. In this regard, the problem of prediction as well as interpretation of the preferred direction of a chemical reaction and product formation under different conditions is still considered as a great challenge.² Thus, the theoretical models have been classified into two different domains based on the classical and quantum mechanical foundations which are very popular among the engineers and scientists, respectively.

The recently developed theories based on the principles of quantum mechanics applied to the chemistry and physics related problems at the atomistic levels, so called quantum chemical methods provide a basic framework

to investigate several problems spanning from the nature of bonding in molecular systems; surface phenomena based properties to electronic conductance, magnetism, etc. with a reasonable accurate way.^{3,4} The applicability of these methods has been realized to small-medium sized systems with the precision to the experimental findings. It should also be mentioned that for the case of larger molecular systems, these methods are still prohibitively expensive from the computational point of view. The present article focuses on such theoretical methods which primarily originates from the philosophy of quantum mechanics and these methods categorically forms the basics of electronic structure techniques and materials modeling. These methods essentially provide the description of electrons present in atoms, molecules and solids by approximately solving the Schrödinger equation for the many electron wave functions. Some of the methods have been developed by involving full parameterization or few external parameterization or first principle based methods without any parameterization while solving the Schrödinger equation which are otherwise classified in the literature as molecular mechanics, semi-empirical or *ab-initio* (meaning “*from the beginning*”) methods, respectively. The level of approximations involved in the methods defines the accuracy of the predictions and material properties. The exact solution for hydrogen atom and hydrogen-like atoms can be obtained by solving the Schrödinger equation and for any systems other than having more one electron, approximations are warranted which can directly affect the accuracy of the outcome of the results. A reliable accuracy in evaluating the molecular and material properties can be achieved reasonably with *abinitio* methods, namely wave-function theory and density functional theory (DFT).^{3,4}

One of the most well-known types of *ab initio* method is the Hartree-Fock (HF) method which approximates the many electron wave functions into one-electron wave functions by adopting the self-consistent central field approximation and it follows the variational principle. This method is one of the most successful method in describing electronic structure and properties of the many electron systems and the introduced error is almost 5-10 % of the total energy of the system, which is the resultant of coulomb repulsion between the electrons explicitly, known as electron correlation error. Unfortunately, the energy corresponding to the correlation error is almost equivalent to the energy corresponding to the inter- and intra- molecular

interaction energy of the molecular systems and most of the chemical phenomena. In addition, it has also been observed that the electron correlation error can severely undermine the electronic properties of molecules and solids. Due to these problems and limitations of HF theory, it has been realized the importance of the formulation of a systematic generalization of the issues pertaining to the electron-correlation problem appropriately. There are basically three different ways, through which the theoretical methods have been developed, viz., configuration interaction (CI), many body perturbation theory (MBPT) and coupled cluster (CC), broadly known as post HF methods.⁵ Although these methods have been very accurate in predicting the electronic structure as well as properties of systems, designing several chemical compounds and explaining most of the physical phenomena, the main disadvantage is that these methods are applicable small to moderate size of the systems due to the high computational cost and they require high amount of computer CPU time, memory, and disk space.

There exists another electronic structure method, known as density functional theory, an alternative theoretical method to handle the problem of heavy computational cost by including the electron correlation problem in an approximate way, by employing density as a functional variable rather than the wave function. Since the density is function of 3 variables in contrast to 6N variables dependent wave function, the computational cost for the heavier and large systems can be reduced drastically.⁶ The basis of DFT stems from two basic theorems of Hohenberg-Kohn and the practical approach to the present DFT method is formulated by Kohn and Sham which is similar in structure to the *ab initio* based Hartree-Fock method. Because of this reason, the computational community has witnessed upsurge growth of DFT applications in the recent years. Since the DFT method with various exchange-correlation functionals are available, one has to be cautious in choosing the correct exchange-correlation functional for the given set of problems.

The present work described in this article focuses on both the *ab initio* and DFT based calculations for modeling the suitable materials for hydrogen energy. In what follows, we will first discuss the importance of hydrogen energy and then, computational design of suitable materials for the hydrogen storage using some of the elegant chemical concepts. The experimental

validation on the theoretically proposed materials has also been discussed in the last section.

Materials for Hydrogen Energy

It has been known for many years that one of the safest and renewable alternative fuels is hydrogen because of its high abundance, nonpolluting nature and renewable form of future energy sources. It is also one of the most important topics of research due to its potential applications for future energy schemes in comparison to the existing carbonaceous fossil fuels, commonly known as hydrogen economy.^{7,8} In spite of many targeted research work towards the hydrogen economy, one of the major challenging aspects is finding a suitable material for hydrogen storage for automobile applications. The most pre-requisite conditions for the hydrogen-storage materials is to have a high volumetric/gravimetric density with fast kinetics for adsorption and desorption of molecular hydrogen and cost effectiveness of the material. In this regard, extensive research has been initiated toward the development of promising novel materials and eventually many materials have been proposed, viz., carbon nanostructures, metal hydrides, zeolites, metallorganic frameworks, polymers, inorganic-organic framework and clathrate compounds for storing the hydrogen. However, none of these materials has been shown to be practically successful materials. It has been now realized that the basic understanding of hydrogen molecular interaction with the solid surface is one of the important criteria to designing the hydrogen storage materials. Such understanding at the molecular scale can only be achieved by employing appropriate electronic structure methods.

Let us now try to understand why the hydrogen molecule being smallest molecule, is still difficult to design a suitable material for its storage. Since the hydrogen molecule is very stable under normal conditions, it is very difficult to polarize and hence, the influence of any neutral surface on the hydrogen molecule is very small. It is due to the following reasons: (i) It has fully occupied molecular orbital with large potential energy depth (ii) high HOMO-LUMO gap (iii) high ionization potential (iv) low electron affinity. For the effective hydrogen adsorption, the adsorbent surface should be able to polarize the hydrogen molecule. In general, the physisorption is possible when the adsorbent surface and molecular interaction is through van der Waals interaction for which the corresponding interaction

energy is basically proportional to the polarizability of the both gas and solid surface, i.e. $BE_{H_2-solid} = P_{H_2}P_{solid}/R^6$, where, R is the distance between hydrogen molecule and solid; P_{H_2} and P_s refer to the polarizability of hydrogen and adsorbent solid system, respectively. Since the polarizability of hydrogen is fixed, the other parameter, polarizability of the adsorbent (P_s) can have a dramatic influence on the interaction with hydrogen molecule. It may also be noted that the highly polarizing surface can polarize the hydrogen molecules to the extent that they can be dissociated into atoms which can bind with the adsorbent surface very strongly. This is type of adsorption, commonly known as chemisorption, which happens with the transition metal surfaces, for e.g. Sc, Ti, Pd, Pt, etc. This process is, on the other hand, unwarranted as it requires more amount of energy for the desorption of hydrogen molecules. Hence, in general, in order to have an efficient storage media along with fast kinetics at ambient conditions, the materials are expected to have the hydrogen adsorption energy in the range of 2-5 kcal/mol. Also a weak non-dissociative hydrogen adsorption is preferred to the stronger binding via hydrogen atomic dissociation over the metal cations.

Based on these observations, we defined some of the prerequisite conditions for the effective hydrogen adsorption, the adsorbing materials should be (a) light weight (b) number of hydrogen molecules should be as high as possible (c) the interaction strength should be moderate (2-5 kcal/mol). Accordingly, we have made an attempt to design suitable hydrogen storage materials and we addressed some of the following issues:

- Can the alkali metal systems be suitable components of materials for hydrogen storage?
- Why alkali metals can be more preferred than the transition metal atoms?
- What is the maximum number of hydrogen molecules can be bound to these metal cations?
- What is the nature of the cation-hydrogen interaction and their impacts on designing hydrogen storage materials?
- Whether can these cations retain their affinity towards the hydrogen even in the presence of solid frameworks (host materials)?

In order to address the above issues, we have proposed some of the elegant chemical concepts for designing the materials for hydrogen storage:⁹⁻¹³

- Ion-Molecule interaction mediated hydrogen adsorption

- b) Aromaticity induced hydrogen adsorption
- c) Nanoscale curvature induced hydrogen adsorption

Apart from the above problems, another major issue is with the selection of theoretical methods. Since the interaction of molecular hydrogen with any surface is very weak, theories should be able to handle the type of interaction from dispersion, van der Waals to dipole-induced interactions. It may be noted that such type of interactions and the associated energies fall roughly within the range of correlation energy and hence, higher level of electronic structure methods including the electron correlations are very necessary. Most of the conventional theories and methods with model potentials can fail and lead to erroneous results. Keeping these conditions as a cautionary warning in our mind, we have applied both the *ab initio* and DFT based methods for exploring the materials for hydrogen storage.

First, we made an attempt to understand the molecular hydrogen adsorption with the s-block metal cations (alkali and alkaline earth metal cations), as they are lighter elements compared to the transition metals. Herein, the proposed mechanism is through the electrostatically driven ion-molecular interaction of dihydrogen with s-block metal cations. Our results demonstrate that the number of hydrogen molecules attached to the metal cation is the highest ($M^+(H_2)_8$, $M=Na, K$) ever reported in the literature and the interaction strength between s-block metal ions with hydrogen is also found to be suitable for designing the materials for the hydrogen storage (**Figure 1A**). The calculated binding energy for hydrogen molecular interaction (MP2 method using cc-pVDZ basis set) is observed to be of the order of -30 to -13.5 kcal/mol for the case of alkali metal cations. Interaction of molecular hydrogen with anions, especially the halide ions (F^- , Cl^- and Br^-) have also been carried out and our results reveal that (i) the halide ion- H_2 bonds are linear but not T shaped (as shown in **Figure 1A**) as in the case of metal cation- H_2 complex and (ii) for the case of chloride ion complex case, maximum of 12 hydrogen molecules are adsorbed in a highly symmetric manner with an icosahedral geometry in the 1st solvation sphere. The interaction energy of hydrogen molecule with chloride ion is observed to be in the range of - 2.2 kcal/mol per

hydrogen molecule. Using this simple ion-molecule interaction, the possibility of the application of these complexes for developing hydrogen storage materials has been made through the carbon nanomaterials, specifically the fullerene based materials. These nanomaterials otherwise are very neutral and the hydrogen adsorption is observed to be very weak. Later, we demonstrated that doping of alkali metal atoms into fullerenes causes a remarkable enhancement in the hydrogen adsorption capacity. For instance, if eight sodium atoms are doped with C_{60} fullerene, the total number of adsorbed hydrogen molecule is found to be 48, with a gravimetric density of ~ 9.5 wt %. The adsorption efficiency of the proposed fullerene based material is observed to be better than other types of complexes particularly with the transition metal atoms.

We further extended the concept ion-molecule interaction for other types of carbon nanomaterials. Our results led to an important conceptual proposal on the curvature of nanosurface. The reactivity of the carbon nanomaterials can be enhanced remarkably not only by the electrostatic forces but also by tuning different types of curvature into the carbon nanosurface. The concept of curvature is basically understood from the structural parameters of the carbon nanosurface (as shown in **Figure 1B**) and it can be also used as one of the descriptors to assess the reactivity pattern of the carbon nanomaterials, including the nanotubes and fullerenes. Herein, we have observed that if we move from a planar benzene type of systems to a curved pattern of carbon hexagonal rings, the binding strength of sodium atom increases drastically with the curvature: 0.5 to -21.3 kcal/mol and there is a spontaneous (gradual) ionization of the sodium atom upon binding with the curved benzene structure. The charge acquired by the sodium atom (+0.6au) due to the effect of curvature in benzene molecule is approximately comparable to that of sodium cation (+0.8au) interacting with the benzene molecule. The high reactivity of the curved carbon surface is related to the weakening of pi-pi bonds between the carbon atoms due to the bending of the carbon hexagonal ring which makes the system to have quasi- sp^2 - sp^3 hybridization with substantial s-orbital character.

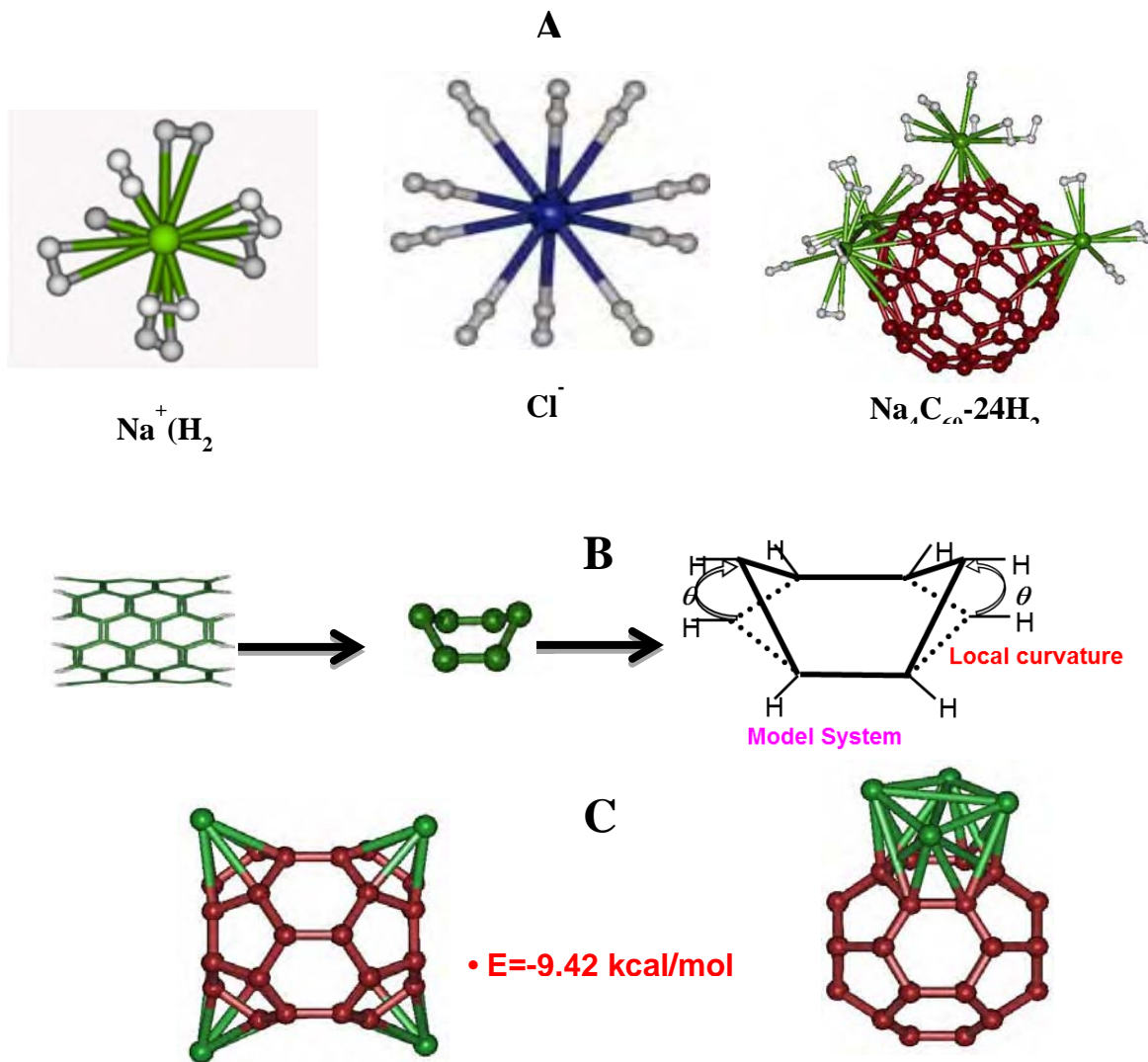


Fig.1: (A) Hydrogen adsorption with cation, anion and cation doped C60
 (B) Concept of curvature and a model system with 6m-carbon ring
 (C) Effect of clustering of sodium atoms around C36 fullerene

One of the main issues with the transition metal ions is the clustering of these metal ions around the material surface due to the high cohesive energy. Due to this effect, individual ion-hydrogen molecular interaction is drastically reduced which directly affects the hydrogen adsorption gravimetric density. In view of this, we also made an attempt to investigate whether the s-block metal elements can cluster on top of the fullerene or not. It can be seen from **Figure 1C** that the carbon surface with individual metal atoms is better stabilized than that of cluster of metal atoms. For the case of sodium atoms interacting with C₃₆ system, the calculated energy difference between the cluster and individual atoms is in the range of ~10 kcal/mol. Thus, our results further

validate on the suitability of the s-block doped materials for hydrogen storage.

Let us now move on to another concept, namely aromaticity and explain how this concept can be useful for designing hydrogen storage materials through the use of organic molecular systems C_nH_n [n=4-6 and 8]. The 5m-carbon ring C₅H₅ has five electrons in the ring which falls short of one electron in order to become six electron containing aromatic system, satisfying the Huckel (4n+2) rule. When sodium atom is brought near to the C₅H₅ ring, it has been seen that a positive charge is created on sodium atom, indicating the possibility of complete electron transfer to the carbon ring from sodium atom. The ionized sodium atom thus can interact with the

hydrogen molecules very effectively, as observed in case of fullerenes and our results demonstrate that maximum of 6 hydrogen molecules can be added effectively with the C_5H_5-Na , with the interaction energy in the range of ~ 1.7 kcal/mol per hydrogen molecule. Since the benzene molecule is already stable aromatic compound, there is no significant interaction between the C_6H_6 ring and sodium atom. Similarly, we also extended this concept to other carbon rings and observed similar hydrogen adsorption pattern. Further, we have also made an attempt to realize hydrogen adsorption efficiency of such molecular systems by converting into molecular materials through a self-assembled pattern by suitable modifications or substituents without affecting the aromaticity of the carbon rings. Accordingly, we designed a C_2 unit as a suitable ligand for the C_5H_5 ring such a way that they form a bridge between several C_5H_5 rings. Our results for the interaction of sodium at each site of $(C_5H_5-C_2)_{10}$ show that the interaction pattern remains the same and the charged surface is created. The subsequent hydrogen adsorption is also surprisingly comparable to the case of C_5H_5-Na without losing any of their characteristic property of the molecular complex, as shown in **Figure 2**.

After we proposed several materials for hydrogen storage, as mentioned above, few experiments have also been carried out on some of the selected materials, especially the alkali metal doped fullerenes and nanotubes.^{14,15} One of experimental results show that a lithium-doped fullerene (Li:C60 mole ratio of 6:1) can reversibly desorb up to 5 wt % H_2 with an onset temperature of ~ 270 °C under optimized conditions. The range of temperature is significantly less than the desorption temperature of hydrogenated fullerenes ($C_{60}H_x$) and pure lithium hydride (decomposition temperature 500–600 and 670 °C respectively). In addition, it has also noted that the fullerene cage is found to be very stable which is slightly modified during multiple hydrogen desorption/absorption cycles. In another related experiment, the hydrogen adsorption efficiency was evaluated for the sodium intercalated (Na_xC_{60}) and it was observed that up to 3.5 mass% hydrogen can reversibly be absorbed in Na_xC_{60} at 200 °C and a hydrogen pressure of 200 bar. Here also, it has been seen that the fullerene cages even with the high hydrogen loadings, the Na_xC_{60} sample stays intact.

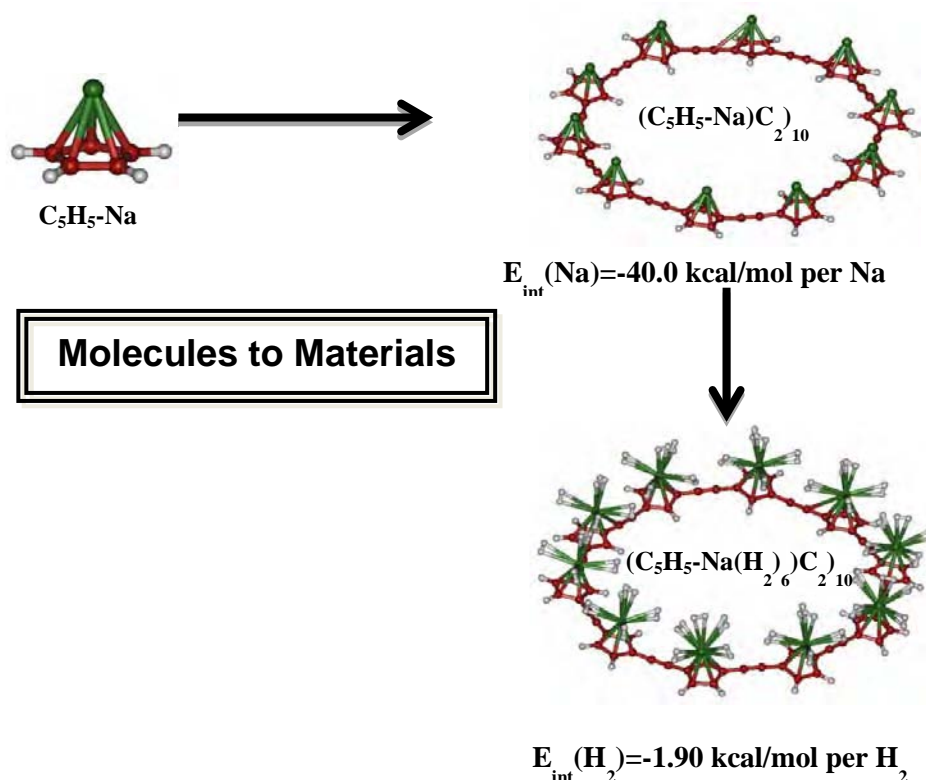


Fig. 2: Hydrogen adsorption in a self-assembled model complex: Alkali metal doped $(Na-C_5H_5-C_2)_{10}$ units:

Concluding Remarks

In conclusion, it is quite evident that there is a close match between the predictions made by the theoretical and experimental methods towards the design of materials for hydrogen storage. More importantly, the simple concept of ion-molecule based electrostatic interactions satisfies some of the important requirements for the hydrogen storage materials, (a) weak interaction (b) significant number of hydrogen molecules at the ionic site (c) light-weight materials through the usage of s-block elements. These proposed materials can stimulate further research in this area; particularly in designing new materials by exploiting the electrostatics mediated ion-molecular interactions.

Acknowledgment

I thank Prof. Swapan K. Ghosh for his encouragement and useful discussions throughout this work. I also thank Dr. B. N. Jagatap for his support and encouragement. My collaborators Drs. Srinivasu, Naresh K. Jena and Manoj K. Tripathy are thankfully acknowledged. I am also grateful to the computer center for providing the high performance parallel computing facility.

References:

1. Richard B. Ross and Sanat Mohanty, (Eds) *Multiscale Simulation Methods for Nanomaterials*, Published by John Wiley & Sons, **2008**.
2. Pauling, L. *The Nature of Chemical Bond and Structure of Molecule and Crystals*; published by Oxford and IBH: New Delhi, **1967**; (b) *Theory of Orientation and Stereo Selection*; by Fukui, K. published by Springer-Verlag, Berlin, **1975**.
3. Richard. M. Martin, *Electronic Structure: Basic Theory and Practical Methods*, published by Cambridge University Press, **2004**.
4. Christopher J. Cramer, *Essentials of Computational Chemistry: Theories and Models*, published by John Wiley & Sons Ltd, **2002**.
5. Attila Szabo and Neil S. Ostlund, *Modern Quantum Chemistry: Introduction to Advanced Electronic Structure Theory*, Published by Dover Publications, Inc. Mineola, New York, **1989**.
6. Robert G. Parr and Weitao Yang, *Density-Functional Theory of Atoms and Molecules*, published by Oxford University Press, New York, **1989**.
7. (a) Russell H. Jones, George J. Thomas, *Materials for the Hydrogen Economy*, published by CRC Press, Taylor & Francis Group, **2007**; (b) Michael Frank Hordoski, *Alternative Fuels: The Future of Hydrogen*, published by CRC Press, Taylor & Francis Group, **2013**. (c) Lennie Klebanoff, *Hydrogen Storage Technology: Materials and Applications*, CRC Press, Taylor & Francis Group, **2012**.
8. (a) Rajeshwar, Krishnan, McConnell, Robert, Licht, Stuart (Eds.), *Solar Hydrogen Generation Toward a Renewable Energy Future*, published by Springer-Verlag New York, **2008**. (b) Luis Gandia & Gurutze Arzamedi & Pedro Dieguez (Eds.), *Renewable Hydrogen Technologies, Production, Purification, Storage, Applications and Safety*, Published by Elsevier Publications, **2013**.
9. Chandrakumar, K.R.S. and Ghosh, S.K. *Electrostatics driven interaction of dihydrogen with s-block metal cations: Theoretical prediction of stable MH_{16} complex*, *Chemical Physics Letters* 447 (4-6), (2007) 208-214.
10. Chandrakumar, K.R.S., Ghosh, S.K. *Alkali-metal-induced enhancement of hydrogen adsorption in C60 fullerene: An ab initio study*, *Nano Letters* 8 (1), (2008) 13-19.
11. Srinivasu, K., Chandrakumar, K.R.S., Ghosh, S.K. *Quantum chemical studies on hydrogen adsorption in carbon-based model systems: Role of charged surface and the electronic induction effect*, *Phys. Chem. Chem. Phys.* 10 (38), (2008) 5832-5839.
12. Srinivasu, K., Chandrakumar, K.R.S., Ghosh, S.K. *Computational investigation of hydrogen adsorption by alkali-metal-doped organic molecules: Role of aromaticity*, *Chem Phys Chem* 10 (2), (2009) 427-435.
13. Chandrakumar, K.R.S., Srinivasu, K., Ghosh, S.K. *Nanoscale curvature-induced hydrogen adsorption in alkali metal doped carbon nanomaterials*, *Journal of Physical Chemistry C* 112 (40), (2008) 15670-15679.
14. Mauron, P.; Remhof, A.; Bliersbach, A.; Borgschulte, A.; Züttel, A.; Sheptyakov, D.; Gaboardi, M.; Choucair, M.; Pontiroli, D.; Aramini, M.; Gorreri, A.; Riccò, M. *Reversible hydrogen absorption in sodium intercalated fullerenes*, *International Journal of Hydrogen Energy*, 37(19), (2012) 14307-14314.
15. Teproovich Jr., J.A.; Wellons, M.S.; Lascola, R.; Hwang, S.-J.; Ward, P.A.; Compton, R.N.; Zidan, R. *Synthesis and Characterization of a Lithium-Doped Fullerane ($Lix-C_{60}-H_y$) for Reversible Hydrogen Storage*, *Nano Letters* 12(2), (2012) 582-589.

Mechanical design and development of DC, RF accelerator and ECR ion source programme of APPD, BARC

S. R. Ghodke, Rajesh Barnwal, Mahendra Kumar, Susanta Nayak, D. Bhattacharjee, J. Mondal, A. S. Dhavle, Vijay Sharma, Shiv Chandan, Nishant Choudwary, R. I. Bakhatsing V. T. Nimje, K. P. Dixit, S. Acharya, P. Roychowdhury
Electron Beam Centre, Accelerator & Pulse Power Division

S.R. Ghodke is the recipient of the DAE Scientific & Technical Excellence Award for the year 2014

Abstract:

APPD, BARC has taken up the indigenous design & development of high power electron accelerators for industrial, research and cargo scanning applications. Pulsed RF Linacs, with on-axis coupled cavity configuration, include the 10 MeV Industrial RF linac, 30 MeV linac for radiation streaming studies of fast breeder reactor as well as 6 MeV compact linac for cargo scanning applications. Industrial DC accelerators include a 500 keV Cockroft-Walton machine and 3 MeV Dynamitron. Several radiation processing applications, such as material modification, waste water treatment, flue-gas treatment, etc. have been demonstrated using these accelerators. 6 MeV linac for cargo-scanning have been successfully commissioned and are being characterized for the required x-ray output. For ADS studies, a 50 keV, 50 mA ECR Ion Source is fabricated including low energy beam transport line. This paper presents the details of the mechanical design and fabrication of these accelerators.

Mechanical design, fabrication and development of components of different programme of APPD are as given below.

1. 6 MeV Compact Linac:

The 6 MeV compact RF Electron Linac as X-ray head (fig-1) for container cargo-scanning applications has been designed and developed by the Accelerator & Pulse Power Division, BARC. In linac-based cargo-scanning systems, the linac acts as the source of x-rays, which fall on the cargo and are then detected by the detector system. This para describes the salient features of the 6 MeV compact linac and its fabrication.

From 6 MeV linac (fig-2) electrons are emitted from electron gun, accelerated up to 6 MeV in linac cavity and hit on a tantalum target to produce x-rays with a dose rate of 1-3 Gy/min/m. The specifications of the linac are given in Table-1 below:

Table-1: Specification 6 MeV compact linac

| | |
|-----------------------|---------------------|
| Beam energy | 6 ± 0.1 MeV |
| Peak beam current | 160 mA |
| Average beam current | 700 W (max) |
| X-ray beam focal size | 1.5 to 2 mm |
| X-ray dose | 1-3 Gy/min/m |
| X-ray field size | Std. 30 degree cone |

| | |
|-----------------------|--------------|
| Pulse width | 3.4 μs |
| Pulse repetition rate | 250 Hz (max) |
| Length of cavity | 0.6 m |
| RF frequency | 2856 ± 2MHz |
| Injection voltage | 40-85 kV |



Fig. 1: 6 MeV compact linac.

A 75 kV electron gun acts as the injector to the compact linac. The on-axis coupled cavity linac [12] operates at 2856 MHz and is powered by a magnetron-based

microwave power source [5MW(pk)/3 kW(avg)]. An electromagnet with eight pancake coils in series is used to focus the beam to a focal spot of diameter less than 2 mm. A water-cooled tantalum X-ray target is used to produce the required dose of x-rays. A collimator with slit of 4 mm width produces the 30° cone shaped x-ray field. Turbo-backed sputter ion pumps [13] are used to achieve vacuum level of 1×10^{-7} mbar in the linac. PLC-based control and instrumentation system enables remote operation of the linac. DM cooling water system provides cooling for linac, microwave components, focusing coils of the electromagnet and target.

The 6 MeV compact linac has been fabricated and installed. Beam trials on the 6 MeV compact linac have indicated that the linac performance shows a satisfactory trend.

Following components are mechanically designed, fabricated and installed inside rack of 6 MeV X-ray source.

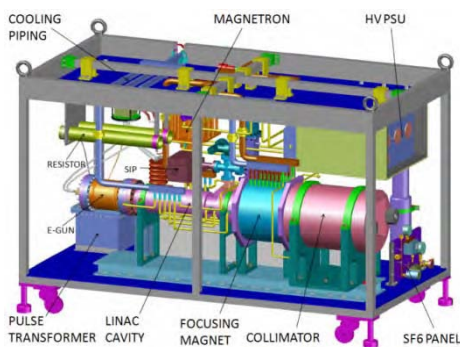


Fig.2 : 6 MeV compact linac model.

Fabrication of Electron Gun for 6 MeV X-Ray Source:

In linac-based cargo-scanning system, to work electron gun (fig-3) on a movable system, it has to be robust. Electron gun is to work at 10^{-7} mbar vacuum and 2000 degree Celsius cathode temperature.

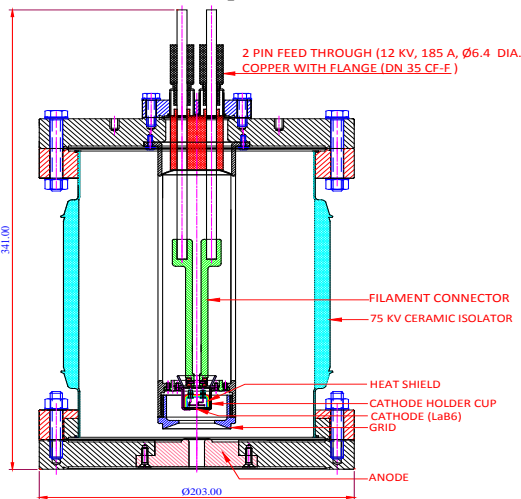


Fig-3: Compact electron gun Assembly.

An effort is made to engineer the gun assembly to make it more robust, easy removal of filament and alignment. Many components are indigenously developed like SS 316 grid, Ceramic insulating ring, Tantalum thermal shield, Tungsten filament and filament guide etc. All above components are to work at 800 to 2500 degree Celsius. Filament connector is made from Invar to reduce heat loss and to make rigid connection. Invar was CNC machined and wire cut by EDM. Invar and Copper electrode feed through is shrink fitted with the help of liquid Nitrogen. Shrink fit (fig-4) tolerances of 15 micrometer are achieved by jig boring machining processes. Tantalum cup for LaB₆ cathode and heat shield are made from die and punch mechanism. For alignment of electron emitter with beam axis this Tantalum cup is a crucial component. Electron gun is assembled and aligned its components with the help of precision jigs (fig-4). The whole assembly was Helium leak tested by MSLD up to 4×10^{-10} mbar.l/s vacuum, no leak was found.

Precision hole in the invar for shrink fit tolerance, Jig boring process is used.



Fig.4: Shrink fitting of two Copper pin feed through with Invar connector and alignment fixture.

Fabrication of cathode holder and heat shield:

Tantalum cups for cathode holder and heat shield housing (fig-5) are to be made from die and punch as shown in figure 3. In the initial trial cups were breaking because of excessive deformation. Then draw the cup in three stages with control deformation by using hydraulic press. The fresh dies are made and trials are taken, it is found that heat shield cups are drawn after few failures as shown in figure 4 and 5. Cathode cup trial is also taken and found it is forming but bend radius was more than 2 mm and also

wrinkling on the flange face. The dies were further corrected and cups are drawn. The final tolerances and design parameters are achieved by machining.

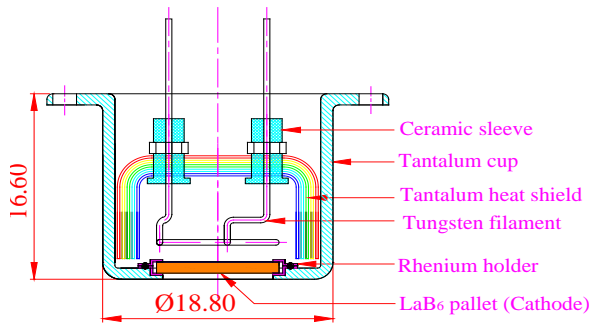


Fig. 5: Cathode holder & heat shield assembly

Fabrication of Tungsten filament:

Tungsten filament (fig-6) of spiral shape of 4 turns within 10 mm circle made from Tungsten wire of diameter 0.5 mm. Tungsten Filament is made from M/S Plansee India Pvt. Ltd. as per prescribed tolerances by Tungsten wire as shown in (fig-6).

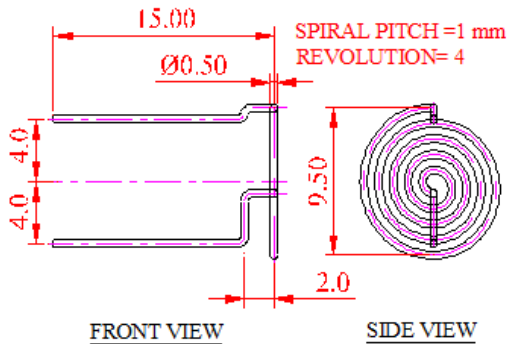


Fig. 6: Spiral Tungsten Filament

Alignment

Special jig and fixtures are made to ensure the alignment (fig-4) of grid, cathode and anode assembly within 50 micrometers as shown in figure 6, 7 and 8.

Design and development of primary collimator for 6 MeV X-ray source:

The primary collimator (fig-7&8) is designed to function with a 6 MeV x-ray source for cargo scanning application. It is installed and tested with linac. The accelerated electron beam hits a tungsten target and x-ray generated through the target is fed to the collimator. Thereafter, collimated high energy x-rays will be used for cargo scanning. The collimator plates are made up of mild steel blocks of is 2062 grade ensuring high geometrical stability. Each plate has been machined with high precision electric

discharge machining (EDM) and surface grinding processes. The assembly rods are hard chrome plated to provide corrosion resistance and increase surface hardness. It is aligned with x-ray source and being use for linac experiments. Fig-6 shows EDM wire cut plates with alignment gauge.



Fig. 7: Assembly of collimator plates with alignment gauge.

It is used for qualification of linac by ANSI object. The collimator assembly after mounting on support will be required to move in x, y, z direction and angularly so as to achieve desired shape of the X-ray beam and to align it with X-ray beam coming from 6 MeV Accelerator.



Fig.8: Primary collimator assembly.

After assembly all the eight number of plates, the whole assembly mounted on a mild steel support structure having two numbers of bearing with housing of size 360 mm OD for easy rotation through the central axis of the collimator. The support structure also equipped with a worm and worm wheel gear arrangement for fine control the rotation of collimator which is powered by a stepper motor.

Fabrication of accelerator tank and SF₆ gas handling system of 3 MeV DC Accelerator:

The 3 MeV Accelerator Project (fig-9) involves designing, fabrication, installation and commissioning of a 3 MeV, 30 kW Industrial Electron Beam Accelerator with a terminal voltage of 3 MV and is housed inside the Electron Beam Centre building at Kharghar, Navi Mumbai. For ecological and economical reason, the SF₆ gas is reincorporated into closed cycle.

SF₆ Gas Handling System of 3 MeV project mainly covers SF₆ gas transfer system including accelerator tank & storage tank and SF₆ gas cooling system. The aim of the SF₆ gas handling system is to introduce the gas at high pressure to the accelerator tank after evacuation and to bring back into the storage tanks with minimum loss. The gas handling system also provides purification of gas, prevention from mixing with air or any other substances, which may contaminate and thus bring down the high voltage insulation characteristics of the gas. A heat load of 12 kW is coming due to high frequency transformer, electron gun, power supplies, blower motor etc. A radiator type heat exchanger with centrifugal blower and finned tube has been used for cooling the gas.

Accelerator tank:

Accelerator pressure vessel is the main body of the 3 MeV Accelerator (fig-9) which will house high voltage multiplier columns, RF electrodes, corona shields, high voltage terminals, electron gun, accelerating tubes, motor generator set, heat exchangers, RF transformer etc. Normal operating pressure inside the accelerator is 6 kg/cm². The accelerator tank has to be evacuated to vacuum of 10⁻¹ torr before filling the gas. Detail design and fabrication of the accelerator pressure vessel using ASME B&PV SEC-VIII, DIV-1 Code was carried out.

SF₆ gas transfer system:

SF₆ gas transfer system (fig-10) has 150-meter long pipe line of 3" size pipeline, compressor, vacuum pump, dryer, filter, heater and blower.

SF₆ compressor is a non lubricating type, vertical double acting, single stage air compressor de-rated for SF₆ use with a free air delivery of 55 CFM and a maximum discharge pressure of 125 psi (g). The 3000 LPM capacity rotary vacuum pump is used to pump all the gas remaining in the tank after one atm. pressure, which is supplied to compressor and then transferred to storage tank. About 0.5 Torr vacuum is achieved in the accelerator tank, storage tanks and pipeline.

Vertical vessel twin column activated alumina filled dryer is used for removal of moisture and breakdown products. Coarse and fine filters are provided to make sure that dust free gas is circulated through the accelerator column.



Fig-9: 3 MeV Accelerator tank & RF tank.



Fig.10: SF₆ Gas Transfer System.

SF₆ gas cooling system:

This system is mainly comprises of 1.5" and 1" SS pipe line, radiator type heat exchanger and blower combination, 5 ton chiller unit, cooling tower, pressure transmitter, temperature sensors, safety interlocks, flow meter, pressure gauges and other instrumentation.



Fig.11: Rectangular Radiator Type Heat Exchanger inside the Accelerator Tank.

The centrifugal blower has been designed and commissioned to achieve special heat transfer requirements under 6-kg/cm² pressures of SF₆ gas. Finned tube heat exchanger with header have been designed and fabricated suitable for inside space of accelerator tank (Fig-11) Heat exchanger assembly is made of such four numbers of bundles and makes an enclosure of size 1100 x 1100 x 150 mm.

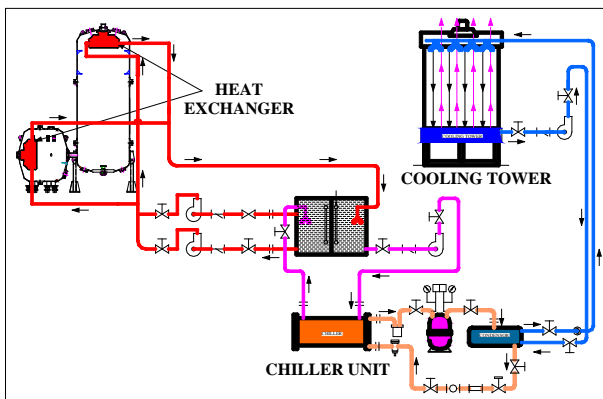


Fig.12: SF₆ Gas Cooling System.

Detailed chilled water flow and heat transfer calculations were done to make sure that high voltage RF Transformer, which is having a maximum heat load of 6-8 kW, is maintained within the permissible temperature limit. It was estimated that a total flow rate of 50 lpm of chilled water at 22°C is required through the heat exchanger for cooling (fig-12) of transformer inside the accelerator tank. Similarly other accelerator components having a maximum heat load of 3 kW requires a flow rate of 20 lpm of chilled water at 10°C.

In fabrication of SF₆ gas handling system we have carried out material test, welding test, hydro & pneumatic test, compressor & blower performance test and chiller performance test.

Fabrication of Buncher Cavity for 30 MeV Linac:

BARC has developed 2856 MHz, 04 cell RF Buncher cavity (Fig-13 &15) required for 30 MeV RF Linac project and it will be proposed to use for Neutron generation. New vendors are developed for fabrication techniques and its successful implementation in Buncher cavity. The fabrication process consists of material procurement, CNC Diamond turning of cavity, preparation of slot for vacuum brazing wire, CNC milling, chemical cleaning, vacuum furnace brazing, Copper-stainless Steel joints, development of fixtures for brazing, various brazing parameters, brazing cycle and helium leak testing etc.



Fig. 13: ETP Copper brazed cavity sample for tensile test.

Water jacket (Fig-14) for cavity cooling is designed such a way that it can be welded with brazed cavity. Performance of resonant frequency of cavity was measured.



Fig.14: Assembled water cooling jacket with welding lip.

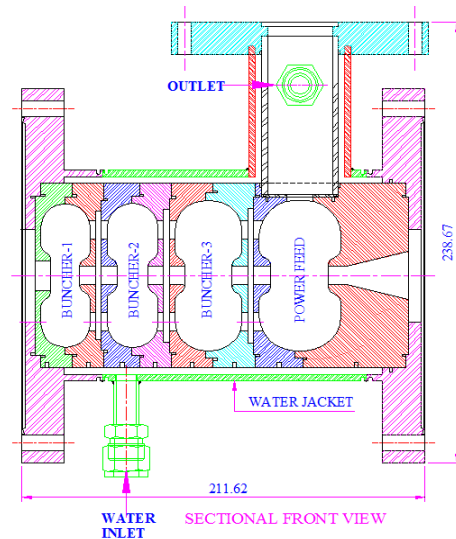


Fig.15: Buncher cavity.

CNC Machining of Copper cavity

Copper cavity is required for different RF Linac projects. CNC Diamond Turning shown in (fig-16) and milling at high accuracy are performed in modern machining workshops to achieve better quality factor of cavity of Linac and mirror finish. Additionally special care has been taken to guarantee good ultra high vacuum and high electric field performance of the finished cavity. For rough machining CNC Spinner lathe machine is used and for final machining CNC Diamond turning machine is used with single crystal and poly crystal Diamond tools.



Fig.16: Internal Diamond turned cavity.

Surface Finish

Internal surface finish should be very good to reduced RF power losses and to improve quality factor of cavity. Skin depth for current of RF power is approximately 1 micrometer. Roughness average (Ra) value of 20 nanometre or better asked in DTM machining. During our inspection we have achieved surface finish 8-15 nanometre of DTM machined cavity. White light interferometer is used for measurement of surface roughness as shown in fig. 3. All brazing surfaces have surface finish of 0.8 micrometer for better brazing.

Vacuum furnace brazing of OFHC Copper cavity

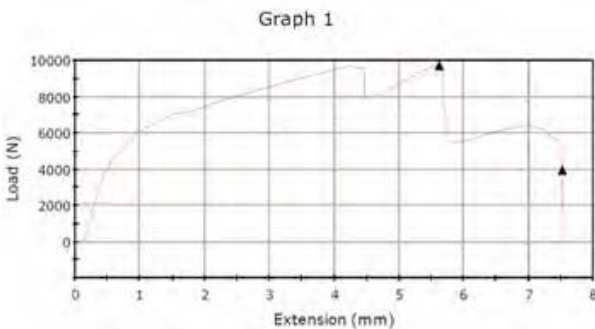


Fig.-17: ETP Copper tensile test of brazed cavity specimen.

Rough machined Copper cavity is annealed for removal of machining stresses. It is heated up to 400 degree Celsius in vacuum furnace and given one hour soaking time. Working vacuum of furnace should not be less than 5×10^{-5} torr in any point of annealing and brazing cycle. Heating rate should not more than 5 degree Celsius per

minutes and vacuum maintain as mentioned above. During vacuum deterioration, hold the job at constant temperature unless good vacuum is achieved.

BVAg-8 Eutectic alloy of melting temperature 780^o Celsius, with 72% Silver and 28% Copper is used in brazing of Copper cavity. BVAg-30 alloy of with 67.63% Silver, 27.54% Copper and 4.82% Palladium is also used.

Two samples of brazed cavity are tensile tested to find out ultimate tensile strength of brazed cavity. It is shown in (fig-17). We achieved strength of 95 MPa. Brazed copper cavity tested by radiographic method for brazed material flow analysis. One brazing joint found to be over flowed and not properly filled with brazing material of BVAg-8.

Successful vacuum brazing of prototype OFE Copper cavity are done. The brazed cavities are leak tested by using Helium leak detector. Leak tightness of the brazed joints found was better than 5×10^{-10} mbar-l/s. Water jacket is fabricated and seen its fit up.

Design and fabrication power feed cavity test setup for various linac:

In a RF electron linac a power is fed to the linac structure through a power feed cavity that connects the waveguide with the accelerating cavity through a coupling aperture. The amount of power fed to the linac depends on the coupling coefficient between cavity and the waveguide that is decided by the size and shape of the coupling aperture. The requirement of coupling coefficient changes with the energy and current in the accelerator. The optimization of the power feed cavity and the coupling aperture to attain required coupling at a required resonant frequency is a tedious task. Our experience shows that improper RF contacts lead to change in resonant frequency and hence the coupling coefficient. Also a frequency shift and change of coupling coefficient is observed in the linac structure in brazed and unbrazed condition. Thus a power feed (PF) test set-up consisting of 8 accelerating cells, 8 coupling cells and one power feed cavity is fabricated.

Also it will be used to study the change in resonant frequency and coupling coefficient with the application of external pressure/load. A load cell (fig-18) is assembled to see the applied load. Pressure transmitter and pressure gauge shows the applied pressure with hydraulic power pack. Hydraulic power pack can give 2.5 ton compressive load in assembly. Special and unique bead bull arrangement is made to do the in situ RF measurement during applied compressive load. Pulley of bead pull run by stepper motor control with PLC display. PLC also shows the load, pressure, bead position etc. It will be simulating the brazed structure in unbrazed condition.

Cavity fabrication requires chemical, micro, macro testing of oxygen free electronic (OFE) Copper.

THK make LM bush and LM rod made of high carbon-chromium bearing steel and hardness of HRC 58 to 64, straightness of shaft is $50 \mu\text{m} / 300 \text{mm}$ or less and precision of fitting between shaft and bush is g5- h5 grade. It has 150 mm long linear motion bush, 1 meter long linear motion rod of diameter 40 mm and end flange fittings. Four numbers of linear motion rods are fixed between two plates of thickness 18 mm and 14 mm, between above two plates one more plate of thickness 14 mm is assembled and it will move up and down with the help of hydraulic cylinder. Hydraulic pressure system is designed based on experiment through which we will get idea about load/stress at which, further no change in frequency and coupling coefficient. As per literature 1 to 2 ton load is sufficient.

PF test set up assembly (fig-20) requires CNC diamond turning for nano machining of cavity in addition to different machines like CNC electric discharge machining (wire cutting), CNC ultra precision lathe machining, CNC vertical milling centre etc for ultra precision work. This involves a lot of tool design and developmental work. Critical instruments like coordinate measurement machine (fig-19), master height gauge, white light interferometer etc is required for metrological inspection. Cavity material used as oxygen free electronic (OFE) Copper UNS No-10100 of purity 99.99 % and Oxygen content is less than 5 ppm.



Fig.18: Load Cell for 2.5 ton load and assembled cavity before brazing.



Fig. 19: Co-ordinate measurement of cavity and surface roughness measurement by white light interferometer.

Copper plating required for SS flange and wave guide (284). SS should be plated with Nickel and then with Copper. Total plating thickness more than $5 \mu\text{m}$ but less than $10 \mu\text{m}$ is used.

Alignment is most important for smooth assembly under heavy loads. Proper tool and fixture is used to get assembly alignment 10-20 micrometer.

All dimension and contour of the cavity is measured in Co-ordinate Measuring Machine (CMM). Parallelity of half cell cavity achieved within 5 micrometer. Bigger equator diameter of 82.66 mm is achieved within 10 micrometer. Concentricity of cavity achieved within 10 micrometer. RF frequency measured in VNA of complete assembly (17-cell assembly, 8 accelerating, 8 coupling and one power feed) with power feed is 2.85615 GHz in ambient and coupling co-efficient measured 2.44.



Fig.20: Power feed test set up assembly in workshop.

Power feed (PF) test set up assembly (fig-20) to test different parameters of power feed cavities is fabricated. Cavities are brazed and its RF measurement is done.

ECR ion source for LEHIPA:

A three electrode ECR proton source (fig-21) has been developed for LEHIPA from local vendor [1] and 42 mA of hydrogen beam current was extracted at 40 keV. A low energy beam transport line has been fabricated also from Indian vendor for measuring beam profile, beam emittance and proton fraction.



Fig: 21: ECR Ion source under leak testing

Acknowledgment

Authors are grateful to R. K. Rajawat, Dr. L. M. Gantayet, Dr. K. C. Mittal, D. P. Chakravarthy, Dr. A. K. ray, Dr. Archana Sharma, Dr. A V Bapat, Shri E Kandawsami and Shri M N Jha, D. K. Sharma, Raheim N. Rajan, S. K. Srivastava, S. P. Dewagan, Vivek Yadav, A. R. Tillu, R. B. Chavan, Mukesh Kumar, Rajnish Tiwari, S. R. Barje, N. K. Lawangare, BARC for their guidance and support.

References

1. "Machining and brazing of accelerating RF cavity", S R Ghodke, R. Barnwal, Mahendra Kumar; S. Nayak, D. Bhattacharjee; R. Tiwari, D. Jayaprakash, R L Mishra, K C Mittal, B K Dutta, L M Gantayet, Published in IEEE Conference Series, , pages 557 - 560, Sept. 28 2014-Oct. 3 2014, Mumbai, India, [2014]
2. "Fabrication of compact electron gun for 6 MeV X-ray source", S R Ghodke, R. Barnwal, Mahendra Kumar; S. Nayak, D. Bhattacharjee; R. Tiwari, D. Jayaprakash, R L Mishra, K C Mittal, B K Dutta, L M Gantayet, Published in: IEEE Conference Series, , pages 101 - 104, Sept. 28 2014-Oct. 3 2014, Mumbai, India, [2014]
3. "Design and experiments of RF transverse focusing in S-Band, 1 MeV standing wave linac", Authors: J. Mondal, , Shiv Chandan, S. Parashar, D. Bhattacharjee, A.R. Tillu, R. Tiwari, D. Jayaprakash, V. Yadav, S. Banerjee, N. Choudhury, S.R. Ghodke, K.P. Dixit, V.T. Nimje, published in Nuclear Instruments and Methods in Physics Research Section-A, Accelerators Spectrometers Detectors and Associated Equipment. Volume 795, 21 September 2015, Pages 343–350. [2014].
4. "Cooling of high pressure insulating gas for 3 MeV DC accelerator: an alternate approach at EBC Kharghar", S R Ghodke, Rajesh Barnwal, Mahender Kumar, Susanta Nayak, Vijay Sharma, S. K. Srivastava, Satyanarayan Acharya, K. P. Dixit, Israel Bakht Singh, D. Jayaprakash, Rehim Rajan, D. K. Sharma, S. Dewangan, K. C. Mittal, L. M. Gantayet, International Linear Accelerator Conference, (LINAC14), CERN, Geneva, Switzerland., [2014].
5. "Fabrication of Buncher Cavity with Water Jacket", S R Ghodke, Jayanta Mondal, Sonali Parashar, Rajesh Barnwal, K. C. Mittal and L. M. Gantayet, InPAC-2013-ID-038, 19-22 Nov. 2013, held at VECC, Kolkata. [2013].
6. "Mechanical Design and Fabrication of Power Feed Cavity Test Setup", S. R. Ghodke, A. S. Dhavle, Vijay Sharma, Shreya Sarkar, V. T. Nimje, K. C. Mittal and L. M. Gantayet, Indian Particle Accelerator Conference, InPAC-2013-ID-134, 19-22 Nov. 2013, held at VECC, Kolkata. [2013].
7. "Testing and Operation of SF6 Gas Handling System for 3 MeV, 30 kW Electron Beam Accelerator at EBC, Kharghar, Navi Mumbai", S R Ghodke, D. Jayaprakash, Rajesh Barnwal, Mahendra Kumar, Susanta Nayak, KC Mittal and L M Gantayet, International Conference and Piping, OPE 2013, ID: C-011, Kalpakkam, INDIA. [2013].
8. "Commissioning and Beam Trials of 6 MeV RF Electron Linac For Cargo Scanning", Shiv Chandan, N. Chaudhary, S.R. Ghodke, D. Bhattacharjee, V. Sharma, J. Mondal, R.B. Chavan, V.Yadav, A.R.Tillu, V.T. Nimje, S. Acharya, K.P. Dixit, K.C. Mittal and L.M. Gantayet, InPAC-2013-ID-019, 19-22 Nov. 2013, held at VECC, Kolkata. [2013].
9. "Design, Fabrication and VNA Testing of an Auto-Focusing Buncher Section for 40 keV, 500 mA DC Electron Beam Injection", J. Mondal, S. Parashar, S. R. Ghodke, K. C. Mittal and L. M. Gantayet, InPAC-2013-ID-081, 19-22 Nov. 2013, held at VECC, Kolkata. [2013].
10. "Design and Development of Compact Electron Gun And its Performance with Compact Linac Operation", D. Bhattacharjee, R. Tiwari, D. Jayaprakash, R. L. Mishra, Shiv Chandan, A. R. Tillu, V. Yadav, S. R. Ghodke, K. C. Mittal and L. M. Gantayet, InPAC-2013-ID-266, 19-22 Nov. 2013, held at VECC, Kolkata. [2013].
11. "Design and development of collimator for 9 MeV BARC-ECIL Linac", Authors: S.R. Ghodke, et. all, Published in Proc. Symp. on Indian Particle Accelerator Conference (InPAC-2011), Delhi, India., during February 15-18, [2011].
12. "Five electrode ECR proton source for LEHIPA", Authors: P. Roychowdhury, S. R. Ghodke, D. P. Chakravarthy, Abhay Kumar, J. J. Roy, and S. Guha, Published in Proc. Symp. on Indian Particle Accelerator Conference (InPAC-2011), Delhi, India., during February 15-18, [2011].
13. D Bhattacharjee, R Tiwari, et al, "Development of Electron Guns for Linacs and DC Accelerator "J of. Phys, Vol 390, 390 012071 (2012).
14. Shiv Chandan, N. Chaudhary, S.R. Ghodke, et al, "Commissioning and Beam Trials of 6 MeV RF Electron Linac For Cargo Scanning", InPAC-2013, Kolkata.

15. Ghodke S. R, et. al. "Tank Design for 3 MeV, 30 kW Industrial Electron Accelerator", InPAC 2003, p-249.
16. R.C.Sethi, V.T.Nimje, M.Sengupta, A.J.Dabeer, K.P.Dixit and P.H.Ron, "Design and Development of 10 MeV RF Electron Linac for Applied research and Industrial Applications", Proc.APAC98
17. D.Jayaprakash, et al, "Renewable Vacuum System of the compact linac", this conference
18. P. Roychowdhury et al, "High Intensity ECR Proton Source Development for LEHIPA", InPAC'09, RRCAT, Feb. 10-13 (2009).
19. V.T.Nimje et. al., "Design and development of 30 MeV, 3 kW RF electron linac" APAC 2007, RRCAT, Indore, India.

Improvements to Gang type Spent Fuel Chopper at TRP, Tarapur

Abhishant, A.K. Jha, K. Agarwal

NRPSD, NRB, Mumbai

Abhishant is the recipient of the DAE Scientific & Technical Excellence Award for the year 2014

Abstract

Spent Fuel Chopper (SFC) is the most critical equipment for a reprocessing plant. SFC is one of the equipment in operating reprocessing plants which does not have a standby. It's down time directly affects the productivity of the plant. The earlier SFC design at PREFRE-1, Tarapur and KARP, Kalpakkam was based on progressive cutting whereas the design of SFC at TRP, Tarapur is based on 'Gang Chopping Concept', which cuts one PHWR spent fuel bundle into multiple pieces in one stroke. During the initial phase of operation, few teething problems related to design emerged which resulted shortfall in the name plate plant capacity. This paper is based on problem case studies and troubleshooting backed up by solution implementation after mock test trials with minimum affecting the plant operations.

Background:

Spent fuel chopping is a first stage activity for reprocessing of nuclear power reactor's spent fuel as it enables the fuel material to interact with the reagents.

The chopping of spent fuel is done by a shearing machine called "Spent Fuel Chopper". The shearing machines installed at PREFRE-1, Tarapur & KARP, Kalpakkam were based on progressive cutting, where fuel bundle was cut in sequential steps of pushing, gripping and shearing.

This process as well as maintenance of shear machine was time consuming & hence a new chopping system based on 'Gang Chopping Concept' was developed & installed at TRP, Tarapur where a fuel bundle is chopped in a single stroke, thus reduces time of chopping considerably.

This machine avoids other aid like fuel gripping etc. Additionally this shearing machine has remotely replaceable modules which reduces the downtime & thereby increase the plant throughput. During initial phase of operation, many technical challenges arose which were overcome in a time bound manner to surpass the plant annual targets year by year.

The problem statements:

Following problems were encountered during the operation of machine in the first few years:

- Interferences of bundle with Component Transfer Tube (CTT).
- Erratic/stuck CTT movements
- Abortive bundle transfers by CTA
- Premature failure of cutting tools
- Time & labour intensive cutting tools replacement activities.
- High man-rem expenditure during shear module's maintenance.
- Pusher link stuck up at home position.

The solution statements:

Each of above problems was analyzed in detail and technically feasible solutions were implemented by modifying the existing design of corresponding components. These design modifications were mock tested up to the extent possible at the existing Component Testing Facility (CTF), at Tarapur before implementing the same in radioactive environment. The major components which needed design modifications were (1) Component Transfer Assembly, (2) Shear Module Assembly and (3) Pusher Link Assembly.

1. Component Transfer Assembly:

The Component Transfer Assembly (CTA) has a pneumatically actuated tube, which reciprocates between moving and fixed blades to receive one fuel bundle at a time from fuel feed magazine. The CTA is locked with the body of SFC by 45° rotation.

The frequent problems of fuel bundle interfering/getting stuck up during pushing and jamming of CTT was affecting the machine availability. Sometimes bundle failed to move along with CTT retraction stroke resulted in obstruction for successive bundle pushing in to the shear zone, which also affected the productivity. Apart from above, a sticky situation resulted when CTT fails to retract due to stuck up after receiving bundle from fuel feed magazine henceforth:

- CTA could not be unlocked from SFC as it was required to be rotated.
- Shear module could not be removed as CTT was extended in space between the blades.
- Fuel bundle could not be retrieved from shear area through CTA port.

On analysis, it was observed that original CTT (Fig. 1(a)) was circular in shape with a slot for bundle stopper. Internal diameter of CTT was less than that of opening port of fuel feed channel but CTT ID bottom level was equal or lower than that of Fuel Feed Magazine (FFM) level. It was also revealed that CTT was over constrained by various closed tolerance guiding elements. Further it was established that transfer of bundle from FFM to CTT was not positive and only dependent upon the relative frictional forces exerted on bundle by CTT and FFM. (Fig. 1(c))

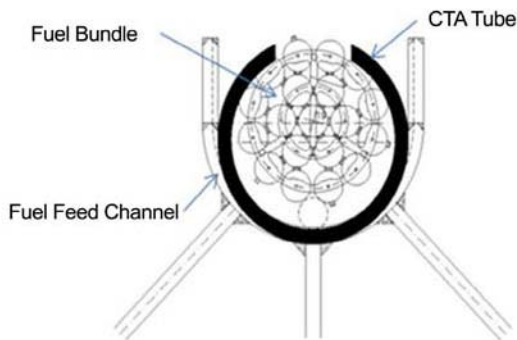


Fig. 1(a): Original Component Transfer Assembly

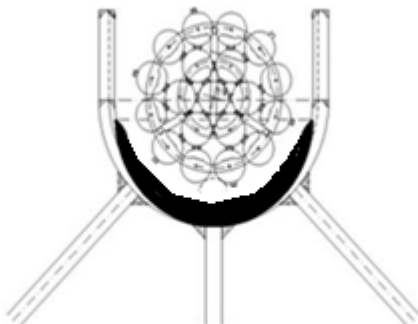


Fig. 1(b): Modified Component Transfer Assembly

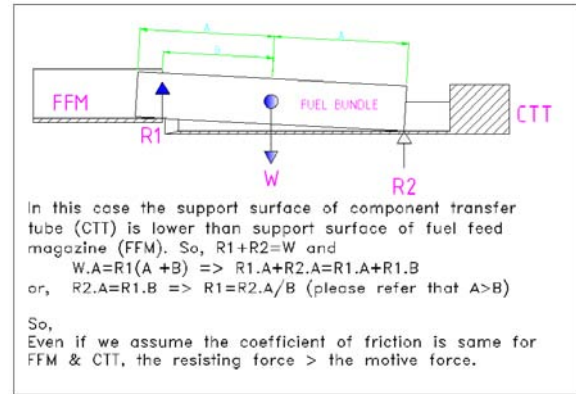


Fig.1(c): Original bundle transfer from FFM to CTT

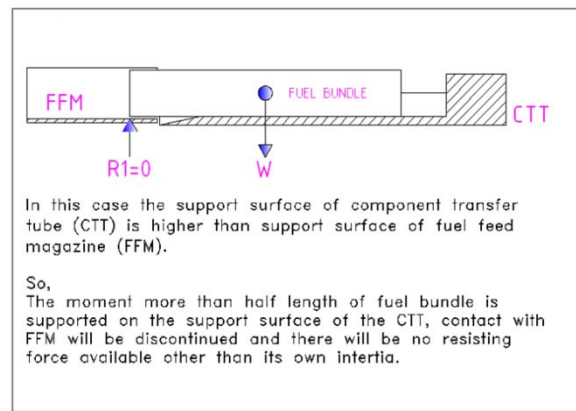


Fig.1(d): Modified bundle transfer from FFM to CTT

To overcome these problems, the design of CTT was modified (Fig. 1(b)). A semi-circular tube with increased and eccentric ID was introduced. The modified CTA design addressed the problem of over constrained by providing a bit liberal fits in the components subjected to relative motions without affecting the functional requirement.

The level of CTT ID was elevated by one mm w.r.to FFM ID level to ensure positive pushing by ensuring no physical contact between bundle and FFM as soon as bundle center of gravity falls in CTT. (Fig. 1(d))

In order to ensure the assembly of CTA with SFC within the prescribed tolerances inside the radioactive cell, a full scale mock set up was made in Component Testing Facility (CTF) & several iterations were tried to suit the cell environment. These modification on CTA has helped in reducing down-time of spent fuel chopper drastically. The semi circular cross section of CTT has also helped to overcome the sticky situation as CTA can rotate, unlock and remove even after receiving the spent fuel bundle from FFM.

With the introduction of new CTT, the feasibility of chopping of even slightly flared irradiated fuel bundles with one or two pins dismantled is also possible.

2. Shear Module Assembly:

Shear Module Assembly (SMA) accommodates the stationary and moving cutting tools. It is located in shear cavity of SFC with the help of four wedges. The movement of moving tools is by virtue of actuation of a hydraulic ram.

Frequent premature tool failures seriously hamper the SFC availability and thus resulted in a suppressed plant throughput. Replacement of damaged tool assembly with a fresh one by dismantling and assembling of SMA resulted in a highly time and man-rem consuming operation.

A comprehensive study was initiated to find out the root cause of failures. Several brainstorming sessions were held with experts from the field of design, analysis, material, maintenance and manufacturing. Strain gauging experiments were conducted for tools to simulate the actual cutting conditions followed by finite element analysis. Even a destructive testing was performed to validate the design parameters.

It was concluded that the cut pieces were accumulating in to the inter blade spaces after the prolonged cutting operations. This accumulation results in the induction of high peak stresses at critical locations of cutting blade much beyond the threshold limits of fracture (Fig. 2(a) and Fig. 2(b)). Need of a modified SMA design was also emerged which can enable remote, quick and easy maintenance and tool replacement.

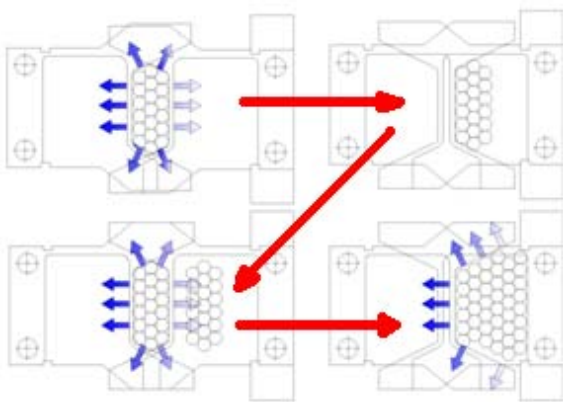


Fig.2(a): Anatomy of tool failure due to accumulation

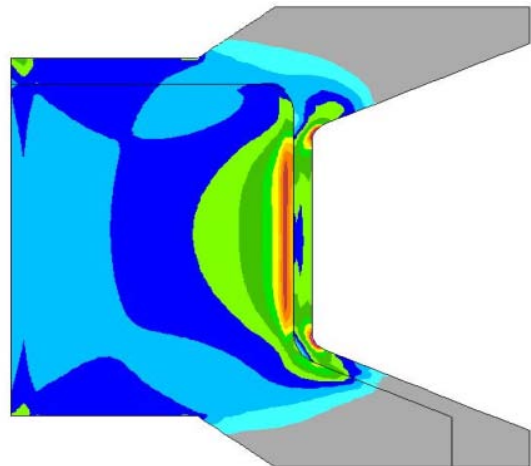


Fig.2(b): Stress distribution in tool during bundle cutting

To mitigate these effects several measures were adopted:

- Upgraded the tool material from AISI D2 to AISI M2.
- Addressing of tool profile w.r.t. stress concentration point of view.
- Providing more clearances to cut pieces for falling under gravity.
- Incorporated features in SMA by which dismantling and assembling is possible by a distance with an ease and within a reasonable time span. (Appendix-A)
- Included administrative checks for monitoring and cleaning of SMA, specially the inter blade spaces.

3. Pusher Link Assembly:

Pusher link assembly, angularly hinged to a horizontally guided rigid chain, allows spent fuel bundles to push through Transfer Port Assembly (TPA) to Fuel Feed Channel (FFC) by retracting itself up to its home position. Subsequently it moves down from its home position to push the bundle's column against bundle stopper for creating further pushing reference. The frontal part of pusher link assembly is a pusher pad which has rotational degree of freedom.

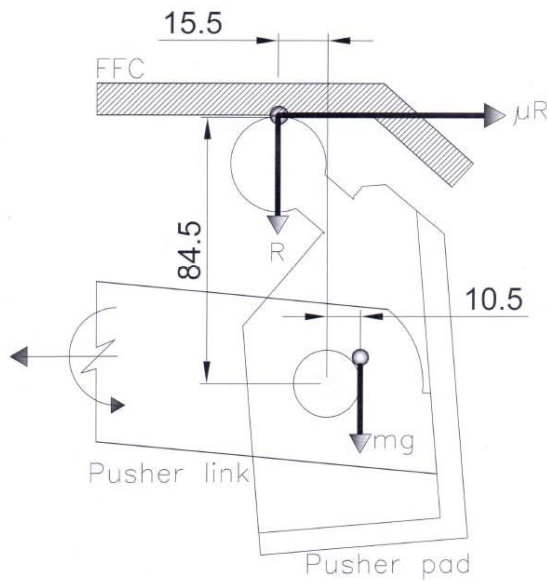
When pusher link approaches to its home position, a pair of guide roller attached to it, ride on a ramp and rotate the pusher link. At the same time, pusher pad also tilts after tilting rod slides on a horizontal rail of FFC.

Above a threshold sliding friction between pusher pad and horizontal rail, the pusher link assembly stuck at its home position with the combined forces at ramp and horizontal guide of chain rollers. The sliding friction is a

function of surface conditions of tilting rod & horizontal rail of FFC and magnitude of reaction force.

The problem was studied analytically and established mathematically that control over frictional forces could resolve the issue. (Fig. 3(a))

As a remedy, a rolling element, track roller, was introduced in tilting rod of pusher pad to interact with horizontal rail of FFC during lifting & tilting. The modification was resulted in trouble free operations of pusher link assembly since implementation. (Fig.3(b) & Fig.3(c))



Note: All dimensions are in mm.

Fig.3(a): Force and reaction diagram of pusher pad

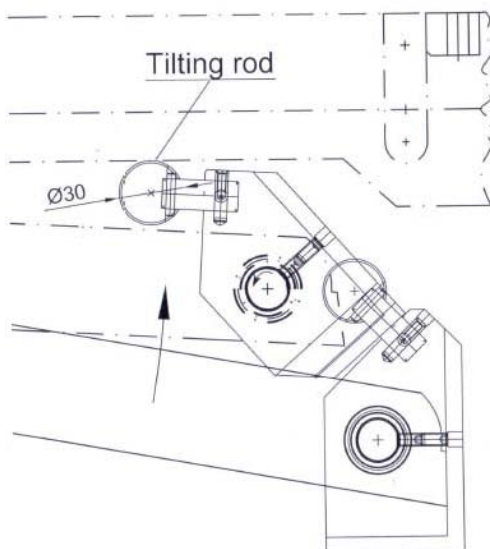


Fig.3(b): Original arrangement for pusher pad tilting

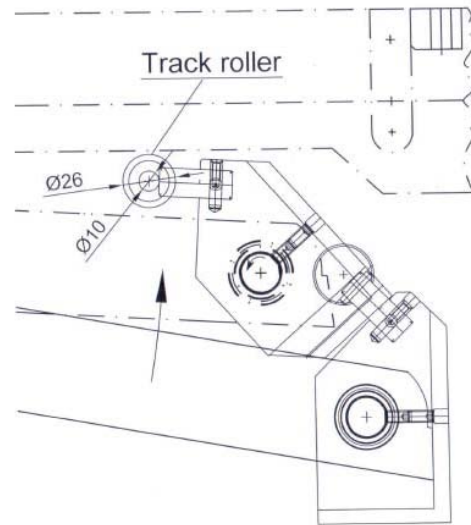


Fig.3(c): Modified arrangement for pusher pad tilting

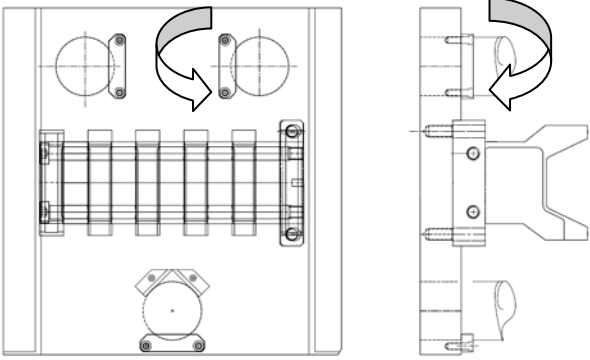
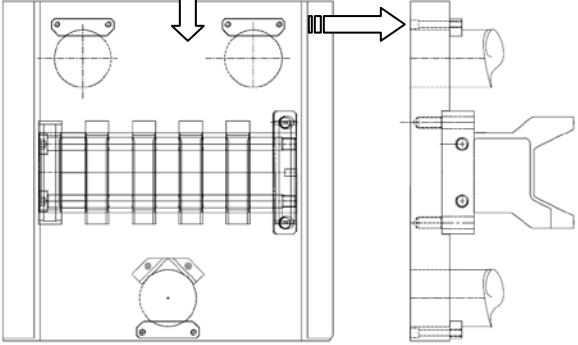
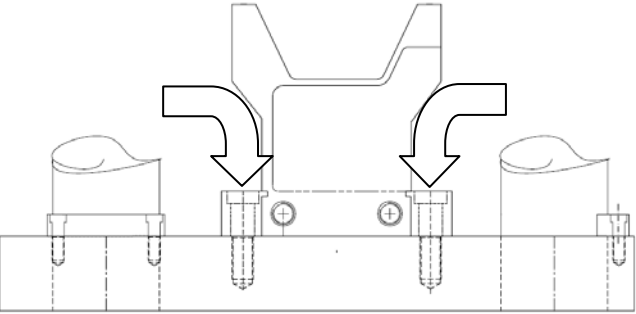
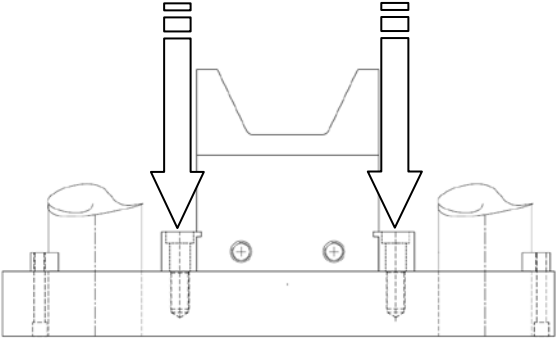
Conclusions:

Design modifications in CTA, SMA and pusher link assembly of SFC have resulted in an increased throughput of the plant by virtue of improved availability of the shearing machine. The modified CTA design has virtually eliminated the breakdown of SFC by reasons attributed to CTA. Similarly measures for SMA also results in an enhanced tool life and a maintenance friendly experience whenever needed, if any. In the last few years, the performance of the plant has comfortably surpassed the targets mainly due to improved performance and availability of the SFC.

Acknowledgement:

The authors gratefully acknowledge the contribution of Shri S. Pradhan, Chief Superintendent, TNRP, Tarapur, Shri K. Dubey, Plant Superintendent, TRP, Tarapur and Shri F. T. Qureshi, Maintenance Superintendent, TRP, Tarapur for encouraging and motivating during conceptualization and successful implementation of these design modifications.

Comparative statements between original and modified shear module design features.

| Original design features | Modified design features |
|---|--|
| <p>In event of cutting tool failure, post retainers of fixed tool holder plate have to remove by accessing from inside the shear module using Allen keys. Maintenance crew has to work in proximity of shear module & for long time period.</p>  | <p>Orientation of post retainers has changed in such a way that it can be handled from outside of shear module. Fixing of the same has modified in such a manner that it can be done by using an extended tool from a distance and in a short span of time.</p>  |
| <p>After removing of fixed tool holder plate from guide posts, cutting tools has to be removed from fixed or moving tool holder plate depending upon which side of cutting tool has failed. Shear module can resume its operation only after replacement of failed cutting tool by new cutting tool to its respective tool holder plate.</p> | <p>Fixed or moving tool holder plate along with tools can be replaced with a spare depending upon which side of cutting tool has failed. The shear module can resume its operation and in parallel replacement of failed tool can be initiated.</p> |
| <p>In case of cutting tool failure in any tool holder plate, the clamp screws have to manipulate with the help of small Allen keys in the proximity of tool holder plate due to limited space available with original profile of cutting tools.</p>  | <p>With the modified profile of cutting tools, the manipulation of clamp screws can be done by an extended tool from a distance and in a short span of time.</p>  |

Augmentation of Blood Transfusion Services through Blood Component Therapy

Susan Cherian

Medical Division

Susan Cherian is th recipient of the DAE Scientific and Technical Excellence Award for the year 2014

Blood transfusion services are a vital part of modern health care system without which efficient medical care is impossible. BARC Hospital Blood bank had obtained license to prepare and store Whole Human blood IP in 1996. However to keep abreast with advances in transfusion medicine, component therapy was needed. This year BARC Hospital Blood bank obtained the license, to prepare and store all Blood Components namely: i) Concentrated Human Red blood Corpuscles IP ii) Fresh Frozen Plasma B.P iii) Platelet Concentrate IP iv) Cryoprecipitated Antihemophilic Factor IP. v) Cryo poor plasma (Factor deficient plasma) USP and vi) Single donor plasma USP. Presently all these components are prepared, stored and issued to patients as per the clinical requirement.

Humankind probably always has been interested in the blood because it is likely that even primitive peoples realized that loss of blood, if sufficiently great, was associated with death. The first transfusion of blood in humans occurred in 1667. Progress was slow thereafter because of the complexities of transfusion. The understanding of genetic differences and blood group between individuals, pioneered by Landsteiner in 1901 and technical progress shortly after World War I, permitted the rapid expansion of blood banking. This resulted in the use of blood transfusion as a therapeutic modality for maintenance of blood volume. The development of anticoagulants, blood preservatives, and sterile techniques allowed the collection and preservation of donor blood

for later use. More recently, component therapy has broadened the application of transfusion therapy from blood volume support to the specific replacement of most blood cells and many plasma proteins. This article outlines the rationale, requirements and procedures for blood component facility.

Rationale for Blood Component Therapy

Blood is a complex mixture of plasma (the liquid Component) in which red blood cells, white blood cells and platelets are suspended. Plasma consists mostly of water that contains dissolved salts (electrolytes), numerous metabolic substances and proteins. Proteins include albumin, immunoglobulins and clotting factors. Each of these components of blood has a specific function; also various diseases cause deficiency of different components.

A blood donor donates the product known as whole blood, from which components are prepared. The rationale to separate various components from whole blood is for the following reasons:

1. Separation of blood into components allows optimal survival of each constituents. For example after 24 hours storage of whole blood at 2-6°C, it has few viable platelets and levels of labile Factors V and VIII decrease, while after separation platelets can be stored for 5 days at 22°C and Factors V and VIII can be stored at FFP for 1 year at 30°C or below.

2. Component preparation allows transfusing only specific blood component that the patient requires. For example a patient suffering from complications of Dengue Hemorrhagic fever requires only platelet transfusion.
3. Transfusion of only the specific constituent of the blood needed avoids the use of unnecessary component, which could be contraindicated in a patient. For example, because of the risk of hypervolemia, an elderly anemic patient in congestive heart failure may not easily tolerate the transfusion of two units of whole blood, while the same patient can be transfused two units of red blood cells easily.
4. By using blood components, several patients can be treated with the blood from the donor, giving optimal use of every unit of donated blood.
5. Use of blood components, supplements blood supply – adds to blood inventory.

Statutory requirements of Blood Component Separation Facility

Blood and blood components are biological products and considered as Drugs under Section 2(b) of Drugs and Cosmetic Act. Hence Blood bank compliance with standards prescribed in the Drugs and Cosmetic Act is a mandatory requirement of the Drug Controller General of India (DCG-I) and FDA. All blood bank operations are regulated under this Act and a licence is granted/renewed for operating the blood bank by the State Licensing and Central Licence Approving Authorities after inspection. The requirements include conditions set out in Schedule F, Part XIIB and Part XIIC of the Act. These are requirements of accommodation, personnel, maintenance of premises, equipment, supplies/reagents, standard operating procedures (SOPs), Good Manufacturing Practices (GMP), Good Laboratory Practices (GLP), Quality Control

and traceable documentation of every step. This is to ensure good manufacturing in blood bank in order to protect the health of both blood donors and recipients of blood and its products.

General Principles and steps of Component Preparation

Different blood components have different relative density, sediment rate and size they can be separated when centrifugal force is applied.

In increasing order, the specific gravity of blood components is plasma, platelets, leucocytes (Buffy Coat-BC) and packed red blood cells (PRBCs).

Blood component preparation to separate blood products from one unit whole blood is done by specialized equipment called as refrigerated centrifuge. Preparing only PRBC and fresh frozen plasma (FFP) is by single-step heavy spin centrifugation, however preparing platelet concentrate (PCs), PRBC concentrates and FFP is by two step centrifugation. The two main procedure of preparing PC are either by platelet-rich plasma (PRP) method or BC method.

The Whole blood is collected as 350 ml or 450 ml in double/triple/quadruple or penta bags with anti-coagulant CPDA-1 or additive solution (SAGM). After blood collection components should be separated within 5-8 hours. Component room should be a separate sanitized room. All precautions to avoid red cell contamination have to be taken such as tapping the segment ends, proper balancing of opposite bags, following standard programs and protocols described in the manual of refrigerated centrifuge manufacturer. The programme is run with mainly two spins-heavy (e.g. 5000 G for 10-15 min) and light spin (e.g. 1500 G for 5-7 min). The heavy and light spin configuration varies with manufacturer and model. Here *G* is relative centrifugal force calculated using revolutions per minute and rotor length. Whole blood is centrifuged to

sediment the red blood cells (RBCs). Most of the supernatant “platelet-rich plasma” is pushed off through integrally attached tubing into a sterile satellite bag. The bag containing platelet-rich plasma may be centrifuged at a higher rate to sediment the platelets. All but 40 to 70 ml of plasma is then removed into a third satellite bag. The platelet pellet is resuspended in the residual 40 to 70 ml of plasma, called a platelet concentrate. The plasma is frozen at –30 °C or lower. If it is frozen within 8 hours of collection, it is called fresh frozen plasma (FFP). FFP may be further processed into Cryoprecipitated AntiHemophilic Factor (AHF) (“cryo”) by subsequently thawing the FFP at 1 to 6°C in a refrigerated water bath, removing the supernatant, and refreezing the cold, insoluble cryoprecipitate within 1 hour of preparation. The supernatant from the

cryoprecipitate preparation, depleted in factor VIII and fibrinogen, may be labeled as Cryo poor plasma.

Functional efficiency of each component is dependent on appropriate processing and proper storage hence these are tightly regulated.

Storage of Blood Components Prior to Transfusion

The “Blood Cold Chain “is the system for storage and transportation of Blood and Blood Components so that they are kept at the correct temperature at all times from collection from the donor to administration to the patient. Different components need different storage conditions and temperature requirements for therapeutic efficacy as shown in Table 1.

Table 1: Storage requirements and shelf life of Blood Components

| Sr No | Component | Storage Temperature | Shelf Life |
|--------------|--|--|--|
| 1. | Concentrated Human Red blood Corpuscles IP | 4 ± 2 ⁰ C | In CPDA-1 for 35 days In SAGM for 42 days |
| 2. | Fresh Frozen Plasma B.P | • 30 ⁰ C | 12 months |
| 3. | Platelet Concentrate IP | 20-24 ⁰ C with continuous gentle agitation in a Platelet Agitator | 5 days |
| 4. | Cryoprecipitated Antihemophilic Factor IP | • 30 ⁰ C | 12 months |
| 5. | Cryo poor plasma (Factor deficient plasma) USP | • 30 ⁰ C | 12 months |
| 6. | Single donor plasma USP | • 18 ⁰ C | 12 months |

Issuing Blood and Blood Components

In order to avoid outdating, First in First out (FIFO) policy is implemented in blood bank. The blood components are issued only as per written request for the same in the medical file of the patient by the treating medical officer. The following are checked before issue:

1. Ensure compatibility testing has been carried out.
2. Ensure that the compatible units are tested for Transfusion Transmitted Diseases (TTD) and found suitable for use.
3. Remove the correct unit from the blood bank refrigerator.
4. Keep it in the thermal box for transport.
5. Make entries in the issue register.
6. Instruct the individual to take the unit straight to the Operation theatre/Ward for transfusion.

Summary

Haemovigilance (making blood transfusion a safe practice) is achieved by ensuring quality assurance at every stage, well-trained technical personnel, proper collection and proper storage, use of quality products, properly calibrated equipment, quality reagents and

proper documentation. Safe and effective blood transfusion requires the combined efforts of blood transfusion services and clinicians, to ensure that the right patient receives the right blood component for the right reason. The role of blood donors is equally important as; the first line in defense in providing a safe blood supply and minimizing the risk of transfusion-transmissible infections, is to collect blood from well-selected, repeat voluntary non-remunerated blood donors. All this will help in achieving the goal to judiciously transfuse blood products that are safe, pure, potent and adequate to meet patient's need.

References:

1. Wintrobe MM. Blood, pure and eloquent: a story of discovery, of people and of ideas. New York: McGraw-Hill, 1980
2. Drugs and Cosmetics Act and rules 1940 (along with Amendments), Section XB and XIIB Ministry of Health and Family Welfare Govt. of India.
3. AABB technical Manual, 17th edition (2010), AABB Press USA.
4. Transfusion Medicine – Technical Manual. 2nd ED. New Delhi, India: Directorate General of Health Services (DGHS), Ministry of Health and Family Welfare, Government of India; 2003.



Centrifugation of whole blood in refrigerated centrifuge.



Separation of packed red cells and plasma in the laminar flow.



Separation of platelets from the plasma in the laminar flow.



Blood component storage room with Platelet agitator and deep freezers (-40&-80 degree Celsius).



Issue of the Concentrated Human Red blood Corpuscles IP.

Suspendable Servo Manipulator for Hot Cell Application

B. Sony, P.V. Sarngadharan, K. Jayarajan, and D.N. Badodkar

Division of Remote Handling & Robotics

Shri B. Sony and P. V. Sarngadharan are the recipients of the DAE Scientific & Technical Excellence Award for the year 2014

Abstract

The paper discusses the design considerations, development, mission trials and deployment of a tele-manipulator arm for removal of radioactive vitrified waste in hotcells. Due to their limited reach, conventional manipulators installed in the cell cannot be used for the mission. The customized arm was designed specific to the site operational requirements such as easy installation in cell with minimal human intervention, short term deployment, flexible reach and survival of equipment for the operation lifecycle. The design parameters are optimized to achieve the above mentioned objectives using commercially available components.

Introduction

In processing plants, high temperature process melters are used to vitrify radioactive waste in glass medium. Molten vitrified mass from melters is poured into stainless steel canisters for storage and their subsequent disposal at geological disposal facilities. At the end of each pouring cycle, some molten waste solidifies as a rigid glass thread. These threads, which are formed at the outlet of the furnace, break during canister handling and fall on a circular turntable below the furnace. The manipulators installed for long term use in the cell are usually employed to pick up the threads. However, a few glass pieces remain inaccessible due to limited reach of the manipulators. Over a period of time, vitrified waste pieces accumulated on the turn table resulting in very high levels of radiation dose inside the cell. Removal of glass threads was essential to allow personnel access to cell for undertaking maintenance and associated activities relating to plant operation.

A customized electromechanical tele-manipulator arm was developed for the activity reduction campaign to handle and dispose the waste. Essential design inputs for the equipment were obtained through initial site survey and interaction with plant personnel. A video survey of the operating area provided the basic design inputs such as: approximate number of threads to be picked (around 50), sizes of glass threads (5-30 cm in length and 5-50 mm in diameter), and their distribution pattern. The glass pieces were brittle and weighed up to few tens of grams.

A rough estimate of radiation dose rates in the operating area was obtained from previously measured site readings, analytical methods of dose rates evaluation and relevant statistical data.

Mechanical Design Considerations

Arm configuration

Due to large number of active vitrified waste pieces accumulated below the melters, there was high radiation dose in the cell. As personnel entry was restricted, it was not possible to install a remote handling gadget in the cell. The cell has a highly unstructured environment with limited free space. Moreover, the waste pieces were distributed over a wide area. These constraints imposed severe limitations on capability of conventional remote handling systems to access all target locations. A novel design concept was therefore formulated to overcome these issues.



Fig 1: Vitrified waste pieces in cell

As the cell is equipped with an overhead crane, it was envisaged to develop a customized slave manipulator arm

which can be suspended from the crane hook during operation. It would be easier to introduce such an arm in the cell and would also provide necessary reach for the operation as the arm could be dynamically transported to the area of interest. Vertical motion of crane load hook would allow coarse vertical movement of the manipulator. Using a combination of arm joint motions, fine adjustment required for correct positioning of the gripper could be achieved. As per site layout constraints and target locations, a five axis articulated arm consisting of one base rotation, two arm swivels, two wrist motions, and a grip motion was found adequate to accomplish the task. The ranges of base and arm motions were limited to $\pm 180^\circ$ and $\pm 90^\circ$ respectively.

A small master arm was developed to remotely control the slave arm. It was placed in control centre as shown in figure 6. The two arms were electrically connected using a long sheathed cable. Slave was operated using video feed provided by the cameras installed in cell and manipulator.

As the slave arm is suspended, any abrupt change in manipulator joint configuration could cause oscillation of the arm. One of the precautionary design aspect incorporated to minimise the oscillations is meticulous balancing of the joints. Shoulder joint and elbow joint were designed with appropriate counter weights such that joints are perfectly balanced. This arrangement has also reduced torque demand at the joints. Vibrations due to small actuations of the arm joints were effectively minimized through inertial damping provided by the non moving base of slave arm. The base fitted with electronic control elements of the equipment and its lead shielding weighed double the remaining arm of the manipulator. The shape and configuration of the gripper was decided based on diameter of the smallest glass piece to be picked up, nature of the surface upon which the objects are lying and the surface finish of the object. Extensive trials were conducted using grippers having parallel and angular jaws (figure 5) to pick a variety of objects. Based on the results obtained



Fig. 2: Suspended Slave arm

from the trials, it was concluded that a parallel jaw gripper with long fingers would be most suitable for the operation.

The gripper must apply minimal gripping force to pick delicate glass objects. Also it should be able to firmly grip electrical cables, which are attached to the arm and may obstruct its free movement during operation. To meet these requirements, a control scheme was designed to provide different gripping forces to the end effector as per requirement.

The electrical/electronic components in the arm require shielding from radiation to reliably operate for the service duration. Based on the available data for cell dose rate and component life under radiation, shielding schemes were implemented for various components like electric motors, encoders, drives and controller.

Torque estimation

The heavy manipulator suspended from the overhead crane behaves like a huge pendulus mass. Any swift rotation of joints may cause oscillations in the suspended robot arm. Therefore fast movement of joints are restricted in the design. The design torque selected for each joint is the maximum torque experienced in fully extended configuration under rated load. The torque required to overcome frictional load is also considered in the computation. Acceleration torques for joint rotations are excluded as the operating speeds are low.

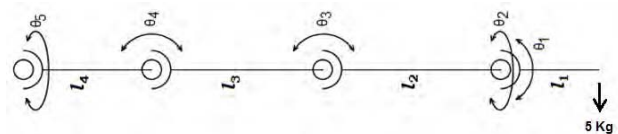


Fig 3. Joints and links of manipulator

Let 'T_i' be the torque required at the *i*th joint of the arm, (*i*=1,2,3,4,5). If 'P' denotes the payload of the arm, then:

$$T_1 = (l_1) \times P + T_{1f}$$

$$T_2 = T_{2f}$$

$$T_3 = (l_1 + l_2) \times P + T_{3f}$$

$$T_4 = (l_1 + l_2 + l_3) \times P + T_{4f}$$

$$T_5 = T_{5f}$$

Where T_{5f}, T_{4f}, T_{3f}, T_{2f}, T_{1f} are friction torque values of the joints. Joint θ_5 experiences the weight of the manipulator in the axial direction. Therefore torque required to overcome friction alone is considered at

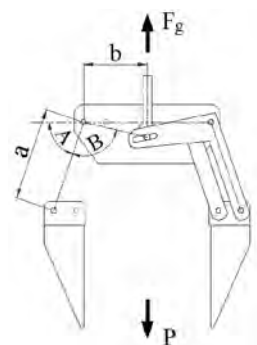


Fig 4. Gripper links and forces

θ_5 . Apart from these joints, there is a gripper at the end of the link l_1 . It is operated by applying an axial pull as shown in figure 4. The axial force F_g required to grip a payload P is given by:

$$F_g = P \text{ a cosec}(A + \theta) / \mu b;$$

where, μ = coefficient of static friction between gripper jaw and work piece.

Electrical Design Considerations

Movement of manipulator over large area was unavoidable in this mission. So a mobile manipulator has been envisaged to cover the workspace. Considering the difficulties of cable management, it was decided to keep provision for complete cordless operation of the system. This influenced the selection of electric supply for slave side as 48 volt DC. However anticipating regulatory restrictions on the usage of storage cells in radioactive area, the choice of cordless mode of operation was discarded. Instead it was decided to use an umbilical cable to feed power and control separately to the slave arm.

Speed and torque required at every joint of the manipulator was computed based on which, Brushless DC motors, drives and multi-axis motion controller were selected from vender's catalogue. Brushed DC motor was an alternate economical choice for the selection; however immediate availability of appropriate size favoured selection of Brushless DC motors.

Knowledge of radiation levels a component might survive is an important input for designing layout and general arrangement for control components. In this respect, an analysis of radiation survival limit of control components has been examined. Most of the commercial silicon based electronics survive radiation levels in the range of 500 - 1000 rads. Electrical motors with passive feedback sensors also survive 30 - 40 Kilo rads.

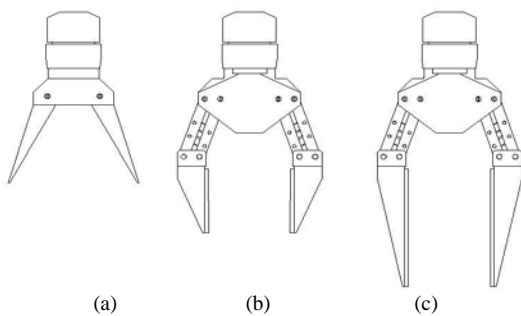


Fig 5. (a) Angular jaw gripper ; (b&c) Parallel jaw grippers

Components on the arm get radiation exposure in relation to their distance from the source. The layout of critical components was decided according to their safe level of

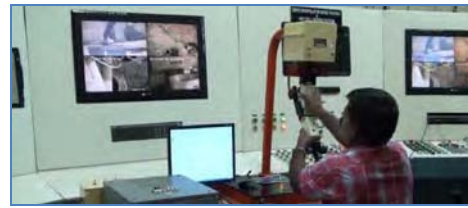


Fig.6: Master arm operated at the control

tolerance. The gripper located closest to the radiation source receives highest exposure. The electrical components such as motors and sensors, which control the gripper operation, were mounted at a distance of one meter from the gripper near the elbow joint. The mounting distance is adequate for electric motors to survive the mission as they have a higher radiation tolerance. A thick metallic shield was fitted to protect the feedback elements, which are more vulnerable to radiation damage, located at the rear end of the motors.

In general, commercial grade control components are vulnerable to radiation damage if total exposure of the component exceeds 400 rads. All such electronic elements were mounted in a shielded zone at the base of the manipulator. This zone was located around two metres away from the radiation source in most of the circumstances. The zone was shielded with thick lead bricks to bring down the radiation level below 400 rads during the mission. As the size of the shielded zone must be minimised, a compact multi-axis sandwiched type drive and controller were chosen for control.

The slave manipulator arm has six motors and each of these motors have power, feedback and brake cables. Considering the difficulty of handling several multi core cables over a long distance, it was decided to install the controller and drive on the slave arm. The choice of multi-axis sandwiched type multiple drives helped in reducing the trouble of cable handling as this scheme demands only



Fig. 7: Image of slave arm in operation

an umbilical cord for power and an Ethernet cable for communication.

The requirement for the system was urgent and lead time for design and development was barely adequate to undertake a detailed analysis. The design philosophy of single mission based equipment, simplistic design approach, and use of standard bought out parts, was adopted to reduce development time.

There are several in-cell cameras installed in the plant which provided video images of slave arm in operation as shown in figure 7. To enhance visual feedback, two more cameras with pan, tilt and zoom facilities have been mounted on the manipulator. Real time views from these cameras were displayed to the operator for close look of the object. Towards the end of the mission one camera, which was installed near the gripper, lost its functionality.

Field Trials and Deployment

Prior to cell deployment, field trials were conducted to ensure the worthiness of the system in the cell. The slave manipulator was suspended from an overhead crane in site as shown in figure 2. The system repeatedly operated for a period exceeding expected mission duration to test the reliability of operation and to train the operators to operate the system. Extensive trials were carried out on picking of inactive glass threads of similar dimensions to evaluate the efficacy of gripping without damaging the fragile glass objects. Picking of small diameter glass threads was tried with angular jaw gripper and parallel jaw gripper and 100 mm wide parallel jaw gripper was found more acceptable for the operation.

Conclusion

Suspendable servo manipulator is a novel design which uses transporter to access a much larger work space in comparison to conventional systems. The system was built in a short duration using commercial grade components. The following key concepts were utilised in the development of the equipment for short term application in highly radioactive area.

- a) Every component has a finite survival time in radiation field. Hence in principle all such devices are useful in radiation fields for limited duration.
- b) Some part of the equipment is less exposed to radiation than the other. Component layout may be designed such that critical and sensitive components have reduced exposure to radiation fields.
- c) Without sacrificing the core functionality of the remote handling equipment, shielded zones can be created which would enhance the life of critical and vulnerable components.
- d) Use of compact and efficient components reduce heat dissipation and hence enable to have compact shielded zones.

Extensive trials were conducted to make the system worthy for deployment. These trials were instrumental in reducing the actual duration of the mission as the operators gained experience.

Acknowledgment

We are grateful to authorities and personnel of WIP, NRG for extending immense support and coordination throughout the programme.

References

1. "Development of Suspendable Servo Manipulator for Activity Reduction in Vitrification Cell - WIP, Trombay", *BARC Newsletter Issue No 336, Jan-Feb 2014*, [2014]
2. "Development of Four Piece Servo Manipulator", R V Sakrikar, U Sarkar, D D Ray, B Sony, D C Biswas, and K Jayarajan, *BARC Newsletter Special Issue, October 2014*, [2014]
3. "Development of sealed three piece master slave manipulator", B Sony, Vivek Mahadev, K Jayarajan & Manjit Singh, *National Conference on factory automation, manufacturing and soft computing*, [2007]

Design and Development of Radiation Detectors for Nuclear Reactors

Mary Alex

Electronics Division

Mary Alex is the recipient of the DAE Scientific & Technical Excellence Award for the year 2014

Abstract

Several ^{10}B lined ionization chambers with and without gamma compensation have been developed with cylindrical and parallel plate electrode geometry. These detectors have been developed after extensive studies on the optimization of the neutron and gamma sensitivities, the voltage /current (V/I) characteristics and the response of the detectors as a function of neutron flux. The reliability and long term performance of these chambers is improved by use of some special techniques which include the use of composite stainless steel aluminum clad plate and use of easily machinable polyether ether ketone (PEEK) insulators. These materials have successfully withstood accelerated tests up to 1.26×10^{19} nvt at Dhruva reactor. Gamma Compensated boron lined ionization Chambers (GCIC) employing the parallel plate electrode geometry with specially designed springs and ceramic spacers have been developed for the first time for LWRs. The use of the innovative design has resulted in mechanically rugged detectors for continuous operation up to 300°C with linearity of better than 10% over flux range of 10^4 nv to 10^{11} nv. These detectors have been successfully integrated with hanger assemblies and qualified for shock, vibration and LOCA conditions. Inconel 600 SPND has been developed as an alternative to the Cobalt SPND for in-core neutron monitoring for reactor safety & control applications. Aquadag coated plastic ionization-chamber for gamma dose measurement has been developed for LWR and the chamber has withstood shock test. The paper delineates a summary of the innovations and special techniques used in the design of chambers, performance and the qualification tests conducted on the various chambers developed for the reactors. It also describes the setting up of calibration facility for the testing of the neutron chambers at KAMINI reactor.

Keywords: Boron, PEEK, SS-Al clad plate, ionization chambers and cables

Introduction

Gas filled radiation detectors viz. ^{10}B lined ionization chambers with and without gamma compensation and Self-Powered Neutron Detectors (SPNDs) are used as ex-core and in-core neutron detectors respectively for the safety and control of reactor instrumentation. These neutron detectors provide continuous and on line information of the neutron flux level which is essential for the safe operation of the reactor. Typically the ^{10}B lined ionization chambers have neutron sensitivity of $10\text{fA}/\text{neutron}/\text{cm}^2/\text{secto}$ $20\text{fA}/\text{neutron}/\text{cm}^2/\text{sec}$ and gamma sensitivity of $1\text{pA}/\text{R}/\text{h}$ to $10\text{pA}/\text{R}/\text{h}$ and are used to measure neutron flux from 10^4 neutron/cm²/secto to 10^{11} neutron/cm²/sec in the presence of gamma radiation levels varying from $100\text{R}/\text{h}$ to $10^6\text{R}/\text{h}$. The SPND's have typical neutron sensitivity of $10^{-21}\text{A}/\text{nv}$ and are used to measure neutron flux from 10^{12} neutron/cm²/sec to 10^{14} neutron/cm²/sec. Gamma radiation dose measurement in nuclear plants and facilities is essential for monitoring health of personnel operating the plants. The aquadag

coated air equivalent gamma dose monitoring plastic chamber has been designed and developed to estimate integrated dose in such areas.

^{10}B Lined Ionization chambers

- **Uncompensated Chambers with stainless steel-Aluminium composite end Plate**

^{10}B lined ionization chambers have been developed using coaxial cylindrical electrodes and outer housing made of high purity aluminum to minimize neutron induced radioactivity. The salient specifications of the chambers are given in Table 1. In the early design of chambers used in Dhruva reactor, the ceramic to metal insulators were soldered to the high purity aluminium end plates. In these chambers it was observed that after a period of few years of operation, the saturation characteristics of the chambers began to deteriorate (Fig. 1). Upon investigation it was found that this deterioration was due to gas leak from the soldered joints of the ceramic to metal feed thru to the aluminium end plate

Table 1 Salient specification of the Uncompensated ^{10}B lined chamber

| | |
|----------------------------|--------------------|
| Overall length: | 540mm |
| Overall dia | 90mm |
| Boron 10 content | 350mg |
| ^{10}B enrichment | 92% |
| Gas fill | Nitrogen at 0.7bar |
| Sensitive volume | 60cc |
| Connectors | HN |

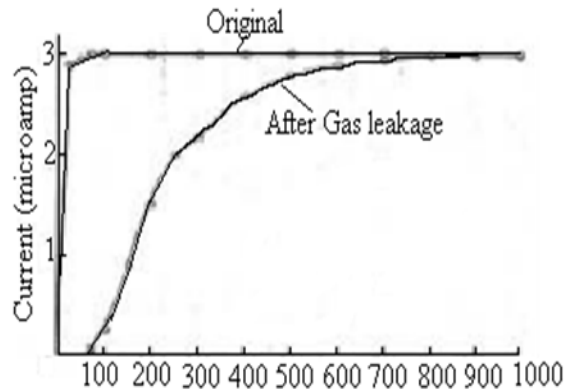


Fig.1: Deterioration in the current-voltage characteristic of the ion chamber due to gas leak

To ensure long operational life and stability in performance of the chamber, a significant design innovation was carried out to develop all-welded ion chambers. The welding of the SS components of the ceramic to metal (C/M) insulators shown in fig.2 to the aluminum body of the chambers was facilitated by employing SS-Al clad material as shown in fig.3. Several ion chambers were developed using this technique and two of the chambers were installed in Dhruva reactor to assess

their long term performance. The performance of the chamber was monitored regularly and the chamber has withstood 14 years of operation at an average flux of 10^9 neutrons/cm²/sec with no deterioration in performance. One gamma compensated ^{10}B lined ionization chamber developed using this technique shown in fig 4 was subjected to accelerated tests for 320 days at 4.57×10^{11} neutrons/cm²/sec at Dhruva reactor with no deterioration in the performance of the chamber¹.



Fig.2 Ceramic to metal feed thru insulator

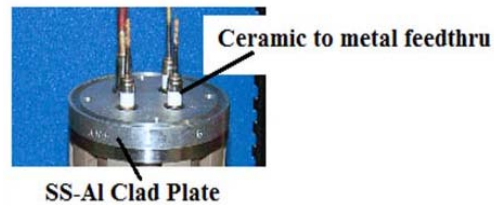


Fig.3 Ceramic to metal feed thru insulator

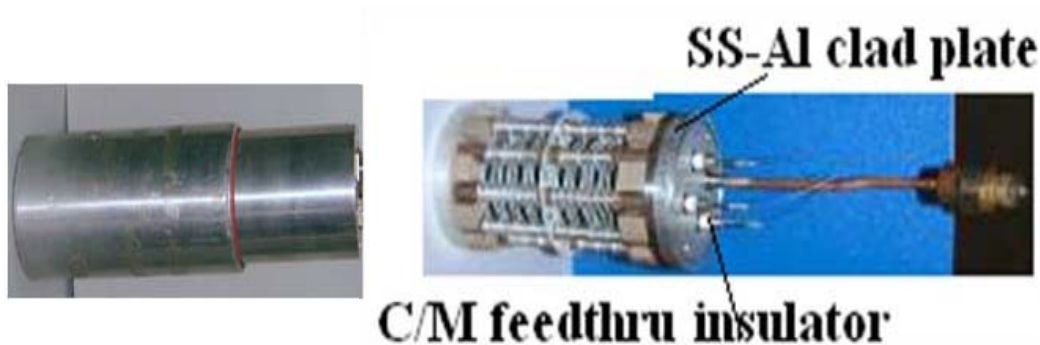


Fig.4: Gamma compensated ^{10}B lined ion chamber with SS-Al clad plate

- **Gamma Compensated chambers with Peek Insulators**

Insulators are an important component in the design and construction of the chamber. To eliminate the extra chamber volume and to improve the gamma compensation characteristics of the detector, a design innovation using a special radiation tolerant, easily machinable Poly ether ether ketone (PEEK) material as insulating spacers was employed as an alternative to ceramic spacer for the first time in the development of radiation detectors. Fig.5 shows some of the PEEK spacers used in the development of gamma compensated ionization chambers. The use of

PEEK spacers at the ends of the electrodes eliminated the extra volumes and enabled the designing of chamber with well-defined sensitive volume thereby improving the performance of the chambers in terms of gamma compensation. Several boron lined ionization chambers with gamma compensation have been developed with PEEK spacers^{2, 3, 4} and one of the chambers as mentioned above has been subjected to accelerated tests. No deterioration in the performance of the chamber was observed and the material withstood the accelerated tests. Another ion chamber with PEEK insulators has successfully withstood temperature tests up to 125°C.

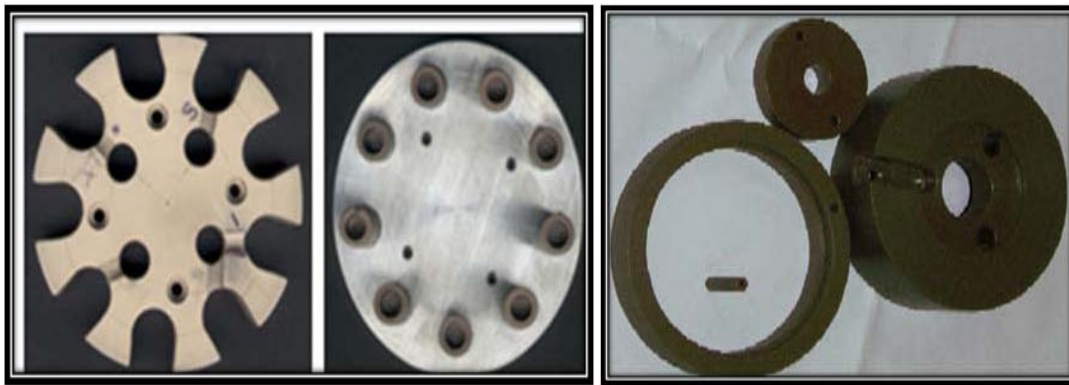


Fig.5: PEEK spacers used in the development of chambers

- **Chambers with Various Electrode Geometry**

Boron-10 lined gamma compensated ionization chambers are rugged devices that need to be designed for continuous use in hostile environment (high neutron flux up to 10^{11} neutrons/cm²/sec, intense gamma fields up to 1MR/h and at temperatures up to 300°C) with minimum maintenance and replacement and in limited space. To meet these requirements, gamma compensated B¹⁰ lined ionization chambers of parallel plate type as shown in fig.6 having 102 plates with a gap of 1.5 mm between the plates have been developed with specially designed springs and ceramic spacers for light water reactor projects. The innovative design has resulted in mechanically rugged detectors having measurement linearity of better than 10% over flux range of 10^4 to 10^{11} nV for continuous operation at 300°C. The detector design evolved for the first time has helped achieve the required neutron sensitivity with gamma compensation factor within 5% in limited diameter of 50mm and saturation voltage less than 200V at 10^{10}

neutrons/cm²/sec. The detectors are integrated with MI cables of 3mm diameter and about 4mtrs long and terminated with ceramic to metal feedthrus. These detectors have been tested in KAMINI reactor for performance in mixed neutron and gamma fields and successfully integrated with hanger assemblies and qualified for shock, vibration and LOCA conditions. Gamma compensated boron lined ion chamber with cylindrical geometry as shown in fig.7 and radiation resistant polyamide cables was also developed, tested in neutron and gamma radiation fields and qualified for LOCA at 140°C and 40psi pressure. The detector has also successfully withstood vibration tests at ECIL. The detectors have been successfully installed and used in the P4 Hot and cold facilities. Table 2 gives the main specifications of the parallel plate type and cylindrical type chamber



Fig. 6: Chambers with parallel plate construction



Fig. 7: Chambers with cylindrical construction

Table 2: Specifications of gamma compensated ^{10}B lined neutron chambers

| Detector | Parallel Plate | Cylindrical |
|---|---|--|
| Electrode spacing | 1.5mm | 2.5mm |
| Sensitive length | mm | 250mm |
| Surface Area | 400cm ² | 945cm ² |
| Boron-10 enrichment and Coating thickness | 94% and 0.75mg/cm ² | 40.5% and 0.75mg/cm ² |
| Boron content | 300mg | 700mg |
| Gas fill | N ₂ at 128cm of Hg | |
| Neutron Sensitivity | 15fA/nv | 5fA/nv |
| Av. Compensation factor | 5% | 3% |
| Comp. Gamma Sensitivity | 0.6pA/R/h | 0.35pA/R/h |
| Overall length | 572 mm | 315mm |
| Overall dia | 50 mm | 85mm |
| Cables | Mineral Insulated (3mmdia and 4mtrs long) | Radiation resistant Kapton (5mmdia and 4mtrs long) |

Facility for Testing of Neutron Detectors at Kamini

A first of its kind in-situ calibration facility for calibration of neutron detectors covering wide range of 10^4 nv to 10^{10} nv flux in the presence of gamma radiation from 100R/h to 10^5 R/hr has been set up at KAMINI reactor as shown in fig.8. It consists of two dry high purity aluminum tubes of 80mm diameter and 109mm diameter

respectively and each of 4mtr long installed at a distance of 33cm and 90 cm from the centre of the core. To prevent radiation streaming due to the installation of the tubes, suitable shields consisting of SS, polyethylene and lead were fabricated and installed. The facility is being used by several users for testing and calibration of all types of gas filled detectors.

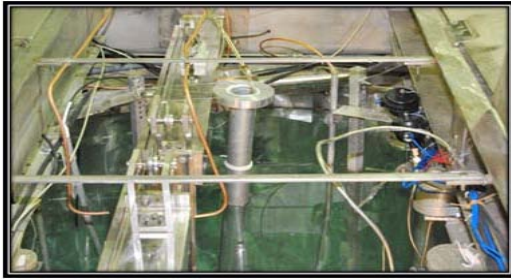


Fig.8 Calibration Facility at KAMINI reactor being used for testing of neutron detectors

Development of an Inconel Spnd for In-Core Neutron Flux Monitoring in Power Reactors.

Cobalt SPNDs are being used in Indian PHWRs for reactor control applications. These detectors have relatively short useful life in a high flux power reactor because of the currents attributable to the buildup of ⁶⁰Co and ⁶¹Co. As an alternative to the cobalt SPNDs, an Inconel SPND has been developed⁵, installed and qualified for long term operations as shown in fig.9. The main specifications of the detector are given in Table 3. The advantages of the

Inconel detector include prompt response, long life, no interfering signals such as ⁶⁰Co and ⁶¹Co, lower activation and low gamma response. The long term performance of the detector was monitored for 5 yrs of continuous operation and the detector performance showed good correlation between power level and detector signal. The development of this detector has been a boon to the nuclear industry due to its improved features and all the cobalt detectors have now been replaced with the Inconel SPNDs in the existing 540MW reactors in the country.

Table 3: Main specification of the Inconel SPND

| | |
|-----------------|---------------------|
| Overall length: | 250mm |
| Overall dia | 3.5mm |
| Emitter | 2mm dia x 21cm long |
| Insulator | Alumina |
| Collector | Inconel 600 tube |
| MI cable | 2mm dia and 10mtrs |
| Connectors | LEMO |



Fig.9: Inconel Self Powered Neutron Detector

Development of Aquadag Coated Plastic Ionisation Chamber for Gamma Dose Measurements

An air filled ion chamber with Perspex housing has been developed for absorbed dose in air measurement⁶. The main specifications of the ion chamber are given in Table 5. The photograph of the chamber is given in Fig.10. The ion chamber has been designed for gamma sensitivity of the order of 100 pA/R/hr. A special technique employed in the development of the chamber has been the use of graphite coating on the inner diameter of the Perspex tube.

The coating is provided to make the electrode conducting. The ion chamber was tested for its performance at the calibrated source facilities at RSSD, BARC for gamma sensitivity, energy response V/I characteristics and linearity of response. The ion chamber assembly integrated with electronics and housed in aluminum housing has successfully qualified the shock test conducted on the K-200 machine in the X and Y directions. The design of the detector has been transferred to M/s ECIL for production.

Table 4: Main specifications of the aquadag coated plastic ion chamber

| | |
|-------------------|----------|
| Overall Dia | 78mm |
| Overall Length | 300mm |
| Housing Material | Perspex |
| Gas | Air |
| Sensitive volume | 1122cc |
| Gamma Sensitivity | 84pA/R/h |



Fig.10: Aquadag coated plastic ionisation chamber

Conclusions

Boron lined ionization chambers with and without gamma compensation has been successfully designed, developed, qualified and installed in the various reactors. The detectors developed for LWRs meet the technical challenges of high sensitivity in limited space, high radiation and high temperature. Several design innovations which include the use of composite SS-Al clad plate and PEEK spacers has resulted in long life and better performance of the detectors. The first of its kind a permanent in-situ calibration Facility in KAMINI reactor for testing of neutron detectors over wide range of 10^4 nv to 10^{10} nv flux is the only facility available in the country, at the moment, and is being used extensively to calibrate the detectors. The Inconel 600 based SPNDs developed has drastically improved the maintenance and on-line recalibration issues in power measurements due to the detector's improved features of long life, lower activation and having no build-up issues. The know-how of the detector design have been transferred to ECIL and are being produced commercially.

Acknowledgements

The author would like to express her special gratitude to Shri Y.S. Mayya, Director E&I Group and Shri Debashis Das, Head, Electronics Division for their constant support and encouragement. My thanks are also due to Shri P V Bhatnagar, Head, RIS for his guidance and valuable suggestions. The author would also like to express her sincere thanks to colleagues from Reactor Instrumentation Section, Electronics Division, Centre for design and Manufacture Division, Radiation Safety Systems Division, Material Science Division, Research Reactor Maintenance Division, and Electronics Corporation of India Ltd., Hyderabad. The author is also thankful to KAMINI

Reactor authorities for their support in setting up the calibration facility and Dhruva reactor authorities for providing the reactor facility for conducting accelerated tests.

References

1. Accelerated tests on gamma compensated boron lined ionisation chamber for reactors safety and control applications, Mary Alex et al, 2nd International Conference on Reliability, Safety & Hazard (ICRESH-2010), 2010.
2. Development of a gamma compensated boron lined ionization chamber for reactor safety and control applications, Mary Alex et al, Nuclear Instruments and Methods in Physics Research-A, Vol. 580, 2007, 1395-1399.3
3. Development of neutron chambers with improved electrode design, Mary Alex and K.R.Prasad Nuclear Instruments and Methods in Physics Research - A, Vol. 527, 2004, 562-566.
4. Development of Gamma Compensated Boron lined Ionization chamber with Intermediate Range Monitor for reactor applications, Mary Alex et al, Proceedings of the DAE BRNS, National Symposium on Nuclear Instrumentation, 2013.
5. Development of an Inconel self-powered neutron detector for in-core reactor monitoring, Mary Alex and M.D.Ghodgaonkar, Nuclear Instruments and Methods in Physics Research-A, Vol. 574, 2007, 127-132.
6. Development of Air Equivalent Gamma Dose Monitor, Mary Alex et al, Proceedings of DAE-BRNS national symposium on nuclear instrumentation, 2010

Development of technologically important/special glasses and glass-ceramics for various strategic applications

Madhumita Goswami
Glass & Advanced Materials Division

Dr. (Smt.) Madhumita Goswami is the recipient of the DAE Scientific & Technical Excellence Award for the year 2014

Abstract

Few selective glass & glass-ceramics having potential applications in the field of sealing, high voltage and high vacuum, energy storage/battery, bio-medical, consumer items, nuclear and optical were developed. Among these, machineable quality magnesium alumino-silicate(MAS) glass-ceramics were developed through glass route, the flow sheet for the preparation of rods, cylinders and discs were demonstrated. The material developed has been successfully used for the fabrication of high voltage (breakdown voltage 220-250kV/cm) and UHV compatible components for cascade plasma gun, furnace insulation and many other applications for different users within DAE. For fabrication of matched type glass-ceramics to metal/alloys seals, lithium zinc silicate were synthesized and characterized for their compatibility with different metals/alloys. Structural studies of the LZS glass and glass-ceramics using ^{31}P , ^{11}B , ^{27}Al , and ^{29}Si solid state NMR helped in accurate quantification of different phases present in the glass and glass-ceramics. Development of chemically durable phosphate glasses for matched type seals for low melting metals /alloys, like Al/Be alloys, and glasses for high temperature sealing application, especially for use as SOFC sealant (seals fabricated with Crofer interconnect material withstood vacuum of 10^{-6} Torr at RT-800°C) were also carried out. Recent development of phosphate glass-ceramics based Li-superionic conductor for Li-Air rechargeable battery showed a high conductivity value of $2-3 \times 10^{-4}$ S/cm at RT. Thin sheets of this materials are being prepared by tape casting for miniaturization of the devices. Development of Ytria-alumino-silicate (YAS) based glass microsphere for radiotherapy application, surface modification of glasses for improved functionality i.e. toughening of glasses by chemical ion exchange process and super-hydrophobic glass using a novel process of spinodal decomposition also carried out.

Introduction

Glass/Glass-ceramics find applications in various technological fields including vacuum, high voltage, electronics, nuclear, space, biomedical, safety gadgets, energy conservation, optical etc. The most interesting aspects of working on glass/glass-ceramics is that even though they are multi-component materials, their properties can be controlled, thus developing tailor made products for use in technical fields. Moreover, glass-ceramics have considerable advantages over other materials such as glasses, ceramics, metals and polymers. Therefore, glass/glass-ceramics are used in almost every discipline of science, technology and engineering now days. We have developed few important glass and glass-ceramics having potential technological applications in

various fields. Among these, magnesium-aluminum-silicate (MAS) belongs to a special class of technologically important advanced ceramics having applications in the areas related to ultra high vacuum, high temperature, high voltage etc. The unique feature of MAS glass-ceramic is its machineability, i.e. the material can be transformed into desired shape and size by machining to precise tolerance and surface finish with conventional carbide tipped tools. Lithium zinc silicate (LZS) glass-ceramic is another technological important glass-ceramics materials which finds incredible applications in the field of sealing technology. The special features of this materials are wide glass forming region and tuneable thermal expansion characteristics. The thermal expansion coefficient of LZS

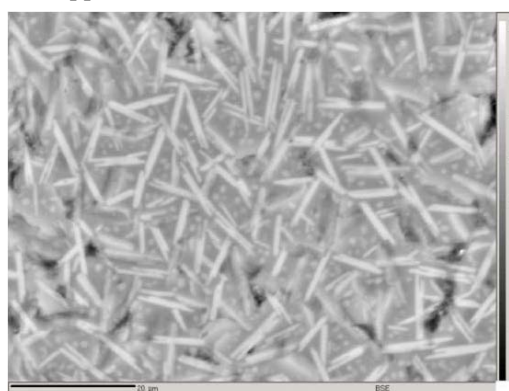
glass-ceramics can be varied in a wide range from 50×10^{-7} to 200×10^{-7} /°C in controlled manner and thus, found suitable for preparation matched type of hermetic seals with a variety of metals/ alloys. In addition, this material also shows superior insulation, higher mechanical strength and good chemical durability. Application of phosphate glasses are limited due to moisture sensitiveness of these glasses. However, phosphate glasses having different additives were found to show better stability under ambient conditions and are extensively used for various applications. Phosphate glasses generally have lower glass transition temperatures and higher thermal expansion coefficients compared to silicate and borate glasses and so are prime materials for glass-metal sealing applications especially with low melting and high expansion coefficient metals like Al, Cu etc. It may be mentioned that Al and Al alloys are important materials for space applications because of lower weight and cost and desired mechanical properties. Alkaline earth silicate glass/glass ceramics are found to be promising candidates for uses as high temperature sealant especially for SOFC application. They shows acceptable long term thermal, mechanical and chemical durability with other electrode materials in oxidizing and reducing atmosphere.

Apart from sealing glass/glass ceramics, phosphate glass-ceramics based on NASICON structure shows potential application as solid state electrolyte in energy storage devices/batteries. They have higher ionic conductivity at RT and thermal and chemical stability compared to liquid and polymer based electrolyte. Uses of glass /glass-ceramics in the field of biomedical as bone/teeth filler, replacement of damaged bone parts and drug delivery are well known. ^{90}Y -a beta emitter in a irradiated $\text{Y}_2\text{O}_3\text{-Al}_2\text{O}_3\text{-SiO}_2$ (YAS) glass microsphere with a half life period of 64hrs and about 934 KeV energy found very useful for localized radiotherapy treatment of hepatic cellular carcinoma(HCC) and synovitis. In addition to improve the properties of glasses modification of surface to enhance hydrophobicity on glass surface and toughening of glass by chemical ion exchange process found useful for use of these materials in many strategic applications..

Machineable (Magnesium Alumino Silicate) MAS glass ceramics:

For the preparation of magnesium alumino silicate(MAS) glass-ceramics with superior machineability, the composition and process conditions were optimized to precipitate requisite amount of the

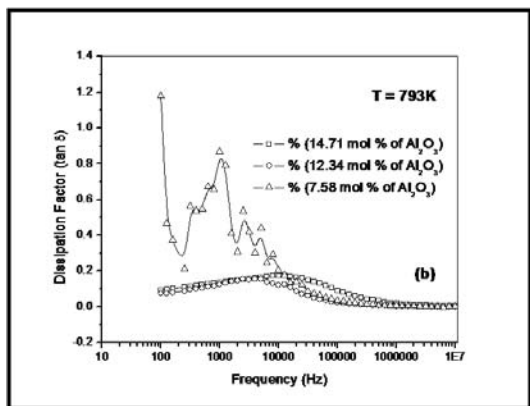
micaceous phase and obtain a cross-linked microstructure that provides a break down strength of 220 – 250 kV/ cm, micro hardness of 2.56 GPa and outgassing rate 7.9×10^{-9} Torr $\text{cm}^{-2} \text{sec}^{-1}$. The flow sheet for the preparation of rods, cylinders and discs of machineable MAS glass-ceramic was developed through a comprehensive optimization of the composition and process conditions. The machineability of the material was elicited by the smooth sectioning of the wafers of 200-500micron thick using a diamond wheel. The dielectric properties of this material studied over a wide frequency range showed low loss at high temperature. Optimization of the composition was achieved through structural information obtained using ^{27}Al and ^{29}Si solid state NMR. MAS glass-ceramic in the form of rods (40mm dia X 120mm L), cylinders (60mm OD, 40mm IDX120mm L), discs (70mm dia X 25mm thick) have been developed. A number of glass/ glass-ceramics developed are widely used for fabricating seals, feed throughs, spacers, lugs and other components for use in different applications within and outside DAE.



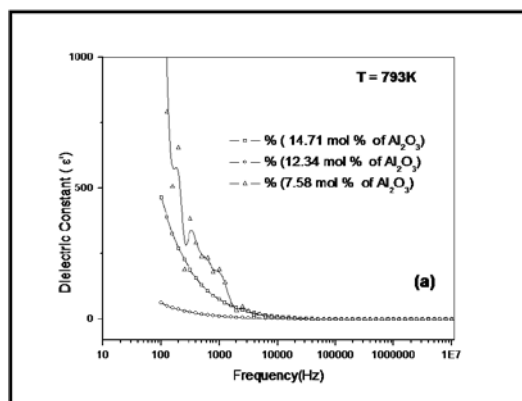
Flake like microstructure of machineable MAS glass-ceramics.



Various components fabricated from machineable MAS glass-ceramics



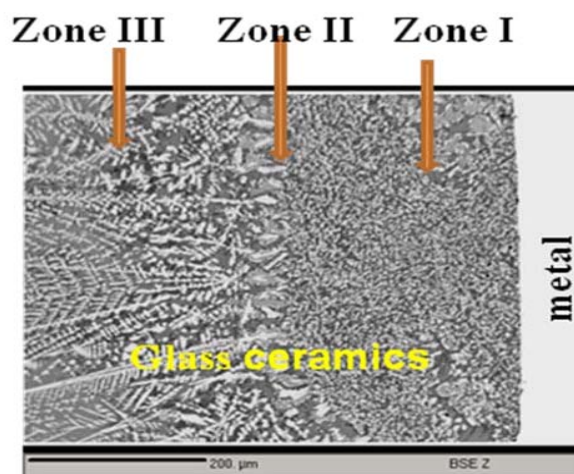
Variation of dielectric constant(ϵ') with frequency for different Al_2O_3 contents in MAS glass-ceramics.



Variation of $\tan \delta$ with frequency for different Al_2O_3 contents in MAS glass-ceramics.



LZS glass-ceramics-to-metal seals



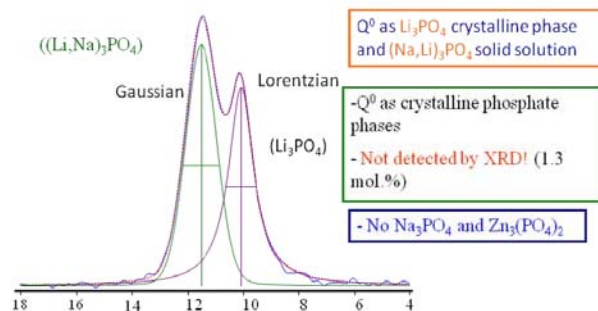
Microstructure at the interface of LZS glass-ceramics-to-metal seal.

Lithium Zinc silicate glass ceramics:

Glass-ceramics of the lithium zinc silicate (LZS) system are a versatile class of materials having application in hermetic sealing with various metals including stainless steels and Ni based super alloys. Development of lithium zinc/aluminum silicate glass-ceramics with tuneable thermal expansion coefficient were carried out for sealing with Cu and SS321. Thermal expansion coefficient of LZS glass-ceramics was tuned by optimizing the glass composition and process parameters. For establishing the process parameters, the in-situ crystallization during heating and cooling cycles was studied. Optimization of bonding at seal interface was established by microstructural studies using SEM-EDX. Single/ multi-pin hermetic seals fabricated with LZS glass-ceramic have withstood vacuum levels of 10^{-6} Torr with a low leak rate of 10^{-9} Torr litre sec^{-1} and pressure upto 13000 psi. Several such seals have been supplied to various users in BARC.

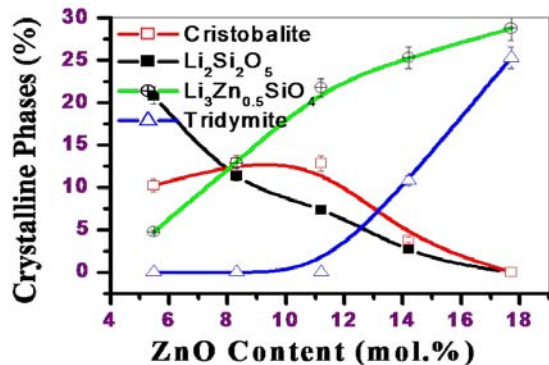
Structural studies using solid state MAS NMR:

Extensive studies on structural aspects of LZS glass and glass-ceramics using ^{31}P , ^{11}B and ^{29}Si solid state MAS NMR were carried out to determine the structural units of Si, Al, P and B, the coordination number and neighbouring atoms, the crystallization behaviour, the effect of phase separation on nucleation and accurate



Crystalline phase analysis using ^{29}Si NMR in LZS glass ceramics.

quantification of crystalline phases in glass-ceramics. These investigations have helped in demystifying the structure-property correlation in this glass-ceramic system and also to improve the material quality.



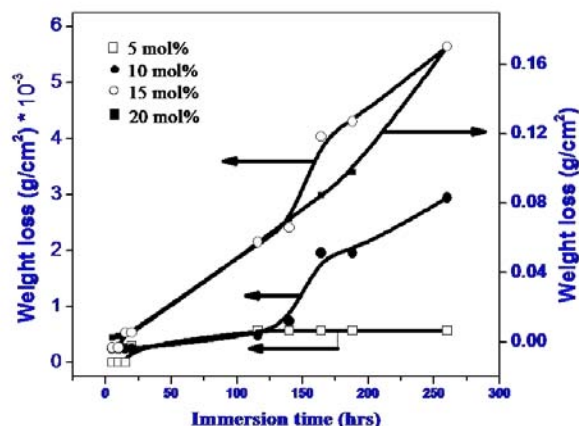
³¹P NMR of LZS glass-ceramics showing formation of phosphate phase

Sodium-boro-phosphate glass:

Chemically durable Na₂O-BaO-B₂O₃-P₂O₅ glasses were developed for sealing with low melting materials such as, Al/Be alloys. The flow sheet for preparation of phosphate glasses with matched thermal expansion and high chemical durability was carried out by the optimization of composition and process parameters. Various constituents like, barium, phosphorus, and boron, were added in proportionate amounts to tune the thermal expansion coefficient value and to improve the chemical durability. The structure-property correlation in these glasses was obtained from studies conducted using ²⁷Al and ³¹P solid state NMR. The glass composition was further optimized by evaluating the chemical durability in various mediums at room temperature and at elevated temperature. Seals fabricated with the optimized composition demonstrate leak tightness upto 10⁻⁶ Torr.



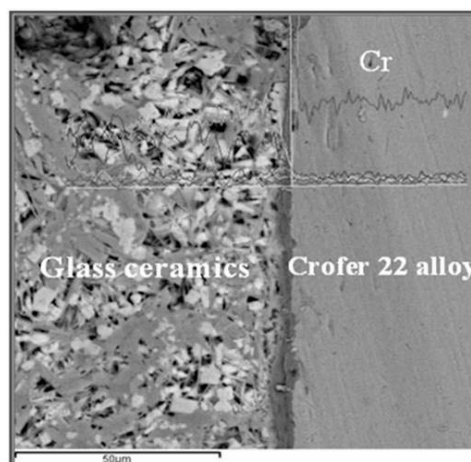
Sodium-boro-phosphate glass-to-metal seals.



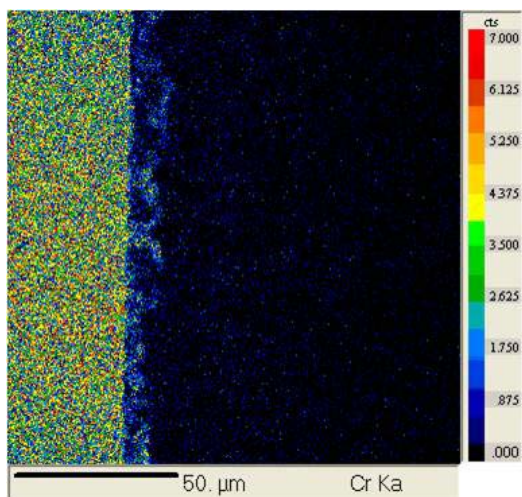
Corrosion study on glasses having nominal composition, 40Na₂O-10BaO-xB₂O₃-(50-x)P₂O₅, where x = 0-20mol% x=5-20mol% in distilled water at room temperature.

Barium alumino-silicate glasses for SOFC application:

Alkaline-earth silicate based glasses were prepared for prolonged use at high temperature under dry and wet H₂ atmosphere. The glass composition was optimized for matched thermal expansion co-efficient with Crofer 22 interconnect and other components of electrolyte cell. Further, various parameters such as, flow temperature, wet ability and adhesion of these glasses with the metal interconnect and cathode materials were evaluated for compatibility. Seals fabricated with the metal interconnect was found to withstand a vacuum of 10⁻⁶ torr at RT as well as at 800°C. Chemical stability of the seal was tested at 800°C for 2000hrs. Interface studies showed inter-diffusion of Ba, Ca, Al, Si and Fe elements and enrichment of Cr at the sealing interface, which is responsible for the good bonding in these seals.



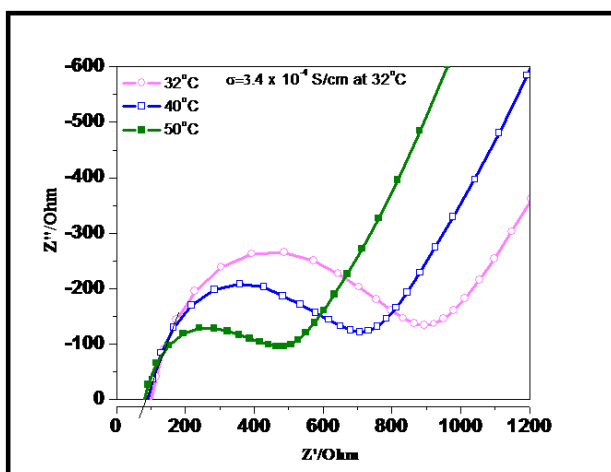
Microstructure and line-scan across the interface of BCABST glass-to-Crofer22 seal



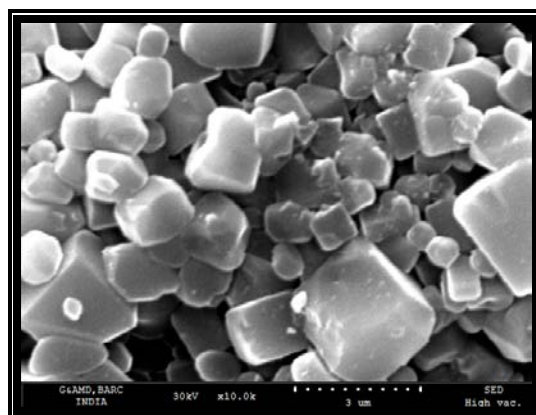
X-ray analysis of Cr element showing diffusion at the interface of BCABST glass-to-Crofer22 seal

LATP glass ceramics for Li-air rechargeable battery:

The development of $\text{Li}_2\text{O}-\text{Al}_2\text{O}_3-\text{TiO}_2-\text{P}_2\text{O}_5$ glass-ceramics for use as Li-superionic conductor in Li-Air rechargeable battery has been recently initiated. The flow chart for preparation of glass-ceramics with NASICON structure was carried out by the optimization of composition and process parameters. The optimized LATP glass-ceramics show electrical conductivity value of $2-3 \times 10^{-4}$ S/cm at RT with very good interconnected LATP microstructure. Thin thin sheets of this materials are being prepared by tape casting for miniaturization of the devices.



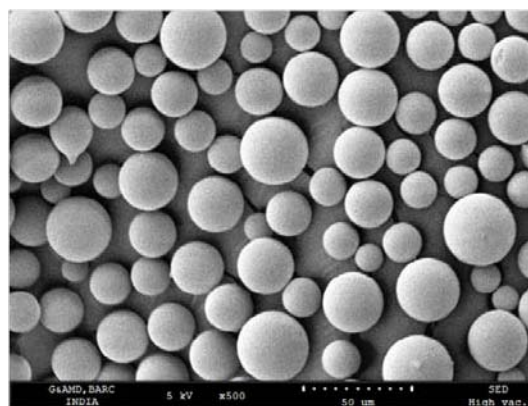
Cole-Cole plot for LATP fast ionic glass-ceramics.



Microstructure of $\text{Li}_2\text{O}-\text{Al}_2\text{O}_3-\text{TiO}_2-\text{P}_2\text{O}_5$ glass-ceramics Li-superionic conductor.

Yttrium-alumino-silicate(YAS) glass microsphere for radiotherapy application:

$\text{Y}_2\text{O}_3-\text{Al}_2\text{O}_3-\text{SiO}_2$ based glass microsphere finds potential application in radiotherapy treatment of hepatic cellular carcinoma(HCC) and synovitis. ^{90}Y -a beta emitter in a irradiated YAS glass with a half life period of 64hrs and about 934 KeV energy found very useful for localized cancer treatment. Microsphere in the range of $10-50\mu\text{m}$ have been successfully prepared by flame pyrolysis process. Attempts are now being made to prepare monodispersed microspheres and YAS glass with high yttrium content for higher efficiency.

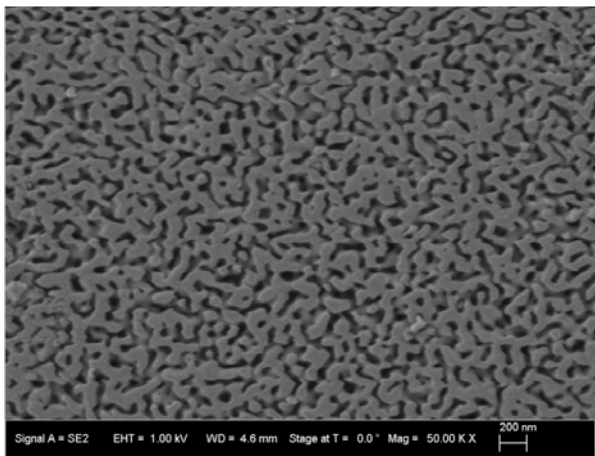


SEM image of $\text{Y}_2\text{O}_3-\text{Al}_2\text{O}_3-\text{SiO}_2$ glass microsphere.

Development of Superhydrophobic glass by spinodal decomposition

Work has been initiated on enhancing the superhydrophobicity of glasses through creating nano-scale structure on the glass surface. This has been achieved through a novel process of spinodal decomposition on nano-metric scale followed by etching. Glasses based on $\text{Na}_2\text{O}-\text{B}_2\text{O}_3-\text{SiO}_2$ system were prepared by melt-quench technique and heat treatment schedule was optimized for a fine scale interconnected

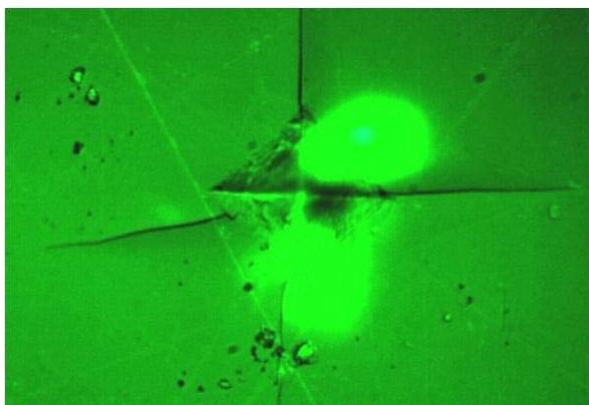
microstructure. SEM showed uniformly distributed interconnecting microstructure after heat treatment at 700°C/1h. Samples were etched for a controlled surface modification to enhance the hydrophobicity of the glass surface.



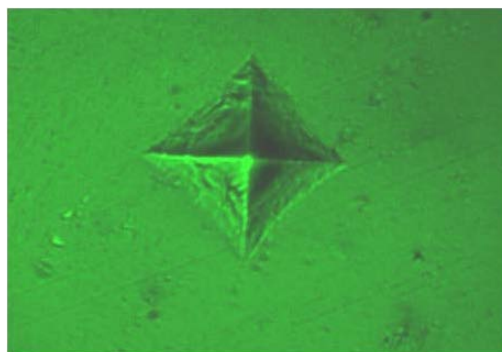
SEM image of interconnected microstructure of NBS glass

Toughening of glass by chemical-ion exchange process

Toughened glasses find potential applications in many fields including aeronautics as cockpit windows, mobile screen/ touch screen, transparent armor, glass substrates for harvesting solar energy etc. Initial work on processing of toughened glass using ion exchange process has been successful. Thin sheets of sodalime glass were treated in molten KNO_3 bath for chemically exchange of the K^+ ion in place of Na^+ ion, which induces compressive stress on the surface and increases the toughness. The distribution of the stresses and densification of structure are under investigation using micro/nano-indentor and micro-Raman spectroscopy.



Optical image of indentation under 500gf load on untreated soda lime silicate glass.



Optical image of indentation under load of 500gf for ion exchanged soda lime silicate glass.

Other Glass and Glass-Ceramics

In addition to above, the development of rare earth doped Yttria-alumino-silicate (YAS) glass/glass ceramics for white LED application, transparent Magnesium alumino-silicate (MAS) glass-ceramics for optical/laser applications, dosimetry glasses and hollow Hydroxy-apatite(HAP) for drug delivery are being carried out.

Acknowledgement

The author gratefully acknowledges Dr. Madangopal Krishnan, Head, G&AMD for his support, encouragement and keen interest in the work. She records her sincere thanks to Dr. V.C Sahni, Ex-Director, RRCAT & Physics Group and Dr. G.P. Kothiyal, Ex-Head, G&ACD for their help, valuable suggestions and guidance. The author expresses her gratitude to all her colleagues in Glass & Glass Ceramic Section, G&AMD, who were associated with her in the work reported in this article.

Reference

1. M. Goswami, S.K. Deshpande, R. Kumar and G.P. Kothiyal, J. Phys. Chem. Solids 71 (2010) 739-744.
2. M. Goswami, Govind P. Kothiyal, Lionel Montagne, Laurent Delevoye, Solid State-Chemistry, 181 (2008) 269-275.
3. M. Goswami, P. Sengupta, Kuldeep Sharma, Rakesh Kumar, V.K. Shrikhande, J.M. Ferreira and G.P. Kothiyal, Ceramics International, 33(5) (2007) 863-867.
4. K.V. Shah, M. Goswami, D.K. Aswal, V.K. Shrikhande, S.K. Gupta and G.P. Kothiyal, J. Therm. Anal. Cal. 98 (2007) 153.
5. M. Goswami, V. Sudarsan, G.P. Kothiyal and S.K. Kulshreshtha, Glass Technology, 46(5) (2005) 341-346.
6. M. Goswami, A. Sarkar, T. Mirza, V.K Shrikhande, Sangeeta, K.R. Gurumurthy and G.P. Kothiyal, Ceramics International, 28 (2002) 585-592

EXPERIMENTAL AND ANALYTICAL STUDY FOR SAFETY OF NUCLEAR RESEARCH REACTORS

Samiran Sengupta, Aniruddha Ghosh and S. Mammen

Research Reactor Design & Projects Division

C. Sengupta

Research Reactor Maintenance Division

S. Bhattacharya

Reactor Group

Samiran Sengupta is the recipient of the DAE Homi Bhabha Science and Technology Award for the year 2014

Abstract

This paper describes some of the key experimental and analytical studies carried out for the design and development of Plate type fuel assemblies, Natural circulation valve, BeO reflector assemblies and Chimney structure to ensure safety of nuclear research reactors.

Keywords: chimney, fuel, model, natural circulation, nuclear safety, radioactivity, reflector, research reactors

Introduction

Apsara reactor, the first research reactor built in Asia, was commissioned in the year 1956. It was a 1 MW swimming pool type reactor using high enriched uranium (HEU) as fuel, demineralised water as coolant, moderator and reflector. Considering the long service period, the reactor was permanently shut down in 2010. Under the upgradation programme, the reactor power is increased to 2 MW and reactor core is replaced with low enriched uranium (LEU) as fuel. The core is surrounded by two layers of beryllium oxide (BeO) reflectors. The maximum thermal neutron flux is enhanced to 6.1×10^{13} n/cm².sec. This paper describes some of the developmental work carried out for the upgraded Apsara reactor. It also presents the experimental studies carried out for the design of chimney structure of proposed High Flux Research Reactor at Vizag.

Plate type Fuel Assembly

The fuel material used for plate type fuel assemblies is U₃Si₂ dispersed in Aluminium matrix. The material has high uranium density in fuel meat, good compatibility with aluminium matrix, high thermal conductivity, excellent blister resistance threshold, stable swelling behaviour under irradiation, high fission gas retaining capability, low release of volatile fission products and good fabricability. U₃Si₂ is synthesized by using powder processing route with uranium metal powder and silicon powder as the starting materials. Aluminium alloy of nuclear grade is chosen as cladding material. The upgraded Apsara core is loaded with two types of fuel assemblies comprising of standard fuel assemblies and control fuel assemblies. The general

arrangement drawing of the standard and control fuel assemblies are shown in Fig. 1.

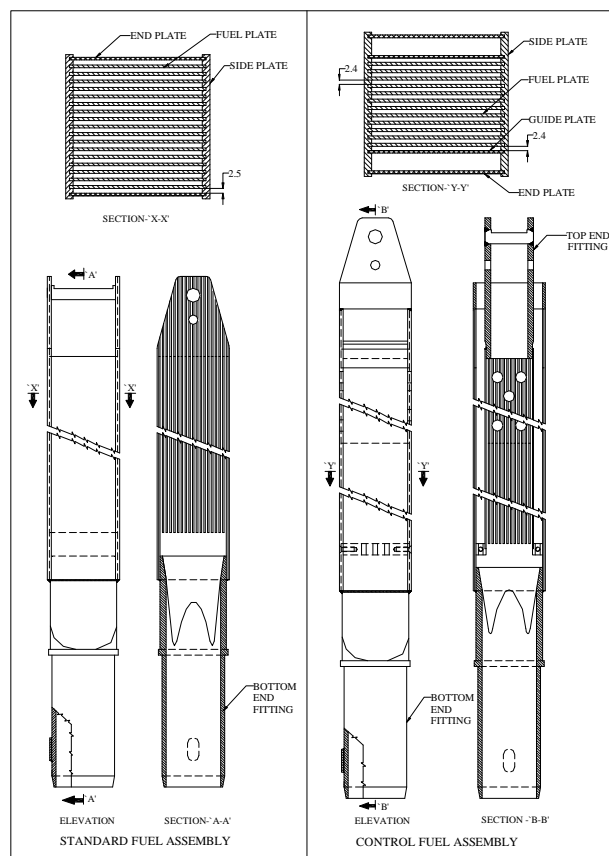


Fig. 1: Details of Standard and Control Fuel Assembly

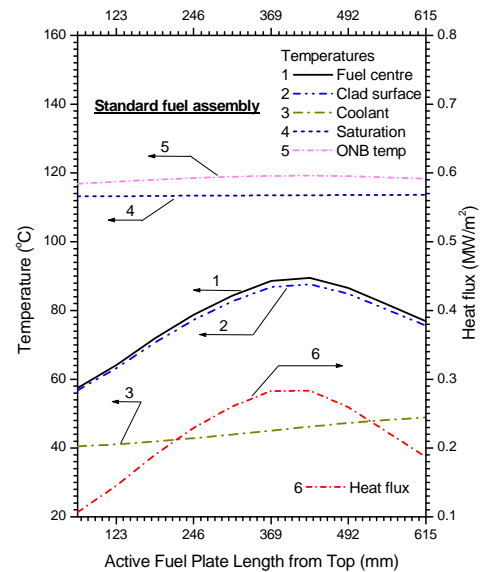
Each standard fuel assembly (SFA) consists of 17 fuel bearing plates. Two 4 mm thick side plates with grooves made in the internal faces are provided for positioning the fuel plates. All fuel plates are swaged into these grooves to maintain a uniform water gap of 2.5 mm between them. Two 1.5 mm thick end plates are also swaged into the grooves of side plates at both the ends to make a fuel box with a confined boundary from all sides using non-fuel bearing plates. The fuel box is connected at the bottom to a lower end fitting which provides a smooth transition from square cross-section of the fuel box to a cylindrical toe for supporting the fuel assembly on the grid plate.

Control fuel assemblies (CFA) are provided to accommodate absorber element (control rod/ shut-off rod) inside it to control the power of the reactor. The Control fuel assembly is similar to standard fuel assembly with five fuel plates removed to create the space required to accommodate the twin blade fork type absorber element made of Hafnium. The twin blades are placed symmetrically with respect to central axis of the fuel element. A recess has been created between the end plate and an aluminium guide plate, which are swaged into the side plates. Two orifice plates are provided at the bottom between the guide plate and the end plate, in order to reduce the bypass flow. The movement of the absorber blade of the control fuel assembly is controlled by the drive unit provided on the platform at the pool top.

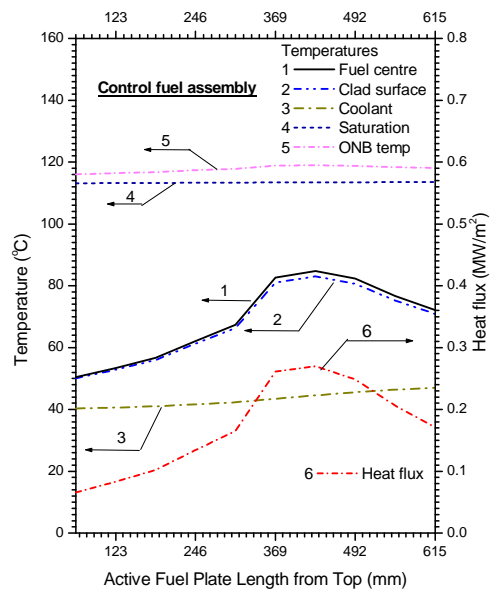
In order to ensure the fuel safety, the coolant velocity has been so chosen that for the hottest standard and control fuel assembly, the fuel meat and clad temperatures do not exceed the prescribed limits. Fig. 3 shows the fuel meat, clad and onset of nucleate boiling (ONB) temperatures along the fuel length of the highest rated standard and control fuel assemblies considering nuclear and engineering peaking factors using the hot channel methodology. The minimum safety margin is found to occur in the standard fuel assembly.

An experimental test facility was installed and commissioned where the fuel assembly was tested for flow induced vibration as well as for the hydraulic characteristics to establish the fuel design considerations. The testing of the fuel assembly was successfully carried out in the experimental set up (Fig. 3). The dummy fuel assembly was made fully out of aluminium. The experiments were carried out to validate resistance characteristics of the fuel assembly with respect to the numerical predictions. The experiments were carried out with water at various temperatures (about 20, 30, 40 and 50 °C) passing through the assembly, to establish the effect of resistance variation due to change in water temperature. The pressure loss across the fuel assembly was found to decrease with increase in coolant (water) temperature. The direction of

coolant flow through the fuel assembly was also reversed to observe the variation due to upward and downward flow directions. The pressure loss for upward flow is found to be less than that for the downward flow. Experimental results are used to validate the methodology utilized for prediction of the developed code. All the experimental results were compared with the numerical results predicted by the computer codes as shown in Fig.4. It is observed that experimental results are well within $\pm 5\%$ of the results predicted by the code.



(a) Standard Fuel Assembly

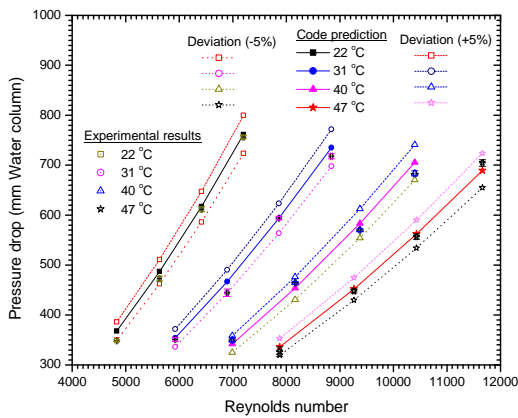


(b) Control Fuel Assembly

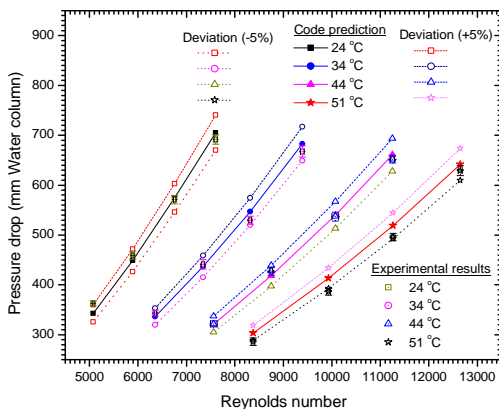
Fig. 2: Temperatures and Heat Flux for Fuel Assemblies



Fig.3: Setup for Flow Test of Fuel Assembly



(a) Results for downward flow



(b) Results for upward flow

Fig.4: Code Validation using Experimental Results

Natural Circulation Valve

An experimental study was carried out on an out of pile test loop to determine the flow characteristics of a natural circulation valve (NCV) to be used in Upgraded Apsara

reactor. Each NCV is a flapper type valve in which a metal disc is attached to the outlet plenum through hinges. The valve is normally kept closed by hydraulic pressure of the primary cooling water pumps through a spring loaded piston cylinder actuating mechanism. On failure of the pumps, hydraulic pressure falls and two NCVs are opened by gravity and the spring force available in the actuator. When NCV opens, natural circulation path between the pool and the outlet plenum is established. NCV being a safety component for providing shut down cooling of the reactor, its flow characteristics is an important design input towards assessing the core flow and temperature distribution for the fuel assemblies. Moreover, inadvertent opening of NCV causes core bypass path reducing the forced convection cooling flow through the reactor core. An experimental setup (Fig. 5) was made for testing NCV by recirculating water through the NCV in a closed loop.



Fig. 5: Experimental Setup for NCV testing

In the setup, the NCV was kept open by a spring force as envisaged in the reactor. Normally the valve would be kept 25° open as shown in Fig. 6a. Reduction in stroke length of spring would decrease the valve opening angle. To determine resistance characteristics of the valve, flow was varied to cover a range of Reynolds number from 4×10^4 to 2×10^5 expected in reactor. The loss characteristic of NCV was measured using purge tubes acting as pressure sensing probe. The purge tubes were mounted in a bank arrangement (Fig. 6b) to keep the high and low pressure tappings at the same elevation. The position of pressure tapping was varied vertically and horizontally to see its effect. It was observed that differential pressure did not change significantly when these tubes are moved horizontally apart by 100 mm. Initially, the experiments were carried out keeping the purge tube bottom at the center elevation of the valve. Subsequently, the bank was moved up and down by 20 mm from the center elevation to see its effect on pressure differential across the valve.

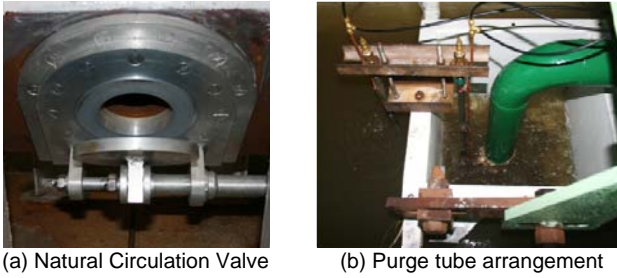
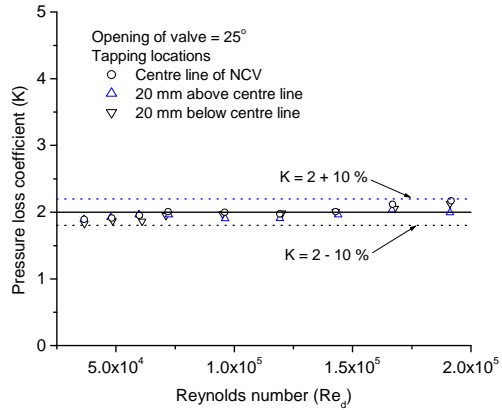
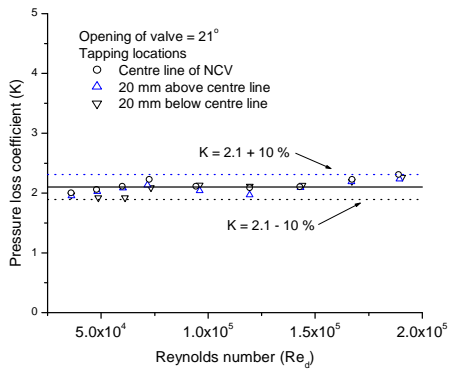


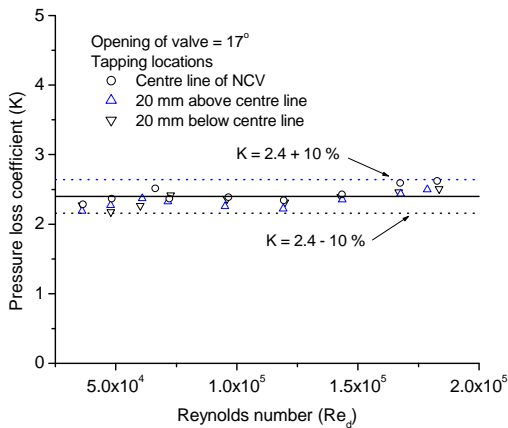
Fig. 6: NCV and Purge tubes



(a) NCV 25° open



(b) NCV 21° open



(c) NCV 17° open

Fig. 7: Resistance characteristics of NCV

The sensitivity of pressure loss towards NCV opening angle was studied by reducing the stroke length of the piston cylinder mechanism in steps of 25 mm which caused 4° reduction of opening angle. Loss coefficients were estimated for 25°, 21° and 17° openings of NCV for a range of flow (Fig. 7). It is observed that the pressure loss is almost independent of the purge tube locations. The loss coefficients evaluated are 2.0, 2.1 and 2.4 respectively within a band of $\pm 10\%$.

Reflector assembly

Reflector assemblies of Upgraded Apsara reactor are provided surrounding the reactor core to provide larger irradiation volume for researchers. These reflectors get heated up due to interactions with neutrons and gamma rays from the reactor core. Since no dedicated forced cooling is provided to cool these reflector assemblies, the heat transfer from them mainly takes place by natural convection. These reflector assemblies are immersed in pool water which acts as the heat sink. Typical geometry of standard reflector assembly is shown in Fig. 8a. The surface temperatures of bottom plate, top plate and aluminum clad were predicted (Fig 8b to d). It is observed that the maximum air gap between aluminium side clad and BeO blocks should not be more than 0.3 mm to keep the temperatures of the surface well below onset of boiling temperature.

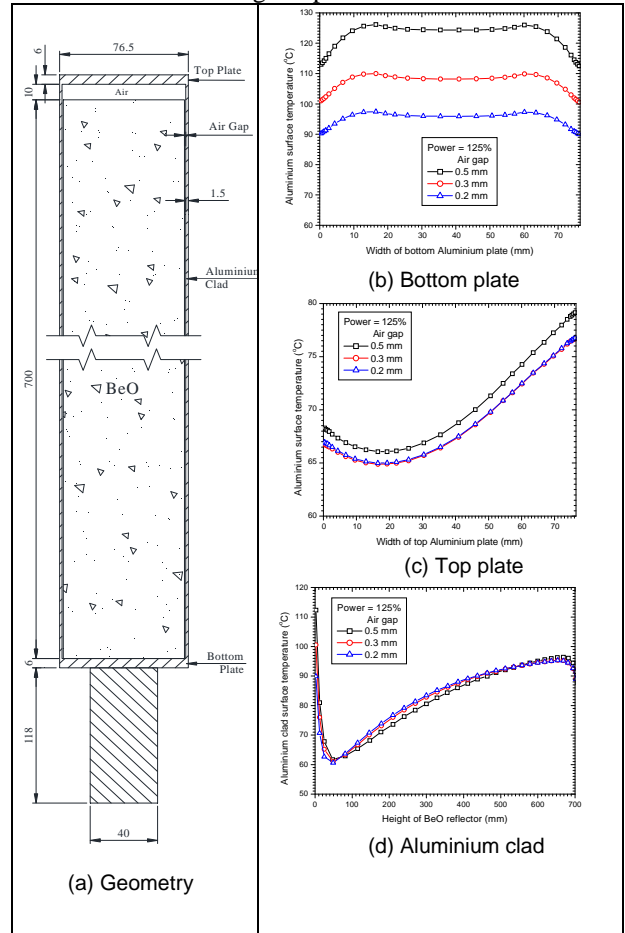


Fig. 8: Geometric Details of BeO Assembly

Chimney

In high flux research reactor, a chimney is provided on the top of reactor core to suppress the radioactive core outlet water reaching the pool so that radiation field at the pool top can be minimum. An experimental set up has been commissioned with a scaled (1/18th) model of chimney using Particle Image Velocimetry (PIV) in collaboration with IIT Bombay. The setup (Fig. 9) consists of a 15 Hz pulsed laser and a camera. The double-pulsed Nd:YAG laser provides pulses of 6 ns duration with a wavelength of 532 nm and maximum energy of 350 mJ per pulse. A thin laser light sheet of 1 mm thickness was obtained using cylindrical and spherical lenses to illuminate the plane of interest. Seeding particles employed were microsphere tracer particles so that the light reflected from the tracer particles could be used to measure the velocity field of the flow under investigation. Seeding particles are made of fused borosilicate glass (size 8-11 μm , specific density 1.1).

The camera was connected to a 64 bit frame grabber to capture and digitize images. A synchronizer was used to synchronize the laser and cameras. Images were captured using laser A and laser B. The delay between them is taken 750 ms for 1800 kg/hr core flow corresponding to Reynolds no 20000. The delay is decreased to 500 ms for 3600 kg/hr core flow with Reynolds no of 40000. The software PIVlab was used to evaluate the recorded images via cross-correlation.



(a) Set up for PIV stud (b) Arrangement for Laser and Camera
Fig. 9: Experimental Setup for flow mixing study

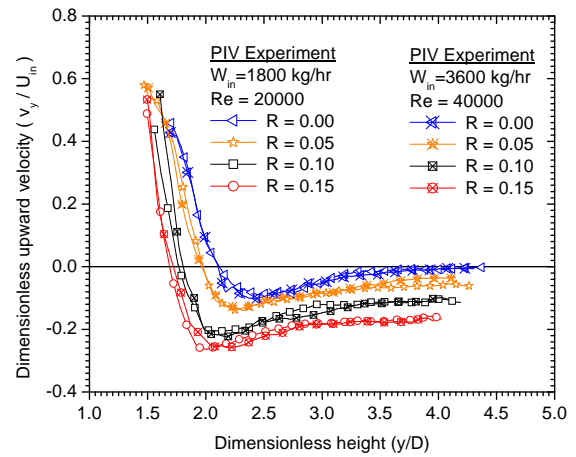


Fig. 10: Centerline velocity variation with height

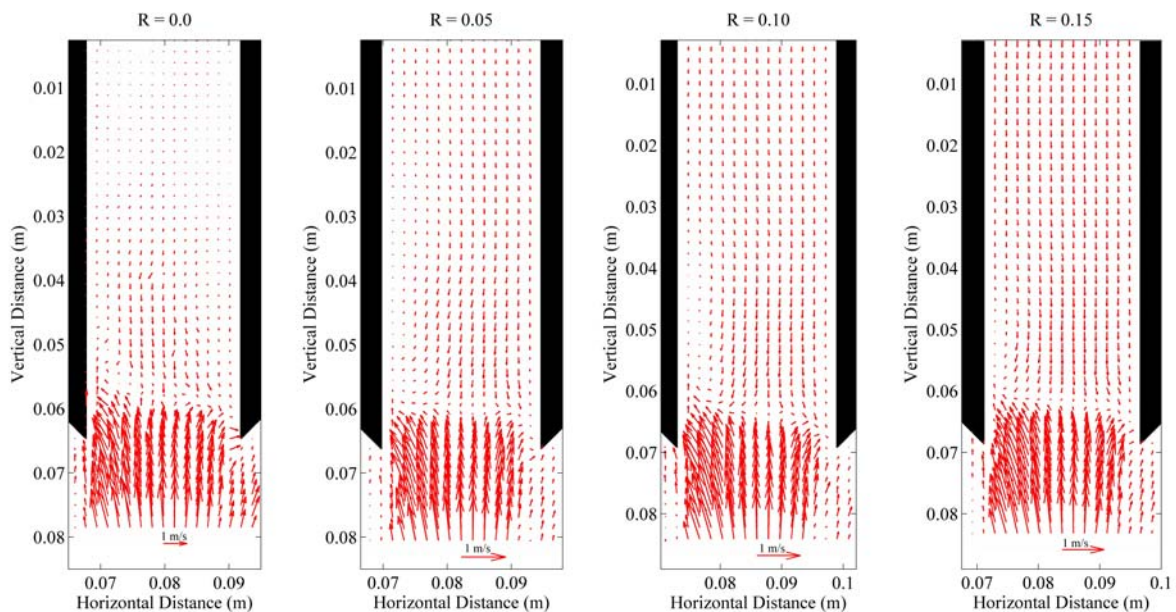


Fig. 11: Velocity vector results from PIV data



(a) Experimental setup



(b) View from front window



(c) View from side window

Fig.12: Experimental Setup for Hot and Cold Fluid Mixing inside Chimney

Fig. 10 shows the experimental results for various bypass flow ratios ($R=0.0, 0.05, 0.1$ and 0.15). It shows that the jet height decreases with increase in bypass flow and it does not vary significantly with increase in Reynolds number. Fig. 11 shows the velocity vectors derived from the PIV data for various bypass flow ratios.

Another experimental setup (Fig. 12) was installed at Apsara reactor hall for establishing the effect of hot and cold water mixing inside the scaled model ($2/9^{\text{th}}$) of the chimney. Flow visualisation using dye and temperature profile measurement using RTDs was done to establish the suppression of hot water jet in the experimental set up. It was established that the bypass flow should be 10% of the core flow in order to suppress the hot water jet within the chimney.

Conclusion

The experimental and analytical studies carried out have helped to establish the safety of the nuclear research reactor and also provided insight for evaluating the design and safety criteria.

Theory of electronic structure and optical properties of graphene nanoribbons

Kodayya Gundra
Theoretical Physics Section
Multidisciplinary Research Group

Kodayya Gundra is the recipient of the DAE Scientific & Technical Excellence Award for the year 2014

Abstract

Graphene nanoribbons (GNRs) attracted a great deal of attention in recent times due to their potential applications in next generation electronics. Using the fact that GNRs are conjugated π -electron systems, we developed an efficient approach based on Pariser-Parr-Pople Hamiltonian to study electro-optical properties of GNRs. We developed a FORTRAN 90 computer code to solve Hartree-Fock (HF) equations for open and closed shell 1D π -electron systems with periodic boundary conditions. We also study the effect of gate voltage on electronic structure and optical absorption spectra by performing HF calculations in the presence of static external electric field. Our work revealed the importance of optical probes in determining the geometry, magnetic order and half-metallic nature of GNRs.

Introduction

Discovery of graphene [1] has stimulated intense theoretical and experimental research worldwide. Though graphene is one atom thick, it is highly stable at ambient conditions with well defined crystal structure. Graphene exhibits exceptional electronic and mechanical properties, however the most fascinating aspect of graphene is that the energy dispersion near the Fermi energy is linear similar to the case of mass-less relativistic quasi-particles, making it *relativistic-condensed matter* system [2]. Therefore, it is a wonder material which can be used to explore the quantum

electrodynamics phenomena on simple table top experiments which otherwise observable only in black holes and high energy particles accelerators. As far as application point of view is concern, being a zero gap semiconductor its use in electronics is limited. Band gap can be introduced in graphene by patterning it into quasi 1D structures known as graphene nanoribbons (GNRs). Quantum confinement of electrons in 1D system is responsible for opening band gaps. GNRs can be produced either by using bottom-up or top-bottom approaches [3, 4, 5].

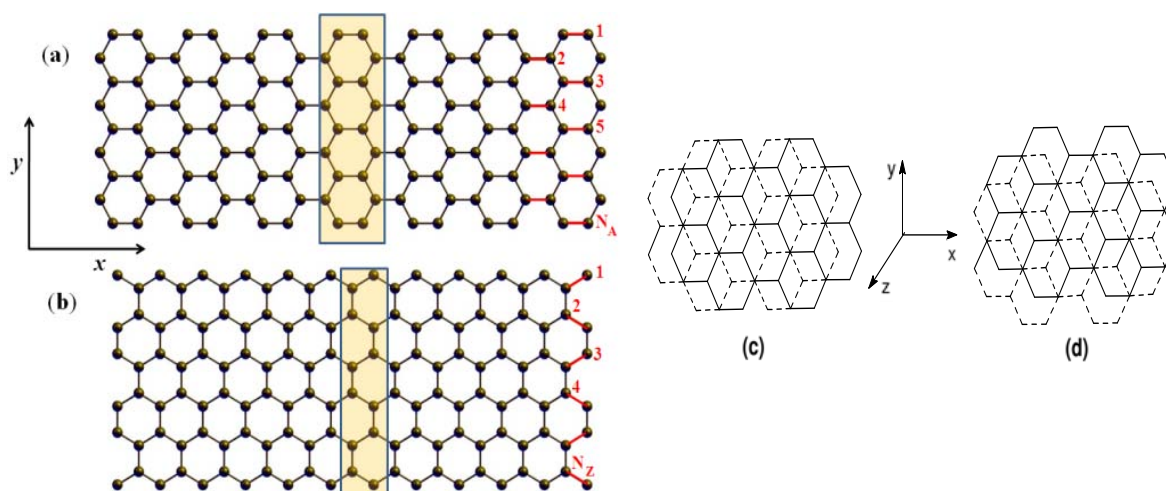


Fig. 1. The schematic representation of GNRs (a) Armchair ($N_A=9$), (b) Zigzag ($N_Z=6$), (c) Bi-layer armchair in γ -alignment and (d) Bi-layer armchair in δ -alignment. The mono layer ribbons are assumed to lie in x - y plane, with periodicity in x -direction. Different layers in Bi-layer ribbons are stacked along z axis.

GNRs have been studied using several theoretical methods starting from simple tight binding (TB) theory [6] to computationally expensive *ab initio* density functional theory (DFT) and electron-correlated Green function based GW methods [7, 8]. However, it is important to note that the low-lying excitations in GNRs are characterized by the itinerant π -electrons. Due to the extended conjugation observed in π -electron systems, long-range electron-electron (e-e) interactions play a significant role in their electronic structure. Motivated by this fact, we have developed an efficient semiempirical approach [9] to study electro-optical properties of GNRs based on the Pariser-Parr-Pople (PPP) Hamiltonian [10] which incorporates long-range e-e interaction in a natural way. GNRs are quasi-1D systems, which need to be studied in the bulk limit. We have implemented PPP model for 1D periodic π -electron systems employing both the restricted Hartree-Fock (RHF) and the unrestricted Hartree-Fock (UHF) methods [11]. The UHF variant can be used to explore magnetic properties of polymers and GNRs whereas RHF version is useful to study the closed-shell systems. We have studied interesting electronic and optical properties of monolayer and multilayer GNRs using the PPP model Hamiltonian. The schematic structures of a monolayer armchair GNR (AGNR) and a zigzag GNR (ZGNR) are portrayed Fig. 1 (a) and Fig. 1 (b) respectively, the unit cells of these ribbons are enclosed in the shaded rectangle. The electronic properties of GNRs crucially depend on their width. In the case of AGNRs, N_A denotes the number of carbon-carbon dimer-lines across the width (Fig. 1 (a)) while, in the case of ZGNRs N_Z denotes the number of zigzag-lines across the width (Fig. 1 (b)). We denote an AGNR (ZGNR) with width N_A (N_Z) in short as AGNR- N_A (ZGNR- N_Z). Regarding multilayer GNRs, two possible edge alignments, named γ and δ are considered, as shown in Fig.1 (c) and (d) [12]. We also explored the anisotropic optical response of GNRs by evaluating the optical absorption spectrum for incident radiation polarized along periodicity direction (*i.e.*, x -direction) and also y/z -directions. Furthermore, we explore the effect of gate bias on the band structure and optical properties of GNRs by performing Hartree-Fock calculations in the presence of a static external electric field [13].

Theoretical methodology

We briefly describe the theoretical methodology of the PPP model in this section. In PPP model only π -electrons are considered explicitly, while the effect of σ -electrons is included in an implicit manner in terms of various parameters. The PPP model Hamiltonian [10] with one π -electron per carbon atom reads as

$$H = - \sum_{i,j,\sigma} t_{ij} (c_{i\sigma}^\dagger c_{j\sigma} + c_{j\sigma}^\dagger c_{i\sigma}) + U \sum_i n_{i\uparrow} n_{i\downarrow} + \sum_{i<j} V_{ij} (n_i - 1)(n_j - 1)$$

$c_{i\sigma}^\dagger$ creates an electron of spin σ on the carbon atom i , $n_{i\sigma} = c_{i\sigma}^\dagger c_{i\sigma}$ is the number of electrons with spin σ , and $n_i = \sum_\sigma n_{i\sigma}$ is the total number of electrons on atom i . The parameters U and V_{ij} represent the on-site and long-range Coulomb interactions, respectively, t_{ij} is the one-electron hopping matrix element. It is obvious that by setting $U=0$ and $V_{ij}=0$, the Hamiltonian reduces to the tight binding model, by setting $V_{ij}=0$, the Hamiltonian reduces to Hubbard model. The parameterization of the Coulomb interactions is Ohno like [14]

$$V_{ij} = U / [\kappa_{ij} (1 + 0.6117 R_{ij}^2)^{1/2}],$$

where, κ_{ij} is the dielectric constant of the system and R_{ij} is the distance in Å between the i -th and the j -th carbon atoms. We chose the Coulomb parameters with $U = 6$ and $\kappa_{ij} = 2$, for $i \neq j$ and $\kappa_{ii} = 1$ [13]. The intra-layer nearest neighbor (n-n) hopping was chosen to be (in eV) 2.7 along with next NN hopping 0.27 and the inter-layer n-n hopping was chosen to be 0.4 along with next NN hopping 0.3 [15].

Next, we briefly describe the theory of linear optical absorption spectra of GNRs. The optical absorption spectrum for the x -polarized (y -polarized) photons is computed in the form of the corresponding components of the imaginary part of the dielectric constant tensor $\epsilon_{ii}(\omega)$ [16] which depends on the momentum matrix elements (MMEs) $\langle c(\mathbf{k}) | \mathbf{p} | v(\mathbf{k}) \rangle$ between valence ($v(\mathbf{k})$) and conduction ($c(\mathbf{k})$) band eigenstates. The MMEs for a general three-dimensional system, can be calculated using the k -space gradient formulation given by [17],

$$\langle c(\mathbf{k}) | \mathbf{p} | v(\mathbf{k}) \rangle = \frac{m_0}{\hbar} \langle c(\mathbf{k}) | \nabla_{\mathbf{k}} H(\mathbf{k}) | v(\mathbf{k}) \rangle + \frac{\text{Im}_o(\epsilon_c(\mathbf{k}) - \epsilon_v(\mathbf{k}))}{\hbar} \langle c(\mathbf{k}) | \mathbf{d} | v(\mathbf{k}) \rangle$$

where m_0 is the free-electron mass, $\nabla_{\mathbf{k}} H(\mathbf{k})$ denote the gradient of the Hamiltonian in the \mathbf{k} space, $\langle c(\mathbf{k}) | \mathbf{d} | v(\mathbf{k}) \rangle$ represent the matrix elements of the position operator \mathbf{d} (defined with respect to the reference unit cell) [17]. The matrix element $\langle c(\mathbf{k}) | p_y | v(\mathbf{k}) \rangle$ required to calculate the absorption spectrum for the y -polarized light for GNRs, by setting the first term on its right hand side to zero. The calculation of the absorption spectra of the GNRs for the y -polarized photons ($\epsilon_{yy}(\omega)$), to the best of our knowledge, has not been done earlier. Because such transverse excitations do not couple to the photons polarized along the longitudinal direction and referred as "dark excitons" in the literature [8].

Results and discussions

AGNRs are classified into three categories with $N_A = 3p$, $3p+1$ and $3p+2$, where p is an integer. TB theory predicts that all the AGNRs with $N_A = 3p+2$ are gapless and other two categories are gapped. But, *ab initio* DFT predicts that all categories of AGNRs are gapped [7].

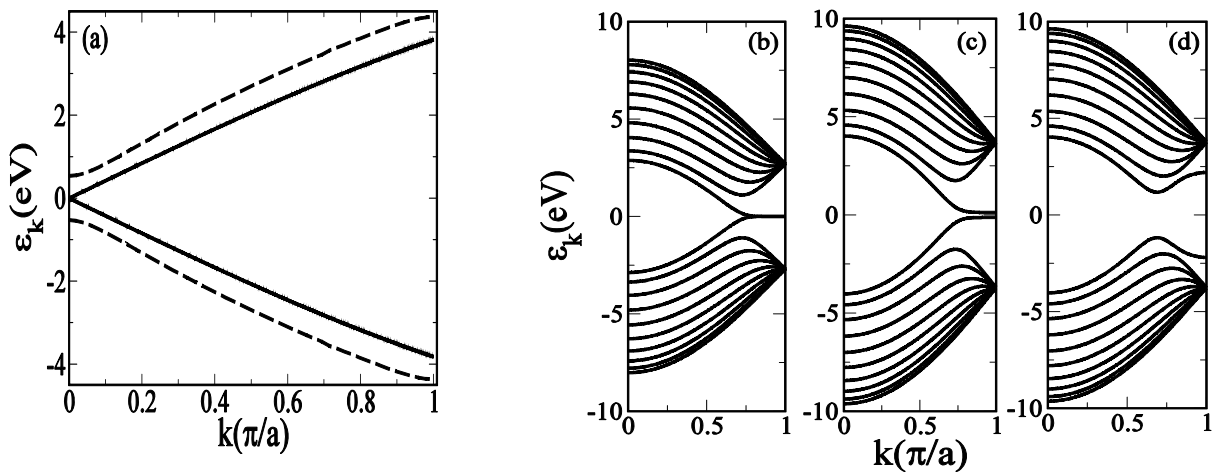


Fig. 2: The band structure near the Fermi energy ($E_F=0$) of: (a) AGNR-11 obtained using the Hubbard Model (solid line), with $U=2.0$ and the PPP-RHF approach (broken line), (b) ZGNR-10 obtained by TB method, (c) ZGNR-10 obtained by PPP-RHF method and (d) ZGNR-10 obtained by PPP-UHF method.

In Fig.2a we present the band structures of 3p+2 class (AGNR-11) obtained using both the PPP mode and Hubbard model with $U=2.0$. We have observed good agreement of our RHF calculations with the DFT results. It is important to note that the Hubbard model, with $U=2.0$ predicts a negligible gap for $N_A=11$ (Fig.2a). Therefore, for AGNRs, long-range Coulomb interactions as included in the PPP model, play a very important role of opening up the gap for the $N_A=3p+2$ case. In the case of ZGNRs, the ground state is predicted to be magnetic with oppositely oriented spins localized on the zigzag edges on the opposite sides of the ribbons [7]. At the TB level, ZGNRs are gapless as depicted in Fig.2b, flat

bands near E_F leads to an intense van Hove singularity at E_F and hence an instability in the system. This indicates a possibility of a magnetic ordering mediated by Coulomb interactions [7]. But, the RHF method predicts a nonmagnetic ground state, even though it takes e-e interactions into account. The small band gap is an artefact of the RHF approach. However, once we perform spin-polarized calculations using the UHF approach, which is based upon separate mean-fields for the up- and the down-spin electrons, we get the ground state exhibiting edge magnetism, and a significant band gap (Fig.2d), and the total energy/cell of is lower than the nonmagnetic state obtained by the RHF calculations.

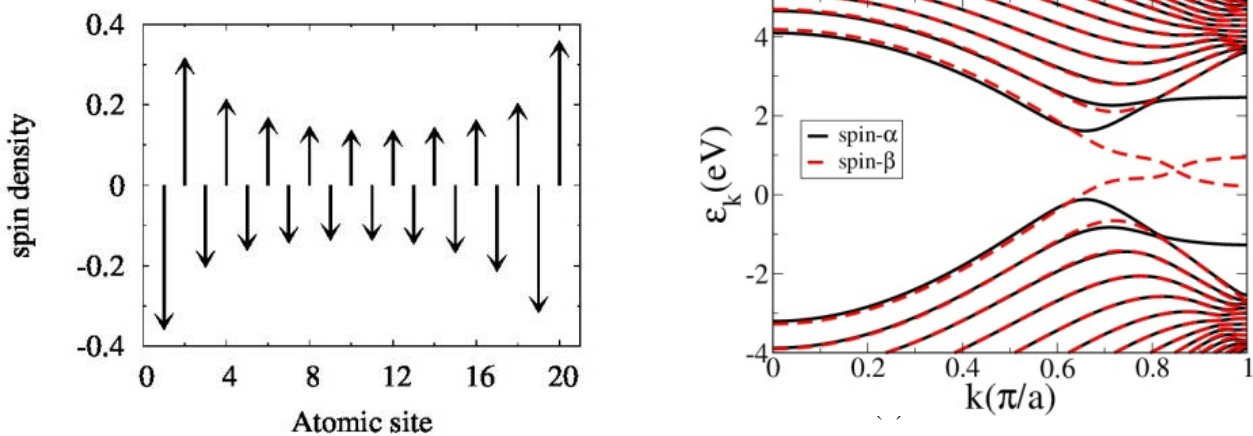


Fig. 3: Spin density of ZGNR-10, obtained using the PPP-UHF calculations, and plotted at different atomic sites of the unit cell across the width of ribbon, starting from top. Antiferromagnetic alignment of spins across the width is obvious. (b) Band structure of ZGNR-14 in the presence of external electric field $E_y= 2$ V/nm, obtained by PPP-UHF method. The solid-black (dotted-red) lines represent the bands of $\alpha(\beta)$ -spin electrons.

In Fig.3a we present the spin density distribution of ZGNR-10, from which it is obvious that across the ribbon width electrons of different spins are localized at adjacent sites indicating antiferromagnetic order;

however, ferromagnetic order can be observed along an edge. In the presence of a lateral electric field, ZGNRs exhibit half-metallic behaviour [18]. In Fig.3b we present the band structure of the ZGNR-14 exposed to

field strength of 2 V/nm. In the absence of the field, as discussed above, the bands of the up- (α) and down-spin (β) electrons are degenerate. The degeneracy is lifted in the presence of electric field, and the band gap for

electrons of spin α is increases and that for the electrons of spin β reduces, indicating the tendency to half-metallic nature.

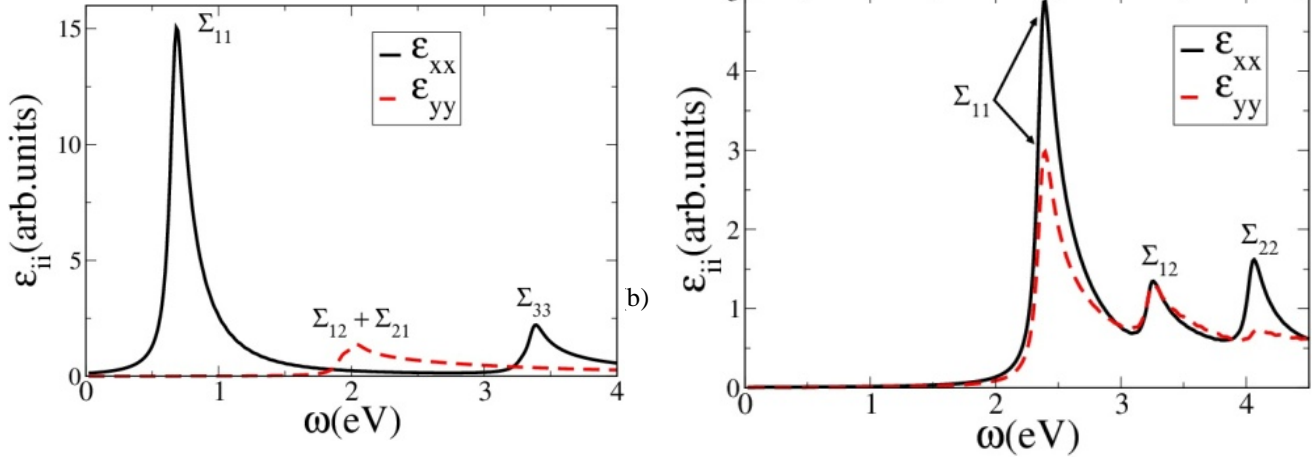


Fig. 4: Optical absorption spectrum of: (a) AGNR-14 obtained by PPP-RHF method. (b) ZGNR-10 obtained by the PPP-UHF method. The solid-black line represents ϵ_{xx} while the dotted-red line represents ϵ_{yy} . A peak in the spectrum due to a transition from m -th valence band (counted from top) to the n -th conduction band (counted from bottom) is denoted by Σ_{mn} . A line width of 0.05 eV was assumed.

The half-metallic nature of ZGNRs can be understood as follows: in the absence of electric field oppositely oriented spin states are localized on the opposite edges of the ribbon. In the presence of the transverse electric field, the electrostatic potential is raised at one edge and lowered on the other edge. Therefore, the localized edge states are shifted to higher energies at one edge and lower energies on the other edge of the ribbon, resulting to different band gaps for different spins.

The anisotropic optical response with respect to the photons polarized along x - or y -direction reveals the structural anisotropy of GNRs. In Fig. 4a we present the optical absorption spectrum of the AGNR-14 obtained using the PPP-RHF method. The noteworthy point is that individual peaks in the spectrum correspond to either x - or y -polarized photons, consistent with the D_{2h} point group of AGNRs. Furthermore, the x - and y -polarized peaks are well separated in energy. In Fig. 4(b) we present the optical absorption spectrum of ZGNR-10 obtained using the PPP-UHF method. In spite of the fact that the point group of ZGNRs is also D_{2h} , yet unlike AGNRs, most of the prominent peaks of ZGNR-10

exhibit mixed polarization characteristics. This is due to the fact that the edge-polarized magnetic ground state of ZGNRs no longer exhibits D_{2h} symmetry because of the fact that the reflection symmetry about the xz -plane is broken, thereby leading to mixed polarizations in the optical absorption. Thus, by performing optical absorption experiments on oriented samples of GNRs, one can predict whether a given ribbon is AGNR or ZGNR by probing the polarization characteristics of the absorption peaks. Next, we discuss electro-absorption (EA) spectrum, which consists of measuring optical absorption in the presence of a static external electric (E) field. In Fig.5 we present the EA spectrum of ZGNR-8 estimated as the difference of the linear absorption spectra with and without an external static electric field along the y -axis. In Fig. 5(a) we present the EA spectrum for the nonmagnetic ground of ZGNR-8, obtained using the PPP-RHF approach. As per symmetry selection rules [19], the Σ_{11} transition in the absence of an external electric field is disallowed for the nonmagnetic state of such a ZGNR for the x -polarized light.

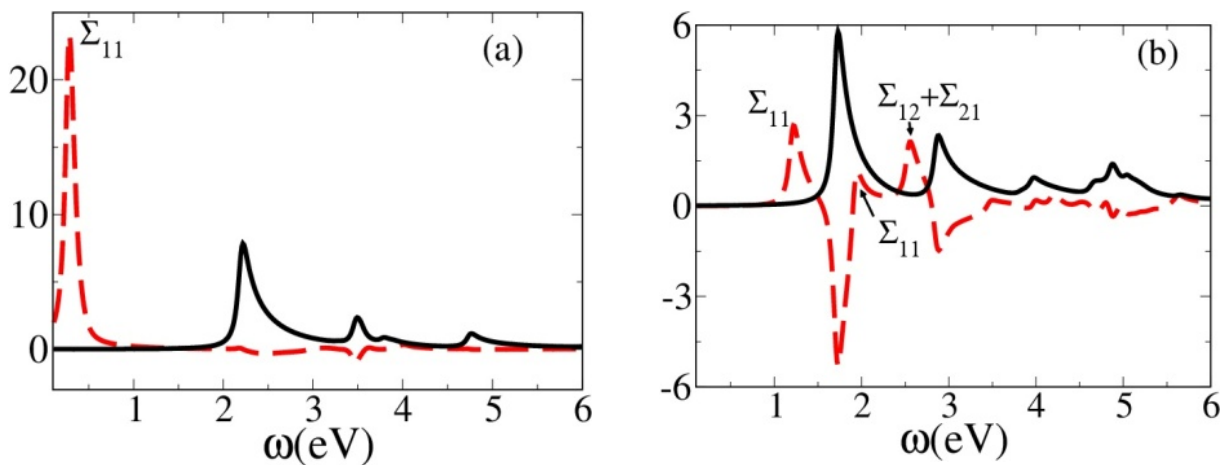


Fig. 5: Linear absorption spectrum (black-solid) and electro-absorption (red broken) of ZGNR-8 for photons polarized along the x -axis for: (a) non magnetic ground state, and (b) magnetic ground state. A line width of 0.05 eV was assumed throughout, and the bands involved in the electro-absorption peaks are indicated.

However, in the presence of the field, this transition becomes allowed due to the broken symmetry, leading to a very strong peak in the EA spectrum. The EA spectrum of the same ZGNR portrayed in Fig. 5(b) for the magnetic ground state. It is evident from the figure that the two energetically split peaks corresponding to two different Σ_{11} transitions among up- and down-spin electrons indicating the tendency towards half-metallicity in the presence of electric field. Therefore EA signal is different for the ZGNRs depending on whether they have a magnetic or a nonmagnetic ground state, a result which can be used to

determine the nature of the ground state of ZGNRs using EA spectroscopy.

The study of optical absorption of gated multilayer AGNRs is very interesting. In the Fig.6a and 6b we present the absorption spectrum for the x -polarized light for bilayer-AGNR-12- γ and the bilayer-AGNR-11- γ respectively, for different values of electric field strength in z -direction E_z . We observe the interesting trends in the optical spectra upon increasing the value of E_z . In bilayer-AGNR-12- γ , peak in Σ_{11} transition is red shifted

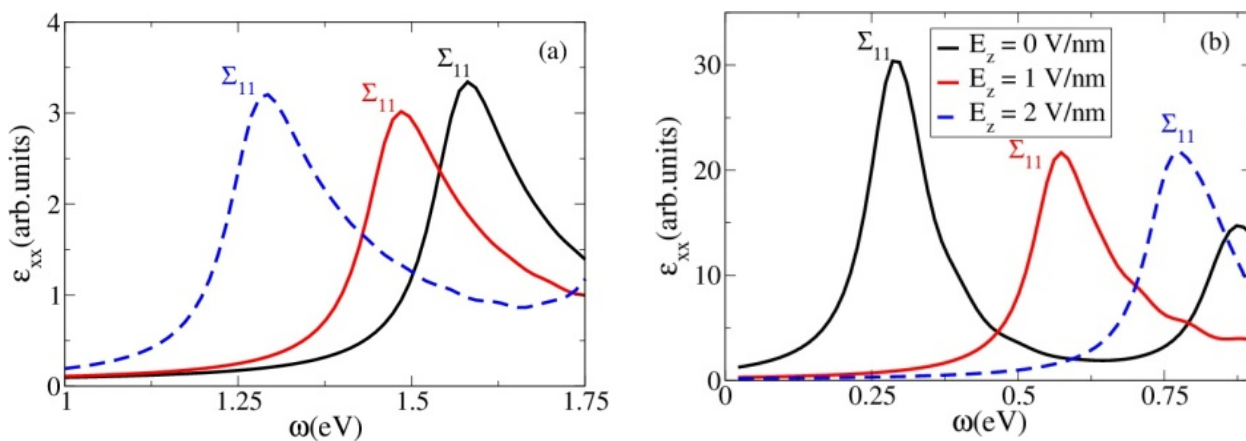


Fig. 6: PPP-RHF absorption spectra at several values of the static electric field E_z , for the incident light polarized along the x -axis for: (a) bilayer-AGNR-12- γ , (b) bilayer-AGNR-11- γ . A line width of 0.05 eV was assumed throughout.

In case of 2-AGNR-11- γ , the Σ_{11} peak expectedly blue shifts with increasing. Therefore, the two ribbons exhibit opposite behaviour as far as the dependence of the oscillator strength of Σ_{11} peak on the bias field is concerned [15].

Conclusions

We have developed an efficient approach to study electronic and optical properties of GNRs using PPP model Hamiltonian. Our study includes monolayer and multilayer GNRs with ideal edge terminations such as AGNRs and ZGNRs. Our work revealed that the optical probes can be employed as useful tools in determining the electronic and magnetic properties of GNRs. Furthermore they can be used to characterize the edge termination (either armchair or zigzag) and relative orientation of adjacent layers in bi-layer GNRs. Furthermore, our studies on electro-optical spectrum of ZGNRs suggest a novel optical route to determine edge magnetism and half-metallic nature.

Acknowledgement

I sincerely thank my co-author Prof. Alok Shukla (IIT Bombay) for introducing me into the field of condensed matter theory of graphene nanoribbons and also for his constant support and encouragement.

References

1. K.S Novoselov, A. K. Geim, S. V. Morozov, D. Jiang, Y. Zhang, S. V. Dubonos, I. V Grigorieva, A. A. Firsov, *Science* 306, 666 (2004).
2. A. H. Castro Neto, F. Guinea, N. M. R. Peres, K. S. Novoselov and A. K. Geim, *Rev. Mod. Phys.*, 81, 109 (2009).
3. Jinming Cai, Pascal Ruffieux, Rached Jaafar, Marco Bieri, Thomas Braun, Stephan Blankenburg, Matthias Muoth, Ari P. Seitsonen, Moussa Saleh, Xinliang Feng, Klaus Müllen, *Nature* 466, 470(2010).
4. Xiaolin Li, Xinran Wang, Li Zhang, Sangwon Lee, Hongjie Dai, *Science* 319, 1229 (2008).
5. Levente Tapasztó, Gergely Dobrik, Philippe Lambin and László P. Biró *Nature nanotechnology* 3, 397 (2008).
6. K. Nakada, M. Fujita, G Dresselhaus, and M. S. Dresselhaus, *Phys.Rev B* 54, 17954 (1996).
7. Y. W. Son, M. L. Cohen, and S. G. Louie, *Phys. Rev. Lett.* 97, 216803 (2006).
8. L. Yang, M. L. Cohen, and S. G. Louie, *Phys. Rev. Lett.* 101, 186401 (2008).
9. K. Gundra and A. Shukla, *Topological Modeling of Nanostructures and Extended Systems, Carbon Materials: Chemistry and Physics, F. Cataldo and P. Milani (Series Eds), page 199, Springer Science* (2013).
10. J.A. Pople, *Trans. Farad. Soc* 49, 1375 (1953); R. Pariser and R.G. Parr, *J. Chem. Phys.* 21, 466 (1953).
11. K. Gundra and A. Shukla, *Comp. Phys. Commun* 183, 677, (2012).
12. B. Sahu, H. Min, A. H. MacDonald and S. K. Banerjee, *Phys. Rev B*, 78, 045404 (2008).
13. K. Gundra and A. Shukla, *Phys. Rev B* 83, 075413 (2011).
14. K. Ohno, *Theor. Chim. Acta* 2 (1964) 219.
15. K. Gundra and A. Shukla, *Phys. Rev. B* 84, 075442 (2011).
16. K. Gundra and A. Shukla, *Physica B* 406, 3538 (2011).
17. T. G. Pedersen, K. Pedersen, and T. B. Kristensen, *Phys. Rev. B* 63, 201101(R) (2001).
18. Y. W. Son, M. L. Cohen, and S. G. Louie, *Nature* 444, 347 (2006).
19. H. Hsu and L. E. Reichl, *Phys. Rev. B* 76, 045418 (2007).

Growth of Single Crystal Scintillators and Development of Nuclear Radiation Detectors

Mohit Tyagi

Technical Physics Division

Dr. Mohit Tyagi is the recipient of the DAE Young Applied Scientist / Technologist Award for the year 2014

Abstract

Single crystal scintillators for nuclear radiation detection were successfully grown from the melt using the Czochralski technique. Various growth parameters were optimized to grow the crack-free single crystals. A systematic approach was adopted to investigate the effect of growth ambient and co-doping on electronic, optical and scintillation properties of the grown crystals. The defect structure of the crystals was studied and altered to obtain improved performance characteristics. The single crystal scintillators having improved performances were coupled to a PMT, photodiodes or SiPM to develop nuclear radiation detector for various applications. A portable gamma-ray spectrometer that could be powered from a USB port of a laptop was also developed by employing single crystal scintillators.

Keywords: Crystal growth, Scintillator, Radiation Detector.

Introduction

Single crystals are vital parts of the modern technology due to the combination of unique properties. They have various applications in industries including electronic, optical, medicals, sensor, nuclear etc. The single crystals of scintillating materials are very useful for radiation detectors also which have several applications, including high-energy physics, medical imaging, geological exploration, nuclear industry and national security etc. [1, 2]. Although there are many conventional scintillators which are being used in many devices, but due to increasing applications, there is continuous demand and interest in the research for new scintillators with improved performances. The characteristics of an ideal scintillator includes high density, high light yield, fast decay time, high radiation hardness, chemical and mechanical resistance, low afterglow, matching emission wavelength with photo-sensors etc. Since there is no ultimate scintillator, that fulfills all these criteria, a number of materials have been tried based on different applications. Based on the luminescence generating sites, scintillators are mainly divided in two categories; intrinsic and extrinsic. Single crystals of PbWO_4 , BaF_2 and $\text{Bi}_4\text{Ge}_3\text{O}_{12}$ (BGO) are well known intrinsic scintillators while CsI(Tl) and NaI(Tl) are commonly used extrinsic scintillators. In recent years, Ce doped single crystals have attracted the attention of many researchers due to their excellent combination of light output and decay time [3, 4]. Oxide crystals with a garnet structure have proven to be promising host materials due to their high density, broad transmission range and easy doping with rare earth elements like Ce [5, 6]. Recently, Kamada et al. have done

extensive combinatorial band gap engineering for multi component garnet compounds having chemical formula of $\text{A}_3(\text{B},\text{Al})_5\text{O}_{12}$ (where A: Gd, Y, or Lu and B: Ga, La, or Sc) [7, 8]. It was found that Ce doped $\text{Gd}_3\text{Ga}_3\text{Al}_2\text{O}_{12}$ (GGAG) crystals have promising scintillation properties [9]. These crystals have a high density of 6.7 g/cm^3 , high scintillation light output (LO) of over 60,000 photons/MeV and a fast decay time of 55 ns [10].

Various single crystal scintillators have been grown in Crystal Technology Section, Technical Physics Division. However, in this communication, we have described the growth of advance scintillator of GGAG:Ce single crystals and development of a USB based portable gamma-ray spectrometer based on these crystals.

Experimental

Single Crystal Growth

The nuclear radiation detectors require high optical quality single crystals of different dimensions. The single crystals can be grown either from solution, melt or vapor phases, depending upon material properties and dimensional requirements. Single crystals of Ce doped GGAG, having high melting temperature of 1850°C , were grown from the melt using the Czochralski technique in an automatic diameter controlled crystal puller system (Model: Oxypuller, Cyberstar). The starting charge was prepared using solid state sintering of constituent oxides Gd_2O_3 , Al_2O_3 , Ga_2O_3 in their stoichiometric molar ratio with 0.2 at% CeO_2 doping. As-prepared material in the form of pellets was loaded in a suitable crucible and heated to 50°C above its melting point to homogenize the melt. A single crystal seed (not oriented in a specific direction)

was employed to initiate the crystal growth. The growth was carried out in a stationary crucible by shifting the position of the solid-melt interface in the hot zone. A continuous flow of Ar through the closed growth chamber was maintained during the growth. The optimized parameters used for the growth of GGAG crystals are listed in Table-1.

Table-1: Crystal growth parameters.

| | | |
|--------------------------|---|-------------------------|
| Melting temperature | : | 1850°C |
| Pull rate | : | 1 mm/h |
| Rotation rate | : | 15 rpm |
| Initial chamber pressure | : | 1×10^{-5} mbar |
| Ar gas pressure | : | 1100 mbar |
| Temperature gradient | : | 30-50°C/cm |
| Cooling rate | : | 20-30°C/h |

Based on some initial results performed on the polycrystalline powders, 0.2 at% co-doping of Boron was also used to grow single crystals with improved performances. The grown crystals were cut and optically polished in the required dimensions for various measurements and fabricating the detector.

Transmission/ absorption/ reflection spectra were measured with a Shimadzu 3600 UV-VIS-NIR spectrophotometer in the range from 200 nm to 800 nm. Photoluminescence (PL) properties were measured with an Edinburgh FLP-920 Spectro-fluorometer. The spectra were corrected for the spectral response of the source, monochromator and the PMT.

Light output and energy resolution measurements were made using a pulse processing chain consisting of a photo-sensor (PMT, photodiode or SiPM), a pre-amplifier, a spectroscopic amplifier and an 8k MCA. The PMT was directly coupled to each sample using optical grease and a hemispherical Spectralon reflector to maximize the collection of light. The output of MCA was plotted in a graph to record the pulse height spectrum. The timing resolution was measured by employing timing coincidence method. The crystal was mounted on SiPM and photodiodes also to explore the possibilities of compact detectors. The scintillation decay was measured using a Tektronix digital oscilloscope.

Results and Discussions

Single crystal growth and characterization

Fig. 1 shows the photographs of single crystals of GGAG grown in initial attempts and an eventually grown crystal after optimizing the growth parameters. The crack-free crystals upto 30 mm diameter and 60 mm length have been successfully grown. More details on the crystal growth have been reported in ref. #11. X-ray diffraction pattern shown in Fig. 2 confirms the formation of single phase. The laue pattern indicates the four fold symmetry for these crystals having cubic structure. The sharpness of the image patterns also indicates the good quality of the single crystal.



Fig. 1: The photograph of GGAG:Ce crystals as grown in an initial run and after optimizing the growth parameters.

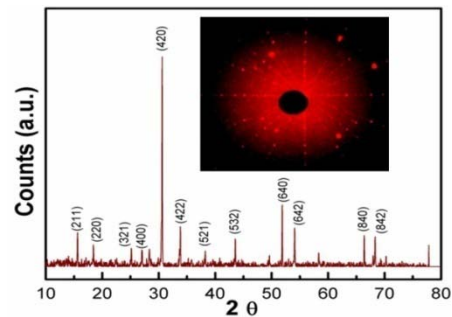


Fig. 2: XRD pattern of the grown crystal. Inset shows the Laue reflection pattern.

Fig.3 shows the transmission, excitation and emission spectra of GGAG:Ce crystal. The excitation bands corresponding to the emission at 550 nm were observed to be at 345 and 445 nm corresponding to the absorption band of Ce^{3+} ions as observed in transmission spectrum. The emission band due to the transition from the lowest excited 5d state to the ground 4f state of Ce^{3+} consists of two bands at 520 and 565 nm due to the splitting of $^4F_{5/2}$ and $^4F_{7/2}$ ground state. The emission band lies in the transmission region of the crystal and therefore indicates less self absorption problem in these crystals. Therefore large size detectors can be fabricated using this material without self-absorption. The green emission from these crystals also matches well with the efficiency of photodiodes. This matching with photodiode enabled us to fabricate compact radiation detectors that operate at significantly lower voltages compared to a PMT.

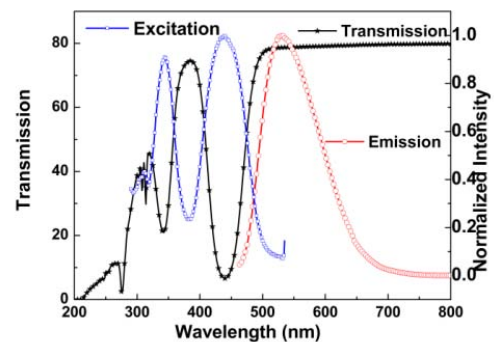


Fig. 3: Transmission, Excitation and Emission spectrum of GGAG:Ce single crystals.

The GGAG:Ce crystals gives fluorescent visible 550 nm (green) light which can be captured easily using CCD cameras as well. Therefore the possibility of using these crystals for applications in X-ray radiographic is also explored as shown in Fig. 4. The image generated due to the fluorescence of single crystal was recorded by employing a CCD based digital camera. A 500 micron mesh and integrated chip was kept in front of X-rays. Fig. 4 shows the images generated on the crystal and captured by the camera. Fig. 4a shows a bright fluorescent image of X-ray beam on the crystal disk. Fig. 4b shows an image of the 500 micron mesh. Fig. 4c and 4d show the internal structure of an integrated chip (IC) when kept between the X-ray and crystal. The bigger images can be recorded by using a divergent beam of X-ray source and a large area scintillator crystal.

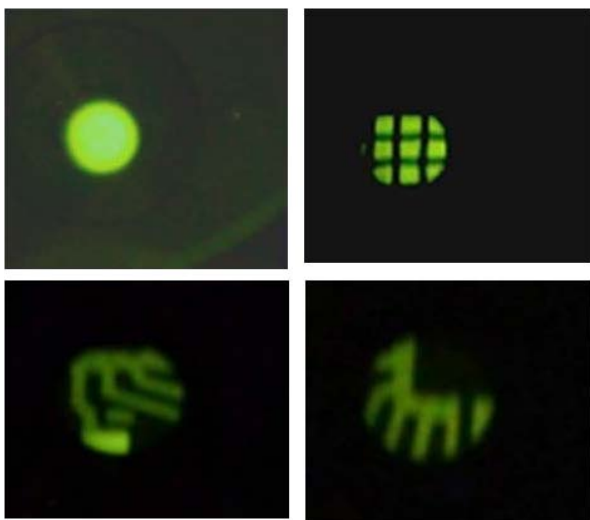


Fig. 4: The images formed on the GGAG:Ce crystal when irradiated by X-rays (a) directly (b) through a 500 micron mesh, and (c) & (d) through an IC.

Scintillation characterization

The effect of various codoping was studied systematically on the light yield of these crystals and the boron codoping was found to improve the scintillation characteristics of these crystals [9]. Further in “B” codoped crystals, the scintillation light yield measured from as-grown crystals was found to be much lower compared to the reported values. It was understood that since the crystals were grown in the Ar ambient, they are prone to have some oxygen vacancies and therefore post growth annealing treatments in air were performed to reduce the defect concentration. The after growth annealing improved the light yield and scintillation decay time significantly [11]. The details about the tailoring the defect structure to improve the scintillation characteristics are published in ref. #11. Therefore further characterization of scintillation properties were studied on GGAG:Ce,B single crystals.

Fig.5 the pulse height spectra of a ^{137}Cs gamma source measured by using GGAG:Ce,B crystal which was coupled on a compact (6 x 6 mm²) SiPM. The processed sample and the in-house made light guide to couple larger crystal with small size photo-sensors is also shown in the

inset of Fig.. The scintillation light output (LO) of the annealed crystals was found to be 57000 photon/MeV having energy resolution of 6% at 662 keV.

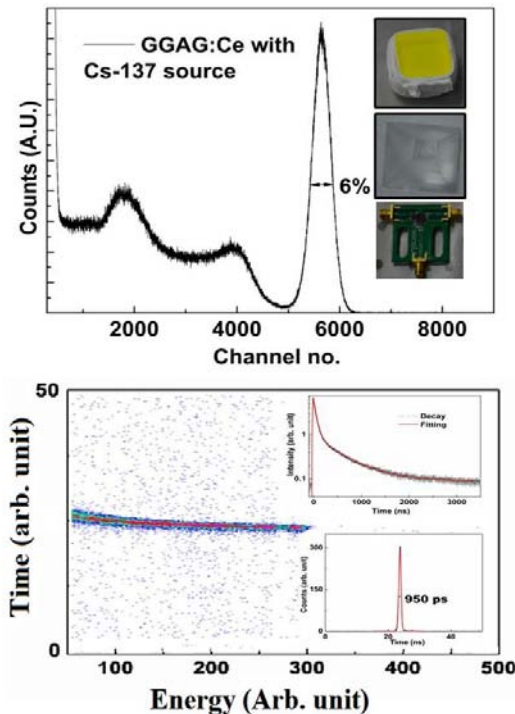


Fig. 5: Scintillation properties of GGAG crystal (a) Pulse height spectrum of a Cs-137 source recorded with SiPM using a light guide as shown in the inset (b) Scintillation decay and Coincidence timing resolution.

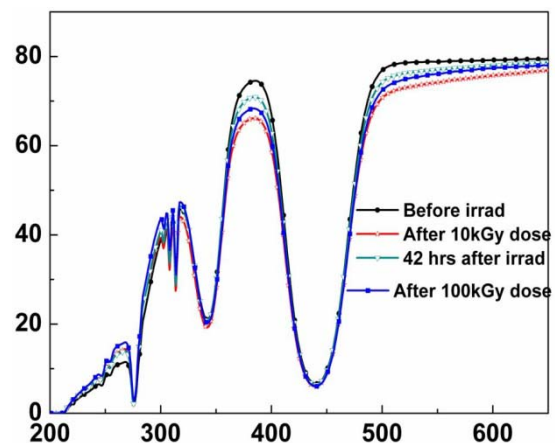


Fig. 6: The effect of irradiation on transmission of GGAG crystal.

The major component of the scintillation decay time was measured as 55 ns (Fig.5b). The coincidence resolution for Co-60 source was measured to be 950 ps for GGAG-PMT detector and 12 ns for compact GGAG-Si(PIN) detector setup. These values are much better in comparison to the CsI(Tl) crystals which are commonly used in timing applications with photodiode[12].

The crystals were found to be radiation hard up to 100kGy irradiation as shown in fig. 6. The slight degradation in

transmission due to irradiation could be found to be restored at room temperature only without annealing treatment [13].

A USB powered detector Setup

After systematic investigations of the performance characteristics of the crystals, a detector setup was developed based on these crystals. A GGAG:Ce crystal sample with dimensions as $18 \times 18 \times 10 \text{ mm}^3$ was cut from the annealed crystal. One surface was optically polished and coupled to a PMT having an active area of 1 inch diameter. The PMT output was given to a pulse processing assembly consisting of a pre- Amp, a shaping amp and an 8k MCA. The power to all the components including HV to PMT was provided from a single USB port by employing necessary DC-DC converters. It made the whole set-up portable and convenient to use with a laptop as shown in Fig.7. The data processing was carried out by the Amptek DppMCA software. The setup was calibrated using Cs-137 and Co-60 gamma sources and the performance was checked using sources of various other radio-active isotopes. The parameters like shaping time of spectroscopic amplifier, PMT voltage and gain were optimized to get the well resolved pulse height spectrum. An energy resolution of about 4% has been achieved at 1332 keV gamma-ray from a Co-60 source, as shown in Fig.7.



Fig. 7: A USB based gamma-ray spectrometer developed using a GGAG crystal.

CONCLUSIONS

Single crystals of Ce doped $\text{Gd}_3\text{Ga}_3\text{Al}_2\text{O}_{12}$ crystals were successfully grown for gamma detection. The various characteristics of these crystals were investigated in details. $\text{Gd}_3\text{Ga}_3\text{Al}_2\text{O}_{12}:\text{Ce}$ crystals grown in argon ambient have defects related to oxygen vacancies which could be eliminated by a post growth annealing treatment of the grown crystals. The light output and energy resolution were improved after annealing the crystal in air. After optimizing the scintillation parameter of the crystal, a portable detector has been fabricated which could be coupled to a USB based electronic set-up that does not need bulky high voltage power supplies or other NIM modules.

References

- [1] Dujardin, C., et al., Optical and scintillation properties of large crystals. *Journal of Physics: Condensed Matter*, 1999. 10(13): p. 3061.
- [2] Melcher, C., Perspectives on the future development of new scintillators. *Nuclear Instruments and Methods in Physics Research Section A: Accelerators, Spectrometers, Detectors and Associated Equipment*, 2005. 537(1): p. 6-14.
- [3] Balcerzyk, M., et al., Future hosts for fast and high light output cerium-doped scintillator. *Journal of Luminescence*, 2000. 87: p. 963-966.
- [4] Baryshevsky, V., et al., Spectroscopy and scintillation properties of cerium doped YAlO_3 single crystals. *Journal of Physics: Condensed Matter*, 1999. 5(42): p. 7893.
- [5] Greskovich, C.D., et al., High speed, radiation tolerant, CT scintillator system employing garnet structure scintillators, 1991, Google Patents.
- [6] Drury, O.B., et al. Garnet scintillator-based devices for gamma-ray spectroscopy. in *Nuclear Science Symposium Conference Record (NSS/MIC)*, 2009 IEEE.
- [7] Atrata, R., P. Schauer, and J. Kuapil, A single crystal of YAG-new fast scintillator in SEM. *Journal of Physics E: Scientific Instruments*, 2001. 11(7): p. 707.
- [8] Kamada, K., et al., Composition Engineering in Cerium-Doped $(\text{Lu,Gd})_3(\text{Ga,Al})_5\text{O}_{12}$ Single-Crystal Scintillators. *Crystal Growth & Design*, 2011. 11(10): p. 4484-4490.
- [9] Mohit Tyagi, et al., "Effect of codoping on scintillation and optical properties of Ce doped $\text{Gd}_3\text{Ga}_3\text{Al}_2\text{O}_{12}$ scintillators" *J. Phys. D: Appl. Phys.* 2013 46 475302 (12pp)
- [10] Samuel B. Donald, et al. "The Effect of B and Ca Co-Doping on Factors Which Affect the Energy Resolution of $\text{Gd}_3\text{Ga}_3\text{Al}_2\text{O}_{12}:\text{Ce}$ ", *IEEE Trans. Nuc. Science* 60 (2013) 4002-6.
- [11] "Improvement of the scintillation properties of $\text{Gd}_3\text{Ga}_3\text{Al}_2\text{O}_{12}:\text{Ce,B}$ single crystals having tailored defect structure" M. Tyagi, A.K. Singh, S.G. Singh, D.G. Desai, G. D. Patra, S. Sen and S.C. Gadkari, *Phys. Stat solidi-Rapid Research Letter*; 9 (2015) 530-534.
- [12] "Timing characteristics of Ce doped $\text{Gd}_3\text{Ga}_3\text{Al}_2\text{O}_{12}$ single crystals in comparison with CsI(Tl) scintillators" M. Tyagi, V. V. Desai, A. K. Singh, S. G. Singh, S. Sen, B. K. Nayak, and S. C. Gadkari, *Phys. Stat solidi A*, 212 (2015) 2213-18.
- [13] "Effect of Co-doping On the Radiation Hardness of $\text{Gd}_3\text{Ga}_3\text{Al}_2\text{O}_{12}:\text{Ce}$ Scintillators" Mohit Tyagi, Fang Meng, Merry Koschan, A.K. Singh, Charles L. Melcher, and S. C. Gadkari, *IEEE Trans. Nuc. Science* 62 (2015) 336-339.

Recovery of uranium from Tummalapalle leach solution using novel precipitating method

Sujoy Biswas

Uranium Extraction Division

Dr. Sujoy Biswas is the recipient of the DAE Young Applied Scientist / Technologist Award for the year 2014

Abstract

The recovery of uranium from carbonate ore leach solution was studied using novel precipitation method. The uranium ore leached using $\text{Na}_2\text{CO}_3/\text{NaHCO}_3$ was recovered as magnesium di uranate (MDU) with excess NaOH in presence of trace amount of Mg^{2+} . The overall uranium recovery of the process was 97% with improved particle size ($\sim 57 \mu\text{m}$). Based on the experimental findings, a process flow-sheet has been developed for the recovery of uranium from carbonate ore leach solution with a uranium concentration of $< 1 \text{g/L}$.

Key Words: Uranium, Carbonate ore, MDU, Tummalapalle, Precipitation

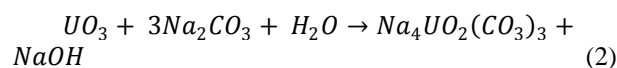
Introduction

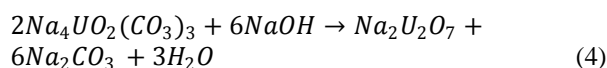
Nowadays nuclear power becomes an important resource of energy worldwide due to its several advantages over conventional energy sources [1,2]. In the development Nuclear Energy Programme, the uranium plays an important role as it is used as a primary nuclear fuel in nuclear reactor [2,3]. The sustainability of Nuclear Power Program depends on the availability of natural uranium in the front-end of nuclear fuel cycle along with established nuclear technology. In a country like India, only 3% of the total energy comes from the nuclear sources [4]. Considering shortage in the availability of fossil fuels and other resources of energy, the nuclear power may play as a big contributor in the total energy production of the country in near future. To meet such nuclear energy requirement, there is a need for constant supply of natural uranium which will come from various resources including lean sources like carbonate ore situated at Tummalapalle, India [5, 6]. The Tummalapalle has a vast deposit of uranium as carbonate ore in the host rock of alkali (dolomite and calcite) containing 0.048 % U_3O_8 and hence considered as lean resource of uranium [7-8]. The chemical composition of Tummalapalle ore was given in Table 1 [8, 9]. The recovery of uranium from such lean source becomes a challenge to the scientist and technologist working in the field of separation science and technology due to non availability of suitable recovery technique [5]. Generally, leaching of uranium from carbonate ore, Tummalapalle was carried out using alkali ($\text{Na}_2\text{CO}_3/\text{NaHCO}_3$) leaching process in an autoclave at high temperature and pressure [7-10]. The

Table 1: Mineralogical composition of the Tummalapalle uranium ore sample

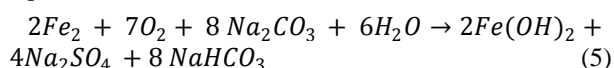
| Mineral | % Weight |
|--|----------|
| Carbonates | 83.2 |
| Quartz + feldspar | 11.3 |
| Apatite | 4.3 |
| Pyrite | 0.47 |
| Chalcopyrite | 0.05 |
| Galena | Traces |
| Magnetite | 0.15 |
| Ilmenite + leucoxene | 0.25 |
| Iron hydroxide (goethite) | 0.27 |
| Pitchblende in association with pyrite | 0.1 |
| Total | 100.0 |

uranium from leach liquor was precipitated as sodium di uranate (SDU) in presence of excess NaOH at $\sim 50-55$ °C. The chemical reactions involving leaching and precipitation of uranium from Tummalapalle ore are given by the following chemical reactions:





The pyrites and other sulphide minerals are also oxidized to sodium sulphate and solubilized in leach liquor during the alkali pressure leaching according to the following equations:



The literatures reports indicate that, the uranium concentration in feed solution must be above 1.2 g/L for complete uranium precipitation using excess NaOH and the precipitate obtained has very small average particle size (7-9µm) which creates problem during filtration. Currently, the uranium concentration in the carbonate leach liquor is < 1g/L and it is impossible to recover all uranium from such lean leach solution using existing processes. Considering the importance of uranium and its vast deposit in Tummalapalle ore, it is important to develop an efficient, alternate precipitation method for recovery of uranium from such carbonate ore leach solution. The present study deals with the development of a new efficient precipitation method for uranium recovery from Tummalapalle ore leach solution containing 0.74 g/L U in feed solution. Based on the experimental results a process flow-sheet has been proposed for recovery of uranium from Tummalapalle carbonate ore leach solution using MgSO₄ as a coagulant in presence of NaOH.

Experimental

Reagents and chemicals

Sodium Hydroxide (A.R. grade, 99% pure), Magnesium Oxide (Industrial grade), Magnesium Sulphate (L.R. grade 98% pure), poly vinyl chloride (E-Merk, > 97% pure), Tetrahydrofuran (E-Merk, > 97% pure) were used without any further purification. The alkaline ore leach solution containing 0.74 g/L U was obtained from Uranium Corporation of India Limited, Tummalapalle, India. All the other reagents used in the experiments were of A.R. grade. **Table 2&3** showed the specification of alkaline ore leach solution used throughout the experiments.

Table 2: Major composition of ore leach solution

| Parameter | Value |
|-------------------------------|------------|
| [U] | 0.74 g/L |
| pH | 9.1 |
| Specific gravity | 1.14 |
| TDS | 154.72 g/L |
| SO ₄ ²⁻ | 69.66 g/L |
| CO ₃ ²⁻ | 13.79 g/L |
| HCO ₃ ⁻ | 18.23 g/L |
| F- | 16 µg/mL |

Table 3: Elemental composition of ore leach solution

| Elements | Concentration, µg/mL | (4) |
|----------|----------------------|-----|
| Fe | 12 | |
| Al | 31 | |
| Cr | <1 | |
| Mg | 10 | |
| Mn | (5) <1 | |
| Ni | <1 | |
| B | 12 | |
| Cd | <0.12 | |
| Co | <0.12 | |
| Ce | <0.12 | |
| Sm | <0.12 | |
| Gd | <0.12 | |
| Dy | <0.12 | |
| Sr | <0.12 | |
| Eu | <0.12 | |
| Y | <0.12 | |
| Yb | <0.12 | |

Instruments

Inductively Coupled Plasma Optical Emission Spectrophotometer (ICP OES, Model No. JY 238) was used for determination of uranium and other trace impurities in various samples. Laser Diffraction Particle Size Analyzer from CILAS (Model No. CILAS 1064 Liquid) was used for particle size analysis of uranium precipitate. A Thermo-Orion make pH meter containing Ross make glass electrode was used to monitor pH of the solution.

Experimental procedure

The uranium precipitation from carbonate leach solutions was investigated at different experimental conditions to obtain best suitable condition. The concentration of U(VI) in carbonate leach liquor was kept constant at 0.74 g/L. The precipitation reaction was carried out in batch mode in 5 L glass reactor containing 4 L carbonate leach solution. The glass reactor contains a marine type 3 bladed propeller for mixing of solution, constant temperature heater, thermocouple, digital temperature controller. The addition of chemicals such as MgO, MgSO₄ etc. were carried out in solid form in the leach liquor whereas addition of alkali (NaOH) was carried out in slurry mode. The solution mixture was stirred at constant r. p. m (300) for a period of 1 hour. The 5 mL samples were withdrawn from the glass reactor with the help of glass pipette at different time intervals for checking the pH and uranium concentration of the solution. The completion of the reaction was assured by checking the concentration of uranium in the filtrate. After completion of precipitation reaction, the

uranium slurry was filtered under vacuum and cake was dried in an oven at 110 °C.

Results and discussions

The precipitation of uranium from carbonate ore leach solution was investigated in presence of $MgSO_4$ for recycling the excess reagents $Na_2CO_3/NaOH$ in the leaching step. Variation of NaOH as well as temperature showed that only at 50 g/L NaOH concentration, above 55 °C, the uranium was precipitated as MDU in presence of $MgSO_4$. Further, it was observed that 1g/L $MgSO_4 \cdot 7H_2O$ is required for effective recovery of uranium (97%) from carbonate leach solution containing 0.74 g/L U. The Mg^{2+} acts as a coagulant for uranium precipitation even in the carbonate /bicarbonate medium in presence of excess NaOH. The uranium precipitated as MDU has improved particle size distribution with the mean particle diameter of 57 μm (Table 4). The MDU precipitate was filtered and washed with hot water to remove any carbonate, bicarbonate and sulphate present as impurities. The MDU was dried at 110 °C in an oven and analyzed for % uranium content and % un-dissolved after dissolving in HNO_3 medium. It was found that, the MDU cake contained 50% uranium with less than 1% un-dissolved substance (Table 5). The Filtrate from filtration of MDU cake was subjected to freeze crystallization to remove sulphate as solid Na_2SO_4 at 0 °C temperature. After freeze crystallization, the solution was analyzed for Mg^{2+} content for five consecutive batches and it was found that the Mg^{2+} concentration in every case was < 0.5 $\mu g/mL$. Since the filtrate after Na_2SO_4 removal contains only Na_2CO_3 and NaOH, the reagent (filtrate) can be recycled for leaching of uranium after passing CO_2 and adjusting proper composition of leaching agent.

Table 4: Particle size analysis of MDU cake prepared from carbonate leach solution using NaOH/ $MgSO_4$; $MgSO_4 \cdot 7H_2O$: 1 g/L; T: 55 °C; NaOH: 50 g/L; Stirring speed: 300 r.p.m; $[U]_{feed}$: 0.74 g/L.

| | |
|-----------------|----------------|
| Diameter at 10% | 20.91 μm |
| Diameter at 50% | 52.52 μm |
| Diameter at 90% | 103.05 μm |
| Mean diameter | 57.47 μm |

Table 5: Analysis of MDU cake prepared from carbonate leach solution using NaOH/ $MgSO_4$; $MgSO_4 \cdot 7H_2O$: 1 g/L; T: 55 °C; NaOH: 50 g/L; Stirring speed: 300 r.p.m; $[U]_{feed}$: 0.74 g/L.

| % U (dry basis) | % Un-dissolved |
|-----------------|----------------|
| 50 | <1 |

Process flow-sheet for uranium recovery

Based on experimental results an optimized process flow-sheet has been proposed for recovery of uranium from carbonate leach solution containing < 1 g/L U (Figure 1). The carbonate ore containing uranium was crushed and ground and the ground ore was taken in a leaching tank containing $Na_2CO_3/NaHCO_3$ mixture as leaching reagents. The leaching of uranium was performed under high pressure and temperature (140 °C). After leaching reaction was over, the solid –liquid separation was performed where leach liquor containing uranium was separated from solid residue. The pH of the leach liquor was ~9 with a uranium concentration of 0.74 g/L. In a precipitation reactor, 1g/L $MgSO_4 \cdot 7H_2O$ was added in solid state in leach liquor with constant stirring. The solution was heated up to 55 °C and excess NaOH slurry was added to it with constant stirring. The solution was left as it is for a period of 1 hour to complete the precipitation. The uranium in presence of NaOH/ $MgSO_4$ mixture was precipitated as MDU cake with large particle size (mean particle diameter ~57 μm). Further, the MDU cake was filtered and washed with hot water to get pure MDU cake which was dried at 110 °C. On the other hand, filtrate containing excess NaOH, Na_2CO_3 and Na_2SO_4 need to be separated for further reuse. The filtrate after precipitation undergoes freeze crystallization where Na_2SO_4 was removed as solid cake. Now the filtrate containing excess NaOH and Na_2CO_3 can be recycled for leaching as $Na_2CO_3/NaHCO_3$ after passing CO_2 through the solution.

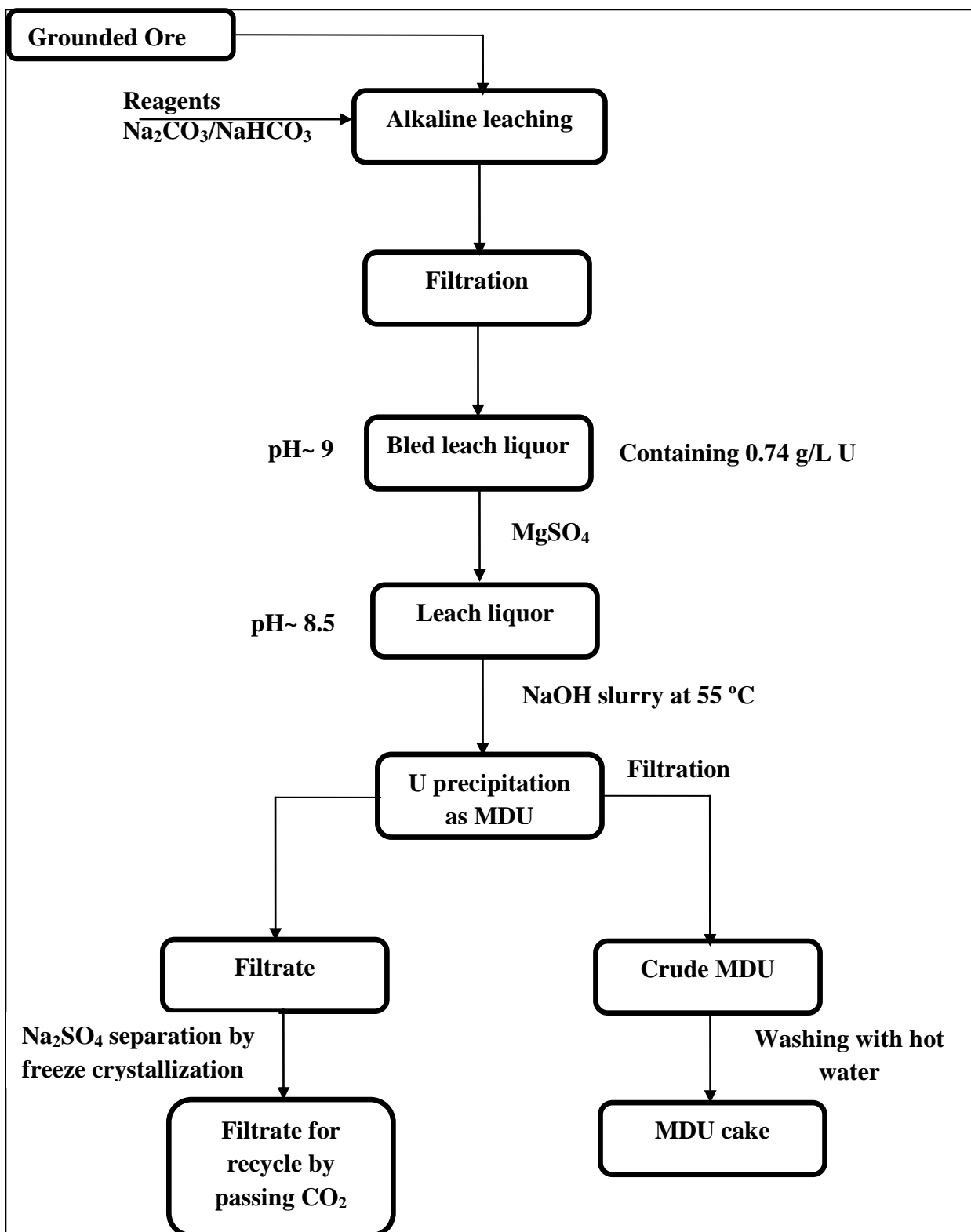


Figure 1: Process flow-sheet for the recovery of uranium from carbonate ore (Tummalapalle, India) leach solution using NaOH/MgSO₄ mixture

Conclusions

Recovery of uranium from carbonate ore leach solution containing 0.74 g/L U was studied using excess NaOH in presence of Mg^{2+} . The precipitation of uranium from carbonate leach solution was also possible without addition of any acid when NaOH was used as precipitating agent and $MgSO_4$ as a coagulant at high temperature (50-55 °C). With increase in Mg^{2+} concentration in the medium, there is an increase in particle size of MDU during precipitation. Based on the experimental findings, a process has been finalized for uranium recovery from Tummalapalle carbonate ore leach solution using NaOH/ $MgSO_4$ mixture at 55 °C. The MDU cake contains 50 % U and filtrate can be recycled in uranium leaching after separation of sulphate as solid Na_2SO_4 using freeze crystallization.

Acknowledgement

The authors are highly thankful to Dr.S.B. Roy, Director, Chemical Engineering Group for her keen interest and encouragement during the course of this work. Authors are thankful to K.N. Hareendran and Shri, V.H. Rupawate/QCS/UED for providing analytical help and Shri. S. Manna, SO (F), UED for making available reactor for precipitation experiments.

References

1. B. Bhattacharjee, An overview of R&D in fuel cycle activities of AHWR, 14th Indian Nuclear Society Annual Conference (INSAC), IT-1 (2003) 1-27.
2. T.K. Mukherjee, H. Singh, 14th Indian Nuclear Society Annual Conference (INSAC), IT-7 (2003) 1-9.
3. A. Kakodkar, Evolving Indian Nuclear Power Programme: Rationale and Perspective, Nuclear India, 41 (11-12) (2008).
4. Integrated Energy Policy: Report of the Expert Committee. Planning Commission Document, Government of India, (2006) p.1-147.
5. N.P.H, Padmanabhan and A. K. Suri, Challenges in augmenting the uranium supply position in India, International Seminar on Mineral Processing Technology ((MPT-2007), Mumbai, India, pp 3-18.
6. A.K. Rai, S. Zakaulla, AnjanChaki, Proterozoic stratabound carbonate rock (dolostone) hosted uranium deposits in Vempalle formation in Cuddapah basin, India, International Symposium on Uranium Raw Material for the Nuclear Fuel Cycle (URAM-2009) 22-26 June 2009, Vienna, Austria.
7. A.K. Suri, Uranium Processing-A New Alkaline Route, Transaction of Indian Institutes of Metals, 61 (1) (2008).
8. A.K. Suri, S.K. Ghosh and N.P.H, Padmanabhan, Recent pilot-plant Experience On Alkaline Leaching of low Grade Uranium Ore in India, International Symposium on Uranium Raw Material for the Nuclear Fuel Cycle (URAM-2009) 22-26 June 2009, Vienna, Austria.
9. A.K. Suri, T. Sreenivas, Developments in processing of conventional uranium ore resources of India, 6th International Mineral Processing Conference (IMPC), New Delhi, India, October, 2012.
10. A.K. Suri, N.P.H. Padmanabhan, T. Sreenivas, K. Anand Rao, A.K. Singh, K.T. Shenoy, T. Mishra, S.K. Ghosh, Process development studies for low-grade uranium deposit in alkaline host rocks of Tummalapalle, Presented at IAEA Technical Meeting on low-grade Uranium Deposits at Vienna, 29-31 March, 2010.
11. S. Bachmaf, B. Planer-Friedrich and B.J. Merckel, Radiochim. Acts. 96 (2008) 359-366.
12. B. Tomazic, M. Samarzija, J. Inorg. Nucl. Chem. 31 (1969) 1771-1782.
13. B. Tomazic, M. Branica, J. Inorg. Nucl. Chem. 34 (1972) 1319-1332.
15. R.M. Rush, J.S. Johnson and K.A. Kraus, Inorg. Chem. (1) (1962) 378
16. B. Tomazic, M. Branica and B. Tezak, Croat.Chem. Acta. 34 (1962) 41

Design of a Permanent Magnet Based Focusing Lens for a Miniature Klystron

Kumud Singh, Janvin Itteera and Sanjay Malhotra

ACnD

Smt. Kumud Singh is the recipient of the DAE Young Applied Scientist / Technologist Award for the year 2014

Abstract—Application of Permanent magnet technology to high frequency miniature klystron tubes to be utilized for space applications improves the efficiency and operational reliability of these tubes. But nevertheless the task of generating magnetic focusing forces to eliminate beam divergence once the beam crosses the electrostatic focusing regime and enters the drift region in the RF section of the tube throws several challenges. Building a high quality magnet focusing lens to meet beam optics requirement in cathode gun and RF interaction region is considered to be one of the critical issues for these high frequency miniature tubes. In this paper, electromagnetic design and particle trajectory studies in combined electric and magnetic field for optimizing the magnetic circuit using 3D Finite element method (FEM) analysis software is presented. A rectangular configuration of magnet was constructed to accommodate apertures for input and output waveguide sections and facilitate coupling of electromagnetic fields into input klystron cavity and out from output klystron cavity through coupling loops. Prototype lenses have been built and have been tested after integration with the klystron tube. We discuss the design requirements and challenges, and the results from beam transmission of the prototype lens.

Keywords— Beam transmission, Brillouin, confined flow, Miniature Klystron.

INTRODUCTION

One of the major challenges associated with beam focusing of high intensity space charged electron beam in high frequency miniature klystron tubes is achieving high field intensity in constrained longitudinal and transverse dimensions. Achieving high beam filling factor in millimetre scale drift tube aperture and shielding requirements for reducing beam boundary oscillations in cathode gun region further aggravates the design complexity.

Beam boundary oscillations in a linear beam tube are governed by Busch's theorem and Gauss's law [1]. At the beam boundary where $r = b$, the electric field, $Er(b)$, is given as

$$Er(b) = \frac{\eta I}{2\pi\mu_0\epsilon_0} \quad (1)$$

The relation given below represents the motion of the electrons on the outer edge of the beam under the influence of electric and magnetic fields:

$$b'' + b\omega_L^2 \left[1 - \left(\frac{B_C b_c^2}{B b^2} \right)^2 \right] - \frac{\eta I}{2\pi i \mu_0 \epsilon_0} = 0 \quad (2)$$

If we let,

$$a = \frac{1}{B} \left(\frac{2I}{\eta \pi \mu_0 \epsilon_0} \right)^2 \quad (3)$$

Using the equilibrium radius beam equation can be written as,

$$\frac{b''}{a} + \omega_L^2 \left[\frac{b}{a} \left(1 - \left(\frac{B_C b_c^2}{B b^2} \right)^2 \right) - \frac{a}{b} \right] = 0 \quad (4)$$

where,

Table 1: Symbol Notations for equation (1), (2), (3) and (4)

| Symbol | Quantity |
|--------------|--|
| ω_L | Larmor frequency, = $\omega/B/2$ |
| I | Beam current |
| B_C | Flux density at cathode position |
| B | Actual Flux density = mB_B for confined flow |
| m | Confinement factor |
| B_B | Brillouin Flux density |
| μ_0 | Free space permeability |
| ϵ_0 | Free space permittivity |
| η | Charge to mass ratio; $\bullet = e/m$ |
| a | equilibrium radius for a Brillouin Beam |

The first term is proportional to the radial acceleration and, therefore, to the radial force on the electrons. When the space charge and centrifugal forces causing the beam to expand are equal and opposite to the magnetic focusing forces that compress the beam, the beam is in equilibrium and there are no forces causing it to expand or contract. Because of high sensitivity of beam to misalignments and RF perturbations, confined flow focusing is a preferred method for majority of klystrons [1],[2]. The primary benefit of confined flow focusing is that beam control is significantly better than Brillouin focusing. It is often convenient to refer the actual flux density used for focusing, B , to the Brillouin value, B_B , by a confinement factor m , where $B = m B_B$. In confined flow focusing, a limited amount of magnetic flux passes through cathode gun region and thus the motion of electron beam is governed by both electrostatic as well as magnetostatic forces in this region. An optimized value of cathode flux prevents translaminal electrons from crossing or coming close to the beam axis and improves the laminarity of the beam.

In the present case, a partially shielded permanent magnet focusing lens is designed with a confinement factor of 2.

A rectangular configuration of PM based lens of 130mm x 65mm transverse dimensions (perpendicular to tube axis) was designed to produce an axial magnetic field of 0.34 T in the RF section of the miniature klystron tube. It was integrated with the miniature klystron tube and tested for its beam transmission efficiency. Deviations from the circular configuration of magnet arrangement lead to the asymmetric field configuration in the cathode gun region and increases design complexities.

Alignment of the subcomponents in the high frequency tubes also demands tight tolerances. If the axis of the electron beam is not aligned with the axis of the magnetic field which could happen if the electron gun was misaligned during tube fabrication. The gun axis could be either off center or tilted with respect to the axis of the tube. Other causes for misalignment include errors in cathode, grid, or control electrode deposition or non-uniformities in magnetic pole piece material. The result of beam misalignment is that the entire beam spirals about the magnetic field axis at the cyclotron frequency. [2]

Electromagnetic Analysis and Simulations

Electron gun simulation studies – Space charge analysis

‘3D SCALAspace charge’ software has been used for estimation of beam current by thermionic emission from cathode surface. Work function and temperature of the cathode surface were defined for calculation of emission current density by applications of child’s law. Fig 1 shows the electron gun model consisting of cathode (red), BFE (green) and anode (yellow) for space charge analysis.

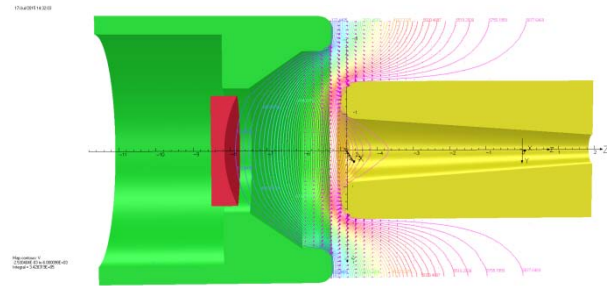


Fig1: 3D SCALA model for electron gun of miniature klystron [Electric potential (V) distribution]

Magnetostatic Simulations

‘3D TOSCA magneto statics’ software has been used for estimation of magnetic field pattern for a permanent magnet solenoid lens. Full model of the focusing lens is solved and Dirichlet boundary condition is applied to arrive at the solution.

Axially magnetized block magnets of trapezoidal shape placed in a particular configuration in aluminum housing, generate the desired axial magnetic field in the beam aperture. Trapezoidal shaped magnets were chosen to increase the magnetic volume when placed in a polar array. End flanges, made out of soft magnetic steel, shape the field distribution along the beam line and also provide the requisite radial fields at the entrance and exit of the RF interaction region. The end flanges mate with the inherent pole pieces brazed on to the cavity at both ends of the RF interaction region [4]. Cover shields are designed to limit the fringe magnetic field in the cathode gun and collector region. Special care in the design of the shield ensured that the electron beam from its inception at the cathode to its end at the collector does not encounter a field reversal in the direction of the axial magnetic field. This is important in case of permanent magnet based design of solenoid focusing systems, as axial magnetic field reverses its direction twice along its travel in the axial direction. End flanges and shield design need to ensure that the field reversal regions are outside of the beam interaction region [4]. Optimization studies have been performed to maximize the magnetic field intensity in the focusing lens aperture by varying the profile of the soft magnetic steel flanges. Outer dimension of the focusing lens is constrained throughout the design of the magnet assembly. Shield dimensions are optimized for desired magnetic flux intensity in cathode gun and the collector region.

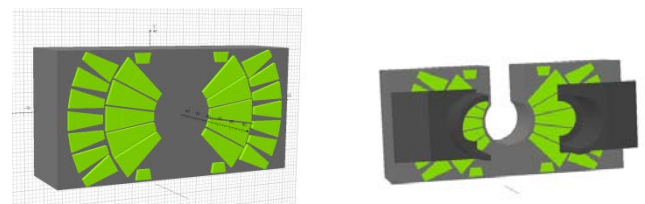


Fig 2: (a) Permanent magnet assembly housed in an aluminium casing, (b) Permanent magnet assembly with soft magnetic steel

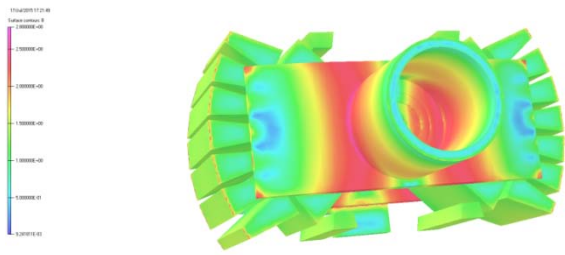


Fig 3: 3D TOSCA Magneto static Model for Permanent magnet focusing lens for miniature Klystron (surface B field plot)

A permanent magnet focusing lens assembly with a partially shielded gun region is designed and developed to produce an axial peak field of 0.34T in the magnet aperture. High energy density rare earth magnets have been used in the design of this solenoid to reduce the magnet volume. Magnet sprocket is inserted from top of the Klystron tube. An alignment tube is mounted on the body of the klystron tube to guide the sprocket and align its axis with the tube. Soft iron flanges are slid from sides and axially aligned with the inherent pole pieces on gun and collector side. Special jigs were fabricated to assemble and guide the soft iron flanges in place. Fig 4 shows simulated values of axial magnetic field profile for the magnet assembly with and without shield. Addition of the shield reduces the peak axial field obtained in the magnet aperture, but shifts the field reversal point away from the beam interaction zone.

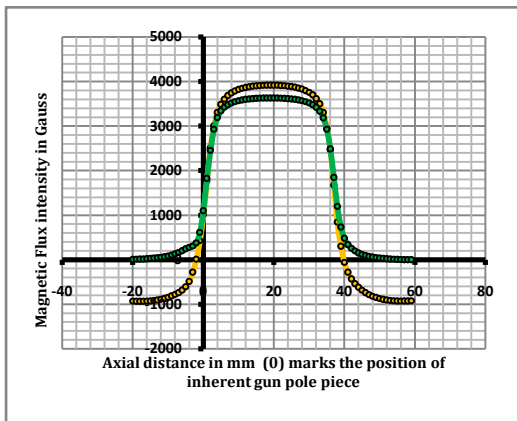


Fig. 4. Magnetic field profile along the longitudinal axis of the miniature Klystron ('0' position marks the inherent gun pole pieces position). Yellow line indicates the B field profile without shield and green line indicates the profile with shield on Gun and collector side

Particle trajectory simulations in combined Electric and magnetic fields

In engineering analysis and design of electromagnetic coupled systems, many phenomena have to be considered in order to predict a technical device's behavior realistically. In order to tackle the physical interactions, the study of the coupled problems is an

important step. Multi-physics simulations using 3D FEM program OPERA-3D were carried out for study of beam behavior in combined electrostatic and magnetostatic fields for miniature Klystron tube [5].

Combined field tracking is used analyze the beam behavior under influence of combined electric and magnetic fields. The electron beam current is calculated in an iterative fashion using Child's law to simulate electron emission off the cathode using FEM electron gun program OPERA-3D/SCALA. The output of the 3D FEM magnetostatic/TOSCA is a table of magnetic fields on all the points/nodes in the solution region [5]. The results of the magnetostatic solver are coupled to electron gun program and the final output is a six dimensional phase space matrix. The six dimensions are specified by the particle's x, y, z position as well as its vx, vy, vz relativistic velocity components. Beam current was calculated at various points in the RF interaction region and collector region and percentage transmission was calculated with respect to the injected current at the exit of thermionic cathode.

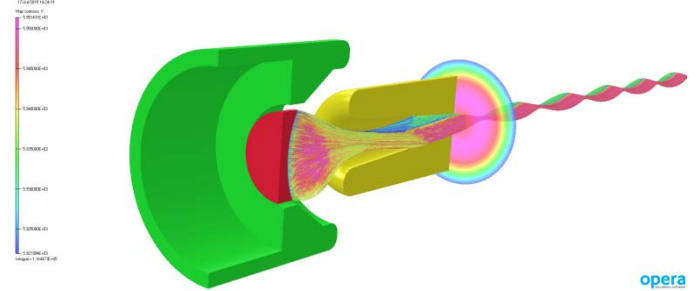


Fig. 5. Particle trajectory under the influence of combined electric and magnetic fields. Current values at required axial locations are calculated by intersecting trajectories with a polar patch.

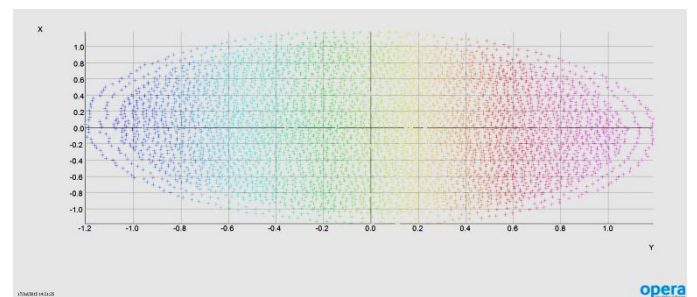


Fig. 6. Beam profile in X-Y plane at the exit of RF interaction region (in the collector region)

Beam Transmission Results

Constructed magnet assembly was integrated with the miniature klystron tube and tested for its beam transmission efficiency [3]. 85% transmission was achieved at full beam energy of 5.6KeV. Deviations from the circular configuration of magnet arrangement lead to the asymmetric field configuration in the cathode gun region increases design complexities. To limit the beam boundary oscillations in the transition region when the

beam leaves the electrostatic focusing regime and enters the drift region in the RF section some amount of shimming is incorporated in the magnetic field profile. The shimming field obtained by few extra magnets in the gun and the collector region nullifies imbalance in the field which hinders with the un-intercepted beam travel through the drift tube. Best beam transmission is achieved when the tube is aligned properly with the magnet sprocket. Alignment is one of the most critical issues in the miniature klystron tubes due to spatial constraints. In the rectangular magnet configuration it was observed that shimming action at a particular energy does not lead to same beam transmission at all beam energies. Various test configurations were tried to study the effect of shimming magnets on the beam transmission.



Fig. 7. Prototype miniature klystron tube integrated with developed magnet assembly

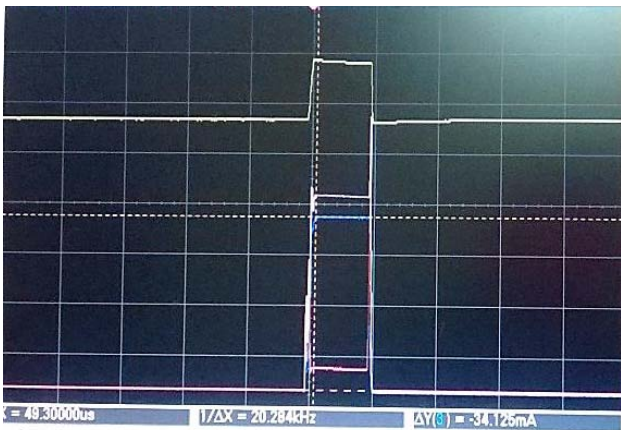


Fig 8. Transmitted current snapshot at Beam energy of 5KeV

Conclusion

The proto-type Permanent magnet focusing lens was integrated with prototype miniature klystron tube and 85 % beam transmission was achieved [3]. Further studies are in progress to find out the action and influence of shimming magnets on higher order harmonics in the primary field. Combined field studies for particle trajectory will be used in future to predict the location and size of shimming magnets. The beam absorbed in

the collector is considered to play a vital role in the RF power amplification at the output cavity. For better power efficiency, the entire beam needs to be rendezvous with the collector after transferring the energy to the output cavity. R&D efforts are being directed towards increasing the beam transmission above 90%.

Table 2 : Summary of the beam transmission results on miniature klystron tube integrated with Permanent magnet focusing lens

| Beam Energy (KeV) | Transmitted current (KeV) | Total current (mA) | % Transmission |
|-------------------|---------------------------|--------------------|----------------|
| 2 | 36 | 40 | 90 |
| 3 | 68 | 73 | 93.15 |
| 4 | 103 | 110 | 93.68 |
| 5 | 143 | 154 | 92.8 |
| 5.6 | 153 | 180 | 85 |

Acknowledgment

The authors would like to thank Shri Chandra Kant. Pithawa, Director, EIG and Dr. Chandra Shekhar, Director CSIR-Central Electronics Engineering Research for their constant motivation and encouragement.

References

1. S. Gilmour, Jr., "Klystrons, Travelling Wave Tubes, Magne-trons, Crossed-Field Amplifiers, and Gyrotrons" 2011 ARTECH HOUSE, pp.133-199.
2. S.I. Molokovsky A.D. Sushkov, "Intense Electron and Ion Beams" Springer Berlin Heidelberg New York, vol. A247, pp. 175-197, May 2005.
3. Joshi, L.M. ; Pal, D. ; Kant, D. ; Ratan, S. ; Choudhury, A.R. ; Jindal, V. ; Jangid, S. ; Sharma, S. ; Meena, R. ; Nangru, S.C. ; Sharma, R.K. ; Sharma, S.M. ; Arya, S., "Development of a 300W peak power J-band klystron," Vacuum Electronics Conference (IVEC), 2010 IEEE International.
4. Y. Fuwa, Y. Iwashita, H. Tongu, S. Ushijima, Kyoto University, Uji, Kyoto, Japan, "PERMANENT MAGNET FOCUSING SYSTEM FOR KLYSTRONS" Proceedings of IPAC2012, New Orleans, Louisiana, USA
5. OPERA v10.0 user guide and reference manual.

Augmented reality assisted telerobotics system for autonomous pick and place operations

Pritam Prakash Shete, and Surojit Kumar Bose

Computer Division

Abhishek Jaju, Prabir Pal

Division of Remote Handling & Robotics

Shri Pritam Prakash Shete is the recipient of the DAE Young Applied Scientist / Technologist Award for the year 2014

Abstract

Robots are deployed to perform repeatable and hazardous tasks because of their inherent reliability, consistency, safety, and accuracy. In this article, we discuss the design and development of a stereo vision guided telerobotics system for autonomous pick and place operations. We describe system architecture, implementation details and overall system competency. We utilize a pair of IP cameras, a 3D enabled monitor and NVIDIA 3D Vision Pro system for developing our stereoscopic vision system. The robot is controlled autonomously by detecting a pre-specified marker attached on objects, then using stereo triangulation to find object's location with respect to the robot using the stereo vision system. We also carried out real-time online stereo rectification of stereo image stream to provide a comfortable stereoscopic view to the operator. We have also developed an augmented reality interface through which an operator can command the robot to any point in the workspace using stereo vision, and also plan robots approach path by avoiding obstacles. We have assessed accuracy and repeatability of the system within the robot working volume. It is highly accurate with errors less than 2mm along X and Y directions, and below 5mm along Z direction which is a viewing direction.

Introduction

Robots are reliable, consistent, safe, and accurate. They are deployed to replace human operations in hazardous environments. Efficient teleoperation of robot essentially needs information about its work environment. Image sensors are widely used for capturing visual information. Typically the robot is manipulated using one or more monoscopic cameras. A mono vision using a single image sensor provides only 2D image. A stereo vision is more effective as a disparity between a left and a right view gives essential depth information.

Stereoscopic system has become an integral part of telerobotics, industrial automation, and 3D reconstruction. A typical stereo vision system consists of image acquisition, camera calibration, stereo calibration, stereo rectification and finally stereo matching for 3D coordinates computation.

Computer Division and Division of Remote Handling and Robotics, BARC have designed and developed a stereo vision guided telerobotics system [1] [3] for autonomous pick and place operations. In this article, we will discuss the system architecture, challenges faced and solution strategy adopted for developing this system.

System Architecture

In this section, we discuss the system architecture of the telerobotics system, which operates at two different sites namely a manipulator site and a remote operation site respectively. It consists of hardware as well as software

components. Fig. 1 shows the architecture of the Telepresence system using the stereoscopic vision.

Robot

A KUKA KR-6 industrial robot installed in the DRHR is remotely manipulated from the Computer Division.

Stereo camera

A stereo camera is constructed by using a Dinion HD 1080p Day and Night IP camera pair. It provides individually configurable image streams in MJPG and H-264 formats using the real time streaming protocol.

PoE switch

IP cameras are powered using a power over Ethernet i.e. PoE protocol enabled switch to provide both data and power connections within a single cable.

Workstation

The workstation has an Intel Core i3-3220 with 3.30 GHz processor and 4GB DDR3 RAM installed. It contains two cores and four threads with SSE-4.x instruction set extensions.

Graphics card

The CUDA enabled NVIDIA Quadro 4000 professional grade graphics card with 2GB GDDR5 memory is employed for the stereoscopic vision, which has 2.0 compute capability and 256 parallel CUDA cores for GPU computation.

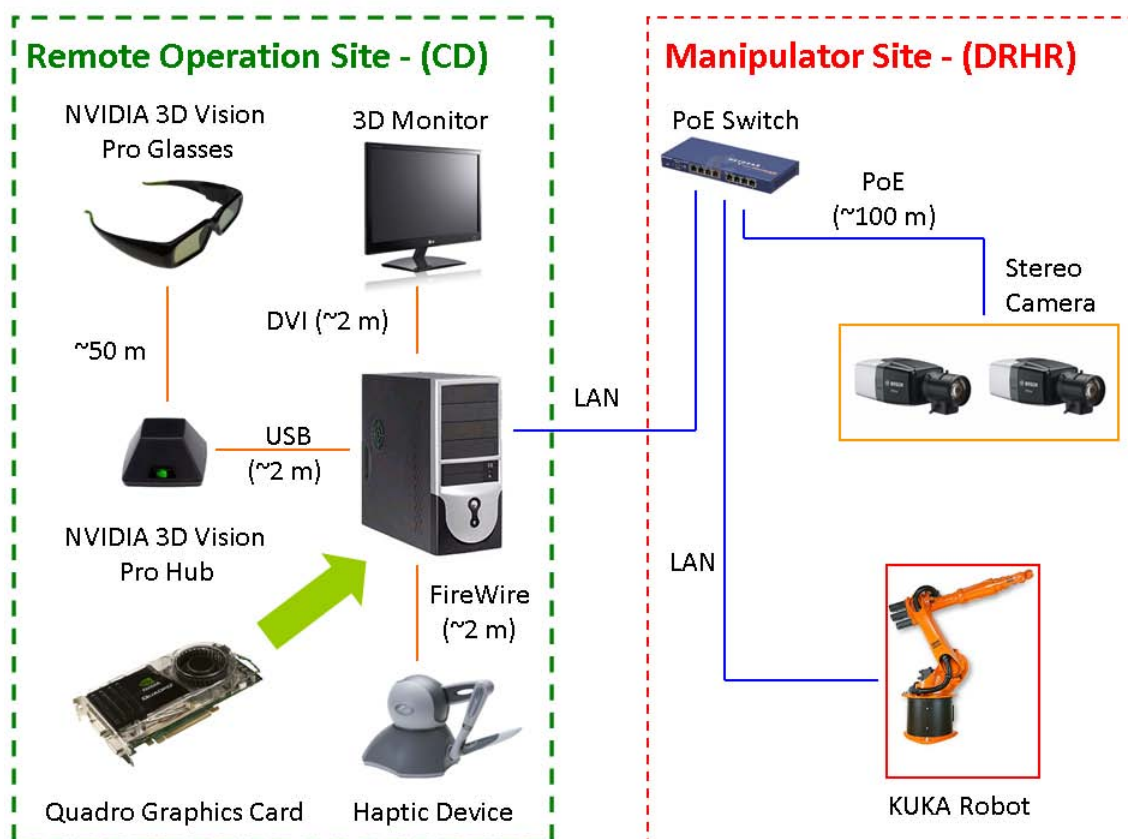


Fig. 1. Architecture of the Telerobotics system using the stereoscopic vision.

3D display

BenQ XL2420T 24 inch full high definition, wide-screen, LED backlight 120 Hz monitor is employed for 3D display. It is compatible with the NVIDIA 3D Vision Pro system.

NVIDIA 3D Vision Pro system

NVIDIA 3D Vision Pro is equipped with an RF operated wireless active shutter glasses, an RF communication hub and stereoscopic driver software. NVIDIA Quadro professional graphics cards and 3D vision ready 120 Hz or better displays are necessary for using the NVIDIA 3D Vision Pro system.

Haptic device

The Phantom haptic device is employed as a master to manipulate the slave robot remotely by looking at a live stereoscopic view through stereo IP cameras.

Force sensor

Sensation of contact with the target and resultant resistance to motion is very important in online telemanipulation tasks. ATI F/T sensor is utilized to get the reaction force, which is mounted on the wrist of the robot. On this sensor, we have mounted the gripper through an adapter plate. We use the output of the sensor to actuate the haptic device for force reflection.

Connectivity

The robot and the workstation are connected by Ethernet. The robot and the workstation communicate with each other using the UDP protocol, whereas the FireWire protocol is utilized for connecting the workstation and the haptic device. The IP camera pair is connected to the workstation using Ethernet cable. Fig. 2 shows the Telepresence system in action from Computer Division for telerobotics.



Fig. 2. Telerobotics system in action from the computer division.

Software Implementation

In this section, we provide software implementation details of the Telepresence system.

Robot control

We are using the KUKA Ethernet RSI XML software package to control the robot in real-time. Cyclical data transmission from the robot controller to an external system and vice-a-versa is in the interpolation cycle of 12ms.

Stereo image acquisition

Real-time stereo image acquisition from the IP camera pair is achieved using the GStreamer multimedia framework [4]. H-264 compressed image stream with the real time streaming protocol (RTSP) is utilized for real-time performance and network bandwidth saving.

Camera and stereo calibration

A 9x6 chessboard calibration pattern with 32mm square size is utilized for camera and stereo calibrations, which are performed using specifically designed input image sequence. Forty eight input images [4], providing a rich set of views are utilized for each calibration phase.

Real-time stereo rectification

Stereo rectification [2] is carried out to remap left and right camera images using a GPU. It aligns image rows with each other up to a pixel level, which facilitates stereo matching with a linear search and makes it computationally achievable.

Coordinate system mapping

The robot and the stereo camera are having their own coordinate systems and respective origins. A coordinate system mapping [1] is carried out to align their respective coordinate systems and origins. A 9x6 chessboard calibration pattern with 32mm square size is employed for calibration purpose.

Stereo matching

An object marker [1] is designed using two concentric circles in the form of a ring and a chessboard pattern within an inner circle, which facilitates detection up to sub-pixel level. The object marker is attached to an object to be picked up by the robot. Markers detected in left and right camera view are used to determine 3D coordinates.

Augmented reality

IP camera stereo views and an OpenGL graphics library are calibrated with each other for inserting virtual

objects in a real world. These assist in telerobotics for autonomous pick and place operations.



Fig. 3: Telepresence system using augmented reality.

Fig. 3 shows the Telepresence system using augmented reality for inserting virtual objects.

Results

In this section, we discuss competency of our telerobotics system.

System latency

IP cameras introduce system latency due to image encoding-decoding, network delays and rendering delays. Left and right IP cameras have same latency and they are synchronized with each other. The measured network latency of synchronized left and right camera pair is approximately 200ms, which is just within acceptable limits of an average human reaction time.

Real-time stereo rectification

An OpenCV image processing library utilizes instruction set extensions such as SSE and AVX for CPU optimization and the CUDA framework for GPU optimization. It is used to benchmark our GPU based realization. Our implementation [2] is more than 4 times faster than the OpenCV realization.

Coordinate system mapping

3D coordinates of chessboard corners are recalculated by performing stereo matching of detected chessboard corners in left and right images. For the best case scenarios a maximum error value is even less than 1.5mm. For the worst case scenario a maximum error value is close to 5mm and mainly the error is produced in a depth direction i.e. along the Z axis.

Stereo matching accuracy

The robot is accurate up to 1mm; hence it is employed to evaluate 3D coordinate accuracy of our system. The error along X axis is minimum and it is even less than 1mm. The error along Y axis is also less than 2mm, whereas the error along Z axis i.e. the depth is maximum

and it is approximately 5mm. Even in worst case the error value is close to 5mm.

Stereo matching repeatability

A repeatability of the stereoscopic system is validated by calculating 3D coordinates of the given gripper position multiple times. Our system has good repeatability with errors less than 1mm error for all coordinate axes.



Fig. 4: The Trimiti system running active and passive stereoscopic vision using surgical microscope.

Trimiti system – AIIMS New Delhi

Human brain is the most vital organ, which makes neurosurgery as one of the most challenging surgery. Doctors and practitioners undergo extensive neurosurgery training, before they can operate on live human being. The 3D stereoscopic visualization system is more effective during such training. Trimiti – a stereoscopic vision system [5] [6] for a surgical microscope is developed and deployed at Neurosurgery Skills Training Facility, Department of Neurosurgery, AIIMS, New Delhi and is being explored as a low cost alternative to commercial systems for conducting neurosurgery skills training sessions. Fig. 4 shows the Trimiti system running active as well as passive stereoscopic vision using a surgical stereoscopic microscope.

Conclusions

Augmented reality assistance provides a new dimension for telemanipulation. This development brings tremendous assistance to master slave operator by providing stereo rectified vision, ability to select object of interest and command robot to reach there and also do path planning for avoiding obstacles in real-time. This makes it possible to navigate robot semi-autonomously and reduce burden on operators. Operators can seamlessly switch between the two modes. For coarse motions operator can use semi-auto mode while to perform fine operation operator can switch to force reflecting master slave mode. We have also assessed accuracy and repeatability of the system on a calibration

plane and within a robot working volume. It is highly accurate with errors less than 2mm along X and Y directions, and below 5mm along Z direction which is direction of viewing.

Acknowledgement

We are grateful to Mr. R. S. Mundada, AD(C), E&I Group & Head, Computer Division, BARC for offering us this wonderful prospect to work on this emerging topic. We are also thankful to our colleagues in the Computer Division and the DRHR, whose timely help has proved quite valuable.

References

1. Shete P. P. and et al., “Stereo vision guided telerobotics system for autonomous pick and place operations”, in Proc. of ACM international conference Advances In Robotics, July 2015
2. Shete P. P. and et al., “A real-time stereo rectification of high definition image stream using GPU”, in Proc. of IEEE international conference ICACCI-2014, September 2014
3. Jaju A. and et al., “Development and evaluation of a telepresence interface for teleoperation of a robot manipulator”, in Proc. of 10th International Conference on Ubiquitous Robots and Ambient Intelligence, October-November 2013
4. Shete P. P. and et al, “A real-time stereoscopic viewer for telerobotics using open source software”, in Proc. of IEEE international conference ICACCI-2013, August 2013
5. Shete P. P. and et al., “Design & Development of 3D Stereoscopic Visualization System for Surgical Microscope”, BARC Newsletter, Issue No. - 347, September-October 2015
6. Shete P. P. and et al, “Trimiti - A Real-time Stereoscopic Vision System for Neurosurgery Training using Surgical Microscope”, in Proc. of IEEE international conference ICACCI-2015, August 2015

An Insight in to the Effect of Ternary Alloying on Hydrogen Isotope Storage Properties of ZrCo based Alloys

Ram Avtar Jat

Product Development Division

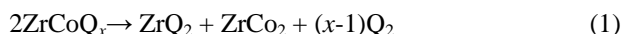
Shri Ram Avtar Jat is the recipient of the DAE Young Applied Scientist / Technologist Award for the year 2014

Abstract

An effort was made to improve the hydrogen isotope storage properties of ZrCo alloy by ternary alloying with suitable transition metal element. Ternary alloys $Zr_{1-x}Ti_xCo$ and $ZrCo_{1-x}M_x$ (M= Ni and Fe) were prepared and characterized. The hydrogen isotope storage behavior of Zr-Co-M ternary alloys was systematically investigated by employing different experimental techniques. The extensive work carried out enabled us to identify a suitable ternary substituent $Zr_{0.8}Ti_{0.2}Co$ for effective storage, supply and recovery of hydrogen isotopes.

Introduction

Solid state storage of tritium in the form of metal tritide is considered as the most safest method in fusion technology and hence is being adapted in International Thermonuclear Experimental Reactor (ITER) program [1]. Conventionally, uranium is used for storage, supply and recovery of hydrogen isotopes. Despite favorable storage properties, uranium has the drawbacks of restrictive use due to its radioactive and pyrophoric nature. Hence, the development of alternate tritium storage materials, which can substitute uranium, is a mainstream of research today among the fusion science community. The intermetallic compound ZrCo has been investigated largely as a suitable candidate material for storage, supply and recovery of hydrogen isotopes in various tritium handling facilities like ITER because of its non-radioactive nature, non-pyrophoricity at room temperature and tritium storage properties similar to uranium. ZrCo has a favorable hydrogen isotope (Q = 1H , 2H or 3H) absorption capacity with maximum stoichiometry of $ZrCoQ_3$. However, ZrCo is prone to hydrogen induced disproportionation upon repeated hydriding-dehydriding cycles [2]. The hydrogen induced disproportionation reaction can be written as:



Disproportionation results in the formation of a hydrogen non-absorbing $ZrCo_2$ and a very stable ZrQ_2 phases. Since, decomposition of ZrQ_2 requires much higher temperature (> 973 K) than that of $ZrCoQ_3$, a significant amount of hydrogen gets trapped within the storage material. This results in reduction of hydrogen storage capacity of ZrCo, which is not desirable for its use in tritium handling facilities. Konishi et al. [3] have reported that the extent of disproportionation can be

suppressed by decreasing the dehydriding temperature. However, decreasing the dehydriding temperature lowers the hydrogen equilibrium pressure of ZrCo- H_2 system due to which the required delivery pressure of 100 kPa of hydrogen couldn't be achieved. Hence, the alternative choice is to alloy ZrCo with an element M which can elevate the desorption equilibrium hydrogen pressure compared to the parent compound $ZrCoQ_3$, at a particular temperature, thereby preventing the extent of disproportionation.

This has led to the onset of consolidated efforts to find a suitable ternary alloy for storage, supply and recovery of hydrogen isotopes. In this context, a systematic approach has been applied to investigate the effect of ternary alloying on the hydrogen isotope storage properties of ZrCo alloy. Ternary alloys $Zr_{1-x}Ti_xCo$ and $ZrCo_{1-x}M_x$ (M= Ni and Fe) were prepared and characterized. The hydrogen isotope storage behavior of Zr-Co-M ternary alloys was systematically investigated by employing Sieverts' apparatus. Hydrogen induced disproportionation behavior of Zr-Co-M ternary alloys was studied by isothermal studies. The phenomenon of hydrogen induced disproportionation in different Zr-Co-M ternary alloys was further investigated by employing neutron powder diffraction (NPD) technique.

Experimental

Zr-Co-M based ternary alloys of compositions $ZrCo_{1-x}Ni_x$ (x = 0.0, 0.1, 0.2 and 0.3), $ZrCo_{0.9}Fe_{0.1}$ and $Zr_{1-x}Ti_xCo$ (x = 0.1, 0.2 and 0.3) were prepared by arc-melting method and characterized by different techniques like XRD, SEM, EDS and Elemental mapping. Alloy samples were activated by using an indigenously designed, developed and fabricated Sievert's type volumetric apparatus (Fig. 1).



Fig. 1: Indigenously designed Sieverts' type volumetric apparatus.

H₂/D₂ desorption Pressure-Composition isotherms (PCIs) for all the systems were generated in the temperature range of 523–603 K, using a Sievert's type volumetric apparatus (PCT Pro-2000, SETARAM Instrumentation, France). The isothermal disproportionation studies of all Zr-Co-M ternary alloys were carried out at 750 K for 10 hrs under delivery conditions, above 1 bar over pressure of hydrogen.

Neutron powder diffraction (NPD) patterns of Zr-Co-M ternary alloy deuterides were recorded by neutron powder diffractometer ($\lambda = 1.2443\text{\AA}$) at Dhruva reactor, Bhabha Atomic Research Centre, Mumbai, India.

Results and Discussion

The XRD patterns of Zr-Co-M ternary alloys confirm the formation of single b.c.c. (CsCl type) phase (space group *Pm-3m*) similar to ZrCo. A trace amount of ZrCo₂ impurity phase is also present in all the alloys since ZrCo₂ is the most stable phase in the Zr-Co phase diagram. The SEM images of Zr_{0.9}Ti_{0.1}Co alloy and the hydride (Fig. 2) infer that the alloys exhibit a cleavage type surface, whereas the hydride phases show a cleavage type fracture surface. The cracks generated in the hydride phase are attributed to the lattice expansion of alloy upon hydrogenation. The EDS microanalysis confirms the composition of the alloys and the elemental mapping images reveal the homogeneous nature of alloys.

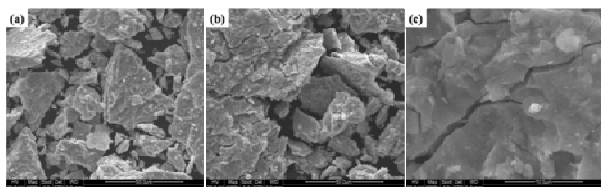


Fig. 2: SEM images of (a) Zr_{0.9}Ti_{0.1}Co alloy, (b) & (c) its hydride, respectively.

The H₂/D₂ desorption PCIs of all Zr-Co-M-H₂/D₂ systems revealed that in the temperature range of investigation, a single desorption plateau is observed for all the isotherms and the plateau width found to decrease with increase in temperature. Typical PCIs for

Zr_{0.8}Ti_{0.2}Co-H₂/D₂ systems are shown in Fig. 3. The reaction involved in de-hydrogenation/de-deuteration of Zr-Co-M hydrides/deuterides which results in single desorption plateau for all the isotherms can be written as;

$$2/3 \text{ZrCoMQ}_3 \leftrightarrow 2/3 \text{ZrCoM} + \text{Q}_2 \quad (2)$$

Using the plateau pressure data, van't Hoff plots were constructed and the thermodynamic parameters were calculated using the van't Hoff equation, given below.

$$\ln(P/P^0) = -\Delta_r H/RT + \Delta_r S/R \quad (3)$$

where, $\Delta_r H$ and $\Delta_r S$ are the enthalpy and entropy changes for the dehydrogenation/de-deuteration reaction as mentioned above in Eq. (2). P^0 is the standard pressure.

The desorption temperature (T_{des}) for the release of 100 kPa of Q₂ for all the alloys were calculated using the van't Hoff relations and listed in Table 1 along with the other thermodynamic parameters [2, 4, 5]. It is evident that the T_{des} decreases with increase in Ni or Ti content and increases with the addition of Fe. The comparison of $\Delta_r H$ and $\Delta_r S$ for hydrides and deuterides revealed that all ternary alloys show normal hydrogen isotope effect where the equilibrium pressure of D₂ is higher than that of H₂ at all experimental temperatures [4, 5]. Based on these observations, it is expected that at the operating conditions of hydrogen isotope handling facilities, the equilibrium pressure will follow the order of $p(\text{T}_2) > p(\text{D}_2) > p(\text{H}_2)$ for all ternary alloys.

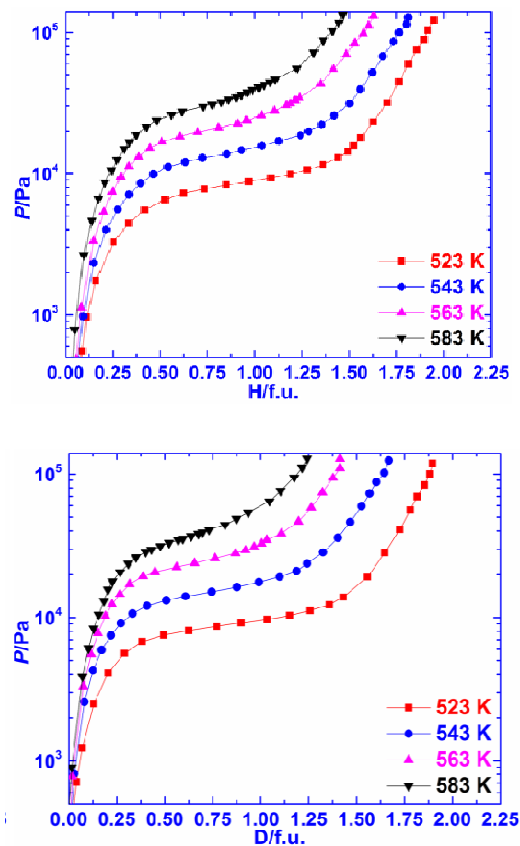


Fig. 3: H₂/D₂ desorption PCIs for Zr_{0.8}Ti_{0.2}Co-H₂/D₂ systems.

Table 1: Thermodynamic functions for H₂/D₂ desorption in Zr-Co-M-H₂/D₂ systems [2, 4, 5].

| System | | $\Delta_r H^\circ$ (kJ/mole H ₂) | $\Delta_r S^\circ$ (J/(mole H ₂ ·K)) | T_{des} (K) |
|--|-----------|--|---|------------------|
| ZrCo | Hydride | 83.7 ± 3.9 | 122.2 ± 3.9 | 683 |
| | Deuteride | 84.3 ± 0.6 | 124.5 ± 1.1 | 677 |
| ZrCo _{0.9} Ni _{0.1} | Hydride | 95.4 ± 0.9 | 144.1 ± 0.8 | 664 |
| | Deuteride | 95.5 ± 0.4 | 145.5 ± 1.2 | 656 |
| ZrCo _{0.8} Ni _{0.2} | Hydride | 93.4 ± 3.3 | 143.9 ± 3.4 | 650 |
| | Deuteride | 94.4 ± 1.3 | 145.5 ± 1.2 | 645 |
| ZrCo _{0.7} Ni _{0.3} | Hydride | 92.6 ± 2.3 | 143.9 ± 2.5 | 644 |
| | Deuteride | 92.9 ± 1.6 | 145.5 ± 2.3 | 638 |
| ZrCo _{0.9} Fe _{0.1} | Hydride | 69.2 ± 1.5 | 95.7 ± 1.0 | 723 |
| | Deuteride | 69.6 ± 1.2 | 97.7 ± 1.0 | 712 |
| Zr _{0.9} Ti _{0.1} Co | Hydride | 66.5 ± 0.3 | 97.7 ± 0.2 | 681 |
| | Deuteride | 71.9 ± 1.9 | 109.1 ± 1.8 | 658 |
| Zr _{0.8} Ti _{0.2} Co | Hydride | 63.7 ± 0.2 | 101.5 ± 0.2 | 628 |
| | Deuteride | 67.6 ± 0.3 | 109.1 ± 0.3 | 620 |
| Zr _{0.7} Ti _{0.3} Co | Hydride | 57.7 ± 2.0 | 101.5 ± 1.9 | 568 |
| | Deuteride | 59.3 ± 2.5 | 105.3 ± 2.4 | 563 |

In order to find the best suitable ternary alloy among the alloys studied, the isothermal disproportionation studies were performed under delivery conditions. The isothermal disproportionation behavior of ternary alloys, at 750 K for 10 hours under the over pressure of hydrogen above 1 bar, reveals that Ni and Fe catalyse the disproportionation reaction in its ternary alloys (Fig. 4).

The disproportionation rate was found to be slower in Fe substituted alloy as compared to Ni substituted alloys. Also, the XRD analysis before and after disproportionation studies, shown in Fig. 5, reveal that hydrides of parent ZrCo along with Fe and Ni substituted

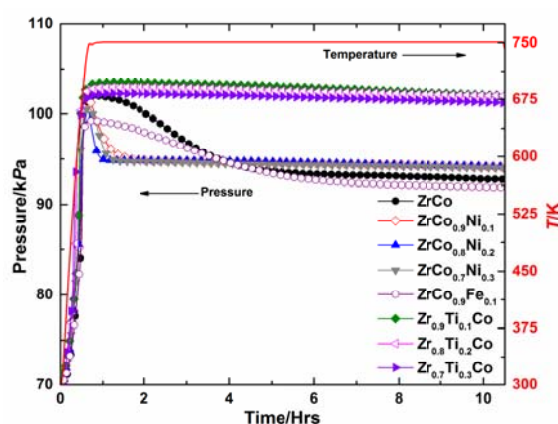


Fig. 4: Change in pressure with time for Zr-Co-M-H₂ systems at 750 K.

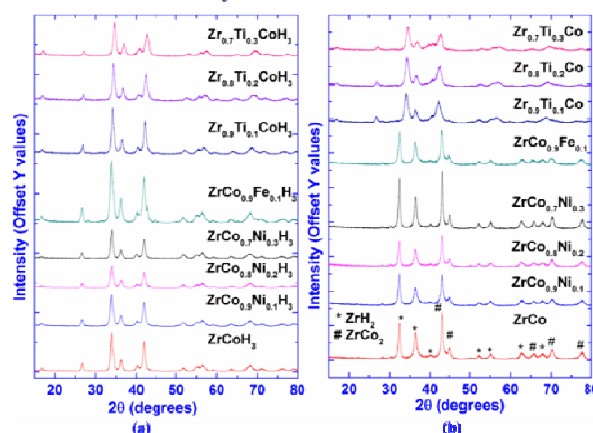


Fig. 5: XRD patterns of Zr-Co-M hydrides (a) before and (b) after disproportionation studies.

alloys completely disproportionate according to Reaction (1) and convert into ZrCo₂ and ZrH₂ phases. However, the extent of disproportionation is marginal for Ti substituted alloys and XRD after disproportionation studies does not show any detectable ZrCo₂ and ZrH₂ phases. Hence, it can be inferred that among all ternary alloys studied the Zr_{1-x}Ti_xCo (x=0.1, 0.2 and 0.3) alloys found to have higher durability against hydrogen induced disproportionation. The difference in hydrogen induced disproportionation behavior of Zr-Co-M ternary alloys, was explained by neutron powder diffraction (NPD). NPD patterns of ternary alloy deuterides was analysed by varying the background, occupancies and position of atoms. The deuterium atoms are allowed to occupy a new site 8e in addition to the earlier reported [6], 4c₂ and 8f₁ sites. A significant reduction in χ^2 was observed with addition of these extra site for deuterium occupation. It is evident that for ZrCoD₃ the occupancy of 8e site is ~3.8% which is in accord with the prediction of Bekris et al. [6]. Based on these observations, the crystal structure of Zr-Co-M deuterides with new deuterium site (8e) is proposed and shown in Fig. 6 [5, 7].

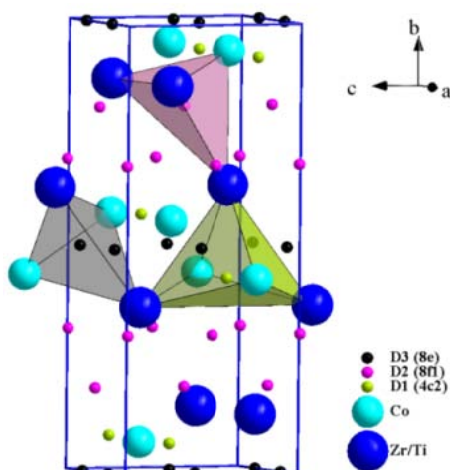


Fig. 6: Crystal structure of $Zr_{0.8}Ti_{0.2}CoD_3$ with occupancy of new interstitial site $8e$.

Occupancy of $8e$ site is found to be responsible for hydrogen induced disproportionation [5, 7]. Systematic investigations on all ternary alloy deuterides establish the effect of ternary alloying on the occupancy of new $8e$ site and Zr-D distance. Among all Zr-Co-M deuterides studied, $Zr_{0.8}Ti_{0.2}Co$ showed the lowest occupancy of $8e$ site.

Summary and Conclusion

The XRD patterns of all Zr-Co-M ternary alloys confirm the formation of b.c.c. phase similar to ZrCo. A single desorption plateau is observed in all pressure-composition isotherms (PCIs). Investigation of thermodynamic parameters like enthalpy and entropy of H_2/D_2 desorption reactions in these alloys show normal hydrogen isotope effect wherein the equilibrium pressure of deuterium is higher than that of hydrogen at all experimental temperatures. Considering the PCT studies, hydrogen induced disproportionation studies and structural studies, it is proposed that among the alloys investigated, $Zr_{0.8}Ti_{0.2}Co$ alloy is the best suitable non-pyrophoric and non-radioactive ternary alloy as a substitute for the conventionally used highly pyrophoric uranium bed for tritium storage applications. This alloy has potential for its use in ITER facility for storage, supply and recovery of hydrogen isotopes.

Acknowledgement

I wish to acknowledge Dr. S.C. Parida, Head, SMDS; Dr. Renu Agarwal, Head, ATS; and Dr. S.K. Mukerjee, Head, PDD for their guidance and support in fulfilling this work. I express my sincere thanks to Dr. K.L. Ramakumar, Director RC&I Group for his invaluable mentoring. I also acknowledge my collaborators Shri Ripandeep Singh, Shri Santu kaity, Shri J. Nuwad, Dr. A. Das and Dr. P.U. Sastry who were associated with this work by way of providing the facilities for XRD, SEM, EDS and NPD.

References

1. Jat RA, Parida SC, Nuwad J, Agarwal R, Kulkarni SG. "Hydrogen sorption-desorption studies on ZrCo-Hydrogen system" *Journal of Thermal Analysis and Calorimetry*, 112 (2013): 37-43.
2. Jat RA, Parida SC, Agarwal R, Kulkarni SG. "Effect of Ni content on the hydrogen storage behavior of $ZrCo_{1-x}Ni_x$ alloys" *International Journal of hydrogen energy*, 38 (2013): 1490-1500.
3. Konishi S, Nagasaki T, Okuno K. "Reversible disproportionation of ZrCo under high temperature and hydrogen pressure" *Journal of Nuclear Materials*, 223 (1995): 294-9.
4. Jat RA, Parida SC, Agarwal R, Ramakumar KL. "Investigation of hydrogen isotope effect on storage properties of Zr-Co-Ni alloys" *International Journal of hydrogen energy*, 39 (2014): 14868-73.
5. Jat RA, Singh R, Parida SC, Das A, Agarwal R, Ramakumar KL. "Determination of deuterium site occupancy in $ZrCoD_3$ and its role in improved durability of Zr-Co-Ni deuterides against disproportionation" *International Journal of hydrogen energy*, 39 (2014); 15665-9.
6. Bekris N, Sirch M. "On the Mechanism of the Disproportionation of ZrCo Hydrides" *Fusion Science and Technology*, 62 (2012): 50-5.
7. Jat RA, Singh R, Parida SC, Das A, Agarwal R, Ramakumar KL. "Structural and hydrogen isotope storage properties of Zr-Co-Fe alloy" *International Journal of Hydrogen Energy*, 40 (2015): 5135-43.

Development of Novel Radionuclide Generators for Use in Nuclear Medicine

Rubel Chakravarty

Isotope Production and Applications Division

**Dr. Rubel Chakravarty is the recipient of the
DAE Young Scientist Award for the year 2014**

Introduction

Over the last 5 decades, radionuclide generators have attracted substantial attention, indeed close scrutiny of the nuclear medicine community owing to their ability to provide short-lived radioisotopes without the need for on-site nuclear reactor or cyclotron facilities for preparation of a wide variety of diagnostic and therapeutic radiopharmaceuticals [1]. The radionuclide generators not only provide no-carrier-added (NCA) radionuclides on-demand basis, but also in a cost-effective way where the payoff of benefits is substantial and invaluable [1]. Nuclear medicine and radionuclide generator feed off of one another, thereby, propelling both forward. Utility of radionuclide generators has virtually pervaded most areas in the field of nuclear medicine and their importance has been well demonstrated and recognized [1].

The current importance and success of diagnostic imaging in nuclear medicine is primarily due to $^{99}\text{Mo}/^{99\text{m}}\text{Tc}$ generator [1]. A large number of the nuclear medicine procedures in remote areas far from the site of a cyclotron or reactor facility would not have been possible but for the availability of this radionuclide generator [1]. It would not be an exaggeration to state that the field of nuclear medicine owes its existence to the development of this generator in 1957 at Brookhaven National Laboratory in United States [1]. The subsequent years have seen an enormous increase in the use of generators such as $^{90}\text{Sr}/^{90}\text{Y}$ and $^{188}\text{W}/^{188}\text{Re}$ generators to provide therapeutic radionuclides, which has paralleled the development of complementary strategies for targeted radiotherapy [2-4]. With the recent advances in clinical positron emission tomography (PET), use of the $^{68}\text{Ge}/^{68}\text{Ga}$ generator is showing enormous potential as a source of positron-emitting ^{68}Ga which can be used for preparation of a wide variety of radiopharmaceuticals [5, 6].

Basic Concept of Radionuclide Generator

A radionuclide generator is a self-contained system housing an equilibrium mixture of a parent/daughter radionuclide pair [1]. The system is designed to separate the daughter radionuclide formed by the decay of a parent radionuclide by virtue of their differences in chemical properties [1]. The parent-daughter nuclear relationships offer the possibility to separate the daughter radionuclide at suitable time intervals.

Emerging Concepts in Radionuclide Generator Technology

As separation science is subject to continuous evolution, any revolutionary breakthrough in this subject represents not only an important driving force, but also lays the cornerstone towards the development of new radionuclide generators [7]. With the emergence of professionally run centralized radiopharmacies, the use of radionuclide generator technology is pointing to an era of a paradigmatic shift from the present designs and user profiles. In order to sustain the nuclear medicine service using generator derived radionuclides, it is of utmost importance to nurture emerging separation technologies in an appropriate manner, both in absolute, as well as in relative, terms of missions, goals, and requirements, to respond to the foreseeable changes in radionuclide generator technology.

In the recent times, our group has introduced two new concepts in the field of radionuclide generators, which are poised to bring paradigm shift in nuclear medicine practices in the foreseeable future. While the first approach involves the use of electrochemical separation technique [8, 9], the second involves the use of sorbents based on nanomaterials for use as column chromatography matrices [10] for the preparation of radionuclide generators.

Electrochemical Separation

Electrochemical method provides a simple and convenient approach of performing a wide variety of metal ion separations. A mixture of metal ions having adequate difference in their formal potential values in an electrolytic medium can be mutually separated by selective electrodeposition of one metal on an electrode surface under the influence of controlled applied potential (**Fig. 1**). *In-situ* electrodeposition of a daughter radionuclide is an attractive route to develop radionuclide generators. The major advantage of this approach is that the daughter radioisotope can be obtained with very high radionuclidic purity and radioactive concentration, irrespective of the specific activity of the parent radioisotope. This approach has been used for development of a variety of radionuclide generators, such as, $^{90}\text{Sr}/^{90}\text{Y}$, $^{99}\text{Mo}/^{99\text{m}}\text{Tc}$ and $^{188}\text{W}/^{188}\text{Re}$ generators [8].

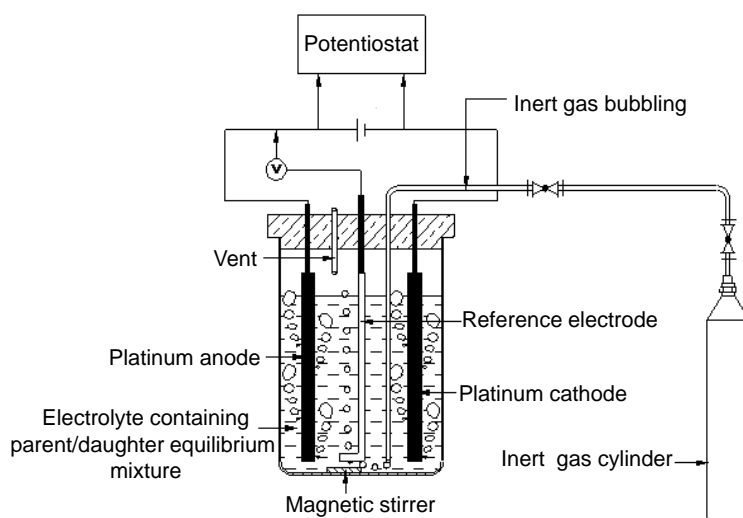


Fig. 1: Schematic diagram of electrochemical radionuclide generator

Column Chromatography using Nanosorbents

The second approach is based on the use of nanomaterials based sorbents as column matrices for the preparation of radionuclide generators (Fig. 2) relies on the unique morphological features, pore structure, high surface areas and high surface charge of nanomaterials [1, 10]. Such sorbents demonstrate much higher sorption capacity and selectivity for sorption of the parent radioisotope compared to their bulk counterparts. The daughter activity can be obtained with appreciably high radioactive concentration and purity suitable for biomedical applications. Over the last 10 years, a wide variety of nanostructured metal oxides such as polymer embedded nanocrystalline titania (TiP), mixed phase nanocrystalline zirconia (nano-ZrO₂), tetragonal nanozirconia (t-ZrO₂), nanocrystalline γ -alumina (γ -Al₂O₃), mesoporous alumina (MA) and nanoceria-

polyacrylonitrile (CeO₂-PAN) composite have been synthesized by our group for preparation of ⁹⁹Mo/^{99m}Tc, ¹⁸⁸W/¹⁸⁸Re and ⁶⁸Ge/⁶⁸Ga generators (Fig. 3) [10]. It is pertinent to point out that in case of all the nanosorbents used for preparation of radionuclide generators, the synthesis methods adopted were neither cumbersome nor used expensive precursors and was amenable for scale-up. All these nanomaterials exhibited good mechanical strength, granular properties and were amenable for column operations. However, all these sorbents consisted of agglomerated nanoparticles (Fig. 3). Agglomeration to a certain extent is essential for use of such materials as sorbent matrices in chromatographic columns. Very fine particles without agglomeration are not suitable for column chromatographic application as such materials are impervious to the flow of liquid through the column bed.

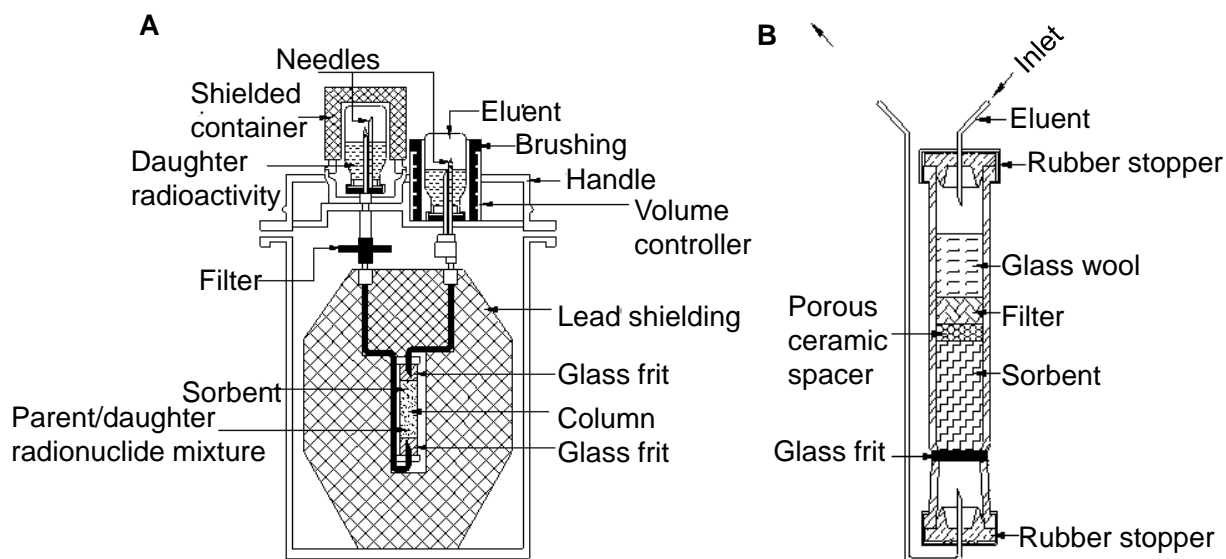


Fig. 2: Radionuclide generator based on column chromatographic separation. (A) Schematic diagram of a column chromatography generator housed in a lead shielded container to provide daughter radionuclide. (B) Schematic diagram of a chromatography column of a radionuclide generator.

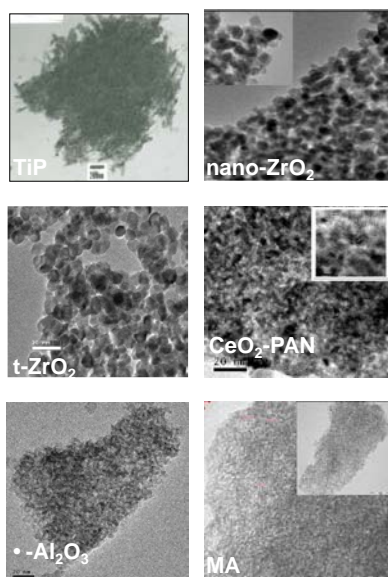


Fig. 3: Transmission electron microscopy images of nanosorbents used in preparation of column chromatographic radionuclide generators

The following sub sections provide an overview of the clinically useful radionuclide generators developed using the novel separation chemistry approaches described above.

⁹⁹Mo/^{99m}Tc generator

Over the last 5 decades, a variety of ^{99m}Tc/⁹⁹Mo generator systems have been thoroughly investigated all over the world due to the everlasting demand for ^{99m}Tc, which is the most commonly used medical radioisotope [1, 3]. This radioisotope is considered as the ‘workhorse’ of diagnostic nuclear medicine and is used for approximately 20–25 million procedures annually, comprising ~80% of all diagnostic nuclear medicine procedures. The column chromatographic ^{99m}Tc/⁹⁹Mo generator using a bed of acidic alumina has emerged as the most popular choice for availing ^{99m}Tc in nuclear medicine departments worldwide [3]. However, the capacity of bulk alumina for taking up molybdate ions is limited (2–20 mg Mo per gram of alumina), necessitating the use of NCA ⁹⁹Mo produced through fission route [3]. Owing to the inherent complexities in production of fission ⁹⁹Mo and the vulnerability of irradiation services from 5 old research reactors which are currently in use for fission ⁹⁹Mo production, there is an increasing consensus to use low specific activity ⁹⁹Mo produced through the neutron activation route [(n,•)⁹⁹Mo] for preparation of clinically useful ⁹⁹Mo/^{99m}Tc generators [3, 11]. However, the specific activity of (n,•)⁹⁹Mo is at least 1000-fold lesser than that of fission ⁹⁹Mo and is therefore not suitable for preparation of bulk alumina based column chromatographic generators [3].

In order to reduce reliance on fission ⁹⁹Mo, our group demonstrated for the first time the utility of

electrochemical separation approach for preparation of clinical scale ⁹⁹Mo/^{99m}Tc generator [12]. This is primarily based on the selective electrodeposition of ^{99m}Tc on a platinum electrode by taking advantage of the difference in formal electrode potentials of MoO₄²⁻ and TcO₄⁻ ions in alkaline media. The preferential electrodeposition of ^{99m}Tc relies on applying a potential of 5 V in 0.1 M NaOH medium for 45 min. With a view to recover the ^{99m}Tc deposit on the cathode, electrolysis was carried out in saline solution by reversing the polarity of the electrode and application of a high positive potential for a few seconds. In this process, the ^{99m}Tc deposit could be quantitatively brought into saline solution, wherein ^{99m}Tc existed as ^{99m}TcO₄⁻. It was demonstrated that the process was suitable for the separation of clinically useful ^{99m}Tc, even from very low specific activity (~1.85 GBq/mg) ⁹⁹Mo.

Our group also demonstrated for the first time, the utility of nanosorbents such as TiP, t-ZrO₂, γ-Al₂O₃ and MA for preparation of clinical scale ⁹⁹Mo/^{99m}Tc generators [10, 13-15]. Recently, a comparative evaluation of the performance of the different nanosorbents reported was carried out to identify the best choice for preparation of ⁹⁹Mo/^{99m}Tc generators using (n,•)⁹⁹Mo [16]. Though, ⁹⁹Mo/^{99m}Tc generators prepared using any of the nanosorbents met the requirements for use in preparation of radiopharmaceuticals, MA and γ-Al₂O₃ were identified as the best choices in view of their higher sorption capacities (~160 mg Mo/g) which could be used for preparation of clinical-scale ⁹⁹Mo/^{99m}Tc generator even while using (n,•)⁹⁹Mo produced in medium flux reactors.

The performances of the ⁹⁹Mo/^{99m}Tc generators prepared by both the approaches remained consistent over a period of 2 weeks, which is comparable to the shelf life of the commercially available (fission ⁹⁹Mo based) ⁹⁹Mo/^{99m}Tc generators. Technetium-99m could be obtained with > 99.99 % radionuclidic purity and the compatibility of the product in the preparation of ^{99m}Tc-labeled formulations was found to be satisfactory.

⁶⁸Ge/⁶⁸Ga generator

The ⁶⁸Ge/⁶⁸Ga generator is an excellent source for availing ⁶⁸Ga (t_{1/2} = 68 min), which is a positron emitter, with 89% positron branching accompanied by low photon emission (1,077 keV, 3.22%) [1, 5]. The cyclotron-independent availability of ⁶⁸Ga from this generator in an ionic form has led to the development of a wide variety of ⁶⁸Ga-based radiopharmaceuticals, which have opened new horizons for molecular diagnostics using PET. Despite excellent attributes of ⁶⁸Ga-radiopharmacy, the low radioactive concentration, high acidity, unacceptable ⁶⁸Ge breakthrough, and the presence of potential metal ion impurities in the generator eluate have emerged as the major deterrents towards preparation of ⁶⁸Ga-based radiopharmaceuticals using ⁶⁸Ga eluted from most of the ⁶⁸Ge/⁶⁸Ga generators available in the market [5]. Also, most of these generator systems demonstrate deteriorating performance in terms

of increased ^{68}Ge breakthrough and reduced ^{68}Ga elution yield on repeated elutions over a prolonged period of time [5]. These limitations could be circumvented with the availability of 'state-of-the-art' automated modules for post-elution processing of ^{68}Ga eluate and subsequent radiopharmaceutical preparation [5]. However, these automated modules are highly expensive and increases the production cost of ^{68}Ga -based radiopharmaceuticals.

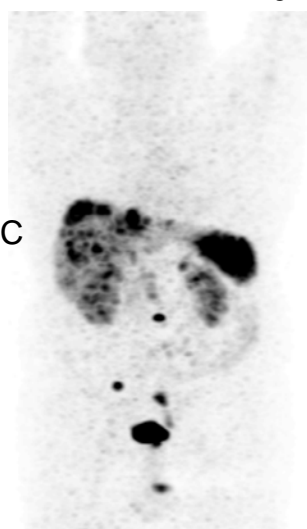
The development of $^{68}\text{Ge}/^{68}\text{Ga}$ generators which could directly be used for preparation of radiopharmaceuticals without the need for post-elution processing of ^{68}Ga was first reported by our group. $\text{CeO}_2\text{-PAN}$ and t-ZrO_2 were used as sorbent matrices in these generators [6, 17]. Gallium-68 could be regularly eluted from these

generators with $> 70\%$ elution yield with high radionuclidic purity ($< 1 \times 10^{-5} \%$ of ^{68}Ge impurity), chemical purity (< 0.1 ppm of Ce, Ti, Ni, Fe and Mn ions) and was directly amenable for the preparation of ^{68}Ga -labeled radiopharmaceuticals. The performances of the generators were evaluated for a period of 1 year. The generators gave consistent performance with respect to the elution yield and purity of ^{68}Ga throughout the period of investigation. The $\text{CeO}_2\text{-PAN}$ based $^{68}\text{Ge}/^{68}\text{Ga}$ generator (named as 'BARC' $^{68}\text{Ge}/^{68}\text{Ga}$ generator) was deployed in Tata Memorial Hospital (TMH), Mumbai (Fig. 4), where it was successfully used for preparation of clinically relevant doses of ^{68}Ga -based radiopharmaceuticals for cancer diagnosis using PET.



'BARC' $^{68}\text{Ge}/^{68}\text{Ga}$ generator

^{68}Ga -DOTA-NOC



PET imaging

Fig. 4: 'BARC' $^{68}\text{Ge}/^{68}\text{Ga}$ generator supplied to TMH, Mumbai was used for preparation of ^{68}Ga -DOTA-NOC, a radiopharmaceutical used for PET imaging of neuroendocrine tumors overexpressing somatostatin receptors.

$^{90}\text{Sr}/^{90}\text{Y}$ generator

Yttrium-90 is a therapeutic radioisotope of enormous interest and radiopharmaceuticals based on ^{90}Y are widely used for the treatment of cancer as well as in radiation synoviorthesis [4]. The broad interest in the use of ^{90}Y in therapeutic nuclear medicine is due to its suitable nuclear characteristics ($t_{1/2} = 64.1$ h, $E_{\text{max}} = 2.28$ MeV, no α emission) and Y^{3+} coordination chemistry suitable for complexation with various ligands and biomolecules. A radionuclide generator system based on the secular equilibrium of ^{90}Sr decaying to ^{90}Y is a convenient method for the production of high specific activity ^{90}Y [4].

Over the past three decades, several separation techniques were reported for the development of $^{90}\text{Sr}/^{90}\text{Y}$ generators [4]. Most of these separation techniques involve multiple steps employing conventional separation approaches such as solvent extraction, ion exchange or extraction chromatography either alone or in combination. However, none of these procedures are amenable for regular use in a hospital radiopharmacy or in a centralized radiopharmacy. This is primarily

because the level of ^{90}Sr impurity in ^{90}Y obtained from these systems does not meet the requirements prescribed in the pharmacopoeias for clinical use [4]. In view of the necessity to achieve a satisfactory degree of separation of ^{90}Y from ^{90}Sr , resorting to an electrochemical separation procedure was found to be effective [18]. The separation of Y from a mixture of Sr and Y is based on the selective electrodeposition of Y on a platinum electrode attributed to the difference in formal electrode potential of Sr^{2+} and Y^{3+} ions in acidic media. This enabled extraordinarily high decontamination factors ($^{90}\text{Sr}/^{90}\text{Y}$ activity ratio $< 10^{-5}$) to be achieved and ^{90}Y was obtained in a form suitable for preparation of radiopharmaceuticals. Adopting the process chemistry developed by our group, a fully automated electrochemical module for the electrochemical $^{90}\text{Sr}/^{90}\text{Y}$ generator (named as 'Kamadhenu') was developed (Fig. 5) and is commercially available from Isotope Technologies Dresden (ITD), Germany. The automated module is already in operation in some countries. The above module is designed for the production of up to 37 GBq (1 Ci) of ^{90}Y per day.



Fig. 5: Automated electrochemical $^{90}\text{Sr}/^{90}\text{Y}$ generator (Kamadhenu)

$^{188}\text{W}/^{188}\text{Re}$ generator

The $^{188}\text{W}/^{188}\text{Re}$ generator is an excellent source for availing NCA grade ^{188}Re , which has immense potential for use in therapeutic nuclear medicine [2, 19]. The pre-eminence of this radioisotope is primarily due to its excellent nuclear decay characteristics [reasonable half-life (16.9 h), high-energy beta radiation ($E_{\text{max}} = 2.118\text{MeV}$), 155 keV (15.8% abundance) suitable for scintigraphic imaging and dosimetry] and convenient on-site availability from $^{188}\text{W}/^{188}\text{Re}$ generators [2]. The chemistry of Re is similar to that of Tc since they belong to the same group in the periodic table, and this is an additional advantage towards preparing therapeutic analogues with molecules that have shown promising results in diagnosis as $^{99\text{m}}\text{Tc}$ -radiopharmaceuticals. Most of the separation methodologies which have been reported for $^{99}\text{Mo}/^{99\text{m}}\text{Tc}$ generators have also been exploited for preparation of $^{188}\text{W}/^{188}\text{Re}$ generators [2]. Out of these procedures, the alumina based column chromatographic approach wherein ^{188}W is absorbed on bulk alumina matrix and ^{188}Re is selectively eluted using saline solution at regular intervals, has been identified as the most reliable method for the preparation of $^{188}\text{W}/^{188}\text{Re}$ generator [19]. Owing to the limited sorption capacity of bulk alumina ($\sim 50\text{ mg W/g}$), clinical-scale $^{188}\text{W}/^{188}\text{Re}$ generator can only be prepared using high specific activity ($150\text{--}190\text{ GBq/g}$) ^{188}W that can be produced in only few high flux ($\sim 10^{15}\text{ n.cm}^{-2}\text{.s}^{-1}$) reactors available in the world [2]. Even while using high specific activity ^{188}W produced in these reactors, the $^{188}\text{W}/^{188}\text{Re}$ generators currently available yield low specific volume (activity/mL) of ^{188}Re and require post-elution concentration procedures prior to radiopharmaceutical preparation which is not always very convenient to perform in hospital radiopharmacies [2]. From this perspective, it is desirable to develop

$^{188}\text{W}/^{188}\text{Re}$ generators where the concentration step can be avoided to simplify the operational procedure for their widespread clinical utility.

Our group has exploited the utility of electrochemical separation approach for preparation of $^{188}\text{W}/^{188}\text{Re}$ generator [20]. Electrolysis was carried out in oxalic acid medium by applying a potential of 7 V for 45 min, using platinum electrodes. The presence of oxalate ions in the electrolyte helps in enhancing the reduction of ReO_4^- ions through formation of a 1:1 rhenium-oxalato complex. The ^{188}Re deposit on the electrode was dissolved in 0.1 M HCl to yield perrhenic acid, which was neutralized and passed through an alumina column for further purification. The recovered ^{188}Re had high radiochemical ($> 97\%$) and radionuclidic purity ($> 99.99\%$) and was suitable for radiolabeling various biomolecules. Repeated electrochemical separation of ^{188}Re from the same stock solution of ^{188}W could be demonstrated for a period of 6 months and reproducible results were obtained.

The feasibility of developing clinical scale $^{188}\text{W}/^{188}\text{Re}$ column chromatographic generators using nanosorbents such as TiP, nano- ZrO_2 and $\bullet\text{-Al}_2\text{O}_3$ was also explored in our laboratory [1, 21]. A comparative evaluation of the nanosorbents was carried out and $\bullet\text{-Al}_2\text{O}_3$ was identified as the best choice for preparation of $^{188}\text{W}/^{188}\text{Re}$ generator since this material exhibited highest sorption capacity for ^{188}W ions ($\sim 300\text{ mg W/g}$) [1, 22]. Leaving aside the difference in sorption capacity, all the generators developed using nanosorbents yielded ^{188}Re with high radiochemical ($> 99\%$) and radionuclidic purity ($> 99.99\%$) and were suitable for use in clinical context without post-elution concentration and purification procedures.

Conclusions

In summary, emerging concepts in radionuclide generator technology has been described, which are expected to make captivating advances in the field of nuclear medicine. The electrochemical separation approach was demonstrated as an innovative strategy for the development of clinically useful $^{90}\text{Sr}/^{90}\text{Y}$, $^{188}\text{W}/^{188}\text{Re}$ and $^{99}\text{Mo}/^{99\text{m}}\text{Tc}$ radionuclide generators. Compared with conventional methods, the electrochemical method provides higher yields as well as higher radioactive concentration of the daughter product, good reproducibility and acceptable product purity. Also, the recent advances in material science have paved the way for synthesis of a wide variety of nanosorbents through different routes. These nanosorbents have been used for preparation of clinically useful $^{68}\text{Ge}/^{68}\text{Ga}$, $^{188}\text{W}/^{188}\text{Re}$ and $^{99}\text{Mo}/^{99\text{m}}\text{Tc}$ radionuclide generators. The utility of $^{68}\text{Ge}/^{68}\text{Ga}$ generator prepared using nanosorbents has actually been demonstrated for cancer imaging at Tata Memorial Hospital, Mumbai.

While the advances made so far are exciting and efforts to develop new generation of radionuclide generators are evolving persistently, we still have a long way to go in terms of regular utilization of these novel generator systems in clinical context. Completing the technology development as well as establishing the economics of the approach is the cornerstone for the survival and strength of such new approaches. Nevertheless, with sustained efforts of all stakeholders, including, radiopharmacists, radiochemists, system designers, automation engineers, nuclear medicine physicians and regulators, the technological and regulatory barriers can be surmounted and the potential rewards at the end are expected to be substantial.

Acknowledgements

The author gratefully acknowledges Dr. Ashutosh Dash, Head, Isotope Production and Applications Division, BARC for his continuous guidance, encouragement and support. The author is also grateful to Dr. A. K. Tyagi, Chemistry Division, BARC for his guidance and support toward synthesis and structural characterization of nanomaterials. The author expresses his gratitude to all his colleagues at Isotope Production and Applications Division, BARC, who were associated with him in the work, reported in this article.

References

1. R. Chakravarty and A. Dash. Development of radionuclide generators for biomedical applications. LAP Lambert Academic Publishing, Germany 2013.
2. M.R.A Pillai, A. Dash, and F.F. Knapp Jr. *Curr Radiopharm* **5** (2012) 228.
3. M.R.A Pillai, A. Dash, and F.F. Knapp. Jr. *J Nucl Med* **54** (2013) 313.
4. R. Chakravarty, A. Dash, and M.R.A. Pillai. *Cancer Biother Radiopharm* **27** (2012) 621.
5. R. Chakravarty, S. Chakraborty, R. Ram, R. Vatsa, P. Bhusari, J. Shukla, B.R. Mittal, A. Dash. *J Labelled Comp Radiopharm* **59** (2016) 87.
6. R. Chakravarty, R. Shukla, R. Ram, M. Venkatesh, A. Dash, and A.K. Tyagi. *ACS Appl Mater Interfaces* **2** (2010) 2069.
7. A. Dash and R. Chakravarty *RSC Adv.* **4** (2014) 42779.
8. R. Chakravarty, A. Dash, and M.R.A. Pillai. *Curr Radiopharm* **5** (2012) 271.
9. A. Dash and R. Chakravarty. *Ind Eng Chem Res* **53** (2014) 3766.
10. R. Chakravarty and A. Dash. *J Nanosci Nanotechnol* **13** (2013) 2431.
11. M.R.A Pillai, A. Dash, and F.F. Knapp Jr. *J Nucl Med* **56** (2015) 159.
12. R. Chakravarty, A. Dash, and M. Venkatesh. *Nucl Med Biol* **37** (2010) 21.
13. R. Chakravarty, R. Ram, A. Dash, and M.R.A. Pillai. *Nucl Med Biol* **39** (2012) 916.
14. R. Chakravarty, R. Shukla, S. Gandhi, R. Ram, A. Dash, M. Venkatesh, and A. K. Tyagi. *J Nanosci Nanotechnol* **8** (2008) 4447.
15. R. Chakravarty, R. Ram, R. Mishra, D. Sen, S. Mazumder, M.R.A. Pillai, and A. Dash. *Ind Eng Chem Res* **52** (2013) 11673.
16. R. Chakravarty, R. Ram, and A. Dash. *Sep Sci Technol* **49** (2014) 1825.
17. R. Chakravarty, R. Shukla, R. Ram, A.K. Tyagi, A. Dash, and M. Venkatesh. *Nucl Med Biol* **38** (2011) 575.
18. R. Chakravarty, U. Pandey, R.B. Manolkar, A. Dash, M. Venkatesh, and M.R.A. Pillai. *Nucl Med Biol* **35** (2008) 245.
19. J.M. Jeong and F.F. Knapp Jr. *Semin Nucl Med* **38** (2008) S19.
20. R. Chakravarty, A. Dash, K. Kothari, M.R.A. Pillai, and M. Venkatesh *Radiochim Acta* **97** (2009) 309.
21. R. Chakravarty, R. Shukla, R. Ram, M. Venkatesh, A.K. Tyagi, and A. Dash. *Anal Chem* **83** (2011) 6342.
22. R. Chakravarty and A. Dash. *Sep Sci Technol* **48** (2013) 607.

Speciation and Binding of Uranyl Ion in Different Environments

Mahesh Sundararajan

Theoretical Chemistry Section, Chemistry Group

**Dr. Mahesh Sundararajan is the recipient of the
DAE Young Scientist Award for the year 2014**

Abstract

Understanding the speciation and binding of heavy metal ions in different environments is central to nuclear waste management processes. Due to the obvious safety and health hazard in experimental studies, theoretical calculations can be used as an alternative tool to study the chemistry of toxic heavy metal ions. Although several quantum chemical methods with variable accuracy are available, a cost effective method such as density functional theory (DFT) is an obvious choice. Here, we have high-lightened some of our studies on the speciation of uranyl ion in aqueous, biological, geo-chemical, carbon based nanomaterials and with synthetic receptor environments.

Introduction

The chemistry of heavy metal ions such as actinyls is receiving increased attention at the present time due to the environmental danger posed by such species. In order to assess the extent of the hazardness, the speciation of toxic and heavy metal ions in various environments is at most essential.^[1,2] As higher oxidation states of actinides such as uranyl ($U^{VI}O_2$) is toxic and soluble in water which is extremely dangerous for aquatic species. Thus viable strategies are needed which can convert toxic and soluble uranyl to non-toxic insoluble forms. One promising strategy is to make use of redox processes.^[3]

Further, performing experiments on toxic heavy metal ions such as uranyl, chromate needs sophisticated laboratories which are generally very expensive. Further, some of the species involved in the conversion of U^{VI} to U^{IV} are usually very short lived intermediates such as U^{V} and Cr^{V} which are often not identified in experimental time scale due to the very short life time of the species. Alternatively, the speciation of heavy metal ions can be studied at the molecular level using molecular modeling methods.^[4] In this regard, one can make use of cost effective molecular mechanics methods which can be used to study more than one million atoms, however, the accuracy is often questionable due to the parameters involved. Further, the electronic structure of the species under investigation can be studied with this classical method. The most accurate quantum chemical methods such as full Configuration Interaction methods (Full CI) with very large basis sets. Here too, due to the over-demanding computational cost even for a small system, some approximate methods are needed to study the chemistry of actinides. In this regard, methods such as CCSD(T) with triple ζ -basis set can now be regarded as affordable *ab initio* methods which can be considered as reference methods for single reference systems. If the system is truly multi-configurational, then methods such as Complete Active Space Self Consistent Field

(CASSCF) should at least be used to treat the ground state degeneracy (often termed as static correlation), and the remaining dynamic correlation can be treated within the framework of MP2 methods. The most popular method is CASPT2 which can be even studied for systems of moderate sizes.^[5]

Besides this, most of the heavy metal ions are often charged species such as tris-carbonate uranyl ($[UO_2(CO_3)_3]^{4-}$). Either, the species is highly solvated or exist in the presence of counter-ions. In addition to the methods chosen above, one need to take care of solvation as well. In this regard, either explicit solvation (treating each solvent molecule at the quantum chemical level) or implicit solvation such as polarizable continuum models are often used. Last but certainly not the least, to some extent relativistic and multiplet effect should be considered approximately. In this regard, scalar relativistic ZORA and DKH methods often predict results at least semi-quantitatively.^[6] In fact, due to the large number of electrons in the heavy metal ions such as uranyl and the inner core electrons are often not involved in bonding, an effective core potential (ECP) is often used to model the inner core electrons. In this regard, a small core (SC) ECP is superior over large core ECP due to the better description of valence electron in SC-ECP.^[4] It should be noted that some portion of relativistic effects are also incorporated in the ECPs which should predict ground state properties such as geometries and vibrational frequencies fairly well.

Our computational predictions on the speciation and binding of heavy metal ions in different environments are discussed in the next section. Due to the larger size of the systems involved, we have used BP86 density functional (DF) in conjunction with SC-ECP for core electrons and the valence electrons are described with double- ζ -basis set for geometry optimizations and triple- ζ -basis set for energetics. Solvent effects are incorporated within the COSMO solvation model.

Speciation of Actinyls in Aqueous Phase

The geometric and electronic structures of several small molecules directly bound to U, Np and Pu in both their (VI) and (V) oxidation states have been investigated using DFT methods.^[7,8] Unlike the methods discussed above, we have accurately modeled the micro-solvation using molecular dynamics simulations and the bulk solvent using a continuum model. We find that two different hydrogen bonding patterns involving the axial actinyl oxygen atoms are sometimes possible, and may give rise to different An–O bond lengths and vibrational frequencies. These alternative structures are reflected in the experimental An–O bond lengths of the aqua and carbonato complexes (Fig. 1). The variation of the redox potential of the uranyl complexes with the different ligands have also been investigated.

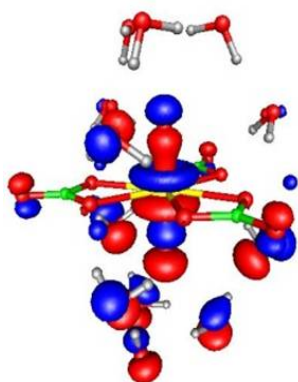


Fig. 1: Solvated structure of uranyl carbonate

Bio-reduction of Uranyl in Biological Systems

We have studied the possible binding, geometric structure and reduction mechanism of hydrated uranyl cation, $[\text{UO}_2]^{2+}$, to the electron transfer cytochrome *c*₇ protein.^[9] Initially, the binding site of Uranyl to the protein is derived from AUTODOCK which is at glutamate and aspartate (Fig. 2). Further, the structures and reduction mechanisms are proposed based on DFT calculations. We proposed that the initial electron transfer takes place from the heme to a single uranyl ion.

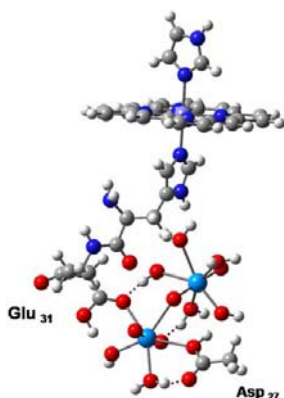


Fig. 2. T-shaped U-U dimer bound to protein

Further, a T-shaped cation-cation $\text{U}^{(\text{V})}\text{-U}^{(\text{VI})}$ complex with a second uranyl cation. A $\text{U}^{(\text{V})}\text{-U}^{(\text{V})}$ complex is formed, which then undergoes disproportionation via two successive protonation steps of one uranyl group, to give a $\text{U}^{(\text{VI})}\text{-U}^{(\text{IV})}$ complex which dissociates to individual $\text{U}^{(\text{VI})}$ and $\text{U}^{(\text{IV})}$ species, the former being bound at the enzyme active site. Intermediate structures along the catalytic pathway are consistent with the experimental data. A similar mechanistic pathways are also reported for chromate and for Pu and Np species.^[10]

Speciation of Uranyl in Functionalized Carbon Nanotubes

One of the most commonly encountered problem in the back-end-of the nuclear fuel cycle is the selective binding of actinides in the presence of other interfering ions. Although many extractants are known, alternative viable extractants are explored. In this regard, we have investigated the use of carbon nanotubes and C_{60} fullerenes for the binding of uranyl.^[11,12] Based on DFT calculations, we have shown that functionalized CNT can be used to bind uranyl ions much more efficiently as compared to their unfunctionalized counterpart. Further, we have also functionalized the CNT with supramolecule such as cucurbituril (CB-[5]). We find that the binding of uranyl with CB-[5] upon bound to CNT is much stronger as compared to bare CB-[5] itself.^[13] Recently, DFT based calculations on a series of uranyl complexes encapsulated with single walled (SW)-CNT to understand their encapsulation affinities (Fig. 3). We find that uranyl-aqua complex ($[\text{UO}_2(\text{H}_2\text{O})_5]^{2+}$) binds stronger as compared to uranyl-hydroxo-complex ($[\text{UO}_2(\text{OH})_4]^{2-}$) due to the variable overall charge of the complex. Further, we have considered the binding

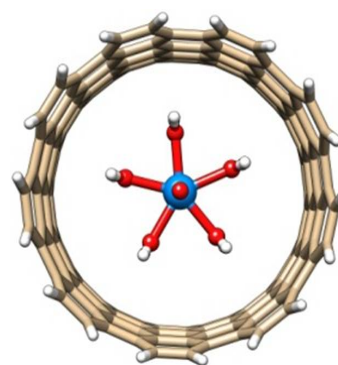


Fig. 3: Encapsulated hydrated uranyl to CNT

affinities of uranyl formate complexes with different formate stoichiometries (1:1, 1:2 and 1:3) with SW-CNT.^[14] Here again, due to variable charges, cationic mono-formate-uranyl ($[\text{UO}_2(\text{FM})(\text{H}_2\text{O})_3]^{1+}$) complex binds stronger as compared to anionic tri-formate uranyl ($[\text{UO}_2(\text{FM})_3]^{1-}$). Further, due to the very weak binding of commonly found in $[\text{UO}_2(\text{FM})_3]^{1-}$ to CNT, we have sealed the tubular ends of SW-CNT with functionalized C_{36} fullerene. We note that binding affinity is not

improved as compared to its unsealed counterpart. However, upon functionalizing (at the hub carbon) the C₃₆ cork, the binding affinity of [UO₂(FM)₃]¹⁻ is larger inside the CNT due to favorable hydrogen bonding interactions with the uranyl oxygens. Our findings are consistent with the recent experimental observations which will help to design novel nanomaterial for NWM processes.^[15]

Selective binding of Uranyl with Novel ligands

Selective separation of uranyl ion from aqueous solution is one of the most important criteria for sustainable nuclear energy production. Very recently, we have investigated a known but unexplored extractant, tetraalkyl urea, which shows supreme selectivity (close to 100%) for uranium in the presence of interfering thorium and other lanthanide ions in nitric acid medium.^[16] The structural characterization of the uranyl complex provides insight into stronger interaction between uranium and the ligand. The uranyl binding with the extractant is thermodynamically more favorable as compared to thorium and the selectivity is achieved through a combination of electronic and steric effects.

Speciation of Uranyl in Humic and Fulvic acid

The speciation of uranyl ion in fulvic acid (FA) and humic acid (HA), based on realistic models are systematically studied using density functional theory.^[17] Due to the lack of crystal structure of availability of HA, a systematic way to attain the possible structure for HA is proposed based on a combined MD and quantum chemical approach. Our predicted geometric structure and energetics reveal many interesting features such as conformational flexibility computed for HA, in agreement with the experimental suggestions. Potential binding sites are proposed for uranyl binding to HA and FA. Our energetics reveals that apart from the uranyl carboxylate binding, additional binding sites such as chelation and hydroxo binding to uranyl should be considered as well.

Outlook

From the variety of systems that we have investigated, we believe that upon incorporating solvent effects and approximate relativistic effects within the DFT framework, we believe that quantum chemical calculations are extremely useful to understand the speciation and binding of heavy metal ions such as uranyl. Our computational strategy is a general strategy and thus can be used for other heavy metal ions such as cesium or americium.^[18-24]

Acknowledgements

I sincerely thank all my collaborators, Dr. S. K. Ghosh, Dr. S. Kannan, Dr. P. K. Mohapatra, Dr. T. Bandyopadhyay, Dr. K. Srinivasu, Mr. B. Sadhu, Mr. L. Mishra and Dr. Pranaw Kumar, for their intriguing discussions. I thank Dr. B. N. Jagatap for his kind support and BARC computer center for providing the high performance parallel computing facility (Adhya and Ajeya Systems).

References

1. J. J. Katz, L. R. Morss and G. T. Seaborg, *The Chemistry of the Actinide Elements*, 2nd ed.; Chapman and Hall: London, **1986**.
2. D. M. Taylor, *Rev. Environ. Health*, **1997**, *12*, 147.
3. D. R. Lovley, E. J. P. Phillips, Y. A. Gorby, E. Landa, *Nature*, **1991**, *350*, 413.
4. G. Schreckenbach and G. A. Shamov, *Acc. Chem. Res.* **2010**, *43*, 19.
5. L. Gagliardi and B. O. Roos, *Inorg. Chem.* **2002**, *41*, 1315.
6. G. A. Shamov and G. Schreckenbach, *J. Phys. Chem. A* **2005**, *109*, 10961.
7. J. P. Austin, M. Sundararajan, M. A. Vincent and I. H. Hillier, *Dalton Trans.*, **2009**, 5902.
8. J. P. Austin, N. A. Burton, I. H. Hillier, M. Sundararajan, M. A. Vincent, *Phys. Chem. Chem. Phys.* **2009**, *11*, 1143.
9. M. Sundararajan, A. J. Campbell and I. H. Hillier, *J. Phys. Chem. A*, **2008**, *112*, 4451.
10. M. Sundararajan, R. S. Assary, I. H. Hillier, D. J. Vaughan, *Dalton Trans.* **2011**, *40*, 11156.
11. Sundararajan, M.; Ghosh, S. K. *J. Phys. Chem. A* **2011**, *115*, 6732.
12. Jena, N, K.; Sundararajan, M.; Ghosh, S. *RSC Adv.* **2012**, *2*, 2994.
13. M. Sundararajan, *Separat. Science & Technol.*, **2013**, *48*, 2391.
14. M. Sundararajan and K. Srinivasu. *Unpublished results*.
15. P. Luksirikul, B. Ballesteros, G. Tobias, M. G. Moloney and M. L.H. Green, *Carbon*, **2010**, *48*, 1912.
16. B. G. Vats, D. Das, B. Sadhu, S. Kannan, I. C. Pius, D. M. Noronha, M. Sundararajan and Mukesh Kumar, *Dalton Trans.*, **2016**, *45*, 10319.
17. M. Sundararajan, G. Rajaraman and S. K. Ghosh, *Phys. Chem. Chem. Phys.*, **2011**, *13*, 18038.
18. P. K. Verma, P. Pathak, N. Kumari, B. Sadhu, M. Sundararajan, V. K. Aswal, P. K. Mohapatra, *J. Phys. Chem. B.* **2014**, *118*, 14388.
19. M. Sundararajan, V. Sinha, T. Bandyopadhyay and S. K. Ghosh, *J. Phys. Chem. A.* **2012**, *116*, 4388.
20. B. Sadhu, M. Sundararajan and T. Bandyopadhyay, *Inorg. Chem.*, **2016**, *55*, 598.
21. P.K. Verma, Neelam Kumari, P.N. Pathak, B. Sadhu, M. Sundararajan, V.K. Aswal, P.K. Mohapatra, *J. Phys. Chem. A.* **2014**, *118*, 3996.
22. M. Sundararajan and T. Bandyopadhyay, *J. Phys. Chem. B.* **2015**, *119*, 10989.
23. B. Sadhu, M. Sundararajan, T. Bandyopadhyay. *J. Phys. Chem. B.* **2015**, *119*, 12783.
24. B. Sadhu, M. Sundararajan, G. Velmurugan, P. Venuvanalingam, *Dalton Trans.* **2015**, *44*, 1545

Computational Modeling of Novel Materials for Hydrogen Energy Related Applications

K. Srinivasu

Theoretical Chemistry Section

**Dr. K. Srinivasu is the recipient of the
DAE Young Scientist Award for the year 2014**

Abstract

Hydrogen is considered to be one of the best alternative, renewable and carbon-free energy carriers. However, its generation, storage and utilization are posing major challenges. Through *ab initio* investigations, we proposed s-triazine based graphitic carbon nitride as a possible metal-free photocatalyst for solar water splitting. We have also shown that the electronic band structure of graphitic carbon nitrides can be tuned through doping with non-metal elements as well as by metal decoration. The detailed mechanism of water splitting reaction on the photocatalyst surface has been studied and the associated overpotentials for each half-cell reactions were measured. For effective storage of hydrogen in molecular form, varieties of light metal decorated molecules and materials were modelled by using some of the elegant chemical concepts such as the electrostatic interactions, curvature of the carbon nanomaterials, aromaticity etc.

Introduction:

Energy is considered to be the key factor in deciding the social and economic development of any country. Worldwide, especially in the developing countries, energy sector has been given prime importance in view of rapidly increasing energy demands due to the day by day improved standards of living along with the industrial revolutions.¹ Gradually depleting fossil fuel resources and their adverse effects on environment are providing the motivation to search for a clean and sustainable energy system. Hydrogen has been accepted worldwide to be one of the best possible alternative renewable energy carriers.²⁻⁴ Though hydrogen is having very high energy density per unit mass, its energy density per unit volume is very less. At ambient conditions of 25 °C temperature and 1 bar pressure, 1 kg of hydrogen requires a volume of ~11 m³. Hence, developing effective hydrogen storage technology for transportation applications is highly challenging and one of the key factors in moving towards the hydrogen economy.

Though hydrogen is the most abundant element on the earth, less than 1% of it is present as the molecular hydrogen and majority of it is in chemically bonded state like water and hydrocarbons. Hence the generation of molecular hydrogen from the other forms requires breaking those molecules which is energetically intensive. The overall water splitting reaction is thermodynamically an uphill reaction with a positive free energy change of $\Delta G = +237.12$ kJ/mol. The hydrogen production from water can be carried out through different means such as thermal, electrical, photonic and biochemical methods. The primary energy needed for different methods to produce hydrogen can be obtained from different green energy sources like thermal and electrical energy from solar, wind,

geothermal, tidal, wave, ocean thermal, hydro, biomass, nuclear energy, etc.⁵ An ideal way for achieving sustainable energy is through the use of solar energy to convert water into hydrogen and oxygen. Solar water splitting using semiconductor photocatalyst has attracted immense research interest after the original work by Honda and Fujishima⁶ using a semiconductor anode such as TiO₂ and a metal cathode like platinum. To be a good photocatalyst for water splitting, the materials should satisfy several requirements, viz. (i) suitable bandgap for efficient absorption of solar visible-light (ii) appropriate band edge potentials for overall water splitting (iii) ability to separate photo generated electron-hole pairs (iv) stability towards chemical and photo corrosion in aqueous environments etc.⁷ For a photocatalyst to complete the overall water splitting, its conduction band bottom should be more negative than the proton reduction potential (0 V vs. NHE) and the top of the valence band should be more positive than the oxidation potential of water (+1.23 V vs. NHE). Apart from the conventional materials such as transition metal oxides, nitrides, oxinitrides etc, polymeric semiconductor materials like graphitic carbon nitride (g-C₃N₄) materials are found to have great potential as photocatalyst. In a recent study, Wang et al.⁸ have reported the melem-based polymeric graphitic carbon nitrides (g-C₃N₄) as a metal-free photocatalyst for visible-light driven hydrogen production through water splitting. g-C₃N₄, with appropriate band structure for overall water splitting along with its high thermal and chemical stability gained lot of interest in designing a metal-free catalyst. However, this material is reported to have a very poor quantum yield of ~0.1% which is attributed to the high recombination rate of electron-hole pairs generated. To overcome this problem, many methods are proposed to tune the properties viz. doping, metal decoration, introducing porosity, making

graphene/C₃N₄ composites etc.⁹⁻¹¹ Pan et al.¹² have shown that the g-C₃N₄ nanotubes have delocalised valence top states unlike sheet which is having strongly localized valence top states indicating the larger mobilities in nanotubes. They have also shown that functionalization of these tubes with metals like Pt and Pd can enhance the photocatalytic properties of these nanostructure materials.

Developing efficient hydrogen storage technology for transportation applications at ambient conditions is another key challenge in hydrogen economy. A good hydrogen storage material should satisfy certain operating requirements such as: (i) hydrogen absorption and desorption enthalpies should be in-between that of chemisorption and physisorption, (ii) fast kinetics at ambient conditions for quick uptake and release of hydrogen, (iii) high gravimetric and volumetric densities for effective hydrogen storage, (iv) effective heat transfer, (v) Long recyclable lifetime of the material for hydrogen absorption/desorption, (vi) high mechanical strength and durability, and (vii) safety at operational conditions.¹³ Currently, hydrogen is usually stored through two technically well-understood technologies, high pressure compression of the gas and cryogenic storage of liquid hydrogen and both these methods are neither safe nor cost effective. Another important way of storing hydrogen is by absorbing it either physically or chemically in the form of metal or chemical hydrides or adsorbing it on the surfaces and inside the pores of a porous solid matrix. In physical adsorption, hydrogen is bound to the substrate through weak van der Waals forces of interaction between the hydrogen and the substrate. As the binding interactions between hydrogen molecules and the substrate are very weak, physisorption typically takes place at low temperature. Doping with light metal atoms like alkali and alkaline earth metals is found to be effective in improving the hydrogen binding energies and varieties of metal decorated materials have been explored for hydrogen storage.

Computational Methods

In all our studies, we have employed different quantum mechanical methods, viz. wave function based Hartree-Fock and MP2 methods and also the density functional theory (DFT) based methods for all the studies carried out. In principle, the molecular level calculations are carried out by using the localised Gaussian basis sets (using GAMESS), while the plane-wave basis sets were used for the periodic solid state calculations (using VASP).¹⁴⁻¹⁶ Within the framework of DFT, we have used several exchange-correlation energy functionals, such as the local density approximation (LDA), generalized gradient approximation (GGA), Becke's three-parameter exchange functional and Lee-Yang-Parr correlation functional (B3LYP), and also the recently developed Minnesota functionals. As it is known that the band gaps calculated from PBE functional are underestimated, we have also used the more accurate

hybrid functional, developed by Heyd, Scuseria, and Ernzerhof (HSE).

Graphitic Carbon Nitride Based Photocatalyst for Solar Water Splitting

Through *ab initio* electronic structure studies, we explored the s-triazine based polymeric graphitic carbon nitride with CN stoichiometry (g-CN) for its photocatalytic activity towards water splitting.¹⁷ The optimized cell parameter from PBE method is found to be 7.127 Å with the C-C and C-N bond distances of 1.510 Å and 1.341 Å respectively. From the PBE calculations, g-CN is found to have a direct band gap of 1.54 eV along the k-vector **K**. However, as it is well known that the band gaps calculated from pure DFT functionals like PBE are underestimated and the hybrid functionals like HSE06 can deliver reasonably good results, we have also calculated the band structure of g-CN using HSE06 method. The band gap of g-CN calculated from HSE06 method is found to be 3.18 eV which is more than double the corresponding value from PBE functional. The conduction band minimum (CB_{min}) calculated from HSE06 method is found to be -3.37 eV which is above the proton reduction potential and the valence band maximum (VB_{max}) is found to be -6.55 eV which is below the water oxidation potential. As the band edge potentials are suitable for the overall water splitting to generate hydrogen, the g-CN can be expected to be a good photocatalyst material for hydrogen generation.

To verify the effect of stacking on the electronic structure of g-CN, we have also studied the bilayer as well as the trilayer of g-CN. For the bilayer, we have considered two different stacking modes, AA and AB. From the optimized structures, the AB stacking mode is found to be energetically more favourable as compared to the AA mode. The optimized inter layer separation from the PBE method is found to be 3.088 Å indicating the strong coupling between the two g-CN layers. The interlayer interaction energy per unit cell is found to be -0.57 eV. The calculated band gap is found to be 2.81 eV which is 0.08 eV less as compared to that of the single layer. This indicates that the band gap is reduced due to the interlayer coupling in g-CN.

To see any further effect of inter-layer coupling on the electronic structure, we have also studied the electronic structure of trilayer g-CN. For trilayer, we have added one more g-CN sheet above the bilayer in two different ways, ABA and ABC. It has been found that the ABC mode of stacking is energetically more favourable with interlayer separation of 3.029 Å and the corresponding inter-layer interaction energy per unit cell is calculated to be -1.19 eV. The calculated band gap is found to be 2.75 eV which is 0.14 eV less as compared to the single layer band gap. We have studied the effect of doping with different non-metal elements like boron, oxygen, sulphur, and phosphorous. The results on non-metal doping reveal that the phosphorous doping will be more

suitable to bring down the band gap of g-CN without creating any undesirable mid gap states. The calculated optical absorption spectra show significant enhancement in visible light absorption efficiency on phosphorous doping. The positions of band edges in pure g-CN as well as phosphorous doped counterpart with respect to water redox levels are found to satisfy the thermodynamic criteria for overall water splitting.

To understand the detailed mechanism of overall water splitting reaction mechanism we have investigated both the oxygen evolution reactions (OER) and hydrogen evolution reactions (HER) on the g-CN surface.¹⁸ The calculated binding energy of a water molecule on the g-CN surface is found to be -0.56 eV and the driving force is the hydrogen bonding between the water hydrogen atoms and nitrogen atoms of g-CN. A systematic study of different intermediate reaction steps involved in both the OER and HER has been carried out. The calculated overpotential for the OER is found to be -0.93 V and the holes in the valence band are at a potential of 2.64 eV (with reference to the NHE). These results on the OER mechanism indicate that g-CN can facilitate the reaction without the aid of any co-catalyst which is highly desirable for designing an active photocatalyst. The study of the HER on g-CN reveals that the reaction has overpotential of around 1.0 eV. As the photogenerated electrons in the conduction band are located just 0.26 eV above the hydrogen reduction level, the reduction reaction requires a cocatalyst. Our computational studies will definitely provide better understanding of the underlying mechanism and useful insights into designing new g-CN photocatalysts and modification of its electronic structure to facilitate the overall water splitting on the g-CN surface.

Hydrogen Adsorption on Light Metal Decorated Molecules and Materials

Carbon nanomaterials are found to be one of the promising candidates for hydrogen storage because of their low molecular weight and high surface area. To understand the effect of charged surface and nature of substrate, we have investigated varieties of organic molecular systems, such as, cyclo-butadiene (C_4H_4), cyclopentadienyl radical (C_5H_5), benzene (C_6H_6) and cyclo-octatetraene (C_8H_8) and their alkali metal-doped complexes for hydrogen adsorption.¹⁹⁻²⁰ We have demonstrated that creating a charged surface on the model system by doping the alkali metal cations can improve the hydrogen adsorption energy significantly. Among the alkali metal cations (Na^+ and Li^+), it is observed that Na^+ can interact with more number of hydrogen molecules as compared to Li^+ . Introduction of a functional group in the model system also affects the binding of the alkali metal cation to the organic system and the hydrogen adsorption significantly due to the electronic induction effects. It can be mentioned that the model studies considered in the present investigation can provide a detailed insight into the adsorption of hydrogen molecules in carbon nanomaterials, metal

organic frameworks and other materials where benzene derivatives are the building blocks. We have also shown that the binding of sodium atom, especially, with the π electron deficient systems like C_4H_4 , C_5H_5 and C_8H_8 is observed to be energetically feasible and there is a charge transfer from the sodium atom to the organic molecules. Such interactions are not possible with benzene molecule due to its exceptional aromatic stability. Among all the alkali metal atom doped complexes, C_5H_5-Na is found to be the most stable and the interaction of molecular hydrogen is also found to be very strong. The aromaticity in such molecular systems plays a very important role in stabilizing the ionized organometallic complex doped with alkali metal atoms. Similar to carbon systems, we have also studied different boron hydrides alkali metal complexes for their hydrogen adsorption characteristics.²¹⁻²²

We have demonstrated the important role of the curvature exhibited by different carbon nanomaterials on the molecular hydrogen adsorption. In order to represent the curvature effects in more realistic manner, we have considered different sizes of fullerenes, C_{20} , C_{28} , C_{32} , C_{36} , C_{60} , and C_{70} .²³ The high reactivity of the surface with the maximum curvature has been attributed to the weakening of the π -conjugation due to the bending of the carbon surface which makes the system have quasi sp^2 - sp^3 hybridization with substantial s-orbital character. Based on our results, it can be mentioned that the metal doped nanotubes with smaller radius will be a better candidate for hydrogen adsorption. We have also shown that the truncated doping of carbon with nitrogen in C_{60} can generate porphyrin-like porous fullerene, $C_{24}N_{24}$ that can bind with transition metal atoms with high interaction energies which are nearly double the cohesive energies of the corresponding metals.²⁴ Hence the clustering problem associated with the transition metals can be avoided. These transition metal sites are found to trap molecular hydrogen through Kubas type of interaction, and the hydrogen adsorption energies are also found to be suitable for ambient temperature hydrogen storage.

We have explored two-dimensional carbon materials graphyne, graphdiyne and conjugated microporous polymers for their energy storage applications.²⁵⁻²⁶ Lithium metal binding to these carbon materials is found to be enhanced considerably and is more than the cohesive energy of lithium which can be attributed to the presence of more electronegative sp carbon in the framework. This strong metal binding energy will ensure the stability of the materials towards recyclability. We have also Due to the electron transfer from lithium metal to the carbon surface in these materials, the lithium sites are found to be cationic and thus adsorb molecular hydrogen with desired adsorption energies.

Metal organic frameworks (MOFs) are found to be promising materials for hydrogen storage because of their porous and robust nature and also exceptionally high specific surface areas and pore volumes.²⁷

However, the main driving force for binding is through van der Waals interaction and requires low temperatures for achieving a significant hydrogen storage capacity. One of the important strategies to improve the hydrogen adsorption enthalpies is through metal decoration. In most of the metal-doped framework materials studied, the metal atom is found to be positioned on top of the aromatic six-membered carbon rings with poor metal binding energies leading to aggregation of adsorbed metal atoms to form clusters, and is therefore not suitable for reversible hydrogen adsorption. We have proposed that the substitutional doping with boron to improve the metal binding energies. From our calculated results, it is observed that the binding energy of metal with MOF-5 can be improved by disturbing the aromatic nature of the linker group through the substitution of its two carbon atoms with two boron atoms, thus making it electron-deficient. The calculated metal binding energy with the modified linker is found to be extremely high. These adsorbed metal sites are shown to possess partial positive charges and thus can adsorb molecular hydrogen. We have also modelled different three-dimensional supercubane based porous carbon materials with varying number of carbon atoms starting from C₈ cubane unit to an expanded C₅₆ cubic unit and also with different inter-cubane C-C linking units.²⁸ The expanded supercubane, C₃₂ is found to adsorb hydrogen with a gravimetric density of 2 wt% and adsorption energy of -2.5 kcal/mol. However, at higher hydrogen densities and in the case of highly porous systems like C₁₄₄, the hydrogen adsorption energies are very low indicating that porous materials with medium size pores are preferred for better hydrogen storage.

Concluding Remarks

Using first principle calculations, we have investigated different molecular systems and materials for their possible applications in hydrogen energy. We have explored the g-CN based materials as an important class of materials for use in photocatalytic water splitting to generate hydrogen. These kinds of polymeric materials are shown to have more advantages over the conventional metal oxide based semiconductors. The modelled g-CN materials are found to be wide band gap semiconductor materials and we have tried to engineer the band gap through doping of different metals as well as non-metals. The importance of the presence of an ionic site on the hydrogen adsorption energies in carbon and boron based materials has been explained. Light metal decorated carbon fullerenes and its hetero atom substituted fullerenes were explored for hydrogen adsorption. Varieties of two-dimensional and three-dimensional porous materials were designed for efficient hydrogen storage. These computational studies can provide valuable insights for exploring new functional materials for hydrogen energy applications.

Acknowledgements

It is a pleasure to thank Dr. Swapan K Ghosh for his kind interest and valuable guidance. I thank Dr. K. R. S. Chandrakumar and Mr. Brindaban Modak who have contributed to the present work. I wish to acknowledge the BARC computer center for providing the high performance parallel computing facility. I thank Dr B. N. Jagatap for his kind support and encouragement.

References

- Hoffert, M. I.; Caldeira, K.; Jain, A. K.; Haites, E. F.; Harvey, L. D. D.; Potter, S. D.; Schlesinger, M. E.; Schneider, S. H.; Watts, R. G.; Wigley, T. M. L. Wuebbles, D. J. *Nature*, 395 (1998) 891.
- Züttel, A.; Remhof, A.; Borgschulte, A.; Friedrichs, O. *Phil. Trans. R. Soc. A* 368 (2010) 3329.
- Lewis, N. S.; Nocera, D. G. *Proc. Natl. Acad. Sci. U.S.A.*, 103 (2006) 15729.
- Lubitz, W.; Tumas, W. *Chem. Rev.* 107 (2007) 3900.
- <http://www.cleanenergystates.org/>
- Fujishima, A.; Honda, K. *Nature* 238 (1972) 37.
- Yerga, R. M. N.; Galván, M. C. A.; del Valle, F.; de la Mano, J. A. V.; Fierro, J. L. G. *ChemSusChem* 2 (2009) 471.
- Wang, X.; Maeda, K.; Thomas, A.; Takanabe, K.; Xin, G.; Carlsson, J. M.; Domen, K.; Antonietti, M. *Nat. Mater.* 8 (2008) 76.
- Wang, X.; Maeda, K.; Chen, X.; Takanabe, K.; Domen, K.; Hou, Y.; Fu, X.; Antonietti, M. *J. Am. Chem. Soc.* 131 (2009) 1680.
- Shalom, M.; Inal, S.; Fettkenhauer, C.; Neher, D.; Antonietti, M. *J. Am. Chem. Soc.* 135 (2013) 7118.
- Lin, Z.; Wang, X. *Angew. Chem. Int. Ed.* 52 (2013) 1735.
- Pan, H.; Zhang, Y.; Shenoy, V. B.; Gao, H. *ACS Catal.* 1 (2011) 99.
- Grochala, W.; Edward, P. P. *Chem. Rev.* 104 (2004) 1283.
- Schmidt, M. W.; Baldrige, K. K.; Boatz, J. A.; Elbert, S. T.; Gordon, M. S.; Jensen, J. H.; Koseki, S.; Matsunga, N.; Nguyen, K. A.; Su, S. J.; Dupuis, M.; Montgomery, J. A. *J. Comput. Chem.* 14 (1993) 1347.
- Kresse, G.; Furthmüller, J. *Comput. Mat. Sci.* 6 (1996) 15.
- Kresse, G.; Furthmüller, J. *Phys. Rev. B.* 54 (1996) 11169.
- Srinivasu, K.; Modak, B.; Ghosh, S. K. *J. Phys. Chem. C* 118 (2014) 26479–26484.
- Srinivasu, K.; Ghosh, S. K. *J. Mater. Chem. A* 3 (2015) 23011-23016.
- Srinivasu, K.; Chandrakumar, K. R. S.; Ghosh, S. K. *Phys. Chem. Chem. Phys.*, 10 (2008) 5832-5839.
- Srinivasu, K.; Chandrakumar, K. R. S.; Ghosh, S. K. *ChemPhysChem* 10 (2009) 427-435.

21. Srinivasu, K.; Ghosh, S. K. *Int. J. Hydrogen Energy* 36 (2011) 15681–15688.
22. Srinivasu, K.; Ghosh, S. K. *J. Phys. Chem. C* 115 (2011) 1450–1456.
23. Chandrakumar, K. R. S.; Srinivasu, K.; Ghosh, S. K. *J. Phys. Chem. C* 112 (2008) 15670–15679.
24. Srinivasu, K.; Ghosh, S. K. *J. Phys. Chem. C* 116 (2012) 25184–25189.
25. Srinivasu, K.; Ghosh, S. K. *J. Phys. Chem. C* 116 (2012) 5951–5956.
26. Srinivasu, K.; Ghosh, S. K. *RSC Adv.*, 2 (2012) 2914–2922.
27. Srinivasu, K.; Ghosh, S. K. *J. Phys. Chem. C* 115 (2011) 16984–16991.
28. Srinivasu, K.; Ghosh, S. K. *J. Phys. Chem. C* 116 (2012) 25015–25021.

Design and Development of Precision Scientific Instruments and Parallel Manipulators

Ramnik Singh, S.P. Srivastava, V.K. Mishra, P.I. Hadagali and K.N. Karn,
Centre for Design and Manufacture

Mala N.Rao, Saibal Basu
Solid State Physics Division

**Shri Sandeep Kumar Singh is the recipient of the DAE Young Engineer Award
for the year 2014**

Introduction

Precision instruments play a vital role in many areas of scientific and engineering applications. The quality of these instruments predicts its performance. Some important quality measures of the instruments are accuracy, precision and reliability. These high precision instruments are designed and manufactured with high end softwares and manufacturing facilities. Subsequently they are tested for functional performance to qualify them.

Neutron Focussing Mechanism for SSPD, Dhruva

It is a PC controlled neutron focusing mechanism[1] known as double curvature monochromator[2] which consists of a 3x5 array of crystals mounted on links provided in the vertical and horizontal direction. The cam and follower based mechanism has been used for designing the instrument. The links are connected to followers at each end which move in the helical groove of the cam for certain rotation of the camshaft. Further the links rotate about pivot points to get the required tilt for given radius of curvature. In the given setup the vertical and horizontal focussing are independent.

Specifications of the instrument

- 1) Crystal-size: 35mmx25mmx10mm.
- 2) Horizontal focussing: 500mm to ∞.
- 3) Vertical focussing: 5 to -1 degrees
- 4) Repeatability is 0.1 deg.

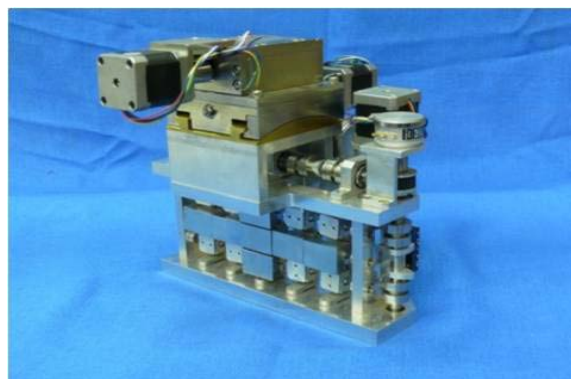


Fig.1: Double Curvature Neutron Focussing Monochromator

Three row Si(113) Crystal Bender(SSPD)

A special type of bender[3] has been designed to bend three nos. of Si(113) crystals arranged in a column simultaneously to focus neutron beam from neutron guide of size 100mm x 25mm to 4mm x 4mm(square). It is to be used as a monochromator for polarised neutron reflectometer in Dhruva Reactor Hall. It comprises of 3 asymmetrically cut Si(113) crystals of size (200mm x 45mm x 4mm(thk)). The crystals are required to be bent precisely in the horizontal plane from infinite radius value to 10-15m. This is being achieved by help of a differential screw and lever mechanism. The vertical focussing is obtained by the inherent nature of the crystals. The double curvature focussing provides a defined range of wavelengths of neutron beam at the sample from the incident neutron beam. The main application of this instrument is to carry out surface film studies.

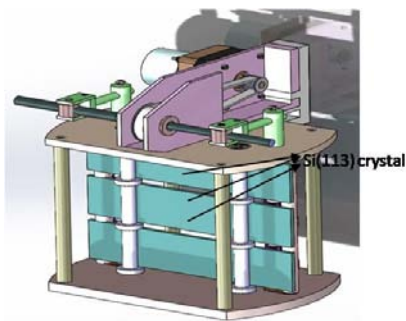


Fig.2: Isometric 3 dimensional view of the three row Si(113) Crystal Bender

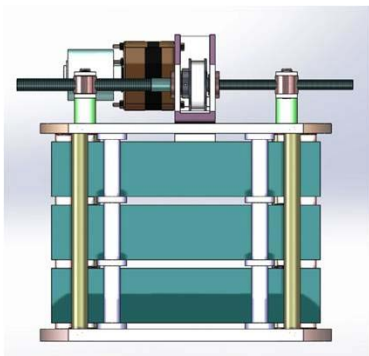


Fig.3 Front view of the three row Si(113) Crystal Bender

Ultra High Vacuum(UHV) compatible miniature hexapods(CDM)

Under the XIIth plan, CDM is developing Ultra High Vacuum (UHV) compatible miniature hexapods[4]. These are required to be of high accuracy and resolution to the level of sub-microns. The typical size of the hexapod will be 200mm(height) x • 120mm(top and bottom plates).The legs of this hexapod will be based on UHV compatible piezo actuators with double hinge joints for connecting the top and bottom plates. These are used for indigenous research and synchrotron beamline applications. The specifications of the same are tabulated below.

| | RANGE | RESOLUTIO N | ACCURACY |
|----------------|-----------------|----------------|----------|
| X | ±15mm | ±.5µm | ±2 µm |
| Y | ±15mm | ±.5µm | ±2 µm |
| Z | ±15mm | ±.5µm | ±2 µm |
| θ _x | ±2 ⁰ | ±.5arcsec | ±1arcsec |
| θ _y | ±2 ⁰ | ±.5arcsec | ±1arcsec |
| θ _z | ±2 ⁰ | ±.5arcsec | ±1arcsec |

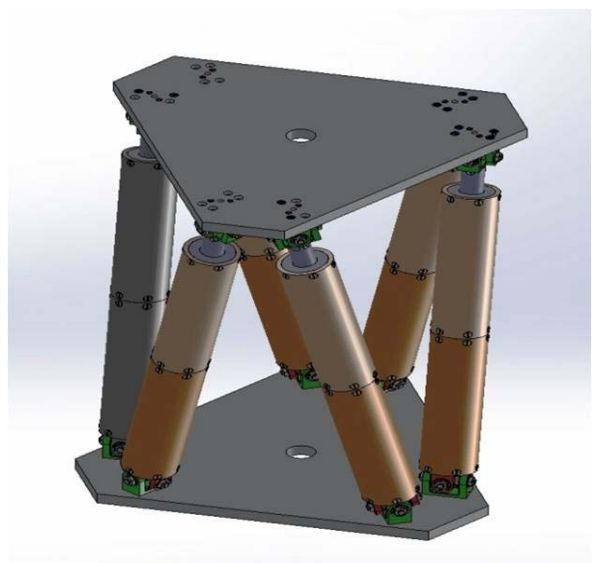


Fig.4: Isometric 3 dimensional view of miniature hexapod

Design and Development of Collimator Shielding for Neutron Radiography at VSSC, Kerala

The assembly comprises of a collimator which is required to collimate from 200 x 200 mm to 10 x 10 mm size and neutron generator for radiography. The complete assembly is mounted on a movable motorised stand using ball screw and LM(linear motion) guides that can translate 500mm along neutron beam direction. The shielding materials used are HDPE(High Density Polyethylene), Lead, Borated Polyethylene. It has been successfully installed and commissioned at VSSC.

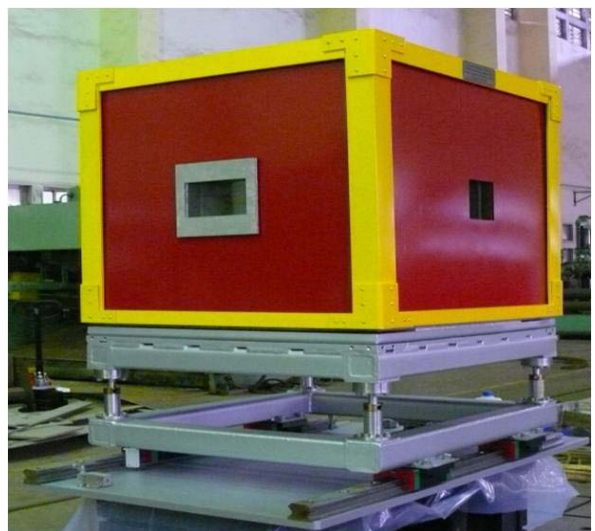


Fig.5: Collimator assembly with stand assembly

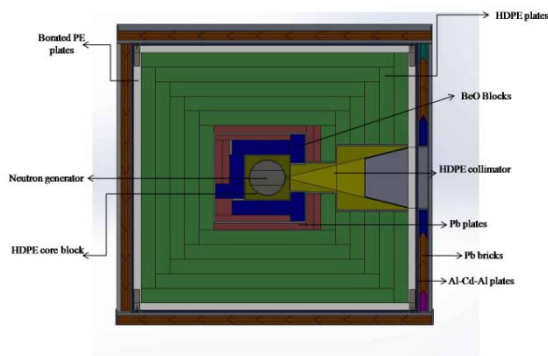


Fig.6: Cross Sectional view of collimator assembly

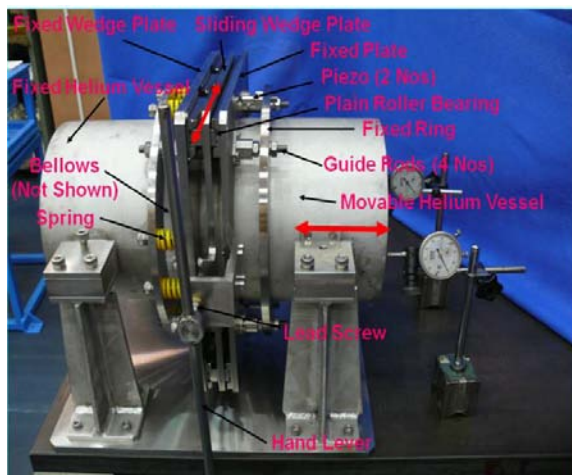


Fig.7: Double Wedge Tuner Assembly

Double Wedge Tuner(DWT) for NPD

A Double Wedge Tuner (DWT)[5] has been designed and developed for compensation of Lorentz force detuning and micro phonics stabilization of the superconducting cavities for International Linear Collider (ILC) operations. This is a co-axial device and can provide both the slow tuning and the fast tuning. DWT is installed around the Helium vessel which is in two halves, one movable and other fixed and is connected by bellows. The RF cavity is located inside Helium Vessel. This tuner mainly consists of two wedges, one fixed and other sliding which can move with respect to the fixed wedge. The fixed

wedge is integral part of the flange of movable half of the Helium Vessel. This has been designed & developed with the perspectives of simple design and less cost, as these are needed in very large numbers for the ILC. To validate the design a manually operated prototype has been developed & tested mechanically at Centre for Design and Manufacture (CDM), BARC.

Specifications:

Range of Double Wedge Cavity Tuner

1. Slow Structure Tuning = 2500 microns
2. Fast Tuning using Piezomaterial = 10 microns

References

1. Ramnik Singh, V.K.Mishra, A.K.Sinha, S.B.Jawale, Mala N. Rao Design and Development of a Double Curvature Neutron Focussing Monochromator, Proceedings of DAE-BRNS National Symposium on Nuclear Instrumentation 2013.
2. U Wildgruber and F Frey, A double focusing neutron monochromator consisting of facets, J. Phys. E: Sci. Instrum. 20 (1987).
3. F Frey and W Adlhart, A bent neutron comb monochromator, J. Phys. E: Sci. Instrum., Vol. 13, 1980.
4. D Stewart A platform with six degrees of freedom. Proc.Instr.Mech Engrs 1965-66, Vol 180 Pt 1 No.15.
5. Mishra, V.K.; Singh, Ramnik; Aravind, T.; Singh, J.V.; Sinha, A.K.; Suthar, R.L.; Singh, P.; Sahni, V.C. Double wedge tuner (DWT) for RF cavities Proceedings of the DAE-BRNS Indian particle accelerator conference, Vol.46 Issue 11,2009

Design and development of High Power Ultra Wideband Systems

Sandeep Kumar Singh, S. Mitra, Senthil K., Ranjeet Kumar, Archana Sharma,
K. C. Mittal, R. K. Rajawat
Accelerator and Pulse Power Division

**Shri Sandeep Kumar Singh is the recipient of the DAE Young Engineer Award
for the year 2014**

Abstract

High power ultra wideband (UWB) systems can be used for various applications like buried target detection, electrical characterization of materials, space debris detection and as a source for vulnerability studies on electronic circuits. Two high power UWB radiator systems have been developed at APPD, BARC Mumbai. The first one is a 120 kV, 66 Ohm system which uses balanced Transverse Electromagnetic (TEM) horn antenna for radiation of UWB pulse into the atmosphere. Pulse power system for this radiator consists of a Marx Generator and a pulse forming line which can generate a 110 kV, 5 ns pulse with a rise time of ~ 300 picoseconds. A balanced TEM horn type antenna was used in this system. Impedance of this antenna is matched to 66 Ohms at feed end and then gradually varies to match with free space impedance. This antenna can effectively radiate this kind of ultra-short sub-nanosecond rise time pulse. This system has generated an electric field of 10 kV/m at 10 m distance from the source. Second system is a Half Impulse Radiating Antenna (HIRA) based UWB system. HIRA based UWB system consists of three components, MARX generator, pulse forming line and HIRA antenna. MARX can generate maximum of 1000kV voltage pulse to charge the pulse forming line. Voltage pulse generated via discharge of pulse forming line sparkgap is radiated by HIRA. This system has generated an electric field of 20 kV/m at 10 m distance from the source. This article discusses the overall system performance with an emphasis on antenna design details and results.

Introduction

Extensive work is going on in the field of compressed high voltage high energy pulses for its immense importance in strategic applications [1]. Different laboratories in the world, are persistently giving efforts in the generation of shorter pulses (in the range of 5-10ns) of very fast rise time (hundreds of picoseconds). This kind of high energy pulses (1-5 Joules) or more can be fed directly to a matched broad band antenna to launch into the environment [2, 3]. These pulses will contain high power wide band frequencies ranging from 100MHz to 2GHz and can be extremely susceptible and lethal for modern day electronics of wide range and variety [2].

To be ideal, a perfect UWB pulser should be defined as a system capable of generating all range of pulses starting from dc to infinite frequency and amplitude of all the frequencies should be identical. Mathematically it can be shown that an impulse function can fulfill such requirement. It is impossible to generate extreme high frequency beyond few GHz by electrical discharges. Hence a practically feasible higher frequency limit is decided for designing UWB pulser. As stated above, an UWB pulser output is radiated into atmosphere using an antenna by the user. Minimum size of an antenna suitable to launch an electromagnetic wave depends on wavelength λ . Hence, if frequency of the launching wave goes low practical size of the required antenna goes very high. In this article details of two high power UWB systems developed at APPD, BARC are narrated.

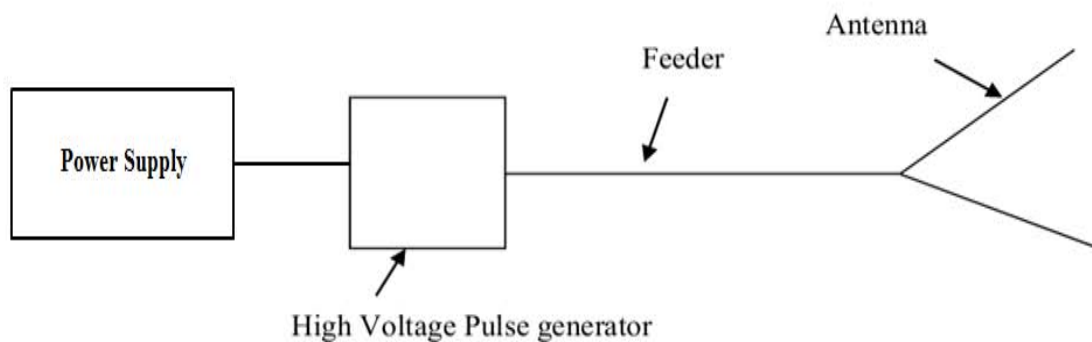


Fig. 1. Block Diagram of an UWB System

These systems can be used for industrial as well as strategic applications. These systems are mainly composed of three distinct components high voltage pulse generator, a pulse forming line and an UWB (ultra wide band) antenna [1, 4, 5]. First system uses a balanced TEM horn antenna as a radiator while the second system uses HIRA antenna for radiation of electromagnetic waves into the atmosphere.

UWB System Description

Block diagram for a general UWB system is shown in figure 1. Any high power UWB system is composed of three main subsystems: the primary source/power supply, the high voltage pulser or generator (which can be decomposed into several subsystems), and the antenna system along with feeding arrangement, as illustrated in figure 1. The first UWB system consists of 240 kV Marx generator, 66 Ω pulse forming line and a Balanced TEM horn antenna matched to PFL impedance. The second UWB system has a 1 MV Marx generator followed by a solid dielectric pulse forming line of 86 Ω impedance and Half Impulse Radiating Antenna.

Balanced TEM Horn Antenna based UWB System

In this system 30kV high voltage power supply is used for charging of the MARX generator. High voltage pulse generator part in this system consists of a Marx Generator, pulse forming line and low inductance switch just before the antenna. Antenna system in this system is a balanced TEM horn antenna along with an unzipper type of balun which converts the coaxial source geometry to a parallel plate feed type geometry. Actual system photograph is shown in figure 2. MARX generator has a maximum output voltage of 240 kV, which is used for the charging of pulse forming line. Pulse forming line terminated with a matched dummy load of 66 ohms, generates a 120 kV, 5 ns

pulse with ~ 300 ps rise time. This is a very compact system with a foot print of 1.7 m*1.5m and weight of the system is less than 200 kg. In actual system pulse forming line feeds the antenna system using a low inductance sparkgap switch which gets fired on reaching the breakdown voltage.

Balanced TEM Horn Antenna Design

TEM Horn antenna is a wideband, non dispersive, travelling wave antenna which consists of two metal plates which are flared in the shape of a horn. If the aperture height is comparable to wavelength, antenna can radiate at that frequency. In this system we have an unbalanced coaxial source feeding a balanced TEM horn antenna. For the interfacing of this unbalanced coaxial source with balanced antenna coaxial feed structure is gradually unzipped into parallel plate geometry [6, 7].



Fig. 2. High Power UWB system with balanced TEM Horn Antenna

Here taking consideration of dimensions of UWB system we have to use a transition for centre conductor of coaxial line also. Antenna performance was evaluated along with this feed arrangement using CST Microwave studio.

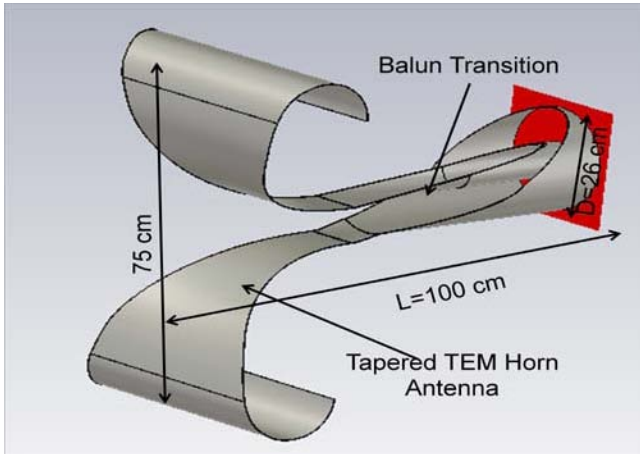


Fig. 3: Model of designed Antenna

Any unipolar pulse has got frequencies from DC to higher frequency limited by pulse rise time. It is not practically feasible to design an antenna which can radiate extremely low frequencies. That is why in case of ‘UWB’ systems for unipolar pulses, lowest frequency of interest is determined by the pulse width and highest frequency is determined by the rise time. In our case lowest frequency of interest will be around 200 MHz and highest frequency is 875 MHz according to rise time of the system. Taking the margins in account bandwidth for antenna was chosen to be 150 MHz to 1 GHz.

Spacing in between the electrodes at feed end was chosen in such a way that only TEM mode is excited onto the antenna. In this kind of transition as it is being fed by a single ended source, common mode currents at outside surface of line are caused by summation of reflections which originate over entire transition length. But the balun transition is smoothly tapered in such a way that net reflection at balun input is very small. Balun design before parallel plate feed was done in such a way that it provides

matching in between coaxial geometry of UWB system (66 Ohms) and parallel plate line (170 Ohm) at TEM horn antenna feed. An unzipper type balun was chosen for At 150 MHz half wavelength corresponds to one meter, practically balun length was chosen to be 60 cm so that antenna along with feed can be limited in 1 m. Design optimization was done in CST Microwave studio to meet performance parameters[6,7].

Simulation and Experimental Results

Model of TEM horn antenna used for simulation in CST Microwave studio is shown in figure 3. Waveguide port was used for exciting the structure in CST microwave studio. Antenna simulation results are shown in figure 4. These results clearly show that reflection coefficient of the designed antenna is better than -10 dB within required frequency range of 150 MHz to 1 GHz. Simulated gain of antenna 6.1 dB at 350 MHz. E plane pattern of antenna is slightly unbalanced as shown in figure 4. Simulated time domain response of designed antenna at boresight for a Gaussian pulse input is shown in figure, which is similar to Gaussian differentiated pulse waveform.

Experimental results for above system include testing of high voltage pulser with a dummy matched load and system’s radiated electric field response at boresight when high voltage pulser is connected to antenna. These results are shown in figure 6. For measurement of fast rising pulse (approximately hundreds of Pico second) of small pulse width (approximately 5ns) specific voltage divider of fast response time, was designed. Experimental results show that the system is capable of generating a pulse of maximum 120kV, 5ns pulse width with rise time of about ~ 300ps as shown in figure 5. Output radiated field of around 10 kV/m at 10 m is recorded. Radiated electric field waveform and waveform across matched load are shown in figure 5. Figure of merit for UWB system is achieved upto 100 kV. UWB gain of ~0.9 is achieved with an antenna of aperture size 75 cm and length 100 cm. Personal computer operation was disrupted at 15 m distance from the source using this system.

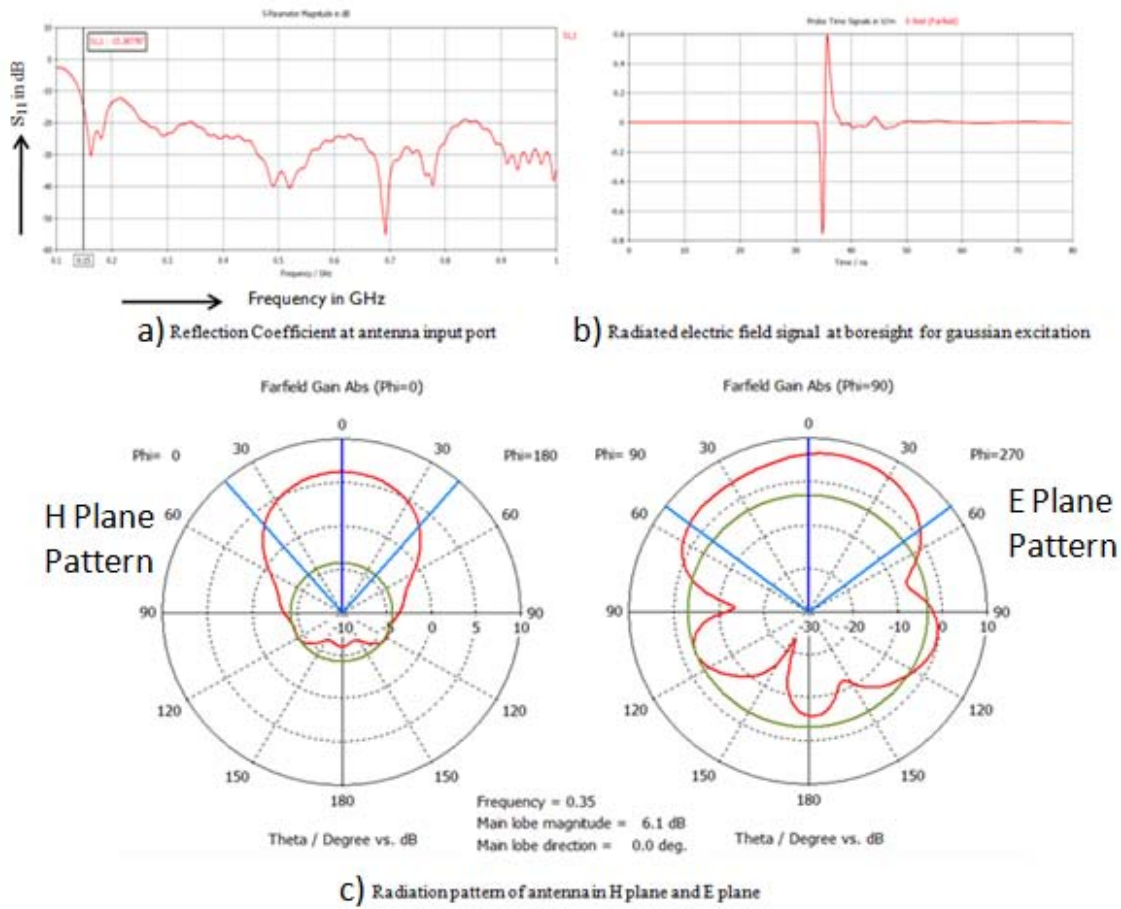


Figure 4. Antenna Simulation results

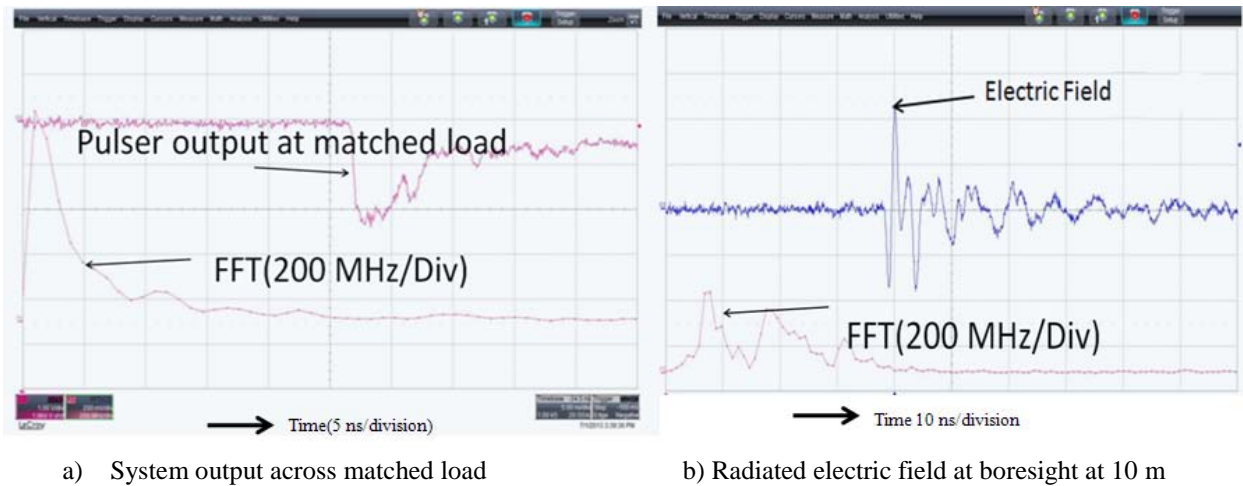


Figure 5. Experimental Results

HIRA Based UWB System

This system consists of a 20 stage Marx Generator which charges a solid dielectric pulse forming line of 100 ohm characteristic impedance using an inductor. Solid dielectric pulse forming line consists of a low inductance spark gap which acts as a peaking switch; output of pulse forming

line is fed to HIRA with 100 ohm impedance. HIRA antenna used in this system is a highly directive antenna with 3 dB beam width is 5 degrees. Actual system is shown in figure 6. This system has been successfully generated an electric field of 20 kV/m at 10 m distance from the source.

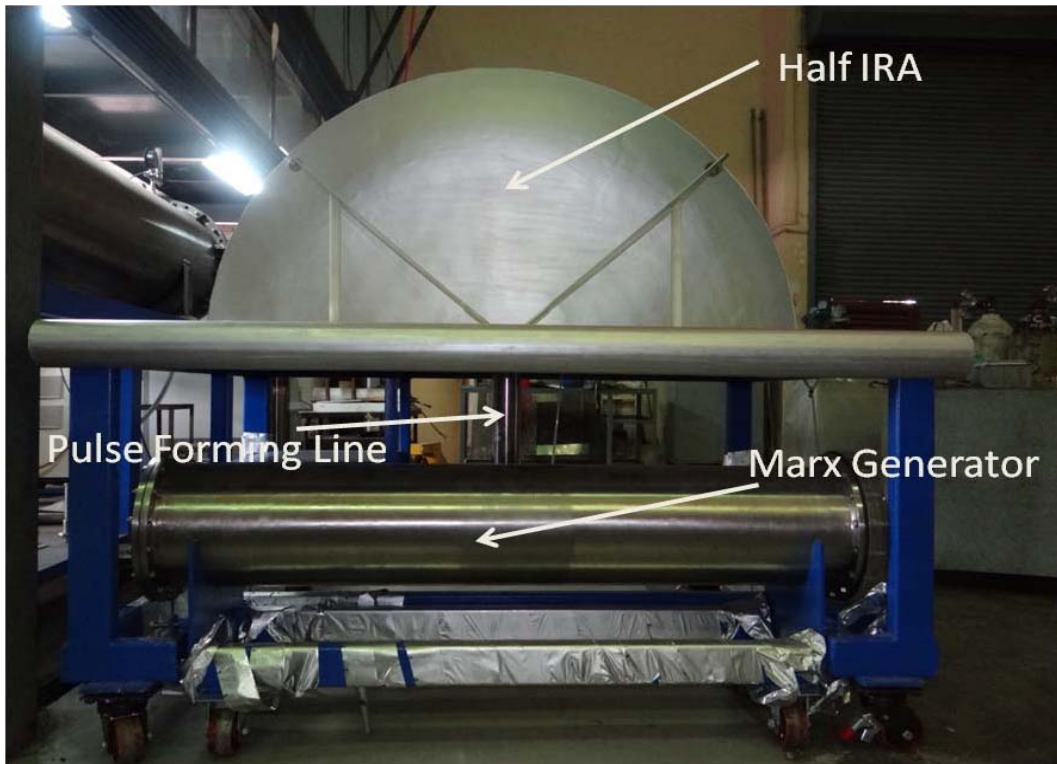


Fig. 6: HIRA based UWB System

Half Impulse Radiating Antenna Design

Half Impulse radiating antenna is used for radiation of UWB pulses in this system. This antenna is a paraboloidal reflector antenna with a TEM feed. Antenna diameter was chosen to be 2 m for appropriate electromagnetic field radiation. Antenna design was carried out using analytical formulas [8]. Same structure was modelled and simulated in CST microwave studio. Two constant impedance coplanar TEM feed lines are used for feeding the reflector antenna. Impedance of each feed line was 200Ω. Each feed arm is terminated with a 200 Ω copper sulphate aqueous resistor to provide low frequency impedance matching.

Far field E_{far} for a Half Impulse radiating antenna is calculated using following formula.

$$E_{far} = \frac{1}{2\pi c r f_g} \frac{D}{4\sqrt{2}} \frac{dV(t)}{dt} \quad (1)$$

Where D is antenna diameter, f_g is impedance ratio of antenna impedance Z_c to free space impedance Z_o i.e. $f_g = Z_c/Z_o$, c is velocity of light in free space. $V(t)$ is the applied voltage function at input of antenna.

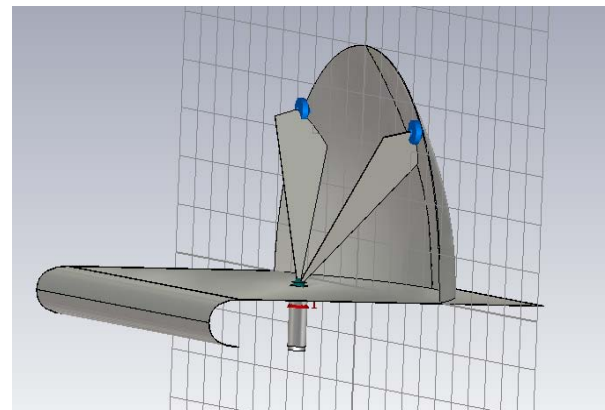


Fig. 7: Model of Half Impulse radiating antenna

Experimental Results

Far field for this system was measured using half TEM horn type of sensor. An electric field of 20 kV/m was recorded at 10 m distance from source. Radiated electric field was measured at different angles in Horizontal plane. Using this peak power pattern was obtained in horizontal plane. From the results it is clear that 3 dB beam width for this system in horizontal plane is 5 degrees, which indicates that the designed antenna has got a very good directivity. Experimental results for this system are shown in figure 8. This system has achieved a figure of merit of 200 kV. Personal computer operation was disrupted at 20 m distance from the source using this system.

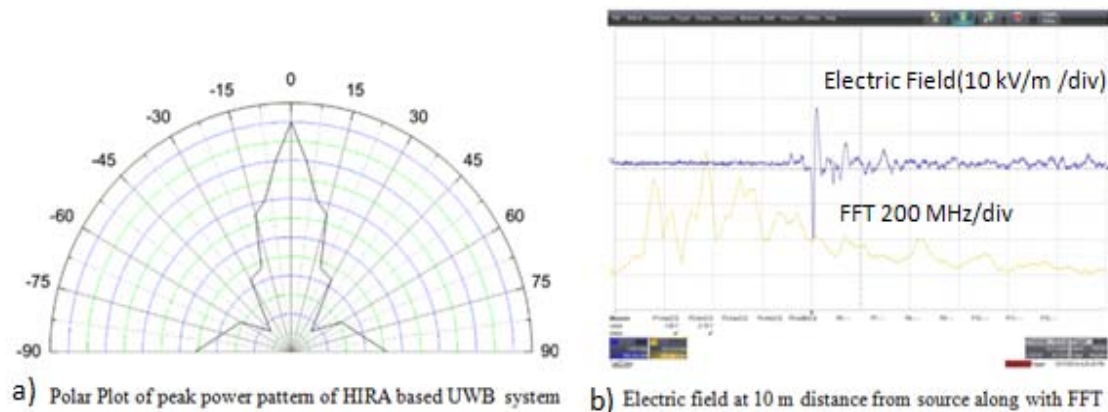


Fig. 8: Experimental results for HIRA based UWB system

Conclusion

Two high power UWB systems using balanced TEM horn antenna and Half Impulse Radiating Antenna have been developed at APPD, BARC. These systems have respectively got a figure of merit of 100 kV and 200 kV. Personal computer operation was disrupted at 20 m distance from the source using these systems. These systems can be used for vulnerability and susceptibility testing of electronic circuits and systems. These types of systems are also used in shielding effectiveness testing, buried target detection.

Acknowledgements

We would like to express our thanks to Dr. Amitava Roy for constant encouragement and valuable suggestions. We would also like to thank Mirza Danish Beg, S. G. Patil and S. P. Vaity for technical assistance provided in this work.

References:

1. V.I. Koshelev, Yu.I. Buyanov, Yu.A. Andreev, V.V. Plisko, K.N. Sukhushin, Ultrawideband Radiators of High-Power Pulses, Pulsed Power Plasma Science, 2001. PPPS-2001. Digest of Technical Papers (Volume:2)
2. Zhenru Gao, Huichang Zhao, Youchao Tu, Xiang Fang, Xingang Zhou, and Jing Liu, Study on the Ultra-Wide Band High Power Microwave Coupling Effect on Electronic Fuze System, Automation Congress, 2008. WAC 2008. World
3. F. Olsson, M. Larbi, M. Karlsson, H. Christensen, G. Filipsson, and B.O. Bergman, Experiments and Simulations of a Compact UWB Pulse Generator Coupled to an Exponential Flared TEM-Horn Antenna. ©2006IEEE
4. D. D. P. Kumar, S. Mitra, K. Senthil, Archana Sharma, K. V. Nagesh, S. K. Singh, J. Mondal, Amitava Roy and D. P. Chakravarthy, "Characterization and analysis of a pulse power system based on Marx generator and Blumlein", Rev. Sci. Instrum. 78 115107 (2007).
5. Adrian Eng-Choon Tan, Kashish Jhamb, and Karumudi Rambabu, "Design of Transverse Electromagnetic Horn for Concrete Penetrating Ultra wideband Radar", IEEE Transactions On Antennas And Propagation, Vol. 60, No. 4 (April 2012).
6. C. A. Balanis, "Antenna Theory Analysis and Design", third edition, John Wiley and Sons (2005).
7. G. D. Sower et al. "Low Voltage Prototype Development of an Ultra-Wideband High-Voltage Unzipper Balun", Measurement Notes, Note 50, December 1996.
8. E. G. Farr and G. D. Sower, "Design Principles of Half Impulse Radiating Antennas," Sensor and Simulation note 390, 1995.

Reaction Dynamics Around Coulomb Barrier With Weakly Bound Nuclei

Vivek Vijay Parkar

Nuclear Physics Division

Vivek Vijay Parkar is the recipient of the Indian National Science Academy Award for the year 2015

Abstract

The effect of weakly bound structure and low separation energies in ${}^6\text{Li}$ and ${}^9\text{Be}$ nuclei on different reaction mechanisms, *viz.*, elastic scattering and fusion reaction is studied in detail with large number of targets at energies around the Coulomb barrier. It is observed that the inclusion of breakup channel brought in by these weakly bound nuclei is playing a major role in different reaction channels in a given nuclear reaction.

Introduction

In recent years, the study of the reaction dynamics involving weakly bound nuclei has become one of the most intriguing and challenging problems in low energy nuclear physics [1]. The interest in understanding the influence of break-up on other reaction channels has indeed received a fillip in recent years, especially because of the recent advent of radioactive ion beam (RIB) facilities in different laboratories around the world. These RIB facilities can accelerate the nuclei away from line of stability (weakly bound unstable/exotic nuclei), which is not possible from conventional particle accelerators. The understanding of the fusion process using RIB has a great impact on the production of super heavy elements and in reactions of astrophysical interest. At present, as the intensities and beam resolution of RIBs are limited, it is difficult to carry out precision measurements using RIBs. Hence experiments with stable weakly bound projectiles like ${}^6\text{Li}$ and ${}^9\text{Be}$ are very important in understanding the various reaction mechanisms, *viz.*, the effect of breakup on the fusion process, significance of incomplete fusion etc. The study of reactions induced by such weakly bound stable nuclei would provide a basis to understand the reaction mechanisms of weakly bound unstable nuclei. Such reactions provide the platform to establish the best experimental techniques and reaction models required for the best study of exotic nuclei available at RIB facilities with low intensities.

The small separation energies e.g., ${}^7\text{Li} \rightarrow \alpha + t$, $S_{\alpha,t} = 2.47$ MeV, ${}^6\text{Li} \rightarrow \alpha + d$, $S_{\alpha,d} = 1.47$ MeV, ${}^9\text{Be} \rightarrow \alpha + {}^5\text{He}$, $S_{\alpha,{}^5\text{He}} = 2.47$ MeV etc., suggests that these nuclei can easily break in the nuclear or Coulomb field, which in turn can

influence the scattering and/or reaction cross-sections. With this in view, we have carried out several investigations to understand the reaction mechanisms involving these stable weakly bound projectiles on a range of target nuclei. Some of the important results are discussed in this report.

Precision measurement of elastic scattering in ${}^7\text{Li}$, ${}^9\text{Be} + {}^{208}\text{Pb}$ reactions below Coulomb barrier energies for investigation of dipole polarizability and cluster structure:

The Coulomb field due to the target nucleus induces a dipole moment in the projectile. The interaction of the electric field with the projectile dipole moment leads to a polarization potential which is attractive. As a result the Coulomb potential gets reduced and which in turn modifies the elastic scattering at energies below the Coulomb barrier. By measuring the small but measurable deviation from pure Coulomb scattering arising due to dipole moment of the projectile, it is possible to determine the dipole polarizability of the projectile. With this in mind, we have carried out high precision elastic scattering measurements for ${}^7\text{Li}$ and ${}^9\text{Be}$ scattering from ${}^{208}\text{Pb}$ at several energies both deep below and around the Coulomb barrier.

Dipole polarizability of a nucleus arises due to the fact that during a collision between two nuclei, the presence of strong electric field distorts the charge distribution of the nuclei as protons and neutrons are forced to move in opposite direction resulting in an additional interaction that modifies the Coulomb potential. As the dipole operator leads to transition between states of opposite parity and for normal nuclei, states of opposite parity are at high excitation energy, the effect of the coupling

between these states and hence dipole polarizability is very small for such strongly bound nuclei. For weakly bound nuclei due to low breakup threshold, continuum states of opposite parity are nearby which helps in excitation to these levels, e.g., in case of ${}^7\text{Li}$ with breakup threshold of only 2.47 MeV, positive parity $\alpha+t$ breakup states can couple to negative parity ground state via dipole operator. Theoretically the dipole polarizability parameter, α is defined as,

$$\alpha = \frac{8\pi}{9} \sum_{n \neq 0} \frac{B(E1, g.s. \rightarrow n)}{(E_n - E_0)}$$

which suggests that this parameter is strongly depending on $B(E1)$ value. Here E_n corresponds to the energy of the discretized state 'n' which is in continuum. Experimentally, the role of electric dipole polarizability (α) can be investigated by accurate measurement of elastic scattering of such weakly bound nucleus in the field of a heavy nucleus. This effect is quantified in terms of deviation from pure Rutherford scattering.

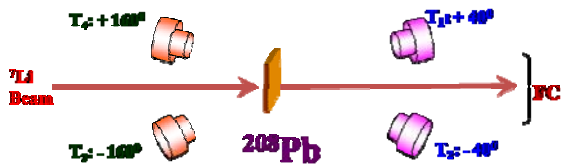


Fig. 1: Schematic illustration of experimental setup for the precise measurement of elastic scattering in ${}^7\text{Li}, {}^9\text{Be}+{}^{208}\text{Pb}$ reaction.

With this aim, measurements of elastic scattering cross-section of ${}^7\text{Li}$ from ${}^{208}\text{Pb}$ have been performed at energies from 18 to 28 MeV (Coulomb barrier \sim 30 MeV). A high precision measurement (statistical error $<$ 0.5 %) was achieved by measuring double ratio (thereby avoiding various systematical errors)

$$R = \frac{\sigma(E_1, \theta_1) / \sigma(E_1, \theta_2)}{\sigma(E_2, \theta_1) / \sigma(E_2, \theta_2)} = \frac{C(E_1, \theta_1) / C(E_1, \theta_2)}{C(E_2, \theta_1) / C(E_2, \theta_2)}$$

where, E_1, E_2 are two bombarding energies and θ_1 and θ_2 are two scattering angles. $C(E, \theta)$ is the number of counts recorded in the detector at energy E and angle θ . In this experiment, $\theta_1 = 40^\circ, \theta_2 = 160^\circ$ and $E_1 < E_2$ ($E_1 = 16$ MeV and $E_2 = 18 - 28$ MeV). Two such identical telescopes were placed symmetrically to the left and right of the incident beam at $\pm 40^\circ$ and $\pm 160^\circ$ to eliminate, in the first order, possible beam wandering. The schematic of experimental setup is given in Fig. 1. The measured ratio was plotted as a function of incident energy which showed the deviation from $R = 1$.

The Continuum Discretized Coupled Channel (CDCC) calculations, which take into account the unbound states of the projectile and coupling with the ground state, were performed to explain this ratio, and the value of dipole polarizability extracted. ${}^7\text{Li}$ was assumed to have $\alpha+t$ cluster structure with the well-known $\alpha-t$ binding potential and couplings were included between ground state, inelastic state of ${}^7\text{Li}$ and the resonant and non-resonant continuum states. The non-resonant continuum states above breakup threshold were discretised into momentum bins of width 0.25 fm $^{-1}$ with respect to the momentum of the $\alpha+t$ relative motion. The wave functions for the continuum bins were normalized to unity. Each bin was treated as an excited state of ${}^7\text{Li}$ with E_x equal to the mean bin energy. The scattering wave functions were then calculated at this energy and energy independence within the bin was assumed. For $\alpha+{}^{208}\text{Pb}$ and $t+{}^{208}\text{Pb}$ potential, required for cluster folding form factor calculations, global optical potentials evaluated at four- and three-seventh of the projectile energy were used. A energy-dependent renormalisation factor was built-in from fitting the existing data at slightly higher energies on elastic and fusion cross section simultaneously which was then extrapolated to the energy of interest. Best agreement between the data and CDCC calculations was obtained and the value of the dipole polarizability ($\alpha=0.045$ fm 3) extracted [2]. In Fig. 2, comparison between measured ratio with CDCC calculations is shown for ${}^7\text{Li}+{}^{208}\text{Pb}$ reaction.

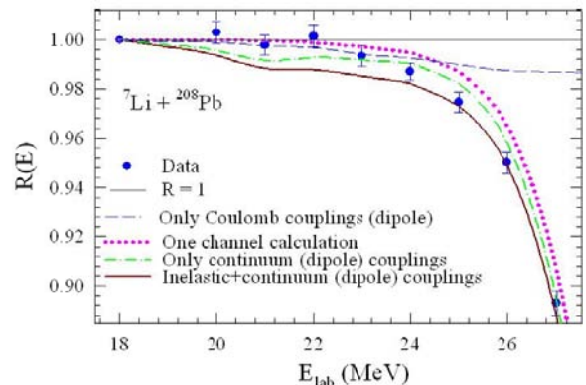


Fig 2: Comparison of measured ratio with CDCC calculations in ${}^7\text{Li}+{}^{208}\text{Pb}$ reaction

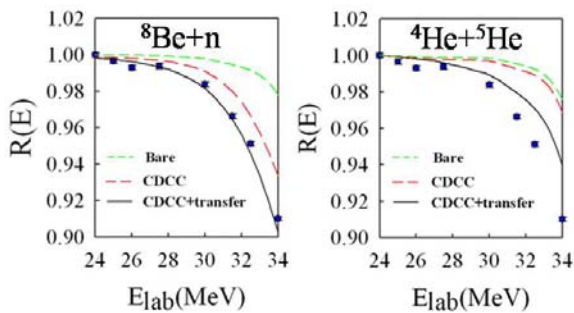


Fig 3: Measured ratio with CDCC calculations in ${}^9\text{Be}+{}^{208}\text{Pb}$ reaction assuming two cluster structures ${}^8\text{Be}+n$ and ${}^4\text{He}+{}^5\text{He}$

Similar precision elastic scattering measurements and CDCC calculations were also performed for ${}^9\text{Be}+{}^{208}\text{Pb}$ reaction. The two cluster structures of ${}^9\text{Be}$, namely ${}^4\text{He}+{}^5\text{He}$ and $n+{}^8\text{Be}$ were used in two independent CDCC calculations along with neutron transfer channel. It is observed that the $n+{}^8\text{Be}$ structure (see Fig. 3) is more appropriate in comparison to ${}^4\text{He}+{}^5\text{He}$ structure for explaining the data over a large energy range [3].

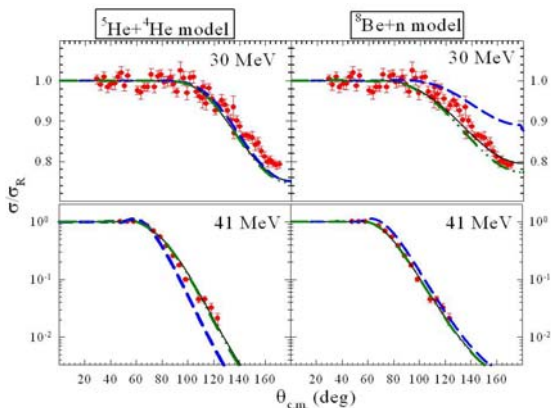


Fig. 4: The comparison of measured elastic scattering data for ${}^9\text{Be}+{}^{28}\text{Si}$ reaction with coupled channels calculations from two models: ${}^5\text{He}+{}^4\text{He}$ (left column) and ${}^8\text{Be}+n$ (right column)

To validate these two cluster structures of ${}^9\text{Be}$, we have also considered the available elastic scattering angular distribution data with ${}^{28}\text{Si}$, ${}^{64}\text{Zn}$, and ${}^{144}\text{Sm}$ targets. The results of the calculations suggest that the breakup coupling effects are significant for the ${}^4\text{He}+{}^5\text{He}$ cluster model above the barrier energies, while they are dominant at relatively lower energies for the ${}^8\text{Be}+n$ model. The addition of a one-neutron stripping channel in the ${}^8\text{Be}+n$ model gives an overall good description of the elastic data for all the systems considered [3]. In Fig. 4, the measured elastic scattering angular distribution data for ${}^9\text{Be}+{}^{144}\text{Sm}$ reaction is shown along with calculations using two cluster structures.

Fusion cross-sections in ${}^6\text{Li}$ and ${}^9\text{Be}$ induced reactions:

Fusion of two colliding nuclei around the Coulomb barrier is a complex phenomenon. Quantum mechanical barrier penetration occurs in a multidimensional space and coupling to the internal degrees of freedom of the participating nuclei plays an important role. There are several interesting features associated with the fusion process. Experimentally measured sub-barrier fusion cross sections for tightly bound nuclei are enhanced by several orders of magnitude over the predictions of the simple one-dimensional barrier penetration models (1DBPM). The observed enhancement is understood in terms of couplings to the low-lying collective excited states of target and projectile and to transfer of one or more nucleons. Understanding the fusion process with weakly bound nuclei, either stable or short-lived, brings in a new set of challenges. To start with, the definition of fusion cross section itself needs to be clarified. There are similar processes such as the incomplete fusion (ICF), wherein only part of the projectile fuses with the target. Hence, a distinction needs to be made wherever possible between complete fusion (CF), which involves the fusion of the projectile as a whole with the target, and total fusion (TF), which also includes the ICF component. The fusion reactions with weakly bound stable/unstable nuclei are of astrophysical interest and can give insight for super heavy element production. As far as the spectroscopy point of view is concerned, fusion evaporation reactions are the usual way to get the high spin structure of excited nuclei. In addition, weakly bound nuclei like ${}^6\text{Li}$, ${}^9\text{Be}$, ${}^{10,11}\text{B}$ beams are ideal for studying high spin states of stable and neutron rich nuclei produced through ICF reactions.

In the case of reactions where at least one of the colliding nuclei has a sufficiently low binding energy, the break-up becomes an important process. This break-up, if considered as a loss of flux from the incident channel, then it should suppress the fusion cross-sections, but if considered as one more channel for coupling in addition to transfer or inelastic, then it is supposed to enhance the fusion cross-section at below Coulomb barrier energies. We have performed several fusion cross-section measurements with stable weakly bound ${}^6\text{Li}$ and ${}^9\text{Be}$ nuclei on several targets viz., ${}^{89}\text{Y}$, ${}^{90}\text{Zr}$, ${}^{124}\text{Sn}$, ${}^{159}\text{Tb}$, ${}^{144,152}\text{Sm}$, ${}^{197}\text{Au}$, ${}^{198}\text{Pt}$ etc. Mainly two methods of online and/or offline gamma ray measurement techniques are utilized to extract the evaporation residue (ER) and hence fusion cross-sections. In Fig. 5 (A-C), one of the

examples for each projectile is shown along with coupled channels (CC) calculations. The measured CF cross-sections are found to be suppressed at above barrier energies by $\sim 32\%$, 26% , and 28% for ${}^6\text{Li}$, ${}^7\text{Li}$ and ${}^9\text{Be}$ respectively w.r.t. CC calculations [5-7]. In Fig. 5 (A) and (C), we have also shown the comparison with the fusion cross-sections from tightly bound nuclei forming the

similar compound nucleus, which also confirms the suppression. In Fig. 5 (D), we have plotted the systematic of this suppression factor (FCF) w.r.t. the product of projectile and target charge ($Z_p \cdot Z_T$) which shows (i) For a particular projectile, the suppression factor is more or less independent of the product $Z_p \cdot Z_T$ and (ii)

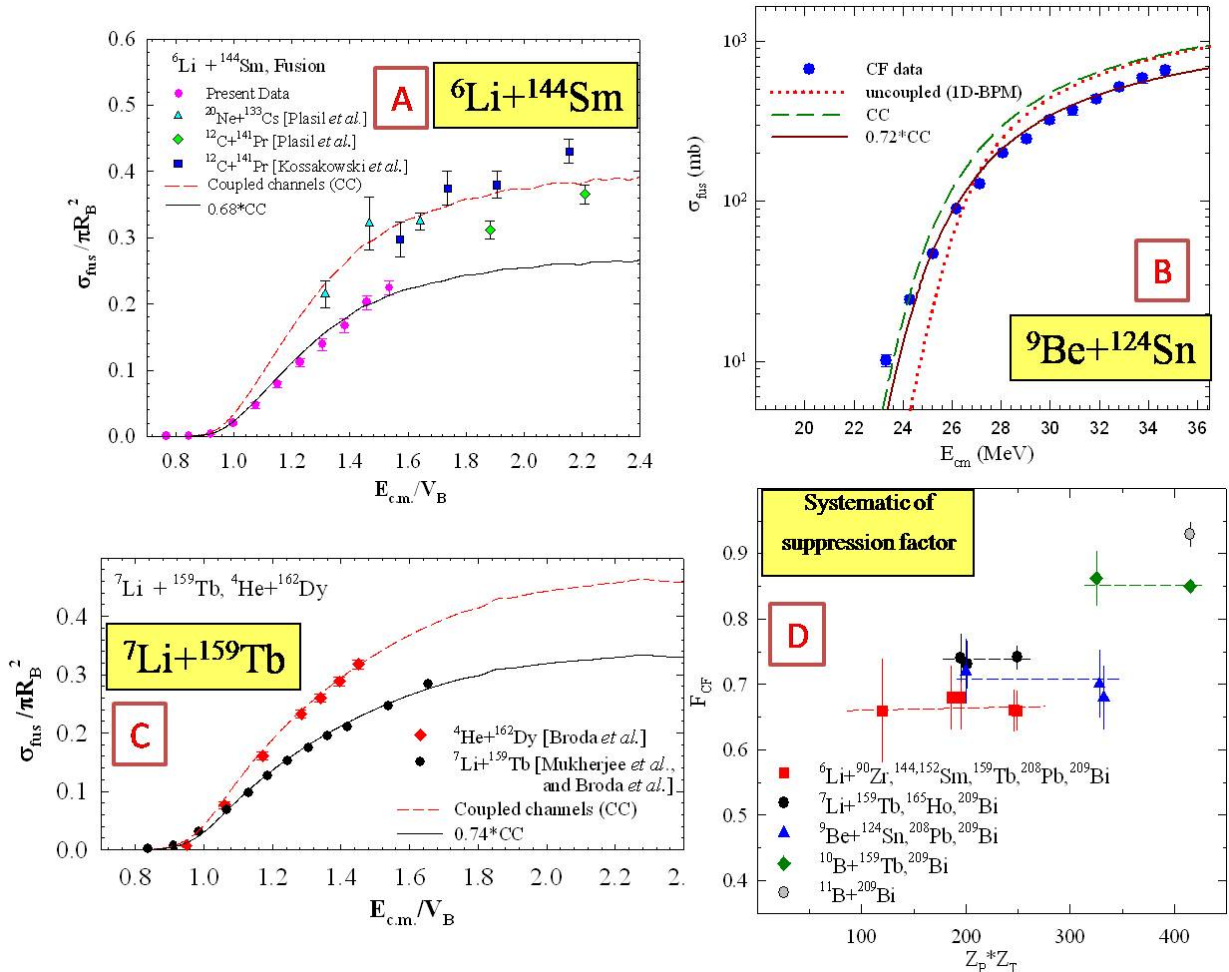


Fig 5: Measured Complete Fusion (CF) cross-sections for (A) ${}^6\text{Li} + {}^{144}\text{Sm}$ (B) ${}^9\text{Be} + {}^{124}\text{Sn}$ (C) ${}^7\text{Li} + {}^{159}\text{Tb}$ were compared with Coupled Channel calculations. The obtained suppression factor for 6Li, 7Li, 9Be is following the systematic w.r.t. $Z_p \cdot Z_T$ as shown in (D). See text for details.

Suppression increases with decreasing breakup threshold of the projectile [5].

Summary and Conclusion:

We have performed high precision elastic scattering measurements over a range of energies, from sub-barrier to near barrier for ${}^7\text{Li}, {}^9\text{Be} + {}^{208}\text{Pb}$ reactions. The ratio method of forward to backward elastic scattering events ruled out all the systematic errors of the measurement. The statistical accuracy obtained was close to 0.5%. The

CDCC calculations have been performed and the dipole polarizability parameter was extracted. Also in the case of ${}^9\text{Be}$, cluster structure of $8\text{Be} + n$ is found to be favorable over ${}^4\text{He} + {}^5\text{He}$ structure.

In the study of fusion of weakly bound nuclei with range of targets, we observed that the complete fusion cross-sections are suppressed compared to the CC calculations. We have plotted the systematic of the observed suppression factor w.r.t. charge product of projectile and

target (ZP^*ZT). The suppression factor (FCF) for a particular projectile is found to be independent of ZP^*ZT . The suppression increases with decreasing the breakup threshold.

In the near future, the rapid development of upcoming Radioactive Ion Beam facilities, viz., FAIR and SPIRAL2, will provide more weakly bound unstable nuclei away from the line of stability, for which one can extend similar kind of study of dipole polarizability as well as cluster structure to great detail using these precision elastic scattering measurements. The systematic of fusion suppression observed with stable weakly bound nuclei can be extended in studies with these Radioactive Ion Beams.

Acknowledgement:

I am grateful to all the collaborators for help and support at various stages during this research work. I also acknowledge the Pelletron-LINAC accelerator staff at TIFR, Mumbai for giving excellent quality of beam during this research.

References

1. L.F. Canto et al., Phys. Rep. 596, 1 (2015)
2. V.V. Parkar et al., Phys. Rev. C 78, 021601(R) (2008)
3. S. K. Pandit et al., Phys. Rev. C 84, 031601(R) (2011)
4. V.V. Parkar et al., Phys. Rev. C 87, 034602 (2013)
5. V.V. Parkar et al., Phys. Rev. C 82, 054601 (2010)
6. P. K. Rath et al., Phys. Rev. C 79, 051601(R) (2009)
7. V. Jha, V. V. Parkar, S. Kailas, Phys. Rev. C 89, 034605 (2014)

AUTHOR INDEX

A

| | |
|------------|----|
| Abhishant | 51 |
| Acharya S. | 42 |
| Agarwal K. | 51 |
| Alex M. | 65 |

B

| | |
|------------------|-----|
| Badodkar D.N. | 61 |
| Bakhatsing R. I. | 42 |
| Barnwal R. | 42 |
| Basu S. | 124 |
| Bhasikuttan A.C. | 6 |
| Bhattacharjee D | 42 |
| Bhattacharya S. | 77 |
| Bhattacharyya D. | 18 |
| Biswas A. | 18 |
| Biswas S. | 93 |
| Bose S.K. | 102 |

C

| | |
|-----------------------|-----|
| Chakravarty R. | 110 |
| Chandan S. | 42 |
| Chandraker D.K. | 24 |
| Chandrakumar K. R. S. | 35 |
| Cherian S. | 56 |
| Choudwary N. | 42 |

D

| | |
|--------------|----|
| Dhavle A. S. | 42 |
| Dixit K. P. | 42 |

G

| | |
|-------------|----|
| Ghodke S.R. | 42 |
| Ghosh A. | 77 |
| Goswami M. | 71 |
| Gundra K. | 83 |

H

| | |
|--------------|-----|
| Hadagali P.I | 124 |
|--------------|-----|

J

| | |
|----------------|-----|
| Jaju A. | 102 |
| Janvin Itteera | 98 |
| Jat R.A. | 106 |
| Jayarajan K. | 61 |
| Jha A.K. | 51 |
| Jha S.N. | 18 |

K

| | |
|----------------|-----|
| Karn K N. | 124 |
| Kulkarni P.P. | 24 |
| Kumar Mahendra | 42 |
| Kumar Mukesh | 24 |
| Kumar P. | 10 |
| Kumar R. | 127 |

M

| | |
|--------------|--------|
| Malhotra S. | 10, 98 |
| Mammen S. | 77 |
| Mishra E. | 10 |
| Mishra V.K. | 124 |
| Mitra S. | 127 |
| Mittal K. C. | 127 |
| Mondal J. | 42 |

N

| | |
|-------------|----|
| Nayak C. | 18 |
| Nayak A.K. | 24 |
| Nayak S. | 42 |
| Nimje V. T. | 42 |

P

| | |
|-------------|-----|
| Pal P. | 102 |
| Parkar V.V. | 133 |

R

| | |
|-----------------|-----|
| Rajawat R. K. | 127 |
| Rao Mala N. | 124 |
| Roychowdhury P. | 42 |

S

| | |
|-------------------|-----|
| Sahoo N.K. | 18 |
| Sandur S.K. | 1 |
| Sarngadharan P.V. | 61 |
| Sengupta C. | 77 |
| Sengupta S. | 77 |
| Senthil K. | 127 |
| Sharma A. | 127 |

| | |
|-----------------|-----|
| Sharma V. | 42 |
| Shete P.P. | 102 |
| Singh Kumud | 98 |
| Singh Ramnik | 124 |
| Singh S.K. | 127 |
| Sony B. | 61 |
| Srinivasu K. | 119 |
| Srivastava S.P | 124 |
| Sundararajan M. | 116 |

| | |
|-----------|----|
| T | |
| Teotia V. | 10 |
| Tyagi M. | 89 |



Edited & Published by :
Head, Scientific Information Resource Division
Bhabha Atomic Research Centre, Trombay, Mumbai 400 085, India